



**Classe di Scienze**  
**Corso di perfezionamento in Astrochimica**  
**XXXIV ciclo**

---

**Transformation pathways of polycyclic  
aromatic hydrocarbons and biomolecule  
precursors of astrochemical origin under  
model conditions of prebiotic relevance**

---

Settore Scientifico Disciplinare CHIM/06

***Candidata:***

Dr.ssa Valeria Lino

***Relatore:***

Prof. Paola Manini

***Supervisione interna:***

Prof. Vincenzo Barone

*Anno accademico 2023–2024*



*"I am among those who think that science has great beauty. A scientist in his laboratory is not only a technician: he is also a child placed before natural phenomena which impress him like a fairy tale."*

*Marie Curie*



# TABLE OF CONTENTS

<b>Abstract</b> .....	1
<b>List of Publications</b> .....	9
<b>Communications at meetings</b> .....	11
<b>List of Acronyms</b> .....	12
<b>Chapter 1. General Introduction</b> .....	14
1.1 Panspermia hypothesis: the exogenous delivery .....	17
1.1.1 Interstellar medium chemistry .....	17
1.1.2 Detection of molecules in the interstellar medium .....	20
1.1.3 Dust grains and photochemistry of icy mantles .....	24
1.1.4 Polycyclic aromatic hydrocarbons (PAHs) .....	35
1.1.4.1 Photochemistry of PAHs .....	49
1.2 Endogenous synthesis of the prebiotic compounds on Earth .....	60
1.2.1 Pioneering ideas and early experiments .....	60
1.2.2 Timeline for the origin of life on Earth .....	64
1.2.3 The link between the origin of life and hydrothermal systems .....	66
1.3 Role of minerals .....	71
1.4 Aims of the research work .....	72
References .....	75

<b>Chapter 2. High-energy proton beam irradiation of oxyPAHs adsorbed on meteorites</b> .....	91
2.1 Introduction .....	91
2.2 Results and Discussion .....	96
2.2.1 Preparation, irradiation and analysis of samples .....	96
2.2.2 Irradiation of 1-naphthalene in presence of meteorites .....	100
2.2.3 Irradiation of 1,8-dihydroxynaphthalene in presence of meteorites .....	112
2.2.4 Mechanistic modelling .....	119
2.3 Conclusions .....	122
2.4 Experimental section .....	125
References.....	140
<b>Chapter 3. Photo-processing and thermal desorption of PA(N)Hs and COMs on ice dust grains</b> .....	147
3.1 Introduction .....	147
3.2 Results and Discussion .....	159
3.2.1 Photo-processing and thermal desorption of acetaldehyde and acetonitrile on ice dust grains .....	160
3.2.1.1 Pure acetaldehyde ice .....	161
3.2.1.2 Pure acetonitrile ice .....	166
3.2.1.3 Ice mixture CH <sub>3</sub> CN:CH <sub>3</sub> COH (1:6) .....	173

---

3.2.1.4 Ice mixture CH <sub>3</sub> CN:CH <sub>3</sub> COH:H <sub>2</sub> O (1:1:3).....	179
3.2.2 Photo-processing and thermal desorption of naphthalene and quinoline on ice dust grain.....	187
3.2.2.1 TPD measurements of naphthalene and quinoline on ice dust grains .....	188
3.2.2.2 UV radiation effects on naphthalene and quinoline adsorbed on cold finger and olivine: mass spectrometry analysis .....	x
3.3 Conclusions .....	x
3.4 Experimental section .....	x
References .....	x

**Chapter 4. OxyPAH-polymers as mediators for prebiotic processes on early Earth: synthesis and characterization**

4.1 Introduction .....	x
4.2 Results and Discussion .....	x
4.2.1 Spectrophotometric analysis .....	x
4.2.1.1 1,8-Dihydroxynaphthalene .....	x
4.2.1.2 1-Naphthol.....	x
4.2.2 Laser flash photolysis (LFP) experiments .....	x
4.2.3 Isolation and characterization of oligomer intermediates in the oxidation of 1,8-DHN and 1-HN .....	x
4.2.3.1 1,8-Dihydroxynaphthalene .....	x

---

4.2.3.2 1-Naphthol .....	X
4.2.4 Isolation and characterization of polymers from 1,8-DHN and 1-HN .....	X
4.2.4.1 1,8-Dihydroxynaphthalene .....	X
4.2.4.2 1-Naphthol .....	X
4.3 Conclusions .....	X
4.4 Experimental section .....	X
References .....	X

**Chapter 5. Catalytic effect of OxyPAH-polymers in the chemical processes leading to the formation of the peptide bond**

5.1 Introduction .....	X
5.2 Results and Discussion .....	X
5.2.1 Study of catalytic effect of OxyPAH-polymers on oligomerization of glycine .....	X
5.2.1.1 IP-HPLC analysis of supernatant solutions .....	X
5.2.1.2 Analysis of residue .....	X
5.2.2 Study of catalytic effect of Solfatara thermal water on oligomerization of glycine .....	X
5.2.2.1 Analysis of thermal water .....	X
5.2.2.2 IP-HPLC analysis of supernatant solutions .....	X
5.2.2.3 Analysis of residue .....	X

---

5.3 Conclusions .....	x
5.4 Experimental section .....	x
References .....	x
<b>Chapter 6. Chemical transformations of PAHs and OxyPAHs in the thermal water of Solfatara</b>	
6.1 Introduction .....	x
6.2 Results and Discussion .....	x
6.2.1 Incubation of PAHs in thermal water samples.....	x
6.2.1.1 Analysis of the solid component .....	x
6.2.1.2 Analysis of the supernatant fraction .....	x
6.2.1.3 Main outcomes .....	x
6.3 Conclusions .....	x
6.4 Experimental section .....	x
References .....	x

---



## **ABSTRACT**

Which are the processes that have led to the emergence of life on Earth? The first forms of life were born on our planet or have been carried out from the Universe on Earth? Is there any possibility to find other forms of life in the Universe?

These are among the most frequent questions that astrochemists and astrobiologists are trying to address.

Various hypotheses have been raised by researchers to delineate the sequence of events that may have led to the formation of the building blocks of life. Miller demonstrated that under the extreme environments found on the early Earth, amino acids may have formed starting from gaseous methane, ammonia and water under the effect of an electrical discharge.<sup>1</sup> This result, together with the Oparin-Haldane primordial soup hypothesis, strongly supports the abiogenesis theory.

In this regard, many researchers suggested that hydrothermal systems and primordial rock pools at volcanic sites could be possible niches for the synthesis of organic compounds on early Earth. This theory was appealing because of the high availability of geochemical variables, such as water, thermal energy, pH, and continuous supplies of nutrient elements (e.g., K and P).<sup>2</sup> Moreover, these extreme natural fluctuating environments are characterized by cycles of hydration and dehydration resulting from evaporation and replenishment by hot springs and rainfall. Thereby, iterative wet and dry cycles and mineral surfaces at pool edges are thought to promote the polymerization of biomolecules. Several lines of evidence suggest that hydrothermal fields on early Earth resemble today's sites like Kamchatka,

Hawaii, Iceland, Yellowstone and Solfatara. This latter, situated to the west of Naples, is a large volcanic area of about 12 km in diameter that comprises 24 craters and volcanic features, including the Solfatara volcano with large and spectacular fumarole vents.

However, the identification of lipid membranes, amino acids, nucleotides and sugars on celestial bodies such as meteorites (i.e. the Murchison meteorite) and comets (i.e. the 67P-Churyumov/Gerasimenko comet) opened to the panspermia hypothesis.

Fundamental in this context is to reconstruct the possible sequence of events by which the complex organic molecules (COMs), such as formamide, formaldehyde, methanol and acetaldehyde, may have formed under the “inhospitable” conditions of the interstellar medium (ISM), where low temperature and density together with the intense ionizing radiations may prevent any kind of chemical reactivity.

An important role in this context is played by polycyclic aromatic hydrocarbons (PAHs). Widely diffused in the ISM, comets and meteorites, PAHs account for more than 20% of the universe’s carbon. Strong infrared (IR) emission bands between 3.3 and 11.3  $\mu\text{m}$ , seen in different astrophysical environments, evidenced their presence.<sup>3</sup> Get embedded in a water-rich ice matrix, PAHs are considered possible starting materials for the formation of molecules related to life.

Polycyclic aromatic nitrogen heterocycles (PANHs), in which one or more nitrogen atoms replace carbon atoms, are also believed to be present in the ISM and in ices.<sup>4</sup>

Besides serving as a possible source of small carbon molecules, PAHs and complex molecular species derived from their polymerization may also

provide protective matrices or mineral coating layers that can both promote or catalyze molecular synthesis and preserve biomolecules from damaging radiations.

In this context, growing interest is currently focused on oxyPAHs<sup>5</sup> because of their chemical properties such as higher polarity, ensuring stronger adsorption on minerals, a much higher reactivity, facility to polymerization. Even when present as minor components, oxyPAH may play a more impacting role in the carbon conversion processes.

Starting from this background, the research activity of my PhD course has been aimed at elucidating the nature of the reaction products that derive from PAHs and oxyPAHs under solid-state irradiation and heating conditions and the catalytic role of their polymers in prebiotically relevant processes.

By pursuing this approach, the work has been structured into two main topics concurring to assess the potential role of some representative components of the putative astrochemical pool of PAHs and oxyPAHs, namely naphthalene (NAPH), 1-naphthol (1-HN), and 1,8 dihydroxynaphthalene (1,8-DHN), in the origin of life scenarios:

1. study of the photochemical susceptibility of PAHs, oxyPAHs and COMs under simulated interstellar conditions;
2. study of the role played by PAHs and oxyPAHs in the chemical transformations occurring under early Earth conditions.

In detail, the attention has been focused on the following research activities:

- 1a. high energy proton beam irradiation of oxyPAHs adsorbed on meteorites;

- 1b. photo-processing and thermal desorption of PA(N)Hs and COMs on ice dust grains;
- 2a. chemical transformations of PAHs and oxyPAHs in the thermal water of Solfatara;
- 2b. synthesis and characterization of oxyPAH-polymers and study of their catalytic effect in the chemical processes leading to the formation of the peptide bond.

**1a. High energy proton beam irradiation of oxyPAHs adsorbed on meteorites**

Among the plausible multicomponent approaches proposed for the generation of biogenic molecules in prebiotic environments, the proton beam irradiation, modelling of the solar wind, in the presence of meteorites is one of the most interesting.

This section has been aimed at the study of the chemical modifications of 1-HN and 1,8-DHN promoted by high energy proton beam irradiation in the presence of meteorites and urea. To this aim, three different meteorites have been selected, including a stony-iron, an achondrite, and a chondrite type.

The structural characterization of the main reaction products was performed by gas-chromatography associated with mass-spectrometry (GC-MS) analysis and by comparison with authentic samples. The analysis of these data shows that the proton beam irradiation promotes the conversion of 1-HN and 1,8-DHN, into complex mixtures of oxygenated and oligomeric derivatives. The main identified products include polyhydroxy derivatives, isomeric dimers encompassing benzofuran and benzopyran scaffolds, and, notably, a range of quinones and perylene derivatives. The addition of urea expanded the range of identified species to include, among others, quinone diimines. The nitrogen

transfer from urea to reactive naphthoquinone intermediates might explain a possible mechanism for the initial formation of the C-N bond in complex heterocyclic derivatives.

### **1b. Photo-processing and thermal desorption of PA(N)Hs and COMs ices on ice dust grains**

The study of the interactions between molecules of prebiotic interest, such as PAHs and COMs, and interstellar ice dust grains is made in the framework of understanding how the solid phase interactions between molecules and grain surfaces and UV irradiation can significantly influence the thermal desorption process and so the presence of molecular species in the gas phase.

By pursuing this approach, we succeeded in identifying a set of products formed after the UV irradiation of water-ice mixtures of acetaldehyde ( $\text{CH}_3\text{COH}$ ), acetonitrile ( $\text{CH}_3\text{CN}$ ), NAPH and quinoline (QUIN) deposited on olivine grains, used as dust analog, thanks to the combination of Temperature Programmed Desorption (TPD) experiments and Electron Ionization (EI) mass spectrometry analyses.

In detail, monolayers of pure  $\text{CH}_3\text{COH}$ , pure  $\text{CH}_3\text{CN}$ , mixture  $\text{CH}_3\text{CN}:\text{CH}_3\text{COH}$  (1:6)  $\text{CH}_3\text{CN}:\text{CH}_3\text{COH}:\text{H}_2\text{O}$  (1:1:3), NAPH: $\text{H}_2\text{O}$  (1:10000) and QUIN: $\text{H}_2\text{O}$  (1:10000) were deposited on a hundred-micron thick layer made of olivine smaller than 5  $\mu\text{m}$ , at 10 K, in an ultra-high vacuum (UHV) chamber and were subjected to UV irradiation with photons in the 4-6 eV range.

Through the deep inspection of the products formed from pure ices and binary and ternary ice mixtures of  $\text{CH}_3\text{COH}$  and  $\text{CH}_3\text{CN}$ , it has been possible to delineate four main reaction pathways occurring under these conditions: photodissociation, recombination, isomerization, and hydrogen addition.

By subjected to UV irradiation the mixture with water (1:1:3), the mass spectrum showed that water dissociated itself and the fragmentation of the target molecules was reduced. Therefore, it seems that the presence of water mitigates the catalytic action carried out by UV irradiation.

A very relevant point emerging from the results is the origin of a series of key molecules, including prebiotic molecules (i.e., formamide, urea) and molecules detected in the interstellar medium (i.e., hydroxylamine, hydrogen cyanide).

The analysis of mass spectra of water-ice mixtures of NAPH and QUIN after UV irradiation indicates a dynamic interplay of species resulting from the fragmentation of water, those arising from the fragmentation of naphthalene or quinoline, and species resulting from the combination of both photo-products. Moreover, the shape of the TPD curves changed in the presence of the olivine substrate with the appearance of a second wider peak at higher temperatures, not shown in all the TPD measurements from the smooth nickel-plated cold finger. This finding highlighted how the interactions between the molecules and the surface of the grains can drive the presence of molecules in the gaseous phase.

The work has been carried out in association with Prof. Robert John Brucato at INAF Arcetri Astrophysical Observatory (FI).

## **2a. Chemical transformations of PAHs and oxyPAHs in the thermal water of Solfatara**

To explore the growth of potential prebiotic molecules in the natural geothermal environment of Solfatara and to investigate the chemical transformations suffered by NAPH, 1-HN and 1,8-DHN, these compounds have been incubated in the thermal water of Solfatara. After 48 h, the reaction

mixture was subjected to a centrifugation step to afford a supernatant solution, analysed by GC-MS, and a solid, analysed by attenuated total reflection (ATR) and UV-vis spectroscopies and mass spectrometry (MALDI).

From the overall view of isolated compounds, it emerges that three main different pathways of PAH transformation operate in concert in hydrothermal environments: 1) the functionalization pathway; 2) the erosion pathway; 3) the polymerization pathway.

Functionalization of the PAH scaffold via addition, removal or modification of functional groups, may generate a range of catalytic and templating sites that can direct self-assembly and synthetic processes. Degradation pathways leading to the erosion of the polycyclic scaffold can afford small aliphatic or chain branched precursors/building blocks with reactive groups like acids or ketones for the construction of diverse scaffolds of higher structural complexity. Polymerization, on the other hand, may generate organic surfaces, coatings, particles and layers on which adsorbed organic molecules can benefit from catalytic and protective effects under UV irradiation conditions.

## **2b. Synthesis and characterization of oxyPAH-polymers and study of their catalytic effect in the chemical processes leading to the formation of the peptide bond**

OxyPAHs can undergo oxidative processes leading to the formation of insoluble organic polymers that may be able to: 1) adsorb prebiotic molecule on their porous surface, 2) promote their interaction acting as a real catalyst, 3) protect the formed product from the impact of high energy radiations.

This study was aimed at assessing the peptide bond formation process starting from the amino acid glycine under wet-dry conditions. In this context, the effect of two novel potential catalytic systems has been investigated: 1) the

thermal water of Solfatara; 2) the polymers obtained from the oxidation of 1,8-DHN and 1-HN.

In a typical experiment, a water solution of glycine was prepared and kept at high temperature to induce the slow water removal. Subsequently, a same amount of water was used to rinse the residue and then another heating cycle was started. After the wet-dry cycles were completed, the water soluble and insoluble fractions were separately analyzed to check for the formation of both low molecular weight and high molecular weight oligomers of glycine.

IP-HPLC data showed the progressive consuming of the starting glycine and the simultaneous formation of dimeric products. This effect is more consistent at higher temperatures and cycling numbers. ATR and MALDI data of the residues indicated the presence of higher oligomeric products of glycine.

Overall, in all the reaction conditions investigated, the catalytic effect of oxyPAH-polymers and thermal water of Solfatara emerged, with higher yields of formation of oligoglycine observed even with respect to reactions carried out in the presence of the inorganic minerals and distilled water, used as references.

## LIST OF PUBLICATIONS

- P. Manini, **V. Lino**, P. Franchi, G. Gentile, T. Sibillano, C. Giannini, E. Picardi, A. Napolitano, L. Valgimigli, C. Chiappe, M. d'Ischia "A Robust Fungal Allomelanin Mimic: An Antioxidant and Potent  $\pi$ -Electron Donor with Free-Radical Properties that can be Tuned by Ionic Liquids" *ChemPlusChem*, 84, 1331-1337, **2019**.  
<https://doi.org/10.1002/cplu.201900195>. **(P1)**
- P. Manini, V. Lucci, **V. Lino**, S. Sartini, F. Rossella, G. Falco, C. Chiappe, M. d'Ischia "Synthetic mycomelanin thin films as emergent bio-inspired interfaces controlling the fate of embryonic stem cells" *J. Mater. Chem. B*, 8, 4412-4418, **2020**. <https://doi.org/10.1039/D0TB00623H>. **(P2)**
- B.M. Bizzarri, P. Manini, **V. Lino**, M. D' Ischia, M. Kapralov, E. Krasavin, J.E. Šponer, E. Di Mauro, R. Saladino "High Energy Proton Beam-Induced Polymerization/Oxygenation of Hydroxynaphthalenes on Meteorites and Nitrogen Transfer from Urea: Modeling Insoluble Organic Matter?" *Chem. Eur. J.*, 26, 14919–14928, **2020**. <https://doi.org/10.1002/chem.202002318>. **(P3)**
- P. Manini, **V. Lino**, G. D'Errico, S. Reale, A. Napolitano, F. De Angelis, M. d'Ischia, "Blackness is an index of redox complexity in melanin polymers" *Polym. Chem.* 11, 5005-5010, **2020**.  
<https://doi.org/10.1039/D0PY00700E>. **(P4)**
- **V. Lino** and P. Manini, "Dihydroxynaphthalene-Based Allomelanins: A Source of Inspiration for Innovative Technological Materials" *ACS Omega*, 7, 18, 15308–15314, **2022**.  
<https://doi.org/10.1021/acsomega.2c00641>. **(P5)**

- **V. Lino**, R. Castaldo, G. Gentile, P. Manini “Reusable Melanin-Based Biosorbents for Efficient Methylene Blue Removal: the New Frontier of Fungi-Inspired Allomelanin Coatings for Sustainable Water Remediation Processes”, *Materials Today Sustainability*, 21, 100283, **2023**. <https://doi.org/10.1016/j.mtsust.2022.100283>. (P6)
- **V. Lino**, P. Manini, M. Galeotti, M. Salamone, M. Bietti, O. Crescenzi, A. Napolitano, M. d’Ischia “Antioxidant Activities of Hydroxylated Naphthalenes: the Role of Aryloxy Radicals” *ChemPlusChem*, 88, e202200449, **2023**. <https://doi.org/10.1002/cplu.202200449>. (P7)
- M. A. Corazzi, **V. Lino**, P. Manini, G. Poggiali, J. R. Brucato “Photoprocessing and thermal desorption of acetaldehyde, acetonitrile, and water ice mixtures on olivine grains: TPD and mass spectra analyses”. Submitted
- **V. Lino**, M. Toscanesi, P. Manini, M. Trifuoggi, M. Moracci, M. d’Ischia “Meteorite organic components generated from PAHs in a model prebiotic environment: reassessing the aromatic world hypothesis of life”. Manuscript in preparation.
- **V. Lino**, M. A. Corazzi, J. R. Brucato, G. D. Fedele, P. Manini “Thermal desorption of PA(N)Hs-water ice mixtures from dust grains”. Manuscript in preparation.
- **V. Lino**, P. Manini, B.M. Bizzarri. “The role of urea and IOM’s precursors in the prebiotic synthesis of uridine and adenosine nucleotides”. Manuscript in preparation.

## COMMUNICATIONS AT MEETINGS

- *Solid State Photochemistry of Hydroxylated Naphthalenes: Modeling Free Radical Pathways of Polycyclic Aromatic Hydrocarbons (PAHs) on Minerals of Astrochemical Relevance.* V. Lino, S. Potenti, P. Manini, O. Crescenzi, A. Napolitano, M. d'Ischia, M. Bietti, O. Lanzalunga, J. R. Brucato, V. Barone. E-WISPOC19, Bressanone, Italy. Poster presentation **(PP1)**.
- *“Blackness” is an index of redox complexity in melanin polymers.* V. Lino, P. Manini, G. D’Errico, S. Reale, A. Napolitano, F. De Angelis, M. d’Ischia. SCI- ViSYOChem 2020. Poster presentation **(PP2)**.
- *High Energy Proton Beam-Induced Polymerization/Oxygenation of Hydroxynaphthalenes on Meteorites and Nitrogen Transfer from Urea: Modeling Insoluble Organic Matter? V. Lino, B.M. Bizzarri, P. Manini, M. d’Ischia, M. Kapralov, E. Krasavin, E. Di Mauro, R. Saladino.* Virtual AbGradE 2021. Oral presentation **(OP1)**.
- VIRTUAL 5<sup>th</sup> NoRCEL Conference, 2021.
- *Catalytic effect of oxy-PAH polymers on oligomerization of glycine under wet-dry conditions.* V. Lino, and P. Manini. VII Congresso Nazionale di Scienze Planetarie 2022. Napoli, Italy. Oral presentation **(OP2)**.
- *The analogy between Insoluble Organic Matter in chondrites and archetypal melanin-like PAH-based reveals a novel scenario at the origin of life.* V. Lino and P. Manini. EAI summer school, Life on Earth and Beyond 2022. Ven Island, Sweden. Poster presentation **(PP3)**.
- Ischia advanced school of organic chemistry (IASOC) 2022, Ischia, Italy.

## **LIST OF ACRONYMS**

<b>ISM</b>	Interstellar Medium
<b>COMs</b>	Complex Organic Molecules
<b>IR</b>	Infrared
<b>PAHs</b>	Polycyclic Aromatic Hydrocarbons
<b>ISO</b>	Infrared Space Observatory
<b>TPD</b>	Thermal Programmed Desorption
<b>QMS</b>	Quadrupole Mass Spectrometer
<b>UIR</b>	Unidentified InfraRed
<b>PDR</b>	Photo-Dissociation Region
<b>DIBs</b>	Diffuse Interstellar Absorption Bands
<b>CCs</b>	Carbonaceous Chondrites
<b>MIRI</b>	Mid-Infrared Instrument
<b>JWST</b>	James Webb Space Telescope
<b>VUV</b>	Vacuum Ultraviolet
<b>2-HN</b>	2-Naphthol
<b>1,4-NP</b>	1,4-naphthoquinone
<b>2,6-DHN</b>	2,6-dihydroxynaphthalene
<b>2,7-DHN</b>	2,7-dihydroxynaphthalene
<b>PANHs</b>	polycyclic aromatic nitrogen heterocycles
<b>1,6-DHN</b>	1,6-dihydroxynaphthalene
<b>DRIFTS</b>	Diffuse Reflectance Infrared Fourier Transform Spectroscopy
<b>IOM</b>	Insoluble Organic Matter
<b>1,8-DHN</b>	1,8-Dihydroxynaphthalene
<b>1-HN</b>	1-Naphthol

<b>NAPH</b>	Naphthalene
<b>QUIN</b>	Quinoline
<b>HRP</b>	Horseradish peroxidase
<b>MB</b>	Methylene blue
<b>GC-MS</b>	Gas-chromatography Mass-spectrometry
<b>Oxy-PAHs</b>	oxygenated polycyclic aromatic hydrocarbons
<b>ATR</b>	Attenuated Total Reflection
<b>MALDI</b>	Matrix-Assisted Laser Desorption/Ionization
<b>UHV</b>	ultra-high vacuum
<b>NMR</b>	Nuclear Magnetic Resonance
<b>EPR</b>	Electron Paramagnetic Resonance
<b>TEM</b>	Transmission Electron Microscopy
<b>SEM</b>	Scanning Electron Microscope
<b>AISSP</b>	Ammonia-Induced Solid State Polymerization
<b>IP-HPLC</b>	Ion-Pairing High-Performance Liquid Chromatography
<b>DKP</b>	Diketopiperazine
<b>GLY</b>	Glycine
<b>SVOCs</b>	SemiVolatile Organic Compounds
<b>MSTFA</b>	2,2,2-trifluoro- <i>N</i> -methyl- <i>N</i> -(trimethylsilyl) acetamide
<b>VOCs</b>	Volatile Organic Compounds
<b>SPE</b>	Solid-Phase Extraction

# CHAPTER 1

## GENERAL INTRODUCTION

*“It must be admitted from the beginning that we do not know how life began. It is generally believed that a variety of processes led to the formation of simple organic compounds on the primitive Earth. These compounds combined together to give more and more complex structures until one was formed that could be called living. No one should be satisfied with an explanation as general as this.”*

-Stanley L. Miller and Leslie E. Orgel, *The Origins of Life on the Earth*, 1974

“When, where and how did life originate on Earth?” remains one of the most ancient questions that has been a subject of a long-standing debate among the scientific, religious, and philosophical fields.

The assessment of Miller and Orgel from around 48 years ago about the origin of life is currently still true in many ways. This doesn't mean that no progress has been made in this field, but rather that this topic is still an unsolved conundrum and a scientific consensus regarding some questions has still not been achieved, leaving many interesting questions yet to be answered.

Thus, nowadays, the question of the origin of life remains one of the most intriguing and challenging problems faced by scientists.

However, two alternative hypotheses have been proposed for the emergence of life on Earth: endogenous synthesis and exogenous delivery.

The endogenous hypothesis, namely the idea that life started on Earth from simple precursors (e.g., NH<sub>3</sub>, HCN, H<sub>2</sub>CO), water and some energy source, is

commonly assumed since the historical contributions by Oparin–Haldane hypothesis, in 1929,<sup>6,7</sup> and the Miller–Urey experiment in 1953.<sup>1</sup>

The scientific merit of these breakthroughs is the assumption that life originated on Earth through physicochemical processes that can be simulated and experimentally tested and not by means of miracles or spontaneous generations.

Recent evidences have revealed that life on Earth may have occurred in a hot little cycling pool near volcanic lands on early Earth, reviving Darwin’s hypothesis which stated that life has begun in a “warm little pond”. In fact, many researchers suggested that hydrothermal systems and primordial rock pools at volcanic sites could be possible niches for the synthesis of organic compounds on the early Earth. This theory was appealing because of the high availability of geochemical variables, such as water, thermal energy, pH and continuous supplies of nutrient elements (e.g., K and P). Moreover, these extreme natural fluctuating environments are characterized by cycles of hydration and dehydration resulting from evaporation and replenishment by hot springs and rainfall. Thereby, iterative wet and dry cycles and mineral surfaces at pool edges are thought to promote the polymerization of biomolecules. Several lines of evidence suggest that hydrothermal fields on early Earth resemble today’s sites like Kamchatka, Hawaii, Iceland, Yellowstone and Solfatara.

The endogenous theory has been the most likely scenario in the last 50 years.

However, with the discovery of a wide range of complex organic molecules in the interstellar medium (ISM) and within several celestial bodies (i.e. comets and meteorites), the exogenous delivery (Panspermia) hypothesis has been gaining increasing acceptance.

Indeed, the idea that the interstellar medium is such as “home” for a plethora of structurally different molecules, even though local temperatures and pressures were considered too low to permit any kind of chemical reactivity, was gradually conceived in the last decades.

This hypothesis predicts that the prebiotic organic materials, that originated elsewhere in the universe, may have been delivered on Earth by asteroids, comets and meteorites. As a matter of fact, it is well known that the typical influx rate for micrometeorites, estimated around  $\sim 10^7$  kg/year, increased significantly during the late heavy bombardment period, which lasted until 4 billion years ago.

Comets and interstellar dust are rich in organic molecules, essential for the emergence of life on Earth. The detection of complex biomolecules, such as amino acids, nucleotides, sugars and lipids, in meteorites collected across the planet, including the most famous Murchison meteorite,<sup>8-11</sup> is a clear evidence that these molecules survived despite the extreme pressures and temperatures of the impact onto the Earth surface also thanks to the presence of a reducing atmosphere.<sup>8</sup>

Therefore, it is conceivable that the starting building blocks of life were a gift from the meteorites, which triggered and accelerated the biosynthesis on Earth. Recently, an extension to this hypothesis has been proposed: the material-based Panspermia hypothesis.<sup>12</sup> In this scenario, Panspermia seeds are made of materials, such as polymers, prebiotically formed on a hypothetical donor planet and landed on a habitable planet via meteorites.

Primitive polymers must fulfil two criteria: 1) be robust and avoid degradation while enduring space exposure and 2) have the ability to modulate and trigger chemical evolution in the new environment.

From these overall considerations, it seems reasonable to conclude that both exogenous delivery and endogenous synthetic pathways provided prebiotically relevant organic material to the early Earth. Although the relative amounts are unclear, it is likely that both sources played significant roles in the emergence of life on the early Earth.

## **1.1 Panspermia hypothesis: the exogenous delivery**

### **1.1.1 Interstellar medium chemistry**

The ISM is the matter in which the stars in the universe are embedded. The ISM is mainly composed by interstellar gases (99%), mainly H and He, and for the 1% by tiny carbonaceous and silicate dust particles.

As stressed in Figure 1, the molecular complexity of the ISM is strongly dependent from the underlying physical evolution occurring during the star formation processes, such as the changes in density, temperature and intensity of irradiation.

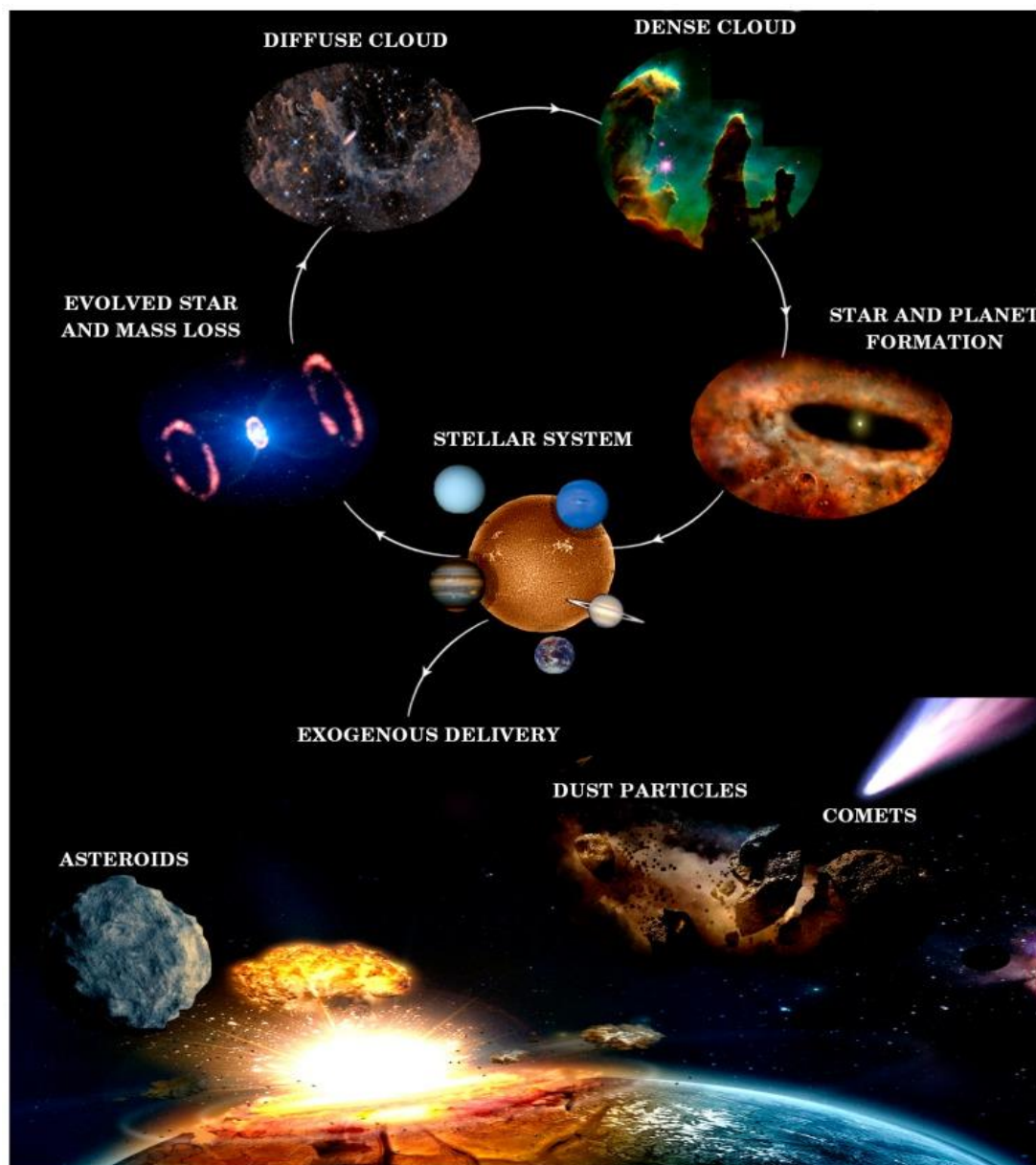


**Figure 1** | The cycle of organic molecules in the universe and the delivery of exogenous material on the primitive Earth. Image adapted from Ref. <sup>13</sup>

Diffuse clouds, with particle densities of  $10^2 - 10^3 \text{ cm}^{-3}$  and kinetic temperatures of a few hundred K,<sup>14</sup> are relatively optically transparent and continuously exposed to radiations, thus few molecules can survive. Hence, these clouds are dominated by atoms and ions, especially H and  $\text{H}^+$ , and most of the chemistry is mediated by gas-phase reactions.<sup>15</sup>

Gravitational forces produce the condensation of gas and dust, increasing the density of particles. Thus, diffuse clouds evolve into so-called dense, dark molecular clouds. As the name suggests, these latter are characterized by higher particle number densities, up to  $10^6 \text{ cm}^{-3}$ , very low temperatures (around 10 K) and are so compact that UV radiation cannot penetrate. In this environment we can observe the formation of icy dust grains and the main chemical reactions occur at the gas-solid interface leading to the formation of several species that are known as complex organic molecules (COMs).<sup>16-18</sup>

The dense clouds are considered to be the ‘stellar nurseries’ because is at this stage that they are formed. During the accretion of the star, we can observe the formation of the so-called protoplanetary disk in which celestial bodies such as planets, comets and asteroids are formed.

This interstellar organic matter underwent chemical processing during the formation of the solar system and was later incorporated into celestial bodies. In this way, dust grains are thought to be one of the main ingredients for planetary formation and the site where life has likely developed.<sup>19</sup>

Thereafter, the remnant planetesimals, in the form of comets and asteroids, impacted the young planets in the early history of the solar system.<sup>20</sup>

The large quantities of extra-terrestrial material delivered to young planetary surfaces during the heavy bombardment phase may have played a pivotal role in the origin of life.

### 1.1.2 Detection of molecules in the interstellar medium

The most appealing challenge of astrochemistry is the detection of prebiotic and biological molecules in the astrochemical environments and understanding the chemical evolution of simple atomic species toward complex organic molecules and the building blocks of life.

For many years, the hostile and inhospitable conditions of ISM, such as typical densities of  $10^4 \text{ cm}^{-3}$ , low temperatures of ices (10-100 K) and the permeation of high-energy radiation fields, including UV radiation, made the astronomers sceptical about the presence of molecular species, in particular those with a prebiotic character. But, surprisingly, the ISM hosts a very rich and varied organic chemistry. This because radical reactions that typically occur at the gas phase, generally lack energy barriers and can thus occur at the low temperatures typical of interstellar ices. Moreover, as mentioned before, the dense molecular clouds are shielded from the onslaught of harsh UV radiations by interstellar dust particles that efficiently absorb them, permitting the synthesis and the survival of gas-phase species.

Interstellar molecules are typically identified by measuring their gas-phase spectra with telescopes. Our knowledge of the universe chemical inventory has been obtained and continuously updated by means of synergy between astronomical observation and laboratory, both experimental and theoretical, studies.

For identifying molecules, some spectroscopic techniques are better than others. The most important of these is microwave or rotational spectroscopy, given its intrinsic high resolution and high sensitivity. Molecules with a dipole moment display rotational lines that can be observed by using radiowaves. Rotational transitions occur between the lowest energy levels ( $E_{\text{rot}} \leq 100 \text{ cm}^{-1}$ ),

and since interstellar gas is typically cold, the population of rotational levels is heavily favored. As a consequence, about 90% of all known interstellar molecules have been detected via their pure rotational transitions. Nevertheless, this technique is blind to completely symmetric molecules (i.e. with no permanent dipole moment), almost blind to very symmetric molecules (i.e. with very small dipole moment) and molecules trapped in the condensed phase that cannot undergo free rotation, making the radio observations impossible.

Another technique is that observing the vibrational transitions occurring in the infrared (IR) region. They require an external field for excitation, such as that of a young/old star or a shock wave,<sup>21</sup> since are sufficiently high in energy ( $E_{\text{vib}} \sim 100\text{--}5000 \text{ cm}^{-1}$ ).

The promotion of an electron to a higher-lying molecular orbital is the highest-energy transition ( $E_{\text{elec}} > 10,000 \text{ cm}^{-1}$ ). Electronic transitions occur in the optical and UV parts of the electromagnetic spectrum (400–700 nm). They are usually observed only in diatomic molecules and typically require background star radiation for the excitation mechanism in the ISM.

Molecules in the solid phase can be observed too. However, solid-state spectra are typically measured in the IR, because are allowed only vibrational motions, but do not have the specificity found in the gas phase.

The field of astrochemistry started in the 1940s with the detection of CH, CN, and CH<sup>+</sup> by optical absorption spectroscopy.<sup>22–24</sup> However, about 30 years passed until the discovery of more complex species, such as ammonia detected by Townes and co-workers.

In 1969, the detection of water and formaldehyde, the first organic molecule, witnessed their ubiquity in interstellar clouds.<sup>25,26</sup>

In the 1970s, the construction of telescopes capable of observing rotational molecular emissions at millimeter wavelengths opened up new avenues for the discovery of a lot of molecules, such as CO, the most abundant interstellar molecule after H<sub>2</sub>,<sup>27</sup> hydrogen sulfide H<sub>2</sub>S, the first alcohol CH<sub>3</sub>OH, ethanol and so on.

To date, with the progress in the sensitivity of detector technology, our understanding of the interstellar medium has increased dramatically, with an explosion of new detections, particularly in the last 2 years. More than 250 molecular species, not counting isotopologues, have been identified in the interstellar medium via their gas-phase spectra. These species range from simple di and tri-atomic molecules to complex ones. The latter, some with ten atoms or more, include aldehydes, alcohols, acids, amines. The current list of detected interstellar molecules is presented in Table 1, sorted by the number of atoms.

**Table 1** | Molecules detected in the interstellar medium or circumstellar shells.

2 atoms	3 atoms	4 atoms	5 atoms	6 atoms	7 atoms	8 atoms	9 atoms
H <sub>2</sub>	C <sub>3</sub>	c-C <sub>3</sub> H	C <sub>5</sub>	C <sub>5</sub> H	C <sub>6</sub> H	CH <sub>3</sub> C <sub>3</sub> N	CH <sub>3</sub> C <sub>4</sub> H
AlF	C <sub>2</sub> H	l-C <sub>3</sub> H	C <sub>4</sub> H	l-H <sub>2</sub> C <sub>4</sub>	CH <sub>2</sub> CHCN	HC(O)OCH <sub>3</sub>	CH <sub>3</sub> CH <sub>2</sub> CN
AlCl	C <sub>2</sub> O	C <sub>3</sub> N	C <sub>4</sub> Si	C <sub>2</sub> H <sub>4</sub>	CH <sub>3</sub> C <sub>2</sub> H	CH <sub>3</sub> COOH	(CH <sub>3</sub> ) <sub>2</sub> O
C <sub>2</sub>	C <sub>2</sub> S	C <sub>3</sub> O	l-C <sub>3</sub> H <sub>2</sub>	CH <sub>3</sub> CN	HC <sub>5</sub> N	C <sub>7</sub> H	CH <sub>3</sub> CH <sub>2</sub> OH
CH	CH <sub>2</sub>	C <sub>3</sub> S	c-C <sub>3</sub> H <sub>2</sub>	CH <sub>3</sub> NC	CH <sub>3</sub> CHO	C <sub>6</sub> H <sub>2</sub>	HC <sub>7</sub> N
CH <sup>+</sup>	HCN	C <sub>2</sub> H <sub>2</sub>	H <sub>2</sub> CCN	CH <sub>3</sub> OH	CH <sub>3</sub> NH <sub>2</sub>	CH <sub>2</sub> OHCHO	C <sub>8</sub> H
CN	HCO	NH <sub>3</sub>	CH <sub>4</sub>	CH <sub>3</sub> SH	c-C <sub>2</sub> H <sub>4</sub> O	l-HC <sub>6</sub> H	CH <sub>3</sub> C(O)NH <sub>2</sub>
CO	HCO <sup>+</sup>	HCCN	HC <sub>3</sub> N	HC <sub>3</sub> NH <sup>+</sup>	H <sub>2</sub> CCHOH	CH <sub>2</sub> CHCHO	C <sub>8</sub> H <sup>-</sup>
CO <sup>+</sup>	HCS <sup>+</sup>	HCNH <sup>+</sup>	HCCNC	HCCCHO	C <sub>6</sub> H <sup>-</sup>	CH <sub>2</sub> CCHCN	C <sub>3</sub> H <sub>6</sub>
CP	HOC <sup>+</sup>	HNCO	HCOOH	NH <sub>2</sub> CHO	CH <sub>3</sub> NCO	H <sub>2</sub> NCH <sub>2</sub> CN	CH <sub>3</sub> CH <sub>2</sub> SH
SiC	H <sub>2</sub> O	HNCS	H <sub>2</sub> CNH	C <sub>5</sub> N	HC <sub>5</sub> O	CH <sub>3</sub> CHNH	CH <sub>3</sub> NHCHO
HCl	H <sub>2</sub> S	HOCO <sup>+</sup>	H <sub>2</sub> C <sub>2</sub> O	l-HC <sub>4</sub> H	HOCH <sub>2</sub> CN	CH <sub>3</sub> SiH <sub>3</sub>	HC <sub>7</sub> O
KCl	HNC	H <sub>2</sub> CO	H <sub>2</sub> NCN	l-HC <sub>4</sub> N	HCCCHNH	H <sub>2</sub> NC(O)NH <sub>2</sub>	HCCCHCHCN
NH	HNO	H <sub>2</sub> CN	HNC <sub>3</sub>	c-H <sub>2</sub> C <sub>3</sub> O	HC <sub>4</sub> NC	HCCCH <sub>2</sub> CN	H <sub>2</sub> CCHC <sub>3</sub> N
NO	MgCN	H <sub>2</sub> CS	SiH <sub>4</sub>	H <sub>2</sub> CCNH	c-C <sub>3</sub> HCCH	HC <sub>5</sub> NH <sup>+</sup>	H <sub>2</sub> CCHCCH
NS	MgNC	H <sub>3</sub> O <sup>+</sup>	H <sub>2</sub> COH <sup>+</sup>	C <sub>5</sub> N <sup>-</sup>	l-H <sub>2</sub> C <sub>5</sub>	CH <sub>2</sub> CHCCH	HOCHCHCHO
NaCl	N <sub>2</sub> H <sup>+</sup>	c-SiC <sub>3</sub>	C <sub>4</sub> H <sup>-</sup>	HNCHCN	MgC <sub>5</sub> N	MgC <sub>6</sub> H	
OH	N <sub>2</sub> O	CH <sub>3</sub>	HC(O)C	SiH <sub>3</sub> CN	CH <sub>2</sub> C <sub>3</sub> N	C <sub>2</sub> H <sub>3</sub> NH <sub>2</sub>	
			N				
PN	NaCN	C <sub>3</sub> N <sup>-</sup>	HNCNH	C <sub>5</sub> S		(CHOH) <sub>2</sub>	
SO	OCS	PH <sub>3</sub>	CH <sub>3</sub> O	MgC <sub>4</sub> H			
SO <sup>+</sup>	SO <sub>2</sub>	HCNO	NH <sub>4</sub> <sup>+</sup>	CH <sub>3</sub> CO <sup>+</sup>			
SiN	c-SiC <sub>2</sub>	HOCN	H <sub>2</sub> NCO <sup>+</sup>	C <sub>3</sub> H <sub>3</sub>			
SiO	CO <sub>2</sub>	HSCN	NCCNH <sup>+</sup>	H <sub>2</sub> C <sub>3</sub> S			
SiS	NH <sub>2</sub>	H <sub>2</sub> O <sub>2</sub>	CH <sub>3</sub> Cl	HCCCHS			
CS	H <sub>3</sub> <sup>+</sup>	C <sub>3</sub> H <sup>+</sup>	MgC <sub>3</sub> N	C <sub>5</sub> O			
HF	SiCN	HMgNC	NH <sub>2</sub> OH	C <sub>5</sub> H <sup>+</sup>			
HD	AlNC	HCCO	HC <sub>3</sub> O <sup>+</sup>	HCCNCH <sup>+</sup>			
FeO	SiNC	CNCN	HC <sub>3</sub> S <sup>+</sup>	c-C <sub>3</sub> C <sub>2</sub> H			
O <sub>2</sub>	HCP	HONO	H <sub>2</sub> C <sub>2</sub> S				
CF <sup>+</sup>	CCP	MgC <sub>2</sub> H	C <sub>4</sub> S				
SiH	AlOH	HCCS	HC(O)S	<b>10 atoms</b>	<b>11 atoms</b>	<b>12 atoms</b>	<b>&gt;12 atoms</b>
			H				
PO	H <sub>2</sub> O <sup>+</sup>	HNCN	HC(S)C	CH <sub>3</sub> C <sub>5</sub> N	HC <sub>5</sub> N	c-C <sub>6</sub> H <sub>6</sub>	C <sub>60</sub>
			N				

AlO	H <sub>2</sub> Cl <sup>+</sup>	H <sub>2</sub> NC	HCCCO	(CH <sub>3</sub> ) <sub>2</sub> CO	CH <sub>3</sub> C <sub>6</sub> H	n-	C <sub>70</sub>
						C <sub>3</sub> H <sub>7</sub> CN	
OH <sup>+</sup>	KCN	HCCS <sup>+</sup>		(CH <sub>2</sub> OH) <sub>2</sub>	C <sub>2</sub> H <sub>5</sub> OCHO	i-	C <sub>60</sub> <sup>+</sup>
						C <sub>3</sub> H <sub>7</sub> CN	
CN <sup>-</sup>	FeCN			CH <sub>3</sub> CH <sub>2</sub> CH	CH <sub>3</sub> OC(O)CH <sub>3</sub>	C <sub>2</sub> H <sub>5</sub> OC	c-C <sub>6</sub> H <sub>5</sub> CN
				O		H <sub>3</sub>	
SH <sup>+</sup>	HO <sub>2</sub>			CH <sub>3</sub> CHCH <sub>2</sub>	CH <sub>3</sub> C(O)CH <sub>2</sub> OH	1-c-	HC <sub>11</sub> N
				O		C <sub>5</sub> H <sub>5</sub> CN	
SH	TiO <sub>2</sub>			CH <sub>3</sub> OCH <sub>2</sub> O	c-C <sub>3</sub> H <sub>6</sub>	2-c-	1-C <sub>10</sub> H <sub>7</sub> CN
				H		C <sub>5</sub> H <sub>5</sub> CN	
HCl <sup>+</sup>	C <sub>2</sub> N			c-C <sub>6</sub> H <sub>4</sub>	HOCH <sub>2</sub> CH <sub>2</sub> NH <sub>2</sub>	CH <sub>3</sub> C <sub>7</sub> N	2-C <sub>10</sub> H <sub>7</sub> CN
TiO	Si <sub>2</sub> C			H <sub>2</sub> CCCHC <sub>3</sub>	H <sub>2</sub> CCCHC <sub>4</sub> H	n-	c-C <sub>9</sub> H <sub>8</sub>
				N		C <sub>3</sub> H <sub>7</sub> OH	
ArH <sup>+</sup>	HS <sub>2</sub>			C <sub>2</sub> H <sub>5</sub> NCO		i-	1-c-C <sub>5</sub> H <sub>5</sub> CCH
						C <sub>3</sub> H <sub>7</sub> OH	
N <sub>2</sub>	HCS			C <sub>2</sub> H <sub>5</sub> NH <sub>2</sub>			2-c-C <sub>3</sub> H <sub>5</sub> CCH
NO <sup>+</sup>	HSC			HC <sub>7</sub> NH <sup>+</sup>			c-C <sub>5</sub> H <sub>4</sub> CCH <sub>2</sub>
NS <sup>+</sup>	NCO			CH <sub>3</sub> CHCH			2-C <sub>9</sub> H <sub>7</sub> CN
				CN			
HeH <sup>+</sup>	CaNC			CH <sub>3</sub> C(CN)CH <sub>2</sub>			
PO <sup>+</sup>				NCS			

It is worth noting the lack of amino acid detection in the interstellar medium, despite four putative precursors of glycine, methylamine,<sup>28</sup> formamide,<sup>29,30</sup> glycolonitrile<sup>31</sup> and aminoacetonitrile,<sup>32</sup> are detected. In this regard, the compounds containing the -CN moiety are particularly important since are considered potential precursors of amino acids.

Polycyclic aromatic hydrocarbons (PAHs) are another important family of aromatic carbon-bearing molecules found in the ISM. These latter molecules are particularly interesting for their widespread abundance in the ISM and their potential role in the emergence of life. Indeed, besides PAHs don't derive directly from biological processes,<sup>33</sup> they are considered as putative precursors of the molecules of life.<sup>34</sup>

### **1.1.3. Dust grains and photochemistry of icy mantles**

The fundamental role played by dust grains in the formation and evolution of complex organic molecules in the ISM is well known. These particles, called ‘refractory’, since they do not vaporize until temperatures well above 1200 K, are known to have cores of silicates or amorphous carbon.

They have an active role in providing a reservoir for atoms and molecules coming from the gas bringing them closer for a much longer period than in the gas phase. Moreover, they represent a third body enabled to absorb the binding energy of a newly formed molecule, thereby stabilizing and preventing it from dissociating again.

Dust grains are the primary sites of molecular formation and are thought to be responsible for essentially all of the H<sub>2</sub> in the ISM. Molecular chemistry with the complexity observed in space is unthinkable without dust grains acting as reaction site.

In dense cold regions, temperatures below 20 K allow the condensation of volatiles from the gas phase on the surface of dust grains forming ice mantles, consisting primarily of H<sub>2</sub>O ice.

The existence of ice mantles, surrounding interstellar dust grains, and their chemical composition have been confirmed by infrared measurements made by space telescopes such as Spitzer and the Infrared Space Observatory (ISO).

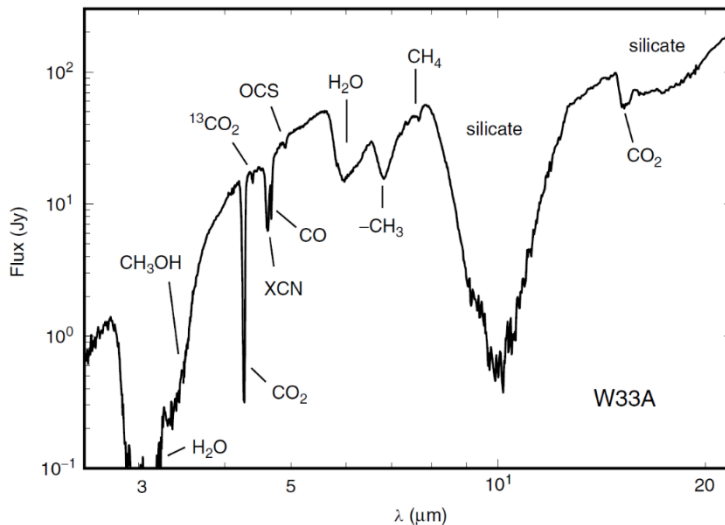


**Figure 2** | W33A Dust-embedded Massive Young star. Image adapted from Ref. <sup>35</sup>

The amorphous solid water was the first icy molecule detected in the ISM through the absorption feature at about  $3300\text{ cm}^{-1}$ , due to the O–H symmetric and anti-symmetric stretching modes.<sup>36</sup> A shift in the position and shape of this feature due to intramolecular H-bond allows distinguishing the solid phase from the gas phase.

Through the comparisons of infrared spectra of laboratory ices with those of molecular clouds, we know that interstellar ice is made also of 5-15% of other species including CO, CO<sub>2</sub>, CH<sub>3</sub>, OH, NH<sub>3</sub>, formed after the accretion of C, O, N and H onto grains.

Grain surface chemistry mostly includes hydrogenation reactions because, at this temperature, H atoms are much more mobile and are 3 to 4 orders of magnitude more abundant than any other ice atoms, such as C, N and O. Therefore, these reactions generated H<sub>2</sub>O, CH<sub>4</sub> and NH<sub>3</sub> molecules. CO is relatively quickly formed in the gas-phase and then condenses out.

After the O condensation, OH will be abundant on the grain surface and its reaction with condensed CO can form CO<sub>2</sub>.

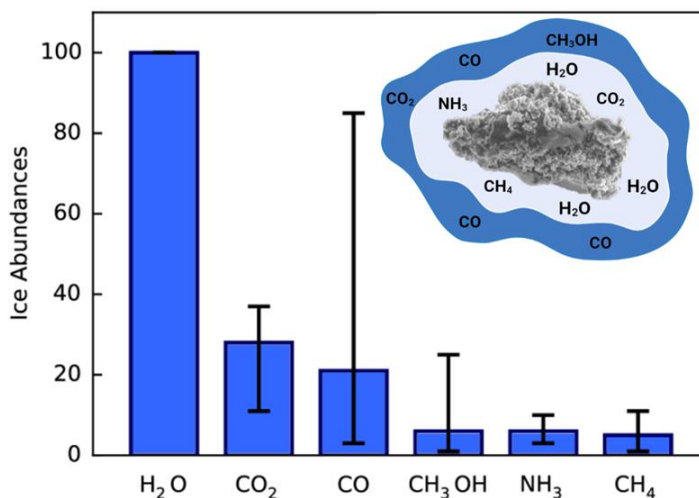


**Figure 3** | The average composition and the structure of ice mantles in the ISM.

The study of ice composition using absorption infrared spectroscopy reveals a layered structure surrounding the grain: a lower water-rich and an upper water-poor layer (also called ‘polar’ and ‘apolar’ ices) (Figure 3).

The water-rich layer is thought to form first in the evolution of a cloud and contains polar, H-bonded molecules such as H<sub>2</sub>O and NH<sub>3</sub>. In contrast, the water-poor layer is observed to form in much denser gas and is characterized by the presence of species that require lower temperatures to stick onto the dust, with carbon monoxide (CO)<sup>37–39</sup> being the most abundant component and related molecules such as CO<sub>2</sub> and CH<sub>3</sub>OH.<sup>17,40</sup> This latter was proposed to be formed by the hydrogenation of CO molecules.<sup>41</sup> Figure 4 displays a schematic drawing of the evolution of interstellar ices composed of a silicate core and an ice mantle in the environment of massive protostars.

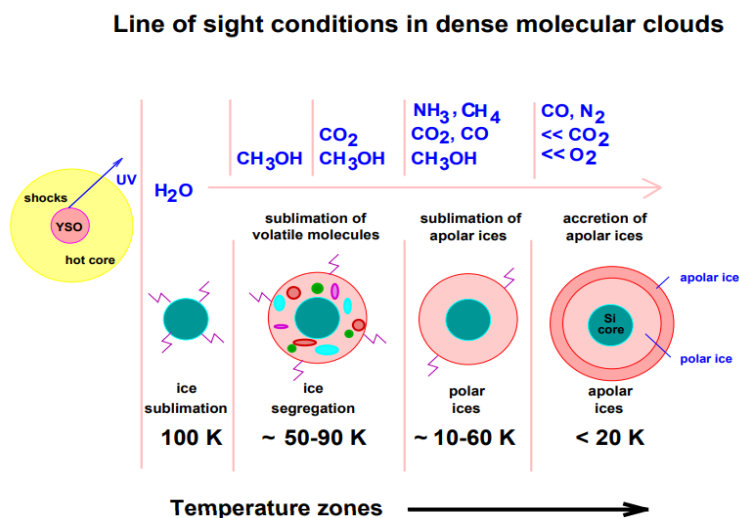


**Figure 4** | A schematic illustration showing the variation in the structure of the ice mantles toward massive protostars YSOs.<sup>42-44</sup> Far from the protostar, in colder (below 20K) and denser regions, where CO is abundant, apolar ice mantles accrete on the underlying polar ice layer. As the temperature rises in the vicinity of protostars, the evolution of interstellar ice mantles occurs. All trapped molecules inside the ice sublimate at specific temperatures: above ~ 50 K the major ice species are CH<sub>3</sub>OH and CO<sub>2</sub>, above 80 K CH<sub>3</sub>OH<sup>45,46</sup> separates from H<sub>2</sub>O and above ~ 90–100 K the majority of ice species sublimate. Image adapted from Ref.<sup>42</sup>

At the low temperature of dense clouds, most chemical and physical processes are thermally inhibited, so chemical processing of the ice mantle is driven by ionizing radiation in the form of cosmic rays and UV photons. These sources of energy can break molecular bonds, and ionize adsorbed molecules forming radical species, which are able to react even at the low temperatures of the ice mantle. Following dissociation, the photo-produced radicals can both recombine into the original molecule and recombine with surrounding radicals

and molecules through radical-radical reactions<sup>17</sup> (Figure 5). This latter process forms more complex molecules, altering significantly the chemistry of ice. Which path will dominate depend on a combination of radical concentration, diffusion and desorption barriers, the importance of non-thermal (“hot atom”) diffusion and desorption, the ice temperature, and whether the radicals form close to the surface or deep inside the ice.

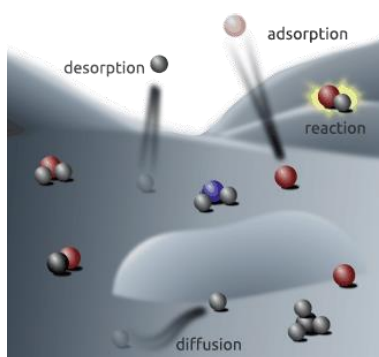


**Figure 5** | Overview of the most important grain surface processes. Image adapted from Ref.<sup>47</sup>

Otherwise, if these dust grains covered by ice mantles get closer to a protostar, experienced raising temperatures, and radicals trapped in the ice can further react driven by thermic energy.

The formation of new species following the rearrangement of chemical bonds of compounds within the ice gives rise to a more complex ice mantle.

Moreover, another effect of high-energy irradiation on ices is the rupture of intermolecular bonds between species on the surface of the ice mantles and their migration within the ice at very low temperatures, leading to the desorption of molecules that would otherwise remain trapped inside the dust. This process is known as photodesorption<sup>48</sup> (Figure 6). In this sense, the ice

mantles contribute a chemically enriched population of molecules to the gas-phase chemistry and the detection of the so-formed species is usually achieved.

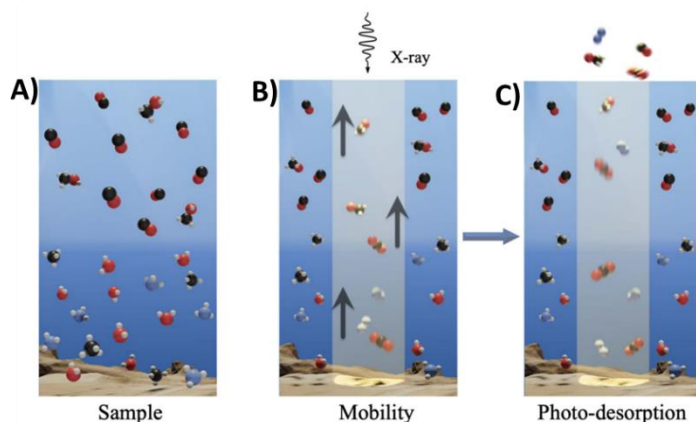


**Figure 6** | Double-layer ice irradiated by soft X-rays. During the irradiation, new species produced in the bottom layer diffuse into the top layer (B), allowing blending and chemical reactions among species of the two layers and likely release into the gas phase (C). Image adapted from Ref. <sup>49</sup>

The desorption from the solid phase to the gas phase could be also accountable to the high temperatures ( $>100$  K), as those found in hot regions, such as hot corinos or FU Ori objects. The increase in molecular vibrations due to thermal heating can overcome the intermolecular energy of the molecules, resulting in thermal desorption.

At 10 K, only hydrogen molecules can desorb from ice mantles. Nitrogen ice needs around 25 K to break the weak intermolecular Van der Waals forces and to desorb. Instead, larger molecules, or molecules with a permanent dipole moment, such as CO, CO<sub>2</sub> or H<sub>2</sub>S, require higher temperatures to desorb, since are bonded stronger. Moreover, intermolecular H bonds established between

molecules with O-H or N-H groups, including H<sub>2</sub>O, NH<sub>3</sub> or CH<sub>3</sub>OH, increased their desorption temperature.

However, thermal desorption is strongly dependent on surrounding species. For example, carbon monoxide (CO), when adsorbed as a pure molecule thermally desorbs around 30 K, but in presence of water, it desorbs during crystallization of water molecules or co-desorbs with water molecules, around 180 K. Similar effects have been found for nitrogen (N<sub>2</sub>), ammonia (NH<sub>3</sub>), or methane (CH<sub>4</sub>).<sup>50,51</sup>

The experimental technique that allows simulating thermal desorption occurring in the interstellar hot regions is thermal programmed desorption (TPD) in which the substrate is heated using a linear temperature ramp.<sup>52</sup> The gas phase composition is monitored as a function of time (and temperature) with the quadrupole mass spectrometer (QMS). The observed desorption curve of a species depends on the number of molecules on the ice, the ice structure, the desorption order, the desorption attempt frequency and the desorption barrier.

Although the icy mantles represent the interface between gaseous and solid phases, their composition doesn't reflect the gas phase composition or abundances. Photochemical processing generates ice compositions strikingly different from the gas phase.

To shed more light on the photochemical evolution of ice grain mantles, a lot of laboratory experiments mimicking ice mantles of dense clouds have been carried out.

The last three decades have shown the importance of laboratory experiments to experimentally verify the efficiency of the mechanisms invoked to explain the formation of COMs.<sup>53-57</sup> Further studies have clarified the evolution and

conservation of COMs in hostile astronomical environments<sup>58,59</sup> where the presence of grains can play a key role.

Ice mixture photochemistry experiments consist of preparing ice samples with known compositions, similar to those in real astrophysical contexts, which commonly include water as the main ice component, since its dominance in most interstellar ice mantles. The presence of water influences the ice photochemistry compared to pure ices: the dissociation of water when exposed to VUV radiation produces reactive radicals that will contribute to the ice chemistry and the interactions between pure molecules and water, for instance by means of hydrogen bonds, could stabilize formed radicals promoting the formation of new molecules.

Over the years, irradiation experiments have shown that the processing of ices containing only a few simple interstellar molecules leads to a lot of complex organic molecules.

The typical structure and processing of an interstellar ice-covered grain are schematically represented in Figure 7.

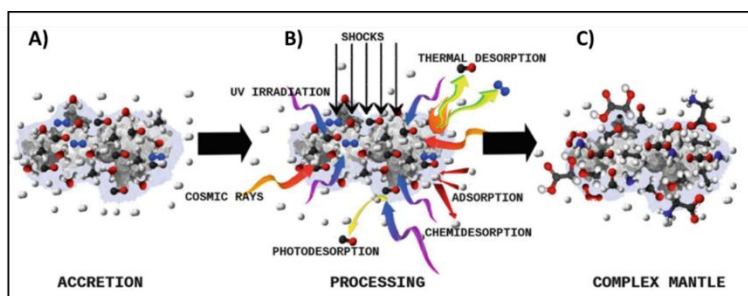


**Figure 7** | Schematic representation of interstellar ice mantle formation and chemical evolution. A) gas-phase molecules accrete onto the surface of cold dust grains to form the ice mantle. B) surface reactions between these species, ultraviolet irradiation cosmic ray bombardment and thermal processes

contribute to the processing of the ice mantle. C) the processed ice mantle becomes a complex ice mantle leading to the formation of the complex molecular species observed in the ISM. Image adapted from Ref. <sup>60</sup>

Some of these compounds are also detected in meteorites and represent the prebiotically relevant building block of life.<sup>5,61–63</sup>

Multicomponent ice mixtures were also explored to evaluate the formation of COMs after warm-up of ultraviolet or ion-processed ices.

Interestingly, the ultraviolet photolysis of water ice mixtures with methanol and ammonia invariably has been shown to yield ribose, the principal structural and functional unit of RNA.

The UV irradiation of frozen pyrimidine in the presence of H<sub>2</sub>O, CH<sub>3</sub>OH, NH<sub>3</sub>, and CH<sub>4</sub> resulted in the formation of the nucleobases uracil, cytosine, and thymine <sup>64–67</sup>

Similarly, the irradiation of purine in ices containing NH<sub>3</sub> and H<sub>2</sub>O leads to the formation of the nucleobases as guanine and adenine.<sup>68–70</sup>

UV photochemistry experiments performed on two interstellar ice analogs, containing H<sub>2</sub>O, NH<sub>3</sub>, CH<sub>3</sub>OH, CO, CO<sub>2</sub> and H<sub>2</sub>O, NH<sub>3</sub>, CH<sub>3</sub>OH, HCN, revealed the presence of amino acids in the residue (Figure 8).<sup>5,62</sup>

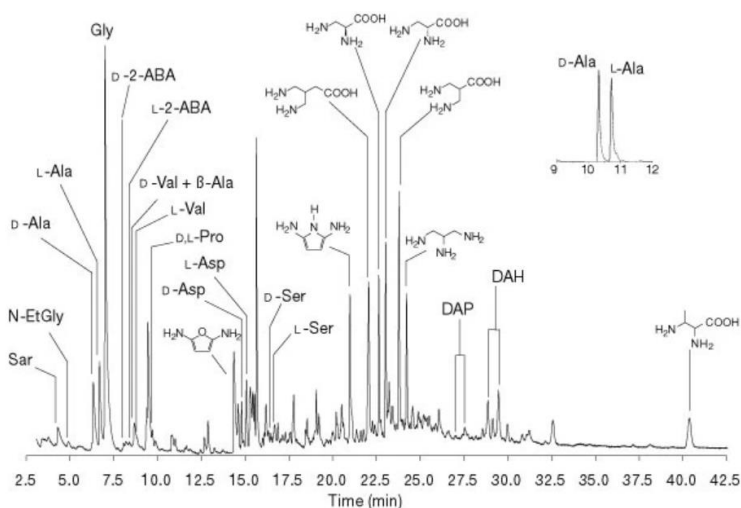


**Figure 8** | A GC-MS spectrum showing the amino acids and other compounds produced by UV irradiation of an ice mixture containing  $\text{H}_2\text{O}:\text{CH}_3\text{OH}:\text{NH}_3:\text{CO}:\text{CO}_2$ . Image adapted from Ref. <sup>62</sup>

The investigation of residues obtained after irradiation of a simple ice mixture containing only  $\text{NH}_3$  and  $\text{CH}_3\text{OH}$ , unveiled the presence of urea, glycolic acid, glycerol, hydroxyacetamide and glycerol amide.<sup>71</sup>

Great interest is aroused by glycerol since it is a sugar and the glycerol backbone is part of all lipids. A proposed pathway for glycerol formation is a reaction between two  $\text{CH}_2\text{OH}$  radicals and  $\text{H}_2\text{CO}$ , all produced from photodissociation of  $\text{CH}_3\text{OH}$ .

More recently, COMs were also formed after the of X-ray irradiation of ice analog mixtures.<sup>49,72</sup>

All these experiments showed that amino acids, sugars, nucleobases, and other prebiotic species are among the main products.<sup>5,55,62,73,74</sup>

Accordingly, laboratory studies are crucial to study the evolution and preservation of processed complex molecules and organic compounds in harsh astronomical environments.

In this sense, experimental astrochemistry can provide tools for the interpretation of molecules observations to look for specific processes in specific environments.

#### 1.1.4 Polycyclic aromatic hydrocarbons (PAHs)

The advent of infrared astronomy revealed the richness and complexity of the astronomical spectra with broad, resolved emission bands centered at 8.6 and 11.2  $\mu\text{m}$ <sup>75</sup> and subsequently at 3.3, 6.2 and 7.7  $\mu\text{m}$ .<sup>76</sup>

These emission bands, that always appeared together, are widely observed in a large range of astronomical environments in our and in other galaxies, including the ISM, reflection nebulae, TTauri stars, Herbig AeBe stars, Hii regions, post-AGB stars, planetary nebulae and more exceptionally in few AGB stars, WR stars, novae and supernovae remnants. Since the carrier of this set of bands remained unassigned for almost a decade, they were collectively called the Unidentified InfraRed (UIR) bands.

In 1981, Duley and Williams<sup>77</sup> made the perceptive observation that some features of the UIR bands correspond to the stretching and bending modes characteristic of aromatic compounds.

Léger and Puget (1984)<sup>78</sup> and Allamandola et al. (1985)<sup>79</sup> proposed a collection of partially hydrogenated, positively charged PAHs as carriers of UIR bands, leading to the birth of the PAH hypothesis.

PAHs are organic molecules containing only carbon and hydrogen and composed of multiple fused aromatic rings, such as those seen in Figure 9.

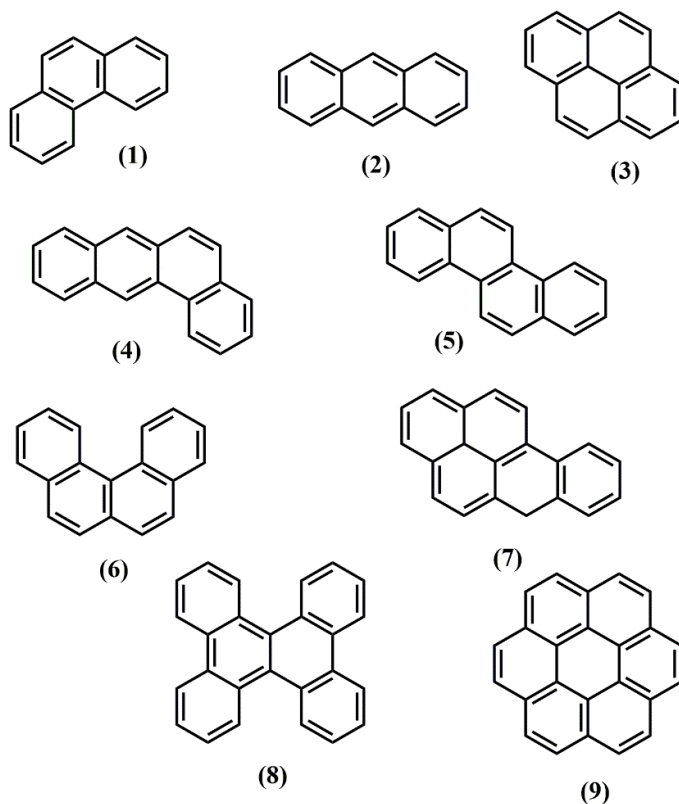


**Figure 9** | Polycyclic aromatic hydrocarbon species: (1) phenanthrene, (2) anthracene, (3) pyrene, (4) benz[a]anthracene, (5) chrysene, (6) dibenzo[c,g]phenanthrene (7) benzo[a]pyrene, (8) tetrabenzonaphthalene, (9) coronene.

The evidences in support of the PAH hypothesis were: (1) the banded rather than continuous nature of the emission spectra from various astrophysical sources; (2) the close connection of the emissions with ultraviolet radiation, suggesting that they are due to the excitation by photons of gas phase molecules than thermal emissions from solid phase; (3) the correspondence between the fraction of the total infrared energy that is emitted from planetary nebulae through these features and the amount of available carbon; and (4) the

correlation between the features of varying emission bands, which correspond to a single class of chemical species.

However, this hypothesis suffered a lot of criticism over the years, including the lack of a good match between a combination of experimental and/or theoretical PAH spectra and the astronomical PAH spectra, the inconsistency between the well-defined sharp features of PAH molecules compared to the broad UIE bands, the absence of detection of specific PAH molecule, in spite of their vibrational and rotational frequencies are well known. Moreover, and most critically, pure PAHs alone cannot account for certain specific spectral data, e.g., the position of the 6.2  $\mu\text{m}$  band, which is not compatible with the strongest C–C stretching of pure PAHs.

In order to account for these discrepancies, the PAH hypothesis has been revised proposing various PAH-related species:

- 1) heteroatom substituted PAHs.<sup>80–82</sup> If nitrogen atoms substitute carbon atoms in specific positions, the position of the C–C stretching band shifts towards shorter wavelengths, while the positions of other vibrational modes remain unaffected. The red shift of this band could be also due to the presence of  $^{13}\text{C}$  in PAHs.<sup>83</sup>

The incorporation of other abundant elements such as oxygen and sulphur into the hydrocarbon compounds has been proposed;

- 2) PAH-metal complexes.<sup>81,82,84,85</sup> Metal complexes can be chelated by the extended aromatic carbon rings;
- 3) PAH clusters such as dimers and trimers;<sup>86,87</sup>
- 4) mixture of PAHs of different size, structure and charge state. Small PAHs (number of carbons (NC)  $\leq 48$ ) emit at 7.6  $\mu\text{m}$ .<sup>80</sup> In contrast,

large PAHs ( $54 \leq NC \leq 130$ ) emit at  $7.8 \mu\text{m}$ .<sup>88,89</sup> Hence, in order to reproduce the  $7.7 \mu\text{m}$ , both small and large PAHs are required;

5) mixture of aromatic and aliphatic components.

Figure 10 shows a recently proposed chemical structure of the carrier of UIE features. The structure is composed of a highly disorganized arrangement of small units of aromatic rings linked by different kinds of aliphatic chains. Commonly, are present other impurities such as oxygen, nitrogen and sulphur.

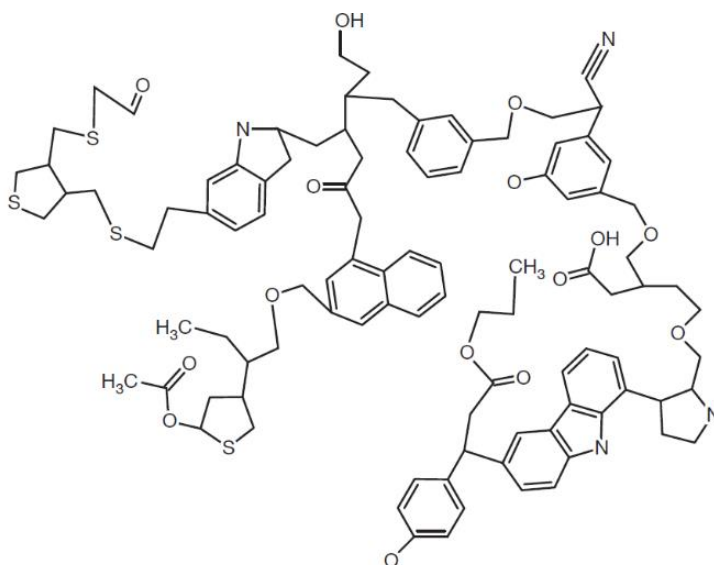


**Figure 10** | Proposed structure of the carrier of UIE features. Image adapted from Ref.<sup>90</sup>

Nowadays, the presence of interstellar PAHs is generally accepted, despite the secure identification of specific PAH molecules in the ISM has been limited to the recent astronomical identifications of a few aromatic species.<sup>91-93</sup> Especially, the unambiguous detection of two nitrile-group-

functionalized PAHs, 1-cyanonaphthalene and 2-cyanonaphthalene<sup>94</sup> in the TMC-1 molecular cloud was of particular interest (Figure 11).

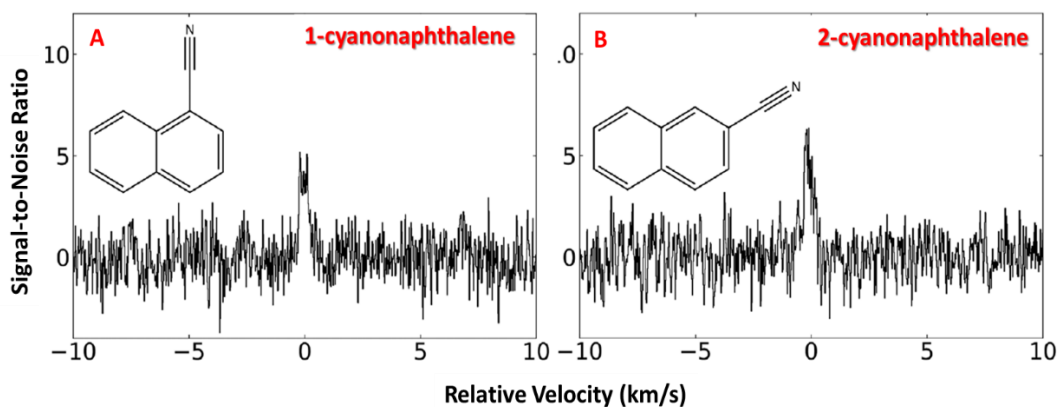


**Figure 11** | Chemical structures and spectral stacks of 1-cyanonaphthalene (A) and 2-cyanonaphthalene (B). Image adapted from Ref.<sup>94</sup>

Polymerization of acetylene via a sequence of stable radicals has been proposed as the most promising mechanism for the formation of PAHs in astrophysical environments.<sup>95</sup> Figure 12 shows two possible chemical routes toward the closure of the first aromatic ring. The first route (A) starts with a three-body collision of acetylene ( $\text{HC}\equiv\text{CH}$ ) with the formation of the propargyl radical ( $\text{H}_2\text{C}=\text{C}=\text{CH}$ ). Reactions of these radicals with each other generate the phenyl radical ( $\text{C}_6\text{H}_5\cdot$ ). The second reaction pathway (B) starts with the isomerization of acetylene to the vinylidene radical ( $\text{HHC}=\text{C}\cdot$ ). Then, this latter radical reacts with acetylene to form benzyne and finally the phenyl radical.

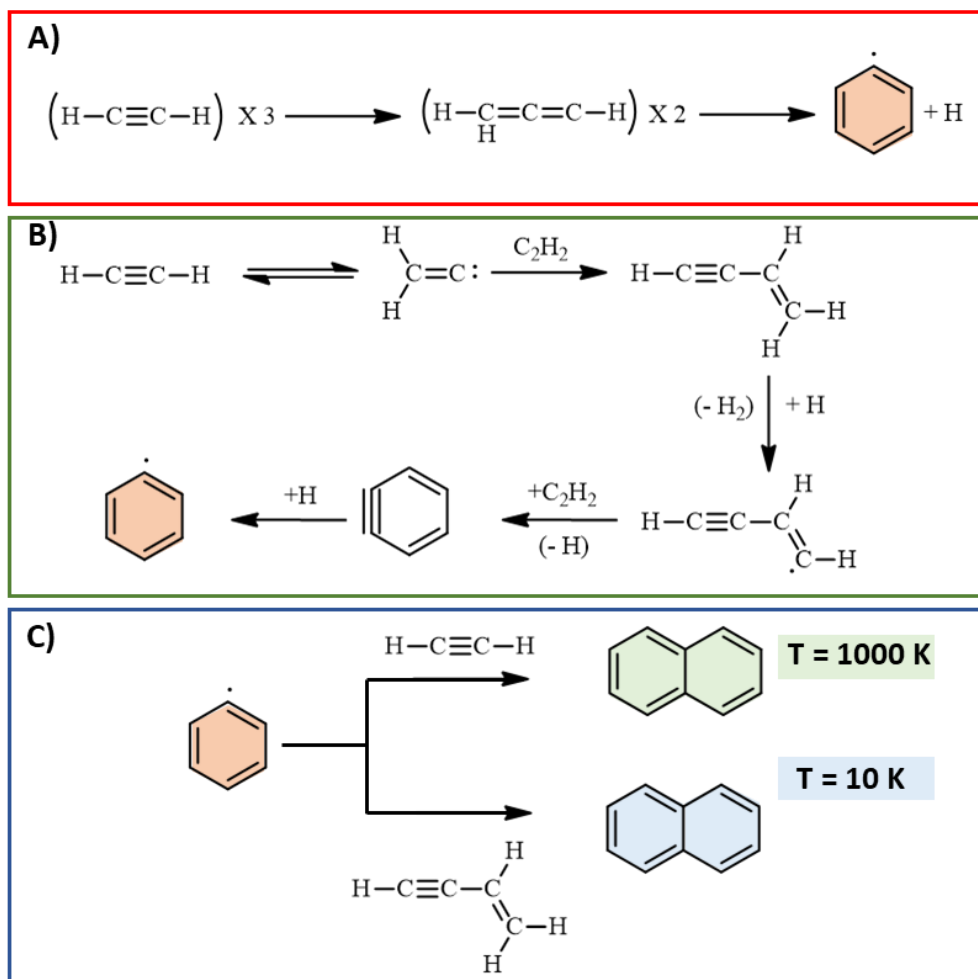


**Figure 12** | Schematic representation for the radical-mediated formation of phenyl radical and naphthalene in astrochemical environments. The closure of the first aromatic ring could occur in two possible chemical pathways A) and B). Panel C) shows the formation of the second aromatic ring from phenyl radical via high energy addition of two acetylene molecules and low energy alternative mechanism based on the addition of vinylacetylene.

The addition of acetylene to the phenyl radical in a further four steps forms two fused benzene rings called naphthalene (C). Recently, has been proposed a low-temperature alternative mechanism to the traditional one that occurs at high temperatures.<sup>96</sup> In a combined crossed-beam and theoretical study, it has been demonstrated that naphthalene can be formed in the gas phase via a barrierless and exoergic reaction between a phenyl radical and vinylacetylene.

PAHs get electronically excited when exposed to high-energy photons (up to 13.6 eV) and increase their temperature considerably reaching up to  $\sim 1000$  K.

They very quickly redistribute the adsorbed energy internally among all different vibrational modes and relax by either near and mid-IR emissions or fragmenting (Figure 13).<sup>97</sup>

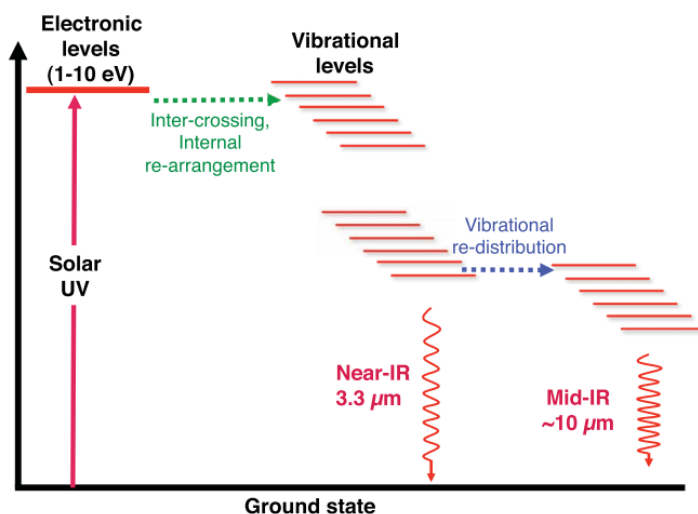


**Figure 13** | Schematic diagram showing the relaxation of the solar energy absorbed by the PAHs in the UV and its re-emission in the near-IR and mid-IR. Image adapted from Ref. <sup>97</sup>

Figure 14 illustrates the richness and variety of the PAH emission features seen in different regions of ISM. While showing small differences in detail, regardless of their environment, all spectra are similar in peak position and shape and are dominated by emission features centered around 6.2, 7.7, 8.6, 11.2 and 12.7  $\mu\text{m}$ .

Specifically, the 3.3  $\mu\text{m}$  band is due to the CH stretching mode, the 6.2  $\mu\text{m}$  band to the CC stretching mode, the 7.7  $\mu\text{m}$  band to coupled CC stretching and CH in-plane bending modes, the 8.6  $\mu\text{m}$  band to the CH in-plane bending mode and the 10-15  $\mu\text{m}$  region to the CH out-of-plane (CHoop) bending modes.

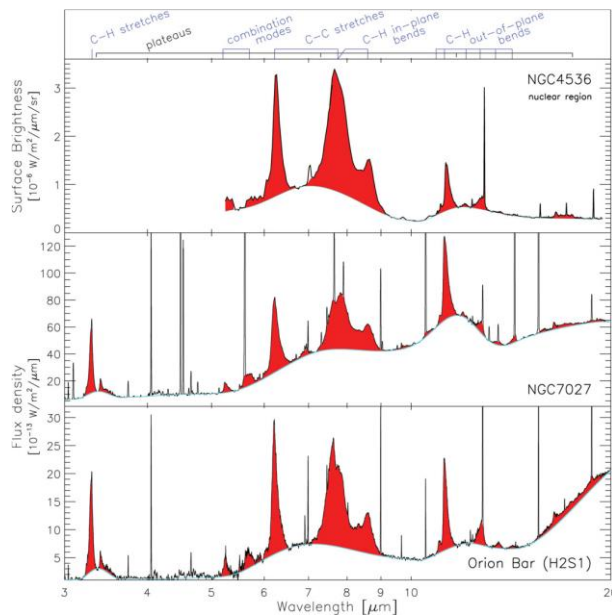


**Figure 14** | The ISO-SWS spectra of the planetary nebula NGC 7027 and the Photo-Dissociation Region (PDR) in the Orion Bar, and the Spitzer-IRS spectrum of the nuclear region of NGC 4536 show a rich set of emission features.<sup>98</sup> At the top, the assignments of the major PAH bands with the vibrational modes are indicated. Image adapted from Ref. <sup>98</sup>

Based on the aromatic infrared bands, it was estimated that PAHs carry up to 20%<sup>99,100</sup> of all interstellar carbon and that they are widely distributed throughout the ISM in both in the gas and solid phases.<sup>101</sup>

Furthermore, PAHs and their cations are considered prominent candidates for the carriers of diffuse interstellar absorption bands (DIBs).<sup>102,103</sup> Significant amounts of PAHs are also detected in carbonaceous chondrites (CCs), for example, in the Allende meteorite,<sup>104</sup> the Murchison meteorite,<sup>105</sup> and samples from the comet 81P/Wild 2.<sup>106</sup> Gas chromatography-mass spectrometry analysis of extracts revealed that PAHs found in CCs display sizes ranging from 10 (naphthalene) to 24 carbon atoms (coronene)<sup>104,107–109</sup> (Figure 15), unlike those found in ISM which ranges from 50 to 100 carbon atoms.<sup>99,110</sup>

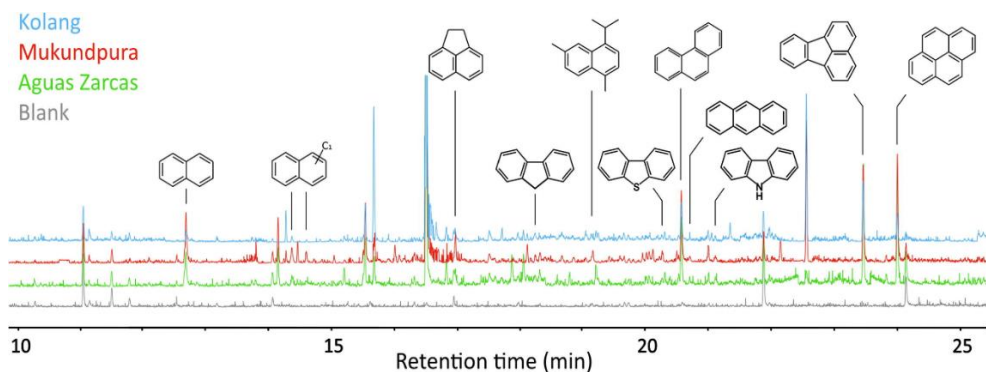


**Figure 15** | GC-MS chromatograms of DCM/MeOH extracts<sup>111</sup> of the Kolang, Mukundpura, Aguas Zarcas meteorites. The blank chromatogram is shown as a reference. More abundant detected PAHs are naphthalene, phenanthrene, fluoranthene and pyrene. Image adapted from Ref. <sup>111</sup>

PAHs, including fluoranthene and pyrene, was recently detected on the surface material from the near-Earth carbonaceous (C-type) asteroid (162173) Ryugu.<sup>112</sup>

The formation of PAH is based on either “top-down” or “bottom-up” chemistries, namely, they are formed both from cleavage reactions of larger structures or by joining together smaller molecules, ions and radical precursors. Therefore, they are thought to be both the key molecules for the formation of grains and a carbon feedstock for the production of small molecules essential for life (Figure 16).<sup>99,113</sup>

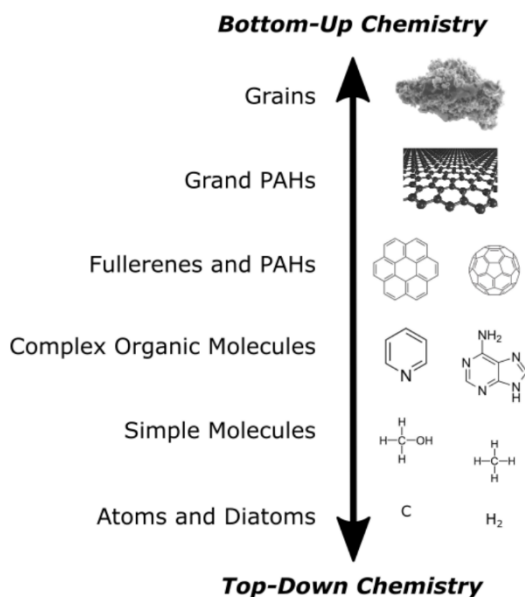


**Figure 16** | Schematic diagram exhibiting the ‘top-down’ and ‘bottom-up’ chemistry for PAHs. In the ‘bottom-up’ perspective, atoms and simple molecules associate to form large molecules. Further additions to the molecular structure may result in the formation of a complex organic molecule, from PAHs to carbonaceous dust grains. The exact opposite of this is the ‘top-down’ chemical perspective, in which larger molecular structures are broken up after

the energetic processing, thus yielding simpler molecules. Image taken from Ref. <sup>114</sup>

Tielens et al. 2015 <sup>115</sup> suggest the concept of grandPAHs as a unique mixture of the most stable PAHs that results from the intense processing of PAHs at the border limit between the PDR and the molecular cloud. Here, the UV radiation destroys the PAH population and as they get closer to the star, their abundance starts decreasing and closed-caged fullerene molecules are formed, as shown in Figure 17.

However, despite some progress has been made, the mechanisms underlying the formation and the chemical role of PAH molecules and fullerenes in interstellar and circumstellar environments are still not fully understood.

Significant steps forwards can be made by a joint effort of the complementary observational, experimental and theoretical approaches along with information coming from very innovative instruments, such as the very recent mid-infrared instrument (MIRI) on the James Webb Space Telescope (JWST). <sup>116</sup>

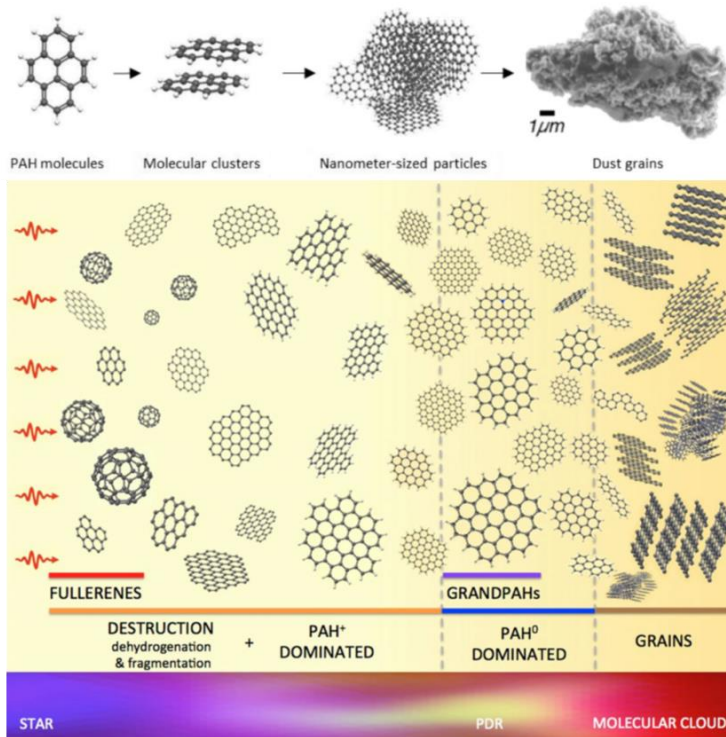


**Figure 17** | Evolution of carbonaceous material across an reflection nebulae RN. The evolution of the PAH population from the molecular cloud (on the right) to the region closest to the star (left side) is shown. PAHs are heavily processed at the edge between the PDR and the molecular cloud, most probably as a consequence of photo-evaporation of larger grains. This intense PAH processing generates the grandPAH population: a unique mixture of the most stable PAHs. This population would initially be dominated by neutral PAHs with small to medium sizes and compact pericondensed structures. As the grandPAH population becomes progressively exposed to more intense radiation, they get ionized and destroyed. Further processing in regions even closer to the star these ionized and fragmented PAHs will end up in the most stable forms of fullerenes. Image adapted from Ref. <sup>115</sup>

#### 1.1.4.1 Photochemistry of PAHs

Given the widespread occurrence of PAHs throughout the astronomically-relevant environments, a crucial question is whether and to what extent PAHs may be susceptible to degradation by UV and cosmic radiation. As well as all other polyatomic gas phase species in cold interstellar regions, PAHs are expected to freeze out onto the grains and become part of the icy grain mantles.

Evidence of this comes from weak, broad absorption bands observed in dense cloud spectra that are consistent with PAHs frozen in the ice mantles.

Unfortunately, the dominant spectral features of the water and other main ice species overshadow the weaker ones of PAHs or of simple hydrocarbons, whereby elucidation of radiation-induced processing in astrophysical ices remains a challenging task.

After exposure to high-energy irradiation, PAHs or their derivatives are expected to react with the surrounding matrix giving rise to a wide array of complex organic molecules,<sup>5,117,118</sup> that could have played a vital role in the emergence of life<sup>119</sup> (Figure 18).

Although the UV photolysis of PAHs in interstellar ices likely acts only on a small fraction of the interstellar PAH population, these modifications are significant from the astrochemical point of view.

The extensive experimental investigation has been dedicated to the photo-processing of PAHs in water ice matrix upon UV irradiation under different astrophysics conditions.

In situ spectroscopic studies have shown that PAHs embedded in a water–ice matrix are easily ionized after high-energy VUV irradiation.

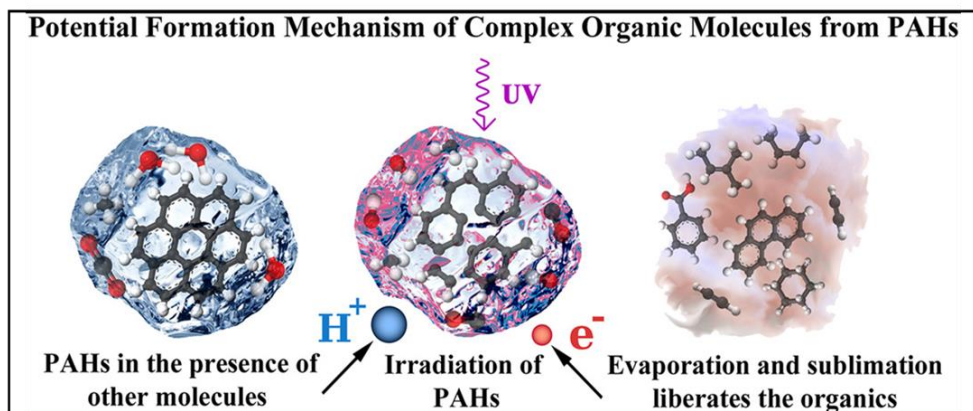


**Figure 18** | Schematic representation showing of the ability of the nearly ubiquitous PAHs in the ISM to serve as the chemical feedstock for astrobiologically interesting molecules found in many solar system objects. Image adapted from Ref. <sup>120</sup>

Gudipati and Allamandola demonstrated that 4-methylpyrene, naphthalene, and quaterrylene in water–ice can be ionized to their cationic forms<sup>121,122</sup> after the Lyman- $\alpha$  (10.2 eV) irradiation.

Similarly, the formation of cationic triphenylene and pyrene in water–ice at 20 K after the VUV broadband irradiation (120–160 nm) were observed by Kofman et al. and Bouwman et al., respectively. <sup>123,124</sup>

In 2012, Cuyllé et al. showed the formation of both anionic pyrene and benzo[ghi]perylene when embedded in ammonia–ice after exposure to Lyman- $\alpha$  irradiation.<sup>125</sup> Since the formation of anionic PAHs increased as the concentration of ammonia increased with respect to water, the authors hypothesized the transfer of an electron to the PAH through ammonia-related photoproducts.

PAH molecules and ions are inherently stable systems and this can explain their abundance in harsh interstellar regions.

Since the high ionization potentials of these molecules, the formation of ion products is believed to occur due to the presence of water that lower the barrier to the photoionization of PAHs.<sup>126,127</sup>

Experimental investigations combined with computational studies have shown that the ionization of PAHs adsorbed on water ice requires about 1.5–2.0 eV less energy than in the case of isolated PAHs,<sup>126,127</sup> and that the resulting radical cations of PAH would be extremely stable over time.<sup>122</sup>

Other experiments on the effect of vacuum ultraviolet (VUV) irradiation of interstellar ice analogs containing trace amounts of PAHs have shown the occurrence of extensive hydrogenation, oxygenation, and hydroxylation reactions and/or the substitution with heteroatoms, mainly nitrogen, in the carbon skeleton.<sup>128</sup> Therefore, the photolysis decorates the edge of parent PAH with chemical side-groups formed from the photoproducts of the other ice constituents. Hydrogen atom addition converts some of the edge rings into cyclic aliphatic hydrocarbons, resulting in molecules with both aromatic and aliphatic properties and a reduction in aromaticity.

Instead, the addition of oxygen to the molecular structure of PAHs leads to the formation of new functional groups such as alcohols, quinones and ethers.

For instance, irradiation of naphthalene, the smallest PAH, and other PAHs in a water ice matrix have been shown to lead to oxygenated products, including mainly phenolic and quinone derivatives, e.g. 1-naphthol and 1,4-naphthoquinone. Computationally, it has been shown that the addition of the OH radical to neutral or cation naphthalene is barrierless.<sup>129</sup>

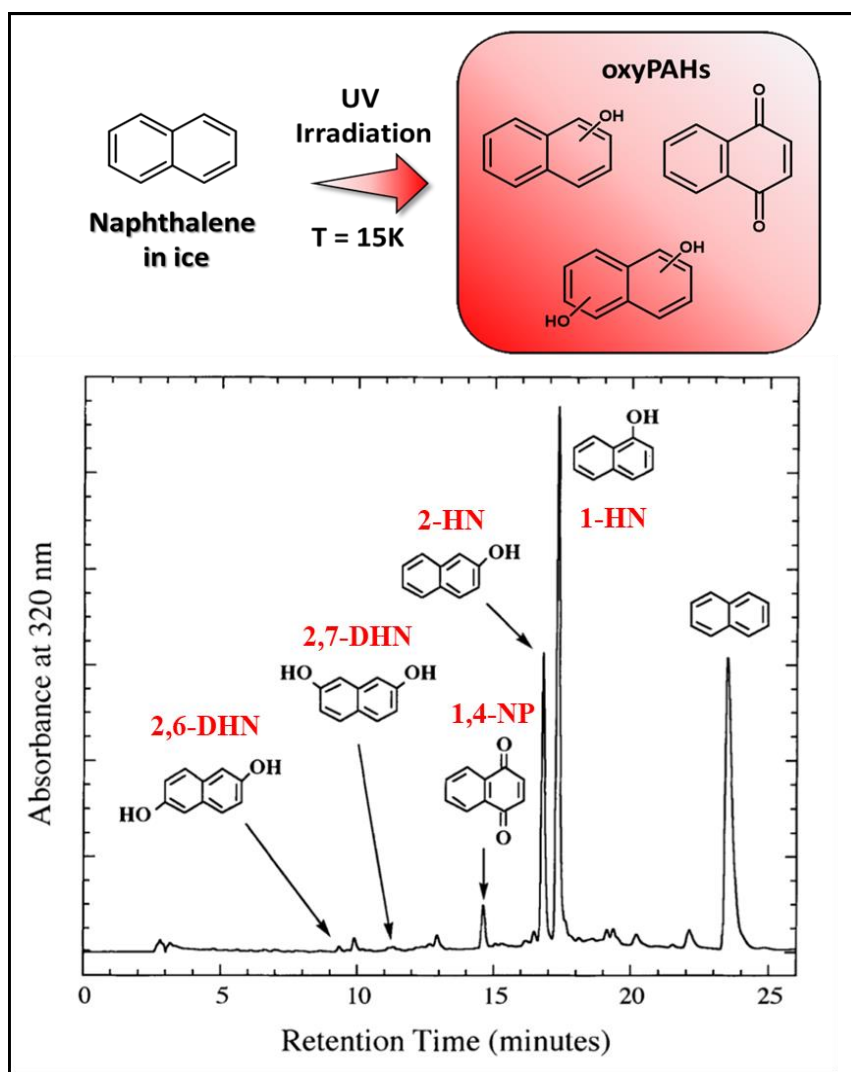


**Figure 19** | The HPLC separation of the material resulting from the UV photolysis of an H<sub>2</sub>O:naphthalene ice at 15 K. The main photoproducts identified are 1-naphthol (1-HN), 2-naphthol (2-HN), 1,4-naphthoquinone (1,4-NP), 2,6-dihydroxynaphthalene (2,6-DHN) and 2,7-dihydroxynaphthalene (2,7-DHN).

With reference to Figure 19, signal intensities should not be misinterpreted: 1- and 2-naphthol might be the most stable photoproducts, but their peak' intensities are not necessarily correlated with the quantum efficiency of their photoproduction. It could rather be possible that 1- and 2-naphthol accumulate even if they are not the most stable photoproducts just because all of their further reactions have very high activation energy, so 1- and 2-naphthol are stuck in their potential wells just for kinetic reasons. On the other hand, the most efficient photoinduced pathways could be the ones producing dihydroxy derivatives which further react very quickly in a sort of steady-state process as long as naphthalene is available so that only very little quantities can be detected after the quench. Thermodynamic and kinetic factors should be taken into account since they both contribute to the photoproducts abundances after the quench (Figure 20).

Quinones are of particular interest from the prebiotic chemistry perspective because closely related compounds are widely used in current living systems for electron transport across cell membranes. Moreover, their presence has been detected in meteorites.<sup>130</sup> Therefore, their formation in several irradiated PAH ice mixtures upon UV irradiation opens up to an entire range of possible chemical reactions that were not available to the parent PAH. Likely, the ease of production of 1,4-naphthoquinone and the ubiquity of 1,4-naphthoquinone-based compounds in biochemistry is not a coincidence.

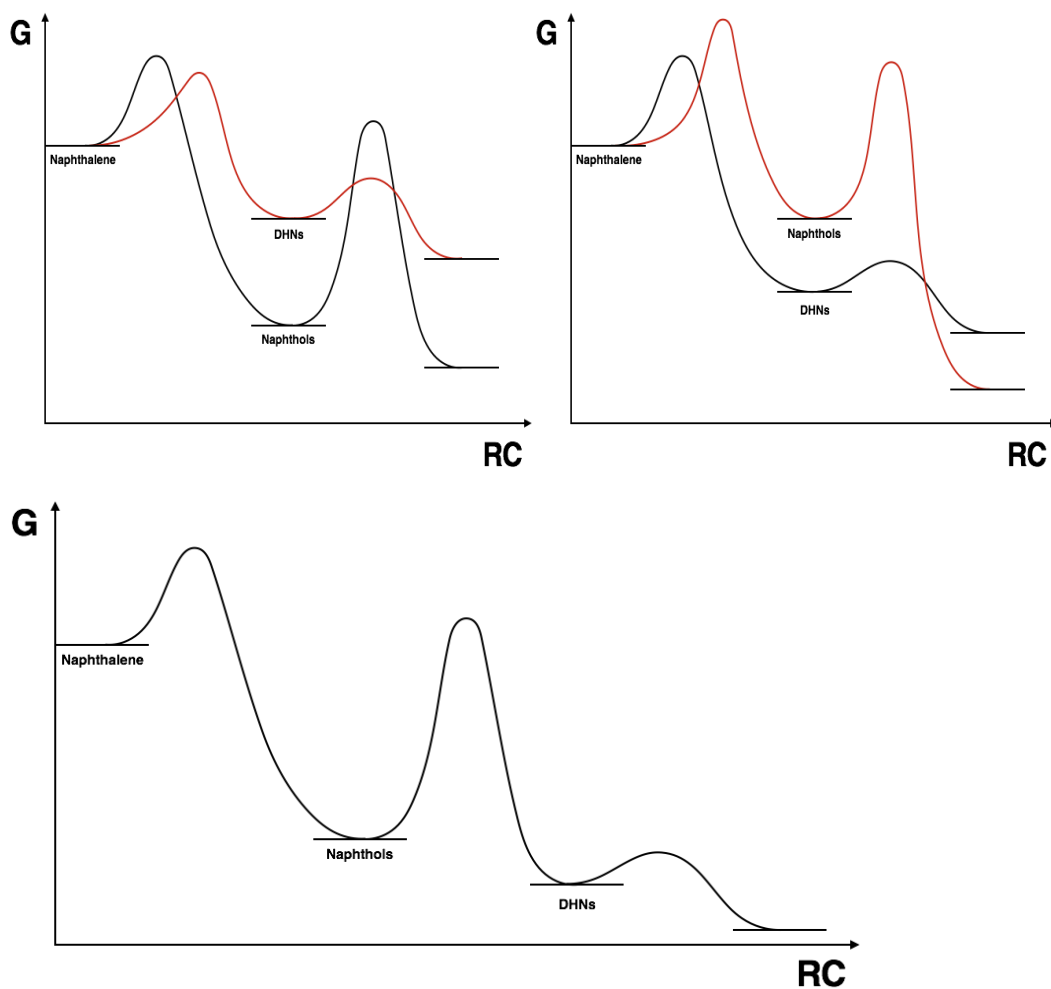


**Figure 20** | Examples of how thermodynamic and kinetic parameters can affect naphthalene photoreaction: different parameters can have similar outcomes if properly combined. In the first two examples, naphthols and dihydroxynaphthalenes (DHNs) are treated as photoproducts of different pathways starting from naphthalene. In the example at the bottom, DHNs are considered as photoproducts of naphthols.

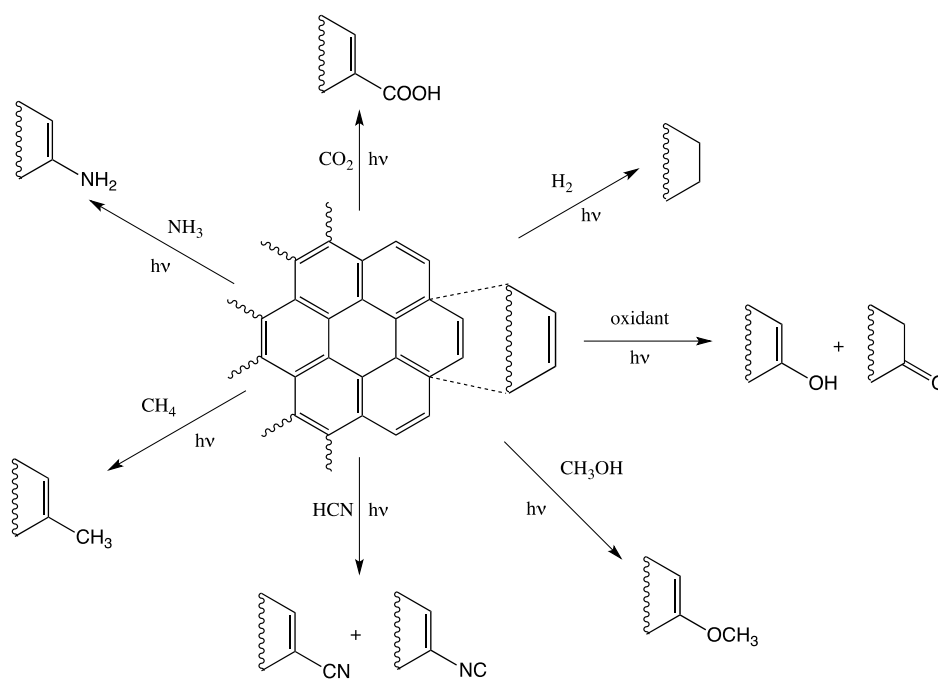
The connection between the interstellar molecular clouds and meteoritic materials suggests the possibility that these aromatic compounds were delivered to the early Earth by meteorites and interplanetary dust particles (IDPs) influencing the selection of this class of coenzymes during the origin of life and/or its early evolution. Since the antiquity of naphthoquinones as chromophores, it is possible that protection was their first function on an early Earth lacking ozone and only later did they become involved in biological systems. Moreover, also aromatic amino acids were produced after the irradiation of naphthalene at 15 K in a water/ammonia ice mixture with photons in the extreme-ultraviolet range.

Figure 21 displays the VUV photolysis of various coronene-ice mixtures resulting in additions of amino, methyl, methoxy, cyano/isocyano, and acid functional groups to the initial PAH molecule.

Hydroxy-substituted PAHs have been shown to form in experiments on interstellar ice analogues also from pyrene and anthracene irradiated by ultraviolet light. However, the processing of these molecules by UV radiation can even partially break them down and increase their reactivity.

Chen et al. (2017)<sup>132</sup> demonstrated that the oxygen-functionalised PAH, bisanthenquinone ( $C_{28}H_{12}O_2$ ) cation, is not photo-stable and preferentially loses neutral CO units via photo-fragmentation.

In this framework, the concentration of small PAHs has a critical role in their reactivity: low concentrations of PAHs in water ice prefer the formation of oxygenated PAHs, rather than erosion processes that lead to the formation of small molecules such as CO, CO<sub>2</sub>, and H<sub>2</sub>CO.<sup>118</sup>



**Figure 21** | Side group addition to PAHs in UV-irradiated cosmic ice analogues. Image adapted from Ref. <sup>131</sup>

Incorporation of heteroatoms into the ring structure of the PAH is also possible,<sup>133</sup> and the resultant heterocyclic molecules are also of great biological significance with nitrogen-containing heterocycles such as pyrimidine and purine being the building blocks for nucleobases.

Recently, the chemistry of polycyclic aromatic nitrogen heterocycles (PANHs) in interstellar ice analogs has been investigated. PANHs are molecules structurally similar to PAHs, with one or more nitrogen atoms substituted for carbon in the molecular skeleton. These compounds are also believed to be present in the ISM and should be present in interstellar ices.

Photolysis of PANHs in interstellar ice analogs leads to the formation of species similar to those formed after UV irradiation of PAHs; these have also

been detected in the Murchison meteorite. For example, the quinoline when embedded in water ice mixed with methane and methanol leads to the formation of oxidized species after exposure to VUV irradiation.

In some cases, all these functionalizations could result in a dipole moment that carries the potential for detection in the radio and microwave spectral regions. These photolysis products could be released into the ISM from dust grains heated by starlight at the edges of clouds. Intriguingly, neither hydroxy nor nitrile substituted PAHs have been found to contribute significantly to the UIBs, even though the former are the dominant photoproducts of PAH photolysis in ice and the latter have been positively identified in cold clouds. Evidently, substituted PAHs formed in dark clouds do not survive in the more diffuse interstellar medium from which the UIBs emanate, and a more detailed understanding of their destruction routes is therefore needed.

Although hydrogenation and oxygenation reactions may occur on PAHs, little is known on the kinetics of the reactions between PAHs and H, O, or OH radicals, and whether such reactions can occur at low temperatures, e.g. 10 K, or if they are active at higher temperatures, which are more representative of planetary environments.

In this framework, oxygenated derivatives of PAHs, namely oxyPAHs, recently captured the interest of the scientific community for their potential properties as prebiotic molecules, including their strong adsorption properties due to higher polarity and their tendency toward polymerization.

From a chemical point of view, oxyPAHs appear to be more plausible candidates than simple PAHs to play a role in prebiotic processes because of their higher polarity, ensuring stronger adsorption on minerals, a higher facility

to give oxygenation and polymerization reactions and phenolic OH bonds photolysis leads to highly stabilized radicals.

More recently, 1-HN, 1,8-dihydroxynaphthalene (1,8-DHN), and 1,6-dihydroxynaphthalene (1,6-DHN) underwent oxidative polymerization via an interplay of competing for free radical and quinone coupling pathways when adsorbed on minerals and after irradiation with UV light.<sup>134</sup>

By combining the results obtained from diffuse reflectance infrared Fourier transform spectroscopy (DRIFTS) analysis and from a computational approach, it emerged that the oxidative reactivity of hydroxylated naphthalenes is significantly affected by the number and relative position of the hydroxyl groups. The formation of polymeric products was revealed by FT-IR spectra that showed absorption enhancement above  $4000\text{ cm}^{-1}$  and band broadening, characteristic spectral changes accompanying autoxidation. Moreover, partial degradation and decarboxylation were supposed to occur since the IR-detectable generation of  $\text{CO}_2$  (Figure 22).

Interestingly, PAHs and complex molecular species derived from their polymerization may play important role in prebiotic environment by serving not only as a source of small carbon molecules but also as protective matrices or mineral coating layers that can facilitate molecular synthesis.

The attractive hypothesis that PAH and oxyPAH-polymers could act as both catalytic and photoprotective layers ensuring that prebiotic molecules can be produced, assembled and preserved by extensive photodegradation, is rooted in the known photoprotective properties of these polymers, strictly associated with their broad band absorption of in the whole UV-visible portion of the electromagnetic spectrum.

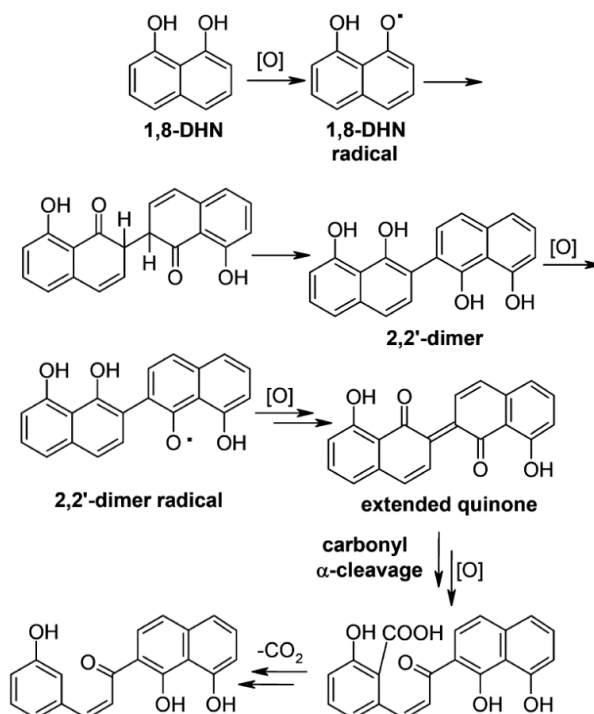


**Figure 22** | Proposed Conversion Pathways of 1,8-DHN under UV Irradiation conditions on Forsterite. Image adapted from Ref. <sup>134</sup>

Another relevant scenario is that oxyPAH formation and photoprocessing are involved as important determinants for the origin of the Insoluble Organic Matter (IOM), the major identified carbonaceous component in meteorites. This is based on the identification of some analogies between the structural and physical-chemical properties of the IOM and polymers deriving by the oxidation of 1,8-DHN.

## 1.2 Endogenous synthesis of the prebiotic compounds on Earth

### 1.2.1 Pioneering ideas and early experiments

Understanding the origin of building blocks relevant for the emergence of life on Earth and explaining the chemical processes from which they were developed, are, undoubtedly, among the most challenging questions of all time and likely we will never address them in full detail.

The idea of an evolutionary origin of life dates to the 19th century, when Charles Darwin published *The Origin of Species*.<sup>135</sup>

Darwin was always reluctant to publish his view on the origin of life, which provided the occurrence of prebiotic chemistry in a warm little pond, rich in nutrient. In 1871, in a private letter to his young botanist friend Joseph Hooker, he speculated on the conditions and principal elements to trigger the spread of life: *“it is often said that all the conditions for the first production of a living organism are now present, which could ever have been present. But if (and oh what a big if) we could conceive in some warm little pond with all sorts of ammonia and phosphoric salts, –light, heat, electricity, etc. present, that a protein compound was chemically formed, ready to undergo still more complex changes, at the present day such matter would be instantly devoured, or absorbed, which would not have been the case before living creatures were formed.”*

The idea that early Earth was dominated by the same physical and chemical laws is nowadays still valid.

Similar ideas on the origin of life on Earth were independently suggested by Oparin<sup>136</sup> and Haldane<sup>6</sup>, in the 1920s. In their landmark works, they resumed the concept of a primordial soup: molecules dissolved in the huge amount of shallow waters of the early oceans, synthesized building blocks and more

complex molecules up to first cells, as the result of the combination of reducing atmosphere and energy sources, such as lightning or UV rays.

The discovery of the submarine hydrothermal vents in the 1970s reinforced this idea and the ocean theory for the origin of life remained the most reliable for more than nine decades.

Since that, many efforts have been done to search for reasonable mechanisms underlying the direct and robust synthesis of biomonomers simulating in the laboratory the initial conditions of Earth.

The most representative example is the famous experiment carried out in 1953 by Miller and Urey at the University of Chicago supporting the Oparin and Haldane's theories.

Miller-Urey experiment<sup>1,137</sup> elegantly showed the easy formation of amino acids from mixtures of simple molecules, such as  $\text{H}_2\text{O}$ ,  $\text{NH}_3$ ,  $\text{CH}_4$ , and  $\text{H}_2$ , purportedly representing the chemical composition of a primitive reducing atmosphere and a warm liquid ocean. An electrical spark was used to simulate the effect of atmospheric lightning (Figure 23).

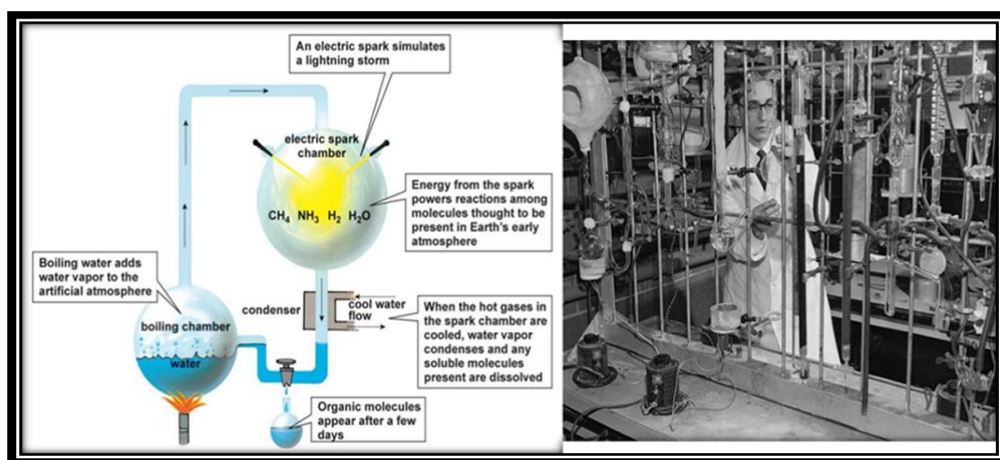


**Figure 23** | The layout of Miller-Urey experiment simulating the conditions of the primitive earth.

At that time the outcome was amazing. This experiment revealed a large yield of hydroxy acids, short aliphatic acids and urea (Table 2), beyond racemic amino acids.

**Table 2** | Yields of small organic molecules from sparking a mixture of methane, hydrogen, ammonia, and water. Yields are given on the base of the carbon added in the form of methane.<sup>139</sup>

Compound	Yield (μmoles)	Yield (%)
Glycine	630	2.1
Glycolic acid	560	1.9
Sarcosine	50	0.25
Alanine	340	1.7
Lactic acid	310	1.6
<i>N</i> -Methylalanine	10	0.07
α-Amino- <i>n</i> -butyric acid	50	0.34
α-Aminoisobutyric acid	1	0.007
α-Hydroxybutyric acid	50	0.34
β-Alanine	150	0.76
Succinic acid	4	0.27
Aspartic acid	4	0.024
Glutamic acid	6	0.051
Iminodiacetic acid	55	0.37
Iminoaceticpropionic acid	15	0.13
Formic acid	2330	4.0
Acetic acid	150	0.51
Propionic acid	130	0.66
Urea	20	0.034
<i>N</i> -Methyl urea	15	0.051

In the flurry of following experimentations, it was demonstrated that the mixture of hydrogen cyanide (HCN) and ammonia (NH<sub>3</sub>) in an aqueous solution has the potentiality to generate also the adenine. This was a great

achievement because adenine is one of the four nucleobases present in RNA and DNA and in the ribonucleotide, ATP.<sup>138</sup>

This and other discoveries led many researchers to give more thought that life could have arisen near the surface of the ocean.

One of the likely main mechanisms of the formation of amino acids in this kind of setting is the Strecker synthesis (Figure 24), a well-known reaction between ammonia, cyanide and aldehydes.<sup>140</sup>

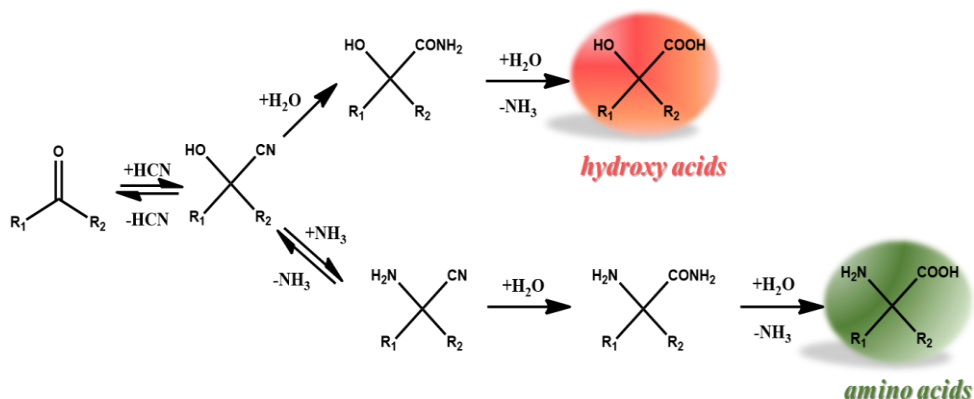


**Figure 24** | The Strecker mechanism for the formation of hydroxyacids and amino acids.

### 1.2.2 Timeline for the origin of life on Earth

Geological records suggested that life on Earth began nearly 4 billion years ago but surely it has existed as far back as these evidences. Nevertheless, there is still intense debate about where on the Earth life began.

The period which precedes the earliest records of life coincides with the late heavy bombardment, a period that is theorized to have occurred between ~3.5 Ga<sup>141</sup> and during which dominant geodynamic processes like impacts and

collisions with asteroids played a key role in the evolution of the young Earth. At that time, the primitive Earth appeared, therefore, violent and desolate, enduring the rain of extra-terrestrial materials (Figure 25).<sup>142</sup>

Little is known about the atmospheric composition and temperature conditions of Earth during the emergence of life. Thanks to geological evidences and some studies, it has been possible to predict that: 1) liquid water could be present on early Earth, indicating a surface temperature above 273 K;<sup>143</sup> 2) the young sun was less bright than today;<sup>144</sup> 3) radiation at the Earth's surface was more intense 3.5 Ga ago;<sup>145</sup> 4) the composition of the atmosphere could have been mainly controlled by outgassing from the early Earth mantle.

In this context, the early Earth could be considered a hot molten globe with an atmosphere consisting mainly of carbon dioxide, nitrogen gas and water vapour<sup>146</sup> with minor contributions of reduced species, such as carbon monoxide, methane, hydrogen and ammonia.<sup>146,147</sup>



**Figure 25** | Artwork representing the early Earth pervaded by intense meteoritic impacts and striking volcanic emissions.

When the frequency of impacts slowed down, the surface of the Earth became cool enough to support liquid water. This eon witnessed the formation of global oceans from torrential rainfalls, early continental crust, essential changes to the atmosphere and the emergence of life.<sup>148</sup>

However, some investigations evidence that the earliest life on Earth corresponds with this period of intense meteoritic assaults.<sup>149,150</sup>

The impact events on the early Earth could have generated a lot of craters filled with water and organic building blocks, developing hydrothermal crater lakes that are considered the perfect crucibles for the prebiotic chemistry of early life.<sup>142,151–155</sup> Indeed, The Late Heavy Bombardment has been postulated as being so catastrophic that conditions of early Earth have been too harsh to allow for the colonization of life; therefore, the impact-generated crater lakes may have been the only protective environment where building blocks could accumulate, concentrate and polymerize into more complex organic compounds, driven by hydrothermal energy, leading to the emergence of the first cells.<sup>151–153,155</sup>

Thus, the chemical landscape on a young Earth offered a wide range of compounds accumulated in the oceans forming the primitive soup.

However, how could monomers like amino acids or nucleotides have assembled into polymers on the early Earth has not been delineated.

In cells today, polymers are continuously synthesized by enzymes that catalyze condensation reactions. However, enzymes themselves are polymers. So, how could the first polymers form on the prebiotic Earth without available enzymes?

Polymers must have been formed spontaneously from monomers under the conditions found on early Earth.

### 1.2.3 The link between the origin of life and hydrothermal systems

During the last three decades, the discovery that hot springs host thriving microbial ecosystems, able to survive and adapt in these challenging environments, hinted at a novel scenario for the origin of life: the hot spring hypothesis.

Many researchers suggested that hydrothermal systems and primordial rock pools at volcanic sites could be possible niches for the synthesis of organic compounds on the early Earth. This theory was appealing because of the high availability of geochemical variables, such as water, thermal energy, pH and continuous supplies of nutrient elements (e.g., K and P).

A hydrothermal origin of life is also important because this implies that life could be widespread in the Solar System, because hydrothermal systems may exist on many of the satellites in the Solar System.

Mulkiđjanian and co-workers (2012) suggested that the chemistry of modern cells may reflect the chemical conditions of the environments in which the first cells emerged.<sup>156</sup>

All living cells are rich in potassium, zinc, manganese and phosphate ions, found only in hot hydrothermal places such as geysers, fumaroles, crater basins, and other geothermal fields.

Therefore, the chemical nature of volcanic pools more closely resembles the cytoplasm composition of cells, supporting the geothermal terrestrial origin of life.

Several lines of evidence suggest that the hydrothermal fields on the early Earth may have been quite similar to sites in Kamchatka, Hawaii, Iceland, Yellowstone, Kawah Ijen and Solfatara (Figure 26).<sup>157</sup>



**Figure 26** | Geothermal springs. On the left: mud pools of the Solfatara volcano located inside the caldera of Phlegrean Fields. On the right: crater of Kawah Ijen volcano containing a highly acidic lake and fumaroles.

A rich literature documents the benefits of this environment for the formation of a range of biomolecules as the key requisite for the development of the primitive forms of life. Noticeable examples include the advantageous synthesis of amino acids and carbohydrates, by means of Strecker-type and formose reactions, under hydrothermal conditions.<sup>158–160</sup>

Furthermore, hydrocarbon derivatives, such as long-chain monocarboxylic acids and alcohols, can be abiotically produced in hot spring settings by Fischer–Tropsch synthesis.<sup>161</sup>

The vapor phase of geothermal systems is particularly enriched in borate, which seems to be important for the stabilization of ribose,<sup>162,163</sup>

moreover, a lot of studies demonstrated the abiotic synthesis of nucleotides and amino acids<sup>164–173</sup> from formamide, via hydrolysis of hydrogen cyanide, which is found in volcanic gases and in exhalations of geothermal fields.<sup>174</sup>

However, the condensation reactions, that lead to the formation of biopolymers with the release of water are very challenging processes in presence of water. Indeed, even if these reactions are mostly favoured under high temperatures for their endothermic nature, the presence of water makes the reverse hydrolytic process thermodynamically favoured.

Unquestionably, water is a mandatory pre-requisite for life and ubiquitous on Earth. It is assumed that water has been readily available on primitive Earth, since also its ubiquity in the universe.

Thus, life requires water but, at the same time, it is inherently “toxic” to polymers (e.g. nucleotides or proteins) necessary for life. In 1986, the biochemist Robert Shapiro, who critiqued the primordial ocean hypothesis,<sup>175</sup> wrote in his book *Origins* that “water is an enemy to be excluded as rigorously as possible”. We are faced with the “water paradox”.<sup>176</sup>

To overcome this difficulty, researchers have tested different methods including the use of condensing agents, high temperatures, and water-free solvents. Besides some of these being successful, not all of these routes would have been plausible on the early Earth.

Recently, regular cycling between wet and dry conditions has been proposed as a crucial driving factor for condensation reactions. Under these conditions, the polymerization does not require activated monomers or condensing agents. Wet–dry cycles are regarded as characteristic of extreme natural fluctuating environments like hydrothermal pools and primordial rock pools at volcanic sites. These are areas of elevated temperatures where water is not stagnant: hot spring water raised to the surface and rainstorms and flooding occurred.

The cycling frequency of wet-dry cycles is as short as minutes, when caused by geysers splash water on surrounding hot rocks, hours, when associated with

the rise and fall of pool levels caused by regularly fluctuating hot springs, or days, if related to complete evaporation of smaller pools followed by refilling during precipitation.

So, dynamic cycling between the anhydrous surface phase and the hydrated bulk phase is established (Figure 27).



**Figure 27** | Hydrothermal pools periodically filled by geyser outflow and rainfall. Wet and dry cycles and mineral surfaces at pool edges are thought to promote the polymerization of biomolecules.

In the wet-dry cycling process, each cycle involves two phases: 1) a hot and dry phase in which the bond formation is favourable, but diffusion is not allowed or much slower than in solution, so only monomers that are very close can polymerize; 2) a wet phase in which diffusion is allowed so that molecules are brought closer each other, ready to polymerize in the next dry phase. The net effect of iterative cycles leads to an increase in the polymerization yields.

So, if nucleotides are present, the hydroxyl and phosphate groups may react forming ester bonds and leading to the assembly of nucleic acid polymers,<sup>177–179</sup> as it happens for the formation of proteins through the formation of peptide bonds between amino acids.

In this context, clays, minerals and silicates located at hydrosphere–lithosphere interface may have played a crucial role both adsorbing the key monomers on their surface, so concentrating them with respect to solution in the pool, both acting as catalysts promoting the polymerization process.

### **1.3 Role of minerals**

Whatever the source of the organic compounds on the early Earth, from meteorites impacting on our planet or via the synthesis at volcanic landmasses, they could be concentrated on the mineral surfaces and then would be flushed into pools inside the hydrothermal systems, enabling their participation in prebiotically significant reactions.

Beyond the sorption capabilities of minerals, they may have played a pivotal role because their surfaces are dynamic and they can act as a template, adsorbing selectively molecules, allowing their concentration, and promoting molecular self-organization processes.<sup>180,181</sup> Minerals can also act as catalysts, accelerating chemical reactions by lowering the corresponding activation energy or promoting selective synthesis of biomolecules on their surface.<sup>180,182–187</sup>

This can happen because mineral surfaces are able to induce the orientation of reacting groups of neighboring molecules through specific molecule-mineral interactions.

Mineral surfaces can also have an enantioselective potential and hence a role in the development of chirality under prebiotic conditions.<sup>188</sup>

Mid- and far-infrared spectra provided striking evidences of the ubiquitous presence of minerals, such as silicates which seems to be highly relevant for the synthesis and accumulation of prebiotic molecules. Indeed, the physical-chemical interactions of biomolecules with the surface of minerals might affect the survival of molecules in space, protecting them against degradation and shielding them from intense radiations, favouring their preservation throughout time.<sup>189,190</sup>

However, the presence of minerals can also increase the probability of molecular photolysis, because the interactions of a molecule with a mineral can weaken intramolecular bonds, thus facilitating their breakage upon exposure to electromagnetic radiation. The degradation of the adsorbed molecules catalyzed by mineral surfaces<sup>186,191,192</sup> could lead to the formation of more complex species.

All these findings suggest a key role of minerals in the prebiotic evolution of complex chemical systems. In this sense, the study of molecule-mineral interactions under plausible prebiotic and interstellar conditions may be a breakthrough in solving unanswered questions about the origin of life on Earth.

#### **1.4 Aims of the research work**

On the basis of this complex and wide scenario, my Ph.D. thesis work has been focused on the study of the transformation pathways of polycyclic aromatic hydrocarbons and biomolecule precursors of astrochemical origin under model conditions of prebiotic relevance.

In detail, the research activity has been aimed at elucidating the nature of the reaction products deriving from PAHs under solid-state irradiation and heating

conditions and the catalytic role of their polymers in prebiotically relevant processes.

In this connection, the work has been structured into the following two main topics concurring at assessing the potential role of some representative components of the putative astrochemical pool of PA(N)Hs and oxyPAHs, namely naphthalene (NAPH), quinoline (QUIN), 1-naphthol (1-HN) and 1,8-dihydroxynaphthalene (1,8-DHN) (Figure 28), in the processes associated with the origin of life:

1. study of the photochemical susceptibility of PA(N)Hs, oxyPAHs and COMs under simulated interstellar conditions;
2. study of the role played by PAHs and oxyPAHs in the chemical transformations occurring under the environmental conditions found on the early Earth.

In particular, the results of the experimental activity have been collected in the following chapters:

Chapter 2- high energy proton beam irradiation of oxyPAHs adsorbed on meteorites;

Chapter 3- photo-processing and thermal desorption of PA(N)Hs and COMs on ice dust grains;

Chapter 4- oxyPAH-polymers as mediators for prebiotic processed on early Earth: synthesis and characterization;

Chapter 5- catalytic effect of oxyPAH-polymers in the chemical processes leading to the formation of the peptide bond;

Chapter 6- chemical transformations of PAHs and oxyPAHs in the thermal water of Solfatara.

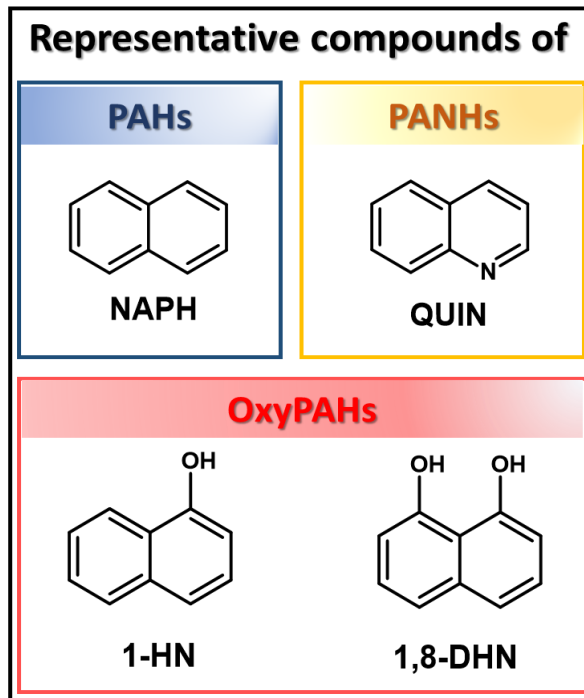


**Figure 28** | Structure of molecules selected for this thesis work.

**REFERENCES:**

1. S.L. Miller. A Production of Amino Acids Under Possible Primitive Earth Conditions. *Science (1979)* **1953**, 117, 528–529.
2. B. Damer, D. Deamer. The Hot Spring Hypothesis for an Origin of Life. *Astrobiology* **2020**, 20 (4), 429–452.
3. E.R. Micelotta, A.P. Jones, A.G.G.M. Tielens. Polycyclic aromatic hydrocarbon processing by cosmic rays. *Astron Astrophys* **2011**, 526, A52.
4. L. Colzi, F. Fontani, V.M. Rivilla, et al. Nitrogen fractionation in high-mass star-forming cores across the Galaxy. *Mon Not R Astron Soc* **2018**, 478 (3), 3693–3720.
5. M.P. Bernstein, J.P. Dworkin, S.A. Sandford, L.J. Allamandola. Ultraviolet irradiation of the polycyclic aromatic hydrocarbon (PAH) naphthalene in H<sub>2</sub>O. Implications for meteorites and biogenesis. *Advances in Space Research* **2002**, 30 (6), 1501–1508.
6. Haldane J. B. S. Origin of life. *Ration. Annu.* **1929**, 148, 3–10.
7. Oparin A. I. The origin of life; MacMillan, New York, **1938**.
8. M.P. Callahan, K.E. Smith, H. James, et al. Carbonaceous meteorites contain a wide range of extraterrestrial nucleobases. *PNAS* **2011**, 108 (34), 13995–13998.
9. B. Damer, D. Deamer. Coupled phases and combinatorial selection in fluctuating hydrothermal pools: A scenario to guide experimental approaches to the origin of cellular life. *Life* **2015**, 5 (1), 872–887.
10. D. Deamer. First Life: Discovering the Connections between Stars, Cells, and How Life Began; **2011**.
11. S. Pizzarello, J.R. Cronin. Non-racemic amino acids in the Murray and Murchison meteorites. *Geochim Cosmochim Acta* **2000**, 64 (2), 329–338.
12. M. Sithamparam, N. Sathiyasilan, C. Chen, T.Z. Jia, K. Chandru. A material-based panspermia hypothesis: The potential of polymer gels and membraneless droplets. *Biopolymers* **2022**, 113 (5).
13. E. Mateo-Marti, O. Prieto-Ballesteros, G. Muñoz Caro, et al. Characterizing Interstellar Medium, Planetary Surface and Deep Environments by Spectroscopic Techniques Using Unique Simulation Chambers at Centro de Astrobiología (CAB). *Life* **2019**, 9 (3), 72.

14. D. Smith. The Ion Chemistry of Interstellar Clouds. *Chem. Rev* **1992**, 92, 1473–1485.
15. W.D. Geppert, M. Larsson. Experimental investigations into astrophysically relevant ionic reactions. *Chemical Reviews*. December 11, 2013, pp 8872–8905.
16. E.A. Bergin, M. Tafalla. Cold Dark Clouds: The Initial Conditions for Star Formation. *Annu. Rev. Astron. Astrophys.* **2007**, 45, 339–396.
17. K.I. Öberg. Photochemistry and Astrochemistry: Photochemical Pathways to Interstellar Complex Organic Molecules. *Chemical Reviews*. American Chemical Society September 14, 2016, pp 9631–9663.
18. C.R. Arumainayagam, R.T. Garrod, M.C. Boyer, et al. Extraterrestrial prebiotic molecules: photochemistry vs. radiation chemistry of interstellar ices. *Chemical Society Reviews*. Royal Society of Chemistry April 21, 2019, pp 2293–2314.
19. G.M.M. Caro, E. Dartois. Prebiotic chemistry in icy grain mantles in space. An experimental and observational approach. *Chem Soc Rev* **2013**, 42 (5), 2173–2185.
20. R. Gomes, H.F. Levison, K. Tsiganis, A. Morbidelli. Origin of the cataclysmic Late Heavy Bombardment period of the terrestrial planets. *Nature* **2005**, 435 (7041), 466–469.
21. M. Goto, T. Usuda, N. Takato, et al. Carbon Isotope Ratio in  $^{12}\text{CO}/^{13}\text{CO}$  toward Local Molecular Clouds with Near-Infrared High-Resolution Spectroscopy of Vibrational Transition Bands. *Astrophys J* **2003**, 598, 1038–1047.
22. P. Swings, L. Rosenfeld. Considerations Regarding Interstellar Molecules. *ApJ* **1937**, 86, 4.
23. A. Mckellar. Evidence for the Molecular Origin of Some Hitherto Unidentified Interstellar Lines. *PASP* **1940**, 52, 187.
24. A. E. Douglas, G. Herzberg. Note on  $\text{CH}^+$  in Interstellar Space and in the Laboratory. *ApJ* **1941**, 94, 3.
25. A.C. Cheung, D. M. Rank, C.H Townes, D.D Thornton, W.J. Welch. Detection of Water in Interstellar Regions by its Microwave Radiation. *Nature* **1969**, 221, 626.

26. L. E. Snyder, D. B., B. Zuckerman, P. Palmer. Microwave Detection of Interstellar Formaldehyde. *Phys. Rev. L.* **1969**, 22, 679.
27. R.W. Wilson, K.B. Jefferts, A.A. Penzias. Carbon Monoxide in the Orion Nebula. *ApJ* **1970**, 161, L43.
28. P.D. Holtom, C.J. Bennett, Y. Osamura, N.J. Mason, R.I. Kaiser. A Combined Experimental and Theoretical Study on the Formation of the Amino Acid Glycine ( $\text{NH}_2\text{CH}_2\text{COOH}$ ) and Its Isomer ( $\text{CH}_3\text{NHCOOH}$ ) in Extraterrestrial Ices. *Astrophys J* **2005**, 626, 940–952.
29. M. Ferus, V. Laitl, A. Knizek, et al. HNCO-based synthesis of formamide in planetary atmospheres. *Astron Astrophys* **2018**, 616.
30. R.H. Rubin, G.W. Swenson, R.C. Benson, H.L. Tigelaar, W.H. Flygare. Microwave Detection of Interstellar Formamide. *Astrophys J* **1971**, 169, L39.
31. S. Zeng, D. Quénard, I. Jiménez-Serra, et al. First detection of the pre-biotic molecule glycolonitrile ( $\text{HOCH}_2\text{CN}$ ) in the interstellar medium. *Mon Not R Astron Soc Lett* **2019**, 484 (1), L43–L48.
32. A. Belloche, K.M. Menten, C. Comito, et al. Detection of amino acetonitrile in Sgr B2(N). *Astron Astrophys* **2008**, 492 (3), 769–773.
33. M.A. Sephton, J.H. Waite, T.G. Brockwell. How to detect life on icy moons. *Astrobiology* **2018**, 18 (7), 843–855.
34. P. Ehrenfreund, S. Rasmussen, J. Cleaves, L. Chen. Experimentally Tracing the Key Steps in the Origin of Life: The Aromatic World. *490 Astrobiology* **2006**, 6 (3), 490–520.
35. Andrew M. Shaw. *Astrochemistry: From Astronomy to Astrobiology*; John Wiley & Sons, Ed.; **2007**; p 334.
36. K.M. Merrill, B.T. Soifer. Spectrophotometric observations of a highly absorbed object in Cygnus. *Astrophys. J. Lett.* **1974**, 189, 27.
37. A.C.A. Boogert, P.A. Gerakines, D.C.B. Whittet. Observations of the icy universe. *Annu Rev Astron Astrophys* **2015**, 53 (1), 541–581.
38. K.I. Oberg, A.C.A. Boogert, K.M. Pontoppidan, et al. The Spitzer ice legacy: Ice evolution from cores to protostars. *ApJ* **2011**, 740, 109.
39. E. Dartois. The ice survey opportunity of ISO. *Space Sci Rev* **2005**, 119 (1–4), 293–310.

40. M. Larsson, W.D. Geppert, G. Nyman. Ion chemistry in space. *Reports on Progress in Physics* **2012**, 75 (6).
41. N. Watanabe, A. Kouchi. Efficient Formation of Formaldehyde and Methanol by the Addition of Hydrogen Atoms to CO in H[TINF]<sub>2</sub>[TINF]O-CO Ice at 10 K. *Astrophys J* **2002**, 571 (2), L173–L176.
42. P. Ehrenfreund, E. Dartois, K. Demyk, L. D’hendecourt. Ice segregation toward massive protostars. *Astron. Astrophys* **1998**, 339, 17–20.
43. E.F. Van Dishoeck, M.R. Hogerheijde. Models and Observations of the Chemistry near Young Stellar Objects. *Annu Rev Astron Astrophys* **1999**, 36, 317–368.
44. J.K. Jørgensen, T.L. Bourke, P.C. Myers, et al. PROSAC: A Submillimeter Array Survey of Low-Mass Protostars. I. Overview of Program: Envelopes, Disks, Outflows and Hot Cores. *Astrophys J* **2007**, 659, 479–498.
45. E. Dartois, W. Schutte, T.R. Geballe, K. Demyk, P. Ehrenfreund, L. D’Hendecourt. Methanol: The second most abundant ice species towards the high-mass protostars RAFGL7009S and W 33A. *Astron Astrophys* **1998**, 342, L32–L35.
46. C.J. Skinner, A.G.G.M. Tielens, M.J. Barlow, K. Justtanont. Methanol ice in the protostar GL 2136. *Astrophys J* **1992**, 399, L79.
47. H.M. Cuppen, C. Walsh, T. Lamberts, et al. Grain Surface Models and Data for Astrochemistry. *Space Sci Rev* **2017**, 212 (1–2), 1–58.
48. A. Jiménez-Escobar, A. Ciaravella, C. Cecchi-Pestellini, et al. X-Ray Photo-desorption of H<sub>2</sub>O:CO:NH<sub>3</sub> Circumstellar Ice Analogs: Gas-phase Enrichment. *Astrophys J* **2018**, 868 (1), 73.
49. A. Jiménez-Escobar, A. Ciaravella, C. Cecchi-Pestellini, et al. X-Ray-induced Diffusion and Mixing in Layered Astrophysical Ices. *Astrophys J* **2022**, 926 (2), 176.
50. A. Bar-nun, G. Herman, D. Laufer, M.L. Rappaport. Trapping and Release of Gases by Water Ice and Implications for Icy Bodies. *Icarus* **1985**, 63, 317–332.
51. S. A. Sandford, L. J. Allamandola, A. G. Tielens, G. J. Valero. Laboratory studies of the infrared spectral properties of CO in astrophysical ices. *Astrophysical Journal* **1988**, 329, 498–510.
52. Gary Attard and Colin Barnes. Surfaces; Oxford Chemistry Primers.

53. G.M. Muñoz Caro, W.A. Schutte. UV-photoprocessing of interstellar ice analogs: New infrared spectroscopic results. *Astron Astrophys* **2003**, 412 (1), 121–132.
54. R.G. Urso, C. Scirè, G.A. Baratta, et al. Infrared study on the thermal evolution of solid state formamide. *Physical Chemistry Chemical Physics* **2017**, 19 (32), 21759–21768.
55. Z. Kaňuchová, R.G. Urso, G.A. Baratta, et al. Synthesis of formamide and isocyanic acid after ion irradiation of frozen gas mixtures. *Astron Astrophys* **2016**, 585, A155.
56. A. Bergantini, S. Pilling, H. Rothard, P. Boduch, D.P.P. Andrade. Processing of formic acid-containing ice by heavy and energetic cosmic ray analogues. *Mon Not R Astron Soc* **2014**, 437 (3), 2720–2727.
57. P.A. Gerakines, M.H. Moore, R.L. Hudson. Ultraviolet photolysis and proton irradiation of astrophysical ice analogs containing hydrogen cyanide. *Icarus* **2004**, 170 (1), 202–213.
58. V. Mennella. Synthesis and Transformation of Carbonaceous Nanoparticles. *Proceedings of the International Astronomical Union* **2012**, 10 (H16), 715–716.
59. G.A. Baratta, D. Chaput, H. Cottin, et al. Organic samples produced by ion bombardment of ices for the EXPOSE-R2 mission on the International Space Station. *Planet Space Sci* **2015**, 118, 211–220.
60. Guillermo M. Muñoz Caro. Laboratory Astrophysics; Muñoz Caro, G. M., Escribano, R., Eds.; Springer International Publishing, **2018**; Vol. 451.
61. M.P. Bernstein, J.P. Dworkin, S.A. Sanford, L.J. Allamandola. Ultraviolet irradiation of naphthalene in H<sub>2</sub>O ice: Implications for meteorites and biogenesis. *Meteorit Planet Sci* **2001**, 36 (3), 351–358.
62. G.M. Muñoz Caro, U.J. Meierhenrich, W.A. Schutte, et al. Amino acids from ultraviolet irradiation of interstellar ice analogues. *Nature* **2002**, 416 (6879), 403–406.
63. J.P. Dworkin, D.W. Deamer, S.A. Sandford, L.J. Allamandola. Self-assembling amphiphilic molecules: Synthesis in simulated interstellar/precometary ices. *Proceedings of the National Academy of Sciences* **2001**, 98 (3), 815–819.

- 
64. M. Nuevo, S.N. Milam, S.A. Sandford, J.E. Elsila, J.P. Dworkin. Formation of uracil from the ultraviolet photo-irradiation of pyrimidine in pure H<sub>2</sub>O ices. *Astrobiology* **2009**, 9 (7), 683–695.
  65. M. Nuevo, Y.-J. Chen, W.-J. Hu, et al. Irradiation of Pyrimidine in Pure H<sub>2</sub>O Ice with High-Energy Ultraviolet Photons. *Astrobiology* **2014**, 14 (2), 119–131.
  66. M. Nuevo, S.N. Milam, S.A. Sandford. Nucleobases and prebiotic molecules in organic residues produced from the ultraviolet photo-irradiation of pyrimidine in NH<sub>3</sub> and H<sub>2</sub>O+NH<sub>3</sub> ices. *Astrobiology* **2012**, 12 (4), 295–314.
  67. P.P. Bera, M. Nuevo, C.K. Materese, S.A. Sandford, T.J. Lee. Mechanisms for the formation of thymine under astrophysical conditions and implications for the origin of life. *J Chem Phys* **2016**, 144 (14), 144308.
  68. P.P. Bera, T. Stein, M. Head-Gordon, T.J. Lee. Mechanisms of the Formation of Adenine, Guanine, and Their Analogues in UV-Irradiated Mixed NH<sub>3</sub>:H<sub>2</sub>O Molecular Ices Containing Purine. *Astrobiology* **2017**, 17 (8), 771–785.
  69. C.K. Materese, M. Nuevo, S.A. Sandford. The Formation of Nucleobases from the Ultraviolet Photoirradiation of Purine in Simple Astrophysical Ice Analogues. *Astrobiology* **2017**, 17 (8), 761–770.
  70. C.K. Materese, M. Nuevo, B.L. McDowell, C.E. Buffo, S.A. Sandford. The Photochemistry of Purine in Ice Analogs Relevant to Dense Interstellar Clouds. *Astrophys J* **2018**, 864 (1), 44.
  71. M. Nuevo, J.H. Bredehöft, U.J. Meierhenrich, L. d’Hendecourt, W.H.-P. Thiemann. Urea, Glycolic Acid, and Glycerol in an Organic Residue Produced by Ultraviolet Irradiation of Interstellar/Pre-Cometary Ice Analogs. *Astrobiology* **2010**, 10 (2), 245–256.
  72. A. Ciaravella, A. Jiménez-Escobar, C. Cecchi-Pestellini, et al. Synthesis of Complex Organic Molecules in Soft X-Ray Irradiated Ices. *Astrophys J* **2019**, 879 (1), 21.
  73. C. Meinert, I. Myrgorodska, P. de Marcellus, et al. Ribose and related sugars from ultraviolet irradiation of interstellar ice analogs. *Science (1979)* **2016**, 352 (6282), 208–212.
  74. Y. Oba, Y. Takano, H. Naraoka, N. Watanabe, A. Kouchi. Nucleobase synthesis in interstellar ices. *Nat Commun* **2019**, 10 (1), 4413.

- 
75. F.C. Gillett, W.J. Forrest, K.M. Merrill. 8-13 micron spectra of NGC 7027, BD +30 3639 and NGC 6572. *Astrophys J* **1973**, 183, 87.
  76. R.W. Russell, B.T. Soifer, W.J. Forrest. Spectrophotometric observations of MU Cephei and the moon from 4 to 8 microns. *Astrophys J* **1975**, 198, L41.
  77. W.W. Duley, D.A. Williams. The infrared spectrum of interstellar dust: Surface functional groups on carbon. *Mon Not R Astron Soc* **1981**, 196 (2), 269–274.
  78. A.; P.J.L. Leger. Identification of the ‘unidentified’ IR emission features of interstellar dust? *Astron. Astrophys.* **1984**, 137, L5–L8.
  79. L.J. Allamandola, A.G.G.M. Tielens, J.R. Barker. Polycyclic aromatic hydrocarbons and the unidentified infrared emission bands - Auto exhaust along the Milky Way. *Astrophys J* **1985**, 290, L25.
  80. E. Peeters, S. Hony, C. Van Kerckhoven, et al. The rich 6 to 9  $\mu\text{m}$  spectrum of interstellar PAHs. *Astron Astrophys* **2002**, 390 (3), 1089–1113.
  81. D.M. Hudgins, Jr., C.W. Bauschlicher, L.J. Allamandola. Variations in the Peak Position of the 6.2  $\mu\text{m}$  Interstellar Emission Feature: A Tracer of N in the Interstellar Polycyclic Aromatic Hydrocarbon Population. *Astrophys J* **2005**, 632 (1), 316–332.
  82. Jr., C.W. Bauschlicher, A. Ricca. The Far-Infrared Emission from the Mg+-PAH Species. *Astrophys J* **2009**, 698 (1), 275–280.
  83. S. Wada, T. Onaka, I. Yamamura, Y. Murata, A.T. Tokunaga.  $^{13}\text{C}$  isotope effects on infrared bands of quenched carbonaceous composite (QCC). *Astron Astrophys* **2003**, 407 (2), 551–562.
  84. A. Simon, C. Joblin. The Computed Infrared Spectra of a Variety of  $[\text{FePAH}]^+$  Complexes: Mid- and Far-Infrared Features. *Astrophys J* **2010**, 712 (1), 69–77.
  85. B. Joalland, A. Simon, C.J. Marsden, C. Joblin. Signature of  $[\text{SiPAH}]^+$   $\pi$ -complexes in the interstellar medium. *Astron Astrophys* **2009**, 494 (3), 969–976.
  86. M. Rapacioli, C. Joblin, P. Boissel. Spectroscopy of polycyclic aromatic hydrocarbons and very small grains in photodissociation regions. *Astron Astrophys* **2005**, 429 (1), 193–204.
  87. A. Simon, C. Joblin. Photodissociation of  $[\text{Fe}_x(\text{C}_{24}\text{H}_{12})_y]^+$  Complexes in the PIRENEA Setup: Iron-Polycyclic Aromatic Hydrocarbon Clusters as

- Candidates for Very Small Interstellar Grains. *J Phys Chem A* **2009**, 113 (17), 4878–4888.
88. C.W. Bauschlicher, E. Peeters, L.J. Allamandola. The Infrared Spectra of Very Large Irregular Polycyclic Aromatic Hydrocarbons (PAHs): Observational Probes of Astronomical PAH Geometry, Size and Charge. *Astrophys J* **2009**, 697 (1), 311–327.
89. Jr., C.W. Bauschlicher, E. Peeters, L.J. Allamandola. The Infrared Spectra of Very Large, Compact, Highly Symmetric, Polycyclic Aromatic Hydrocarbons (PAHs). *Astrophys J* **2008**, 678 (1), 316–327.
90. S. Kwok, Y. Zhang. Mixed aromatic-aliphatic organic nanoparticles as carriers of unidentified infrared emission features. *Nature* **2011**, 479 (7371), 80–83.
91. J. Cernicharo, M. Agúndez, C. Cabezas, et al. Pure hydrocarbon cycles in TMC-1: Discovery of ethynyl cyclopropenylidene, cyclopentadiene, and indene. *Astron Astrophys* **2021**, 649, L15.
92. J. Cernicharo, M. Agúndez, R.I. Kaiser, et al. Discovery of benzyne, o-C<sub>6</sub>H<sub>4</sub>, in TMC-1 with the QUIJOTE line survey. *Astron Astrophys* **2021**, 652, L9.
93. B.A. McGuire, A.M. Burkhardt, S. Kalenskii, et al. Detection of the aromatic molecule benzonitrile (c-C<sub>6</sub>H<sub>5</sub>CN) in the interstellar medium. *Science (1979)* **2018**, 359 (6372), 202–205.
94. B.A. McGuire, R.A. Loomis, A.M. Burkhardt, et al. Detection of two interstellar polycyclic aromatic hydrocarbons via spectral matched filtering. *Science (1979)* **2021**, 371 (6535), 1265–1269.
95. A.G.G.M. Tielens, S.B. Charnley. Circumstellar and Interstellar Synthesis of Organic Molecules. *Origins of Life and Evolution of the Biosphere* **1997**, 27 (1/3), 23–51.
96. D.S.N. Parker, F. Zhang, Y.S. Kim, et al. Low temperature formation of naphthalene and its role in the synthesis of PAHs (Polycyclic Aromatic Hydrocarbons) in the interstellar medium. *Proceedings of the National Academy of Sciences* **2012**, 109 (1), 53–58.
97. A.G.G.M. Tielens. *The Physics and Chemistry of the Interstellar Medium*; Cambridge University Press, **2005**.

98. E. Peeters. Astronomical observations of the PAH emission bands. *EAS Publications Series* **2011**, 46, 13–27.
99. A.G.G.M. Tielens. Interstellar Polycyclic Aromatic Hydrocarbon Molecules. *Annu Rev Astron Astrophys* **2008**, 46 (1), 289–337.
100. A.G.G.M. Tielens. The molecular universe. *Rev Mod Phys* **2013**, 85 (3), 1021–1081.
101. A. Salama, K. Anderson, J.S. Toms. Does community and environmental responsibility affect firm risk? Evidence from UK panel data 1994–2006. *Business Ethics: A European Review* **2011**, 20 (2), 192–204.
102. F. Salama, L.J. Allamandola. Is a pyrene-like molecular ion the cause of the 4,430-Å diffuse interstellar absorption band? *Nature* **1992**, 358 (6381), 42–43.
103. R. Ruitkamp, N.L.J. Cox, M. Spaans, et al. PAH charge state distribution and DIB carriers: Implications from the line of sight toward HD 147889. *Astron Astrophys* **2005**, 432 (2), 515–529.
104. L. Becker, T.E. Bunch. Fullerenes, fulleranes and polycyclic aromatic hydrocarbons in the Allende meteorite. *Meteorit Planet Sci* **1997**, 32 (4), 479–487.
105. H. Sabbah, A. Bonnamy, D. Papanastasiou, et al. Identification of PAH Isomeric Structure in Cosmic Dust Analogs: The AROMA Setup. *Astrophys J* **2017**, 843 (1), 34.
106. N.-M.K., M.D.S. and S.S.A. Clemett S. J. Identification of Aromatic Organic Matter from Comet 81P/Wild 2 by Itra-L2MS. *LPSC* **2007**, 38, 2091.
107. I. Gilmour, C.T. Pillinger. Isotopic compositions of individual polycyclic aromatic hydrocarbons from the Murchison meteorite. *Mon Not R Astron Soc* **1994**, 269 (2), 235–240.
108. H. Naraoka, A. Shimoyama, K. Harada. Isotopic evidence from an Antarctic carbonaceous chondrite for two reaction pathways of extraterrestrial PAH formation. *Earth Planet Sci Lett* **2000**, 184 (1), 1–7.
109. M.A. Sephton. Organic compounds in carbonaceous meteorites. *Nat Prod Rep* **2002**, 19 (3), 292–311.
110. A.G.G.M. Tielens. The Molecular Universe. *Proceedings of the International Astronomical Union* **2011**, 7 (S280), 3–18.

111. M. Lecasble, L. Remusat, J.-C. Viennet, B. Laurent, S. Bernard. Polycyclic aromatic hydrocarbons in carbonaceous chondrites can be used as tracers of both pre-accretion and secondary processes. *Geochim Cosmochim Acta* **2022**, 335, 243–255.
112. H. Naraoka, Y. Takano, J.P. Dworkin, et al. Soluble organic molecules in samples of the carbonaceous asteroid (162173) Ryugu. *Science (1979)* **2023**, 379 (6634).
113. J. Groen, D.W. Deamer, A. Kros, P. Ehrenfreund. Polycyclic Aromatic Hydrocarbons as Plausible Prebiotic Membrane Components. *Origins of Life and Evolution of Biospheres* **2012**, 42 (4), 295–306.
114. D. v. Mifsud, P.A. Hailey, A. Traspas Muiña, et al. The Role of Terahertz and Far-IR Spectroscopy in Understanding the Formation and Evolution of Interstellar Prebiotic Molecules. *Frontiers in Astronomy and Space Sciences* **2021**, 8.
115. H. Andrews, C. Boersma, M.W. Werner, et al. PAH Emission at the Bright Locations of PDRs: the grandPAH Hypothesis. *Astrophys J* **2015**, 807 (1), 99.
116. I. García-Bernete, D. Rigopoulou, A. Alonso-Herrero, et al. A high angular resolution view of the PAH emission in Seyfert galaxies using JWST/MRS data. *Astron Astrophys* **2022**, 666, L5.
117. L.J. Allamandola. PAHs and Astrobiology. *EAS Publications Series* **2011**, 46, 305–317.
118. A.M. Cook, A. Ricca, A.L. Mattioda, et al. Photochemistry of Polycyclic Aromatic Hydrocarbons in Cosmic Water Ice: The Role of PAH Ionization and Concentration. *Astrophys J* **2015**, 799 (1), 14.
119. M.P. Bernstein, S.A. Sandford, L.J. Allamandola, et al. UV Irradiation of Polycyclic Aromatic Hydrocarbons in Ices: Production of Alcohols, Quinones, and Ethers. *Science (1979)* **1999**, 283 (5405), 1135–1138.
120. A.L. Mattioda, G.A. Cruz-Diaz, A. Ging, et al. Formation of Complex Organic Molecules (COMs) from Polycyclic Aromatic Hydrocarbons (PAHs): Implications for ISM IR Emission Plateaus and Solar System Organics. *ACS Earth Space Chem* **2020**, 4 (12), 2227–2245.
121. M.S. Gudipati, L.J. Allamandola. Facile Generation and Storage of Polycyclic Aromatic Hydrocarbon Ions in Astrophysical Ices. *Astrophys J* **2003**, 596 (2), L195–L198.

122. M.S. Gudipati, L.J. Allamandola. Unusual Stability of Polycyclic Aromatic Hydrocarbon Radical Cations in Amorphous Water Ices up to 120 K: Astronomical Implications. *Astrophys J* **2006**, 638 (1), 286–292.
123. J. Bouwman, H.M. Cuppen, A. Bakker, L.J. Allamandola, H. Linnartz. Photochemistry of the PAH pyrene in water ice: the case for ion-mediated solid-state astrochemistry. *Astron Astrophys* **2010**, 511, A33.
124. V. Kofman, M.J.A. Witlox, J. Bouwman, I.L. ten Kate, H. Linnartz. A multifunctional setup to record FTIR and UV-vis spectra of organic molecules and their photoproducts in astronomical ices. *Review of Scientific Instruments* **2018**, 89 (5), 053111.
125. S.H. Cuyllé, E.D. Tenenbaum, J. Bouwman, H. Linnartz, L.J. Allamandola. Ly-induced charge effects of polycyclic aromatic hydrocarbons embedded in ammonia and ammonia:water ice. *Mon Not R Astron Soc* **2012**, 423 (2), 1825–1830.
126. D.E. Woon, J. Park. Photoionization of Benzene and Small Polycyclic Aromatic Hydrocarbons in Ultraviolet-processed Astrophysical Ices: A Computational Study. *Astrophys J* **2004**, 607 (1), 342–345.
127. M.S. Gudipati, L.J. Allamandola. Polycyclic Aromatic Hydrocarbon Ionization Energy Lowering in Water Ices. *Astrophys J* **2004**, 615 (2), L177–L180.
128. M.S. Gudipati, R. Yang. In-situ Probing of Radiation-induced Processing of Organics in Astrophysical Ice Analogs—Novel Laser Desorption Laser Ionization Time-of-flight Mass Spectroscopic Studies. *Astrophys J* **2012**, 756 (1), L24.
129. A. Ricca, C.W. Bauschlicher Jr. The reactions of polycyclic aromatic hydrocarbons with OH. *Chem Phys Lett* **2000**, 328 (4–6), 396–402.
130. R.V. Krishnamurthy, S. Epstein, J.R. Cronin, S. Pizzarello, G.U. Yuen. Isotopic and molecular analyses of hydrocarbons and monocarboxylic acids of the Murchison meteorite. *Geochim Cosmochim Acta* **1992**, 56 (11), 4045–4058.
131. M.P. Bernstein, M.H. Moore, J.E. Elsila, et al. Side Group Addition to the Polycyclic Aromatic Hydrocarbon Coronene by Proton Irradiation in Cosmic Ice Analogs. *Astrophys J* **2003**, 582, 25–29.

132. T. Chen, J. Zhen, Y. Wang, H. Linnartz, A.G.G.M. Tielens. Photodissociation processes of Bisanthraquinone cation. *Proceedings of the International Astronomical Union* **2017**, 13 (S332), 353–359.
133. C.K. Materese, M. Nuevo, S.A. Sandford. N- and O-heterocycles Produced from the Irradiation of Benzene and Naphthalene in H<sub>2</sub>O/NH<sub>3</sub>-containing Ices. *Astrophys J* **2015**, 800 (2), 116.
134. S. Potenti, P. Manini, T. Fornaro, et al. Solid State Photochemistry of Hydroxylated Naphthalenes on Minerals: Probing Polycyclic Aromatic Hydrocarbon Transformation Pathways under Astrochemically-Relevant Conditions. *ACS Earth Space Chem* **2018**, 2 (10), 977–1000.
135. C. Darwin. *On the Origin of Species*, 1859; Routledge, **1859**.
136. A.I. Oparin. *Origin of Life*; **1924**.
137. S.L. Miller, H.C. Urey. Organic Compound Synthesis on the Primitive Earth. *Science (1979)* **1959**, 130 (3370), 245–251.
138. O. Leslie E. Prebiotic Chemistry and the Origin of the RNA World. *Crit Rev Biochem Mol Biol* **2004**, 39 (2), 99–123.
139. S.L. Miller. Production of Some Organic Compounds under Possible Primitive Earth Conditions. *J Am Chem Soc* **1955**, 77 (9), 2351–2361.
140. S.L. Miller. The mechanism of synthesis of amino acids by electric discharges. *Biochim Biophys Acta* **1957**, 23, 480–489.
141. W.F. Bottke, M.D. Norman. The Late Heavy Bombardment. *Annu Rev Earth Planet Sci* **2017**, 45 (1), 619–647.
142. S. Marchi, W.F. Bottke, L.T. Elkins-Tanton, et al. Widespread mixing and burial of Earth’s Hadean crust by asteroid impacts. *Nature* **2014**, 511 (7511), 578–582.
143. C. Sagan, G. Mullen. Earth and Mars: Evolution of Atmospheres and Surface Temperatures. *Science (1979)* **1972**, 177 (4043), 52–56.
144. J.F. Kasting. Faint young Sun redux. *Nature* **2010**, 464 (7289), 687–689.
145. I. Cnossen, J. Sanz-Forcada, F. Favata, et al. Habitat of early life: Solar X-ray and UV radiation at Earth’s surface 4–3.5 billion years ago. *J Geophys Res* **2007**, 112 (E2), E02008.
146. K. Zahnle, L. Schaefer, B. Fegley. Earth’s Earliest Atmospheres. *Cold Spring Harb Perspect Biol* **2010**, 2 (10), a004895–a004895.

147. L. Schaefer, B. Fegley. Outgassing of ordinary chondritic material and some of its implications for the chemistry of asteroids, planets, and satellites. *Icarus* **2007**, 186 (2), 462–483.
148. S.J., and H.T.M. Mojzsis. Vestiges of a beginning. Clues to the emergent biosphere recorded in the oldest known sedimentary rocks. *GSA Today* **2000**, 10, 1–5.
149. E.G. Nisbet. The geological setting of the earliest life forms. *J Mol Evol* **1985**, 21 (3), 289–298.
150. E.G. Nisbet, N.H. Sleep. The habitat and nature of early life. *Nature* **2001**, 409 (6823), 1083–1091.
151. S. Chatterjee. A symbiotic view of the origin of life at hydrothermal impact crater-lakes. *Physical Chemistry Chemical Physics* **2016**, 18 (30), 20033–20046.
152. S. Chatterjee. The RNA/Protein World and the Endoprebiotic Origin of Life. In *Earth, Life, and System*; Fordham University Press, **2015**; pp 39–79.
153. C.S. Cockell. The origin and emergence of life under impact bombardment. *Philosophical Transactions of the Royal Society B: Biological Sciences* **2006**, 361 (1474), 1845–1856.
154. D.A. Kring. Impact events and their effect on the origin, evolution, and distribution of life. *GSA Today* **2000**, 10 (8), 1–7.
155. G.R. Osinski, L.L. Tornabene, R.A.F. Grieve. Impact ejecta emplacement on terrestrial planets. *Earth Planet Sci Lett* **2011**, 310 (3–4), 167–181.
156. A.Y. Mulkidjanian, A.Yu. Bychkov, D. V. Dibrova, M.Y. Galperin, E. V. Koonin. Open Questions on the Origin of Life at Anoxic Geothermal Fields. *Origins of Life and Evolution of Biospheres* **2012**, 42 (5), 507–516.
157. M.J. van Kranendonk. Two types of Archean continental crust: Plume and plate tectonics on early Earth. *Am J Sci* **2010**, 310 (10), 1187–1209.
158. W.L. Marshall. Hydrothermal synthesis of amino acids. *Geochim Cosmochim Acta* **1994**, 58 (9), 2099–2106.
159. R.J.-C. Henket, N.G. Holm, M.H. Engel. Abiotic synthesis of amino acids under hydrothermal conditions and the origin of life: A perpetual phenomenon? *Naturwissenschaften* **1992**, 79 (8), 361–365.

160. D. Kopetzki, M. Antonietti. Hydrothermal formose reaction. *New Journal of Chemistry* **2011**, 35 (9), 1787.
161. A.I. Rushdi, B.R.T. Simoneit. Lipid formation by aqueous Fischer-Tropsch-type synthesis over a temperature range of 100 to 400 degrees. *Origins of Life and Evolution of the Biosphere* **2001**, 31 (1/2), 103–118.
162. E.S. Grew, J.L. Bada, R.M. Hazen. Borate Minerals and Origin of the RNA World. *Origins of Life and Evolution of Biospheres* **2011**, 41 (4), 307–316.
163. A. Ricardo, M.A. Carrigan, A.N. Olcott, S.A. Benner. Borate Minerals Stabilize Ribose. *Science (1979)* **2004**, 303 (5655), 196–196.
164. K. Harada. Formation of Amino-acids by Thermal Decomposition of Formamide—Oligomerization of Hydrogen Cyanide. *Nature* **1967**, 214 (5087), 479–480.
165. A.M. Schoffstall, S.M. Mahone. Formate ester formation in amide solutions. *Origins of Life and Evolution of the Biosphere* **1988**, 18 (4), 389–396.
166. A.M. Schoffstall, R.J. Barto, D.L. Ramos. Nucleoside and deoxynucleoside phosphorylation in formamide solutions. *Orig Life* **1982**, 12 (2), 143–151.
167. A.M. Schoffstall. Prebiotic phosphorylation of nucleosides in formamide. *Orig Life* **1976**, 7 (4), 399–412.
168. R. Saladino. A possible prebiotic synthesis of purine, adenine, cytosine, and 4(3H)-pyrimidinone from formamide implications for the origin of life. *Bioorg Med Chem* **2001**, 9 (5), 1249–1253.
169. R. Saladino, C. Crestini, F. Ciciriello, G. Costanzo, E. di Mauro. About a Formamide-Based Origin of Informational Polymers: Syntheses of Nucleobases and Favourable Thermodynamic Niches for Early Polymers. *Origins of Life and Evolution of Biospheres* **2006**, 36 (5–6), 523–531.
170. G. Costanzo, R. Saladino, C. Crestini, F. Ciciriello, E. di Mauro. Formamide as the main building block in the origin of nucleic acids. *BMC Evol Biol* **2007**, 7 (S2), S1.
171. G. Costanzo, R. Saladino, C. Crestini, F. Ciciriello, E. di Mauro. Nucleoside Phosphorylation by Phosphate Minerals. *Journal of Biological Chemistry* **2007**, 282 (23), 16729–16735.
172. R. Saladino, C. Crestini, F. Ciciriello, G. Costanzo, E. Di Mauro. Formamide Chemistry and the Origin of Informational Polymers. *Chem Biodivers* **2007**, 4 (4), 694–720.

173. R. Saladino, C. Crestini, F. Ciciriello, et al. From formamide to RNA: the roles of formamide and water in the evolution of chemical information. *Res Microbiol* **2009**, 160 (7), 441–448.
174. L.M. Mukhin. Volcanic processes and synthesis of simple organic compounds on primitive Earth. *Orig Life* **1976**, 7 (4), 355–368.
175. R. Shapiro. *Origins: A skeptic's guide to the creation of life on earth*; Bantam, **1987**.
176. S.A. Benner, H.-J. Kim, M.A. Carrigan. Asphalt, Water, and the Prebiotic Synthesis of Ribose, Ribonucleosides, and RNA. *Acc Chem Res* **2012**, 45 (12), 2025–2034.
177. S. Rajamani, A. Vlassov, S. Benner, et al. Lipid-assisted Synthesis of RNA-like Polymers from Mononucleotides. *Origins of Life and Evolution of Biospheres* **2008**, 38 (1), 57–74.
178. V. DeGuzman, W. Vercoutere, H. Shenasa, D. Deamer. Generation of Oligonucleotides Under Hydrothermal Conditions by Non-enzymatic Polymerization. *J Mol Evol* **2014**, 78 (5), 251–262.
179. E. Tekin, A. Salditt, P. Schwintek, et al. Prebiotic Foam Environments to Oligomerize and Accumulate RNA. *ChemBioChem* **2022**, 23 (24).
180. S.J. Sowerby, M. Edelwirth, W.M. Heckl. Self-Assembly at the Prebiotic Solid–Liquid Interface: Structures of Self-Assembled Monolayers of Adenine and Guanine Bases Formed on Inorganic Surfaces. *J Phys Chem B* **1998**, 102 (30), 5914–5922.
181. R.M. Hazen. Presidential Address to the Mineralogical Society of America, Salt Lake City, October 18, 2005: Mineral surfaces and the prebiotic selection and organization of biomolecules. *American Mineralogist* **2006**, 91 (11–12), 1715–1729.
182. N. Lahav, S. Chang. The possible role of solid surface area in condensation reactions during chemical evolution: Reevaluation. *J Mol Evol* **1976**, 8 (4), 357–380.
183. S.J. Sowerby, G.B. Petersen, N.G. Holm. Primordial Coding of Amino Acids by Adsorbed Purine Bases. *Origins of Life and Evolution of the Biosphere* **2002**, 32 (1), 35–46.
184. G. Ertem. Montmorillonite, Oligonucleotides, RNA and Origin of Life. *Origins of Life and Evolution of the Biosphere* **2004**, 34 (6), 549–570.

185. M. Schoonen, A. Smirnov, C. Cohn. A Perspective on the Role of Minerals in Prebiotic Synthesis. *AMBIO: A Journal of the Human Environment* **2004**, 33 (8), 539–551.
186. J.R. Brucato, G. Strazzulla, G.A. Baratta, A. Rotundi, L. Colangeli. Cryogenic Synthesis of Molecules of Astrobiological Interest: Catalytic Role of Cosmic Dust Analogues. *Origins of Life and Evolution of Biospheres* **2007**, 36 (5–6), 451–457.
187. R.M. Hazen, D.A. Sverjensky. Mineral Surfaces, Geochemical Complexities, and the Origins of Life. *Cold Spring Harb Perspect Biol* **2010**, 2 (5), a002162–a002162.
188. R.T. Downs, R.M. Hazen. Chiral indices of crystalline surfaces as a measure of enantioselective potential. *J Mol Catal A Chem* **2004**, 216 (2), 273–285.
189. F. Scappini, F. Casadei, R. Zamboni, et al. Protective effect of clay minerals on adsorbed nucleic acid against UV radiation: possible role in the origin of life. *Int J Astrobiol* **2004**, 3 (1), 17–19.
190. E. Biondi, S. Branciamore, M.-C. Maurel, E. Gallori. Montmorillonite protection of an UV-irradiated hairpin ribozyme: evolution of the RNA world in a mineral environment. *BMC Evol Biol* **2007**, 7 (S2), S2.
191. T. Fornaro, J.R. Brucato, E. Pace, et al. Infrared spectral investigations of UV irradiated nucleobases adsorbed on mineral surfaces. *Icarus* **2013**, 226 (1), 1068–1085.
192. R. Saladino, G. Botta, M. Delfino, E. Di Mauro. Meteorites as Catalysts for Prebiotic Chemistry. *Chemistry - A European Journal* **2013**, 19 (50), 16916–16922.

# CHAPTER 2

## HIGH-ENERGY PROTON BEAM IRRADIATION OF OXYPAHs ADSORBED ON METEORITES

*“The cosmos is within us. We are made of star-stuff. We are a way for the universe to know itself.”*

— Carl Sagan, *Cosmos*, 1980

### 2.1 Introduction

Different kind of experimental setups are available to simulate the space environment in the lab with the aim of addressing the chemical transformations that the complex organic molecules may undergo.

Among these, the most interesting one is based on the analysis of the chemical modifications that organic molecules adsorbed onto the surface of meteorite grains may suffer under high-energy proton beam irradiation, selected to mimic the solar wind. In this connection, we decided to explore the chemical reactivity of oxygenated derivatives of PAHs, oxyPAHs, under such conditions.

Extensive literature data show the identification of oxyPAHs as primary photochemical transformation products in water–ice matrices mimicking the interstellar medium.<sup>1</sup> Most of these studies included NAPH as the probe PAH and indicated extensive oxygenation with the formation of 1-HN as the dominant product, along with dihydroxylated derivatives and naphthoquinones.<sup>2</sup> Other studies showed that the irradiation of naphthalene at 15 K in a H<sub>2</sub>O+NH<sub>3</sub> ice mixture with photons in the extreme-ultraviolet range produced an organic residue containing several amino acids.<sup>3</sup> It was concluded that naphthalene, with other PAHs, can be a source of interstellar-reduced carbon from which amino acids and other prebiotic compounds may be generated, reinforcing the hypothesis of an extraterrestrial origin of life.

In this context, growing interest is currently focused on oxyPAHs because of their chemical properties such as high polarity, ensuring stronger adsorption on minerals and high reactivity.

In a recent study, it has been shown that 1-HN as well as two isomeric dihydroxy naphthalene derivatives, 1,6-DHN and 1,8-DHN, may easily react when adsorbed on forsterite, a model of Martian minerals, under UV irradiation leading to the formation of oxidative polymerization and ring fission/decarboxylation products.<sup>4</sup>

Overall, the results obtained from these irradiation experiments supported a feasible formation of molecules of prebiotic interest from PAHs in a variety of astrophysical environments before reaching the primitive Earth by meteorites falling.

The processes accounting for the formation of oxyPAH and their photodegradation are relevant for their possible implications in the origin of

the Insoluble Organic Matter (IOM), the most abundant carbonaceous component in meteorites.<sup>5</sup>

This hypothesis would be supported by various lines of evidence that have been highlighted in a recent paper<sup>6</sup> such as:

1. The elemental composition of IOM from chondrites provided average values close to  $C_{100}H_{80}O_{20}N_4S_2$ , which can be ascribed to the elemental composition of dihydroxynaphthalenes ( $C_{10}H_8O_2$ ) plus a minor contribution from some nitrogen and sulfur-containing.<sup>5</sup>
2. The results of chemical investigations (i. e. pyrolysis studies) suggested that IOM is made up of small PAH units bearing short, highly branched aliphatic and ester chains. Moreover, NMR data suggested that the PAH components in IOM do not exceed a 1-3 ring size, making naphthalene-based scaffolds likely candidates;<sup>7</sup>
3. The environment in which IOM is supposed to be formed (e.g. the ISM, the nebular or mixed nebular-ISM context) would be compatible with the critical involvement of PAHs, given the abundant presence of these latter in the ISM.<sup>8</sup>

In view of the limited knowledge on the possible involvement of PAHs and oxyPAHs in the generation of IOM in meteorites and in the prebiotic processes occurring on the early Earth, the research activity reported in this Chapter was designed to assess: i) the chemical transformations occurring on oxyPAHs under the irradiation with proton beams, a relatively little explored astrochemically-relevant energy source compared to thermal or UV activation; ii) the effect of the geochemical environment when the same process is carried out on oxyPAHs adsorbed on the surface of meteorite grains; iii) the potential

modulatory role carried out by small nitrogenous molecules of astrochemical relevance (i.e. urea). In particular, the research work was aimed at:

- defining the possible competition among the oxygenation, polymerization and degradation pathways occurring on oxyPAHs on meteorites;
- checking the possible analogies between the resulting products and the IOM components.

Recently, a lot of studies evidenced the rich chemistry that can be promoted by the proton beam irradiation of organic molecules, e.g. in the solar wind-directed synthesis of nucleobases and nucleotides,<sup>9</sup> and in the thermal processes modelling volcanic scenario or the impact events in the Earth atmosphere or surface.<sup>10</sup>

To the best of our knowledge, studies on the irradiation of PAH precursors with proton beams and meteorites are lacking. In this connection, a study on the chemical modifications of 1-HN and 1,8-DHN, selected as model oxyPAHs, promoted by high-energy proton beam irradiation in the presence of meteorites and urea has been carried out and reported in this chapter. To this aim, three different meteorites have been selected, including a stony-iron, an achondrite, and a chondrite type.

The identification of the main reaction products has been performed by gas-chromatography associated with mass-spectrometry (GC-MS) analysis and by comparison with authentic samples.

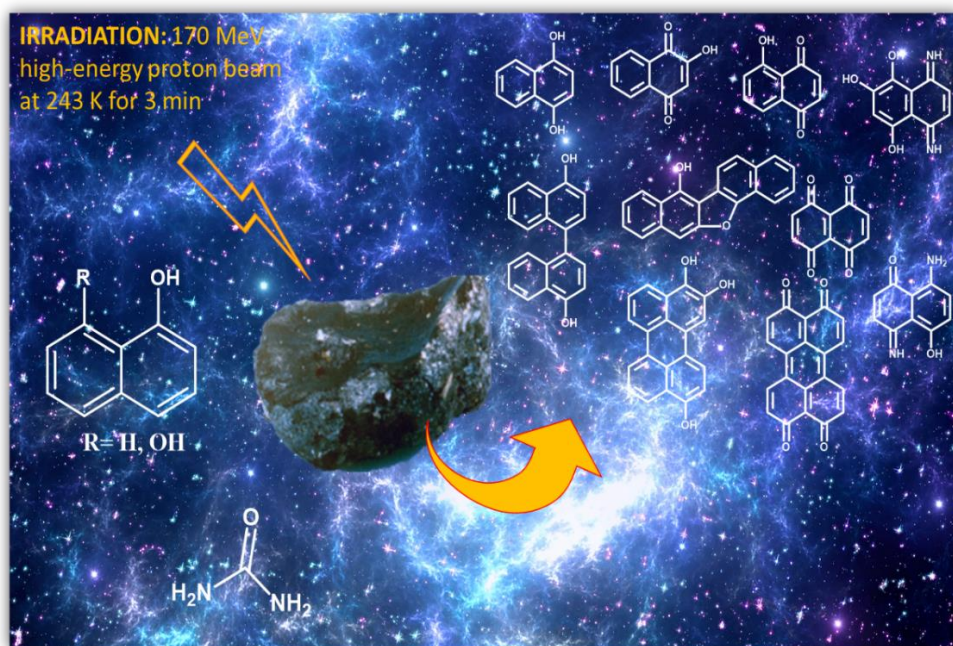


**Figure 1** | Highly functionalized oligomeric derivatives and nitrogen-containing compounds produced by meteorite-catalyzed irradiation of hydroxynaphthalene using proton beams mimicking the solar wind.

This work has been carried out in collaboration with Dr. Bruno Mattia Bizzarri, Prof. Raffaele Saladino and Ernesto Di Mauro of University of Tuscia, Viterbo (Italy), Dr. Michail Kapralov and Prof. Eugene Krasavin from Joint Institute for Nuclear Research JINR's Laboratory of Radiation Biology, Dubna (Russia) and Prof. Judit E. Šponer from Institute of Biophysics of the Czech Academy of Sciences, Brno (Czech Republic).

These results have been published in the paper **P3** and presented in the meeting **OP1**.

## 2.2 Results and discussion

### 2.2.1 Preparation, irradiation and analysis of samples

In this section will be reported the results obtained by subjecting 1-HN and 1,8-DHN, as model oxyPAH species, to high energy proton beam irradiation, modeling of the solar wind, in the presence of meteorites of different types and the effect of urea, a plausible nitrogen-rich component of the organic molecules found both in the space and on primitive Earth and a key precursor in prebiotic conditions. This work involved the collaboration of different research institutions.

Africa's Northwest NWA 4482, Al Haggunia, and Elephant Moraine EET 96029 were chosen as representative samples of the three major classes of meteorites, namely stony iron, achondrite, and chondrite types (for details about mineralogical composition, cosmo-origin, and historical and terrestrial provenience of selected meteorites see the experimental section). Previously, the NWA 4482 and Al Haggunia meteorites have already shown their catalytic effect in reactions of prebiotic relevance, such as the synthesis of nucleobases and nucleosides, and and the oligomerization process of suitable chemical precursors under high-energy proton beam irradiation.<sup>9</sup>

For the preparation, irradiation and analysis of the meteorite sample, the next steps have been followed:

- 1. PURIFICATION OF METEORITE:** before use, the meteorite powders were extracted with  $\text{CHCl}_3$ - $\text{CH}_3\text{OH}$  (2:1 v/v) and dried under a high vacuum to remove the contamination of any organic soluble compounds.<sup>11</sup>

2. **ADSORPTION OF OXY-PAHs:** a methanol solution of 1-HN or 1,8-DHN was adsorbed on the surface of the meteorite powder using a casting procedure and the evaporation of the solvent was performed under mild conditions (40 °C). In addition, to study the efficacy and chemo-selectivity of the irradiation in the presence of a well-recognized and astrochemical-relevant nitrogen-containing prebiotic compound, the meteorite powders have been coated with 1-HN or 1,8-DHN along with urea in equimolar amount with respect to the hydroxynaphthalene derivatives following the same previously reported casting process.<sup>12</sup>
3. **SPECTROSCOPIC ANALYSIS OF METEORITE SAMPLES:** the presence and retention of the structural integrity of 1-HN and 1,8-DHN after the adsorption procedure was confirmed by ATR FT-IR spectroscopy. Figures 2-4 show the infrared spectra of 1-HN and 1,8-DHN after the deposition procedure compared with the pure compounds.
4. **IRRADIATION:** the prepared sample was irradiated with 170 MeV high-energy proton beam at 243 K for 3 min with an averaged linear energy transfer (LET) of 0.57 keV/μm, modelling the high energy component of the solar wind radiation.<sup>13</sup> The irradiation of pure 1-HN and 1,8-DHN was used as a reference. This activity was performed in collaboration with the Joint Institute for Nuclear Research JINR's Laboratory of Radiation Biology, Dubna (Russia).
5. **ANALYSIS:** the reaction mixtures were, then, analyzed by gas-chromatography associated to mass-spectrometry (GC-MS) after standard derivatization of the sample (trimethylsilyl ethers).<sup>14</sup> This

analysis had been carried out in collaboration with Prof. Saladino of the University of Tuscia.

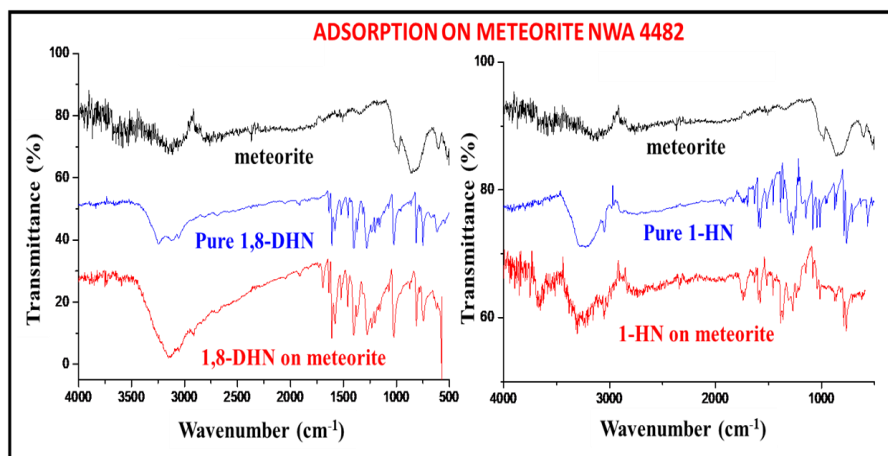


**Figure 2** | ATR FT-IR spectra of the meteorite NWA 4482 before and after the adsorption of 1-HN and 1,8-DHN. The ATR FT-IR spectrum of the pure solid 1-HN and 1,8-DHN are also reported as references.

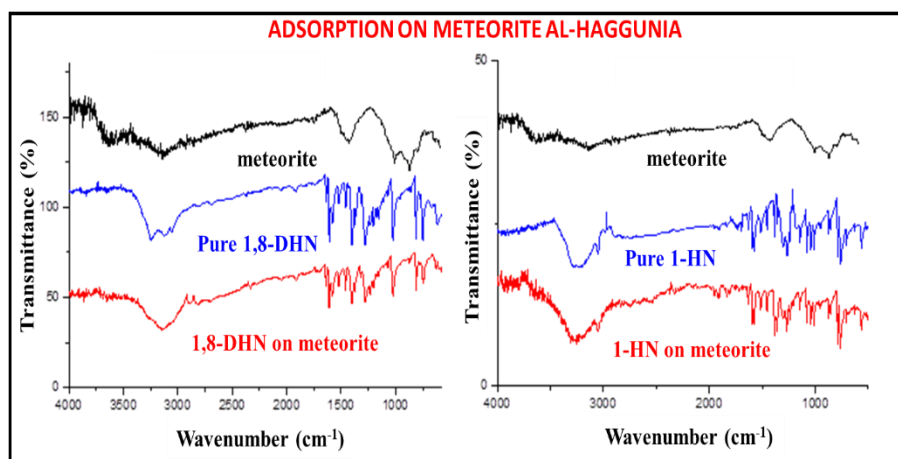


**Figure 3** | ATR FT-IR spectra of the meteorite Al-Haggunia before and after the adsorption of 1-HN and 1,8-DHN. The ATR FT-IR spectrum of the pure solid 1-HN and 1,8-DHN are also reported as references.

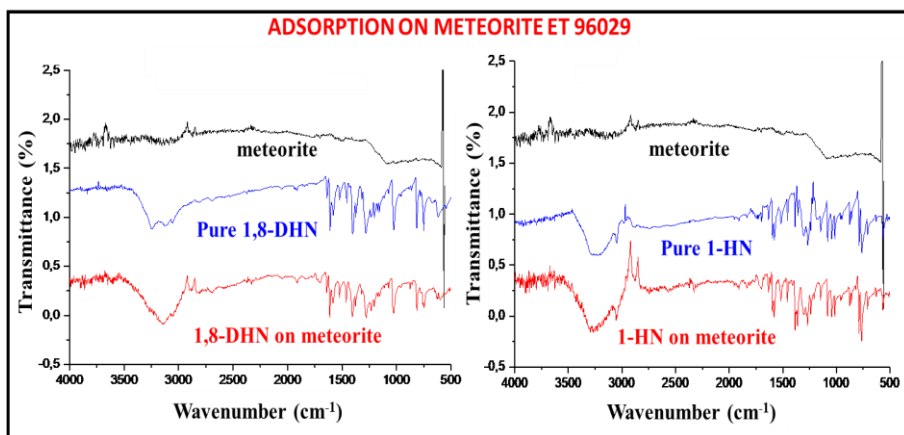


**Figure 4** | ATR FT-IR spectra of the meteorite ET 96029 before and after the adsorption of 1-HN and 1,8-DHN. The ATR FT-IR spectrum of the pure solid 1-HN and 1,8-DHN are also reported as references.

Figures 5 and 6 reported the representative GC chromatograms and Tables 1 and 3 reported the yields of the main reaction products. The structure of products **1-25** was assigned on the basis of the comparison with commercially available electron mass spectrum libraries (i.e. NIST). The assignment of structural isomers was performed by comparison with standard compounds commercially available compounds or, in the alternative, with standard compounds prepared according to reported synthetic procedures (for details see the experimental section).

### 2.2.2 Irradiation of 1-naphthalene in presence of meteorites

An extensive oxidation and oxygenation of the naphthalene ring and radical-coupling mediated oligomerization processes emerged from the

analysis of the reaction mixtures obtained after the irradiation of 1-HN adsorbed on meteorites (Scheme 1, Table 1).

A large panel of polyhydroxylated naphthalene and naphthoquinone derivatives was detected, including 1,4-dihydroxynaphthalene(**2**)<sup>15</sup>, 1,2-dihydroxynaphthalene (**3**)<sup>16</sup>, 2-hydroxynaphthalene-1,4-dione (**4**) (lawsone)<sup>17</sup>, 5-hydroxynaphthalene-1,4-dione (**5**) (juglone)<sup>18</sup>, naphthalene-tetraol isomers (**6a-c**)<sup>19</sup>, naphthalene-1,4,5,8- tetraone (**7**)<sup>20</sup>, 8-dihydroxy naphthalene-1,4-dione (**8**)<sup>21</sup> (naphthazarin), and naphthalene-1,2,4,5,8-pentaol (**9**)<sup>22</sup>.

The reported highest electron density and reactivity of the C-2 and C-4 positions of 1-HN with electrophilic species led to the selective formation of compounds **2** and **3** with respect to other possible isomers.<sup>23</sup> Naphthoquinones **4** and **5** were probably formed by further oxidation of **2** in agreement with the quantitative transformation of 1,4-dihydroxynaphthalene into 1,4-naphthoquinone (see scheme 2).<sup>24</sup>

The order of reactivity of meteorites observed for the conversion of 1-HN is the following: ETT 96029> Al-Haggunia> NWA 4482 (Table 2). The conversion of the substrate was almost quantitative in the case of ETT 96029 and significantly higher than the reference (Table 2, entry 4 versus entry 1), highlighting the higher reactivity of the substrate in the presence of a meteorite of the chondrite type.

In the absence of meteorite, a low value of mass balance was measured (Table 2, entry 1), likely due to the occurrence of over-oxidation processes and the formation of high molecular weight oligomers, not identifiable from the reaction mixture. Whereas, with ETT 96029, Al-Haggunia and NWA 4482 (Table 2, entries 2-4), a progressive improvement of mass balance was obtained.

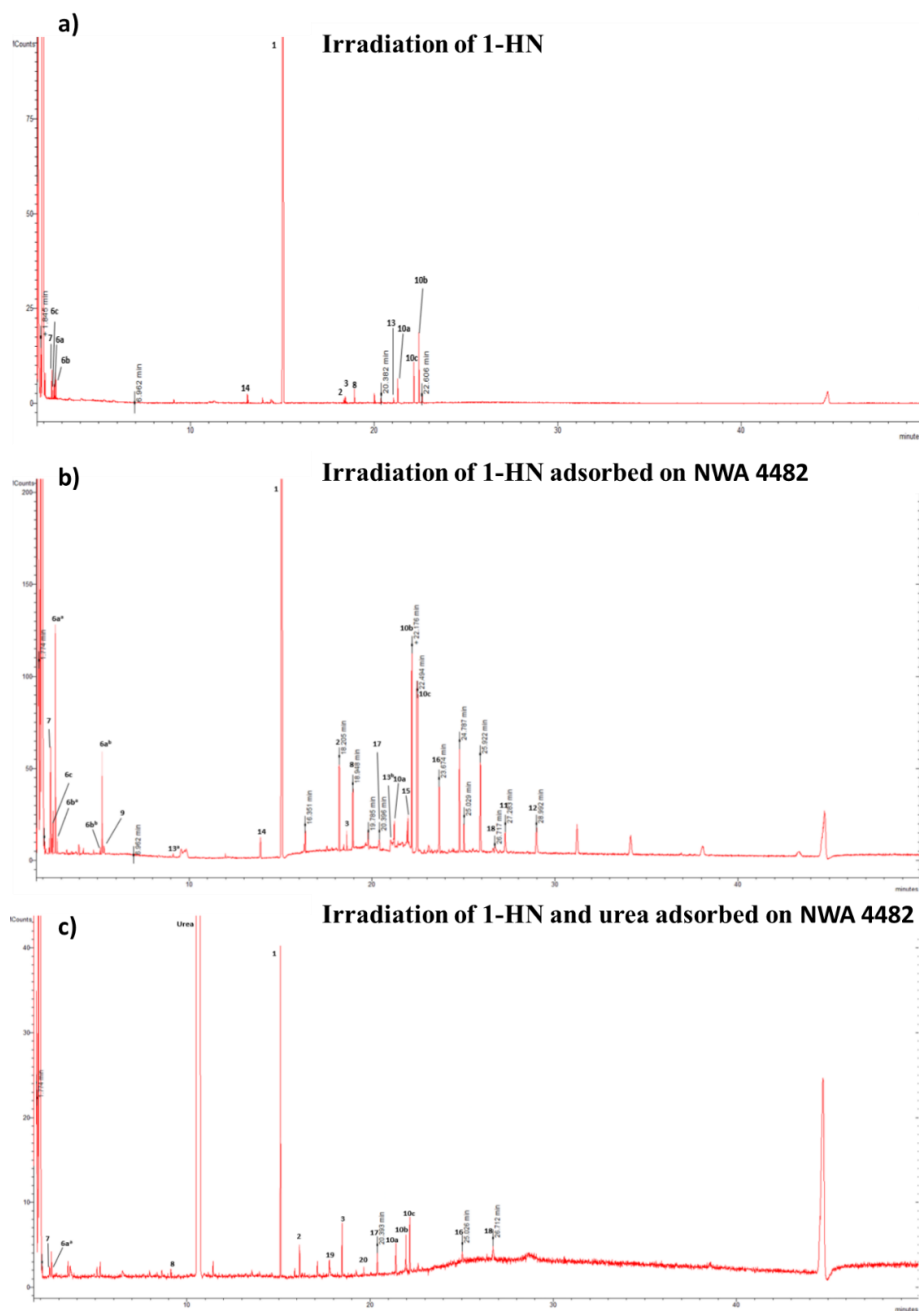


**Figure 5** | Chromatograms of the irradiation of 1-hydroxynaphtalene. a) 1-Hydroxynaphtalene in presence of NWA 4482; b) 1-hydroxynaphtalene in

presence of NWA 4482 and urea; c) with high-energy proton beam. The numbering is referred to assigned compounds.

**Table 1** | Irradiation of 1-hydroxynaphthalene in the presence of meteorites.

Entry	Meteorite	Conversion (%)	Product	R <sub>t</sub> (min)	Amount <sup>e</sup>	Yield(%) <sup>f</sup>
1	None	69.5	2	18.449 <sup>c</sup>	0.03	0.39
2			3	18.480 <sup>c</sup>	0.05	0.65
3			6a	2.650 <sup>a</sup>	0.14	1.52
4			6b	2.617 <sup>a</sup>	0.20	2.17
5			6c	2.583 <sup>a</sup>	0.09	0.97
6			7	2.541 <sup>a</sup>	0.25	2.77
7			8	18.941 <sup>c</sup>	0.10	1.09
8			10a	21.212 <sup>b</sup>	0.17	1.24
9			10b	22.158 <sup>b</sup>	0.39	2.83
10			10c	22.449 <sup>b</sup>	0.28	2.04
11			13	9.124 <sup>a</sup> ; 21.033 <sup>b</sup>	0.01	0.07
12			14	13.901 <sup>a</sup>	0.09	0.66
13	NWA 4482	70.2 [90.2] <sup>g</sup>	2	18.251 <sup>c</sup> (16.156 <sup>b</sup> )	0.21 [0.97]	2.67 [9.76]
14			3	18.484 <sup>c</sup> (18.472 <sup>b</sup> )	0.10 [1.42]	1.27 [14.3]
15			6a	2.651 <sup>a</sup> ; 5.208 <sup>b</sup> (2.564 <sup>a</sup> )	1.0;0.25 [0.65]	10.6; 2.65 [5.45]
16			6b	2.617 <sup>a</sup> ; 5.183 <sup>b</sup> (2.585 <sup>a</sup> )	0.09;0.03	0.95; 0.32
17			6c	2.585 <sup>a</sup>	0.15	1.59
18			7	2.542 <sup>a</sup> (2.542 <sup>a</sup> )	0.33 [0.23]	3.57 [1.97]
19			8	18.948 <sup>c</sup> (9.239 <sup>b</sup> )	0.16 [0.20]	1.71 [1.69]
20			9	5.398 <sup>a</sup>	0.03	0.29
21			10a	21.213 <sup>b</sup> (21.414 <sup>b</sup> )	0.14[1.00]	0.99 [5.63]
22			10b	22.176 <sup>b</sup> (21.960 <sup>b</sup> )	0.80 [1.15]	5.69 [6.48]

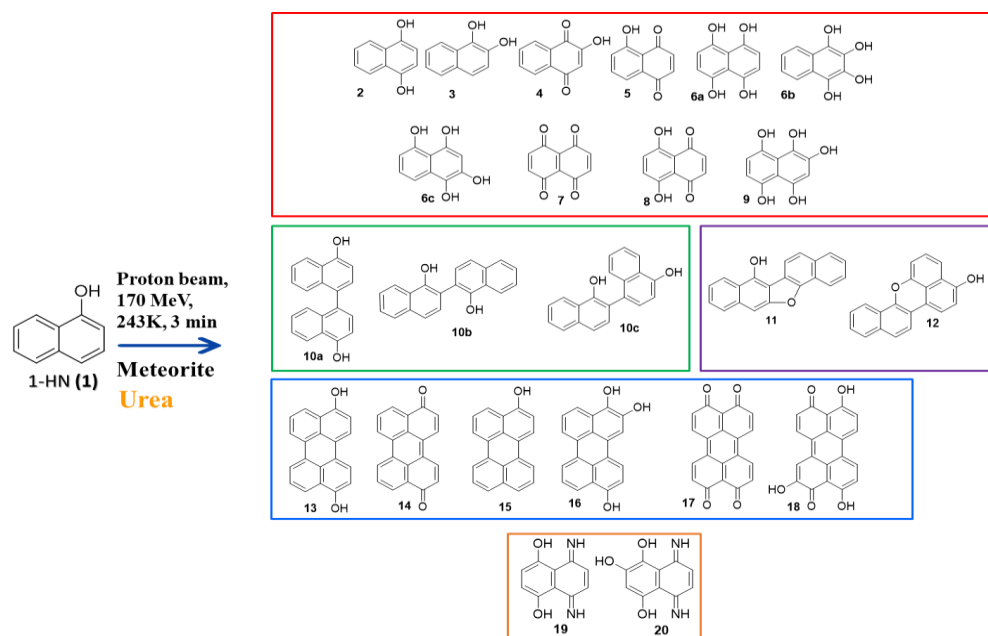
23			<b>10c</b>	22.494 <sup>b</sup> (22.174 <sup>b</sup> )	0.90 [1.55]	6.41 [8.72]
24			<b>11</b>	27.283 <sup>b</sup>	0.12	0.86
25			<b>12</b>	28.992 <sup>b</sup>	0.11	0.79
26			<b>13</b>	21.037 <sup>b</sup>	0.01	0.07
27			<b>14</b>	13.905 <sup>a</sup>	0.13	0.94
28			<b>15</b>	21.959 <sup>b</sup> ;	0.16	1.22
29			<b>16</b>	23.674 <sup>b</sup> ; (25.026 <sup>c</sup> )	0.17 [0.23]	1.15 [1.23]
30			<b>17</b>	20.396 <sup>a</sup> ; (20.393 <sup>a</sup> )	0.1 [0.5]	0.65 [2.58]
31			<b>18</b>	26.717 <sup>b</sup> ; (26.712 <sup>b</sup> )	0.03 [0.3]	0.19 [1.47]
32			<b>19</b>	(17.845 <sup>c</sup> )	[0.43]	[3.68]
33			<b>20</b>	(19.674 <sup>c</sup> )	[0.16]	[1.26]
34	<b>Al- Haggunia</b>	72.0 [>99.99]	<b>2</b>	18.453 <sup>b</sup> (16.156 <sup>b</sup> )	0.63 [1.54]	7.8 [13.8]
35			<b>3</b>	18.486 <sup>c</sup> ; 18.948 <sup>c</sup> ;	0.75	9.36
36			<b>4</b>	10.854 <sup>a</sup>	0.91	10.5
37			<b>5</b>	10.889 <sup>a</sup>	0.49	5.6
38			<b>6a</b>	2.567 <sup>a</sup> ; 4.041 <sup>b</sup> (2.574 <sup>a</sup> ; 5.272 <sup>b</sup> )	0.87 [0.77]	9.1 [5.8]
39			<b>6b</b>	2.526 <sup>a</sup>	Traces	-
40			<b>6c</b>	2.510 <sup>a</sup>	Traces	-
41			<b>7</b>	2.470 <sup>a</sup> (2.471 <sup>a</sup> )	0.21 [0.19]	2.24 [1.44]
42			<b>8</b>	18.939 <sup>c</sup> (9.231 <sup>b</sup> )	0.12 [0.15]	1.26 [1.12]
43			<b>9</b>	5.271 <sup>a</sup>	0.07	0.67
44			<b>10a</b>	21.407 <sup>b</sup> (21.399 <sup>b</sup> )	0.16 [0.24]	1.12 [1.21]
45			<b>10b</b>	22.162 <sup>b</sup> (22.164 <sup>b</sup> )	0.07	0.49
46			<b>10c</b>	22.607 <sup>b</sup>	0.19 [0.11]	1.33 [0.55]
47			<b>17</b>	20.375 <sup>a</sup> (20.385 <sup>a</sup> )	0.13 [0.21]	0.83 [0.97]
48			<b>19</b>	(17.436 <sup>c</sup> )	[0.23]	[1.76]
49			<b>20</b>	(19.657 <sup>c</sup> )	[0.26]	[1.83]

50	<b>ETT 96029</b>	99.2 [99.8]	<b>2</b>	18.430 <sup>c</sup>	0.43	3.9
51			<b>3</b>	18.455 <sup>c</sup> (18.444 <sup>c</sup> )	0.57 [1.38]	5.18 [12.4]
52			<b>6a</b>	2.589 <sup>a</sup> ; (2.577 <sup>a</sup> ; 5.089 <sup>b</sup> )	1.64 [0.61]	12.4 [4.57]
53			<b>6b</b>	2.572	traces	-
54			<b>6c</b>	2.547	traces	-
55			<b>7</b>	2.463 <sup>a</sup> (2.471 <sup>a</sup> )	0.33 [0.27]	2.55 [2.06]
56			<b>8</b>	18.925 <sup>c</sup> (9.207 <sup>b</sup> )	0.75 [1.42]	5.73 [10.8]
57			<b>9</b>	5.254 <sup>a</sup>	traces	-
58			<b>10a</b>	21.403 <sup>b</sup> (21.386 <sup>b</sup> )	0.53 [2.74]	2.69 [13.8]
59			<b>10b</b>	22.156 <sup>b</sup> (21.914 <sup>b</sup> )	0.82 [0.89]	4.16 [4.49]
60			<b>10c</b>	22.601 <sup>b</sup> (22.159 <sup>b</sup> )	0.89 [1.1]	4.53 [5.54]
61			<b>11</b>	27.189 <sup>b</sup>	0.01	0.05
62			<b>12</b>	29.076 <sup>b</sup>	0.02	0.1
63			<b>13</b>	21.111 <sup>b</sup> ,	1.4 [1.6]	6.24 [8.12]
64			<b>15</b>	21.929 <sup>b</sup>	0.51 [0.6]	2.77 [3.23]
65			<b>16</b>	23.549 <sup>b</sup>	0.18	0.87
66			<b>17</b>	20.371 <sup>a</sup> (20.373 <sup>b</sup> )	0.12 [0.03]	0.56 [0.14]
67			<b>18</b>	26.980 <sup>b</sup>	traces	-
68			<b>19</b>	(17.425 <sup>c</sup> )	[0.49]	[3.75]
69			<b>20</b>	(15.654 <sup>c</sup> )	[0.11]	[0.78]

[a] No silylated derivative. [b] Detected as mono-silylated derivative. [c] Detected as bis-silylated derivative. [d] The retention time value (min) of the reaction with urea is reported in the round brackets. [e] The amount of product is corresponding to mg of the product obtained starting from 10 mg of the substrate. The data referring to the reaction in the presence of urea are shown in square brackets. [f] Yield is defined as mmol of product relative to mmol of the converted substrate. In the case of the dimer, the expected mmol of the

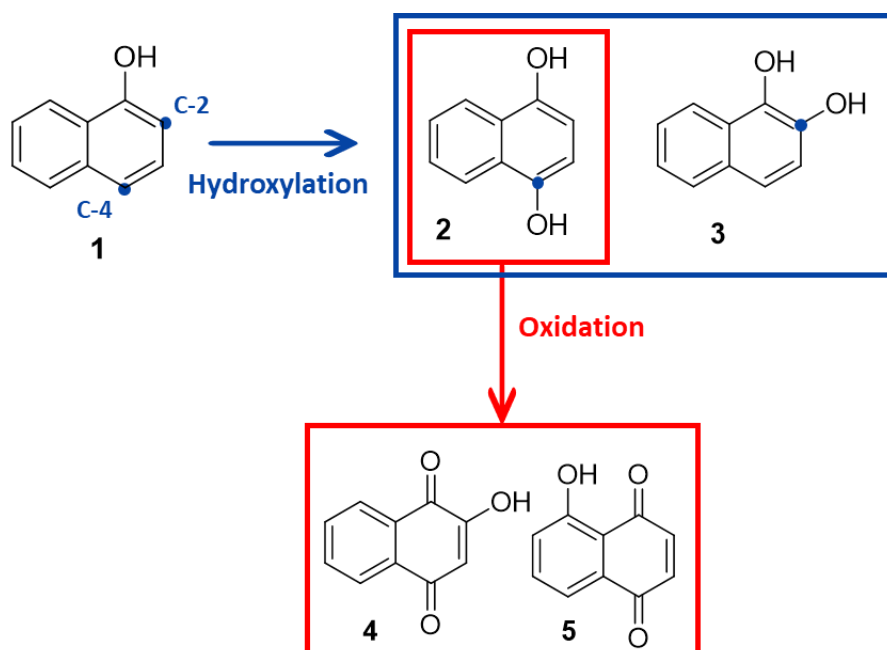
product corresponds to half of those of the starting material. [g] The conversion of the reaction in the presence of urea is reported in square brackets.

Moreover, Al-Haggunia provided a higher total yield of monomeric derivatives than ETT 96029 and NWA 4482 (Table 2, entry 3 versus entries 4 and 2, respectively).



**Scheme 1** | Irradiation of 1-hydroxynaphthalene with high-energy proton beam performed, in the presence of Northwest Africa NWA 4482, Al Haggunia, and Elephant Moraine EET 96029 meteorites and urea.

In the green panel of scheme 1, the detected dimeric compounds are shown. In particular, dihydroxydinaphthyl derivatives **10a-c** were clearly produced by a C-C radical coupling process starting from the initial formation of the 1-HN corresponding *O*-centred phenoxyl radical (scheme 3). All the three energetically favorable coupling isomers were obtained, namely: para-para **10a**, ortho-ortho **10b**, and para-ortho **10c** combinations, respectively.<sup>25,26</sup>



**Scheme 2** | Pathways for the formation of compounds 2-5.

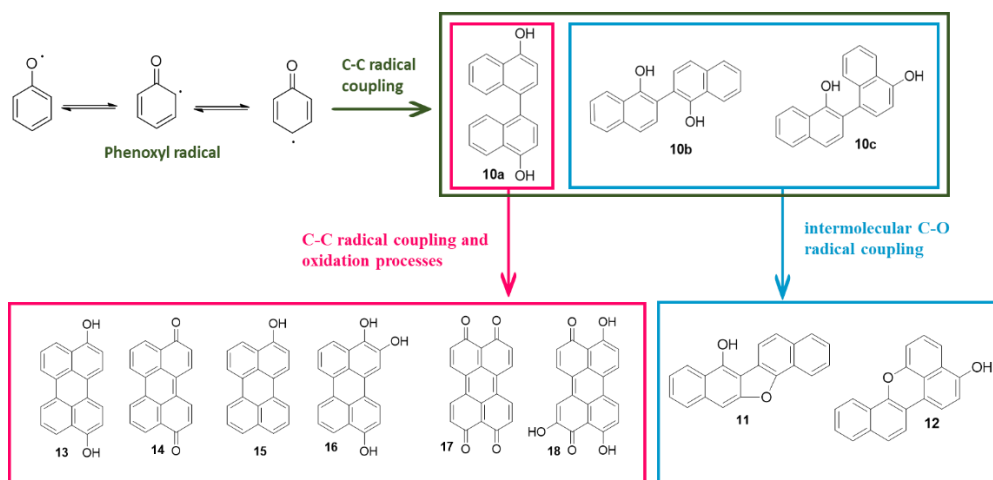
The relative amounts of dimers formed depend on the type of meteorite. In general, compounds **10b** and **10c** were the most abundant derivatives (Table 1, 22-23, 45-46, and 59-60, respectively).

The radiative generation of phenoxyl radicals and the role played in this process by different energy sources and physical states have been investigated

under gas,<sup>27</sup> liquid<sup>28,29</sup> and solid conditions.<sup>30</sup> The occurrence of electron transfer followed by hydrogen abstraction processes emerged as the prevalent mechanism in the irradiation of aliphatic alcohols with low-energy protons (1.0 MeV) under space-like experimental conditions (20 K).<sup>31</sup>

In the presence of NWA 4482 and ETT 96029, dihydroxydinaphthyl derivatives (**10b**) and (**10c**) selectively evolved to the corresponding benzofuran and benzopyran derivatives dinaphtho[1,2-b:2',3'-d]furan-7-ol (**11**)<sup>32</sup> and dibenzo[c,kl]xanthen-3-ol (**12**)<sup>33</sup> (Table 1, entries 22-23 and 59-60, respectively), by intermolecular C-O radical coupling (Scheme 3). The formation of benzofuran and benzopyran rings in hydroxynaphthalene dimers was previously reported as a result of intramolecular radical-mediated oxidative coupling in the biosynthetic melanin pathway.<sup>34</sup>

On the other hand, from the dimer (**10a**), through a cascade of successive C-C radical coupling and oxidation processes, a large panel of polyoxygenated perylene derivatives were formed (Scheme 3), such as perylene-3,10-diol (**13**),<sup>35</sup> perylene-3,10-dione (**14**),<sup>36</sup> perylene-1,2,6-triol (**16**),<sup>37</sup> bis-perylene-3,4,9,10-tetraone (**17**),<sup>38</sup> and 2,4,9-trihydroxy perylene-3,10-dione (**18**).<sup>39</sup> Perylen-3-ol (**15**),<sup>40</sup> a product of deoxygenation of one of the naphthalene rings, was also detected in appreciable yield probably due to the occurrence of a disproportionation process (Table 1).<sup>41</sup>



**Scheme 3** | Pathways for the formation of compounds **10-18** starting from phenoxyl radical.

Benzofuran and benzopyran derivatives **11-12** and polyoxygenated perylene derivatives **16-18** were obtained only when meteorites were present. Moreover, with ETT 96029, the highest production of the perylene derivative **13** was found (Table 1, entry 63). The following order of total yield of dimeric products **10-18** was found: ETT 96029 > NWA 4482 >> Al- Haggunia (Table 2, entries 2-4). Noteworthy, this order of reactivity is different compared with that previously reported for the formation of monomeric derivatives, suggesting that the composition of meteorites affected in a different way the efficacy of the radical coupling process versus the simple oxygenation of the naphthalene ring.

The results obtained after the irradiation of 1-HN (**1**) in the presence of meteorites and urea are reported in Scheme 1 and Table 1. Urea is a ubiquitous nitrogen-containing molecule that has been detected in the interstellar medium.<sup>42</sup> This compound is easily synthesized by sparking mixtures of gas ( $\text{CH}_4$ ,  $\text{CO}$ ,  $\text{CO}_2$ ,  $\text{N}_2$ ,  $\text{NH}_3$ ,  $\text{H}_2\text{O}$ , and  $\text{H}_2$ )<sup>43</sup> and by the irradiation of hydrogen

cyanide (HCN) in both liquid and solid state.<sup>44</sup> Moreover, a mixture of formamide and meteorites under both thermal and high-energy radiative experimental conditions resulted in the formation of urea.<sup>45,46</sup>

In the presence of urea, the formation of the same products of radical-coupling oligomerization, oxidation and oxygenation of 1-HN were observed again, including polyhydroxylated naphthalene and naphthoquinone derivatives **3** and **6-9**, dihydroxydinaphthyl derivatives **10a-c** and polyoxygenated perylene derivatives **16-18**. Under these conditions, the presence of meteorites led to comparable amount of conversion of the substrate (Table 2, entries 5-7). The presence of urea enhanced the conversion of the substrate in the case of NWA 4482 and Al-Haggunia. In agreement with the relative stability of urea toward ionizing radiation once adsorbed on the surface of minerals,<sup>47</sup> a considerable amount of unreacted urea was observed in the reaction mixture (from 50% to 90% with respect to initial amount). Regarding the chemo-selectivity of the reaction, the presence of urea decreased significantly the total yield of monomeric derivatives in the case of Al-Haggunia (Table 2, entry 6 versus entry 3). Instead, in presence of ETT 96029 (Table 2, entry 7 versus entry 4) and NWA 4482 (Table 2, entry 5 versus entry 2), their amount increased. A similar trend was observed for the synthesis of dimeric products (Table 2).

Noteworthy, the presence of urea led to the formation of two novel quinone diamine derivatives 5,8-diimino-5,8-dihydronaphthalene-1,4-diol (**19**)<sup>48</sup> and 5,8-diamino-2-hydroxynaphthalene-1,4-dione (**20**)<sup>49</sup> (Table 1, entries 32-33, 48-49, and 68-69). These products included in their structure the nitrogen atom from urea expanding the inventory of identified species toward the formation of nitrogen-containing oxyPAH systems. Imine derivatives have

been detected in IOM by N-XANES (c.a. 405 eV) and EELS spectra besides amines, amides and nitrogenated heterocycles.<sup>7</sup> The decomposition of urea under  $\gamma$ -irradiation conditions ( $^{60}\text{Co}$ , 0.14–600 kGy) is reported to generate hydrogen, carbon dioxide and ammonia.<sup>50</sup> This latter nucleophilic compound might be responsible for the observed amination of the electrophilic naphthalene quinone ring.

**Table 2** | Total yield and partial yield of polyhydroxylated naphthalene and perylene derivatives recovered from the proton beam irradiation of 1-HN.

Entry	Conditions	Conversion (%)	Total product yield (%)	Yield of monomeric derivatives (%) <sup>a</sup>	Yield of dimeric derivatives (%) <sup>b</sup>
1	no meteorite	69.5	15.74	9.56	6.18
2	NWA 4482	70.2	44.58	25.62	18.96
3	Al-Haggunia	72	50.3	46.53	3.77
4	ETT 96029	99.2	51.47	29.76	21.97
5	NWA 4482/urea	90.2	64.22	38.11	26.11
6	Al-Haggunia/urea	>99.9	28.48	25.75	2.73
7	ETT 96029/urea	99.8	65.68	34.36	31.32

[a] Yield of polyhydroxylated naphthalene and naphthoquinone derivatives.

[b] Yield of dihydroxydinaphthyl and perylene derivatives.

### 2.2.3 Irradiation of 1,8-dihydroxynaphthalene in presence of meteorites

The irradiation of 1,8-DHN in presence of meteorites led to the formation of a similar pattern of products, including **4**, **6a**, **6c**, **7-8**, and **17-18**, highlighting a chemo-selectivity comparable to 1-HN. In addition, the formation of other compounds, such as 1,1'-binaphthalene-4,4',5,5'-tetraol derivatives (**22a-c**)<sup>51</sup> and 4,9-dihydroxy-perylene-3,10-quinone (**23**)<sup>52</sup> was observed (scheme 4, table 3).

Also in the case of 1,8-DHN, the reaction carried out in presence of urea led to the formation of products deriving from the amination of the naphthalene ring (table 3), such as **19**, 4-imino-5-hydroxy-8-amino-1(4H)-naphthalenone (**24**)<sup>53</sup> and 8-hydroxy-4-iminonaphthalen-1(4H)-one (**25**)<sup>54</sup>.

These results indicate that regardless of the hydroxylation state of the starting compound, the reaction pathways were similar.

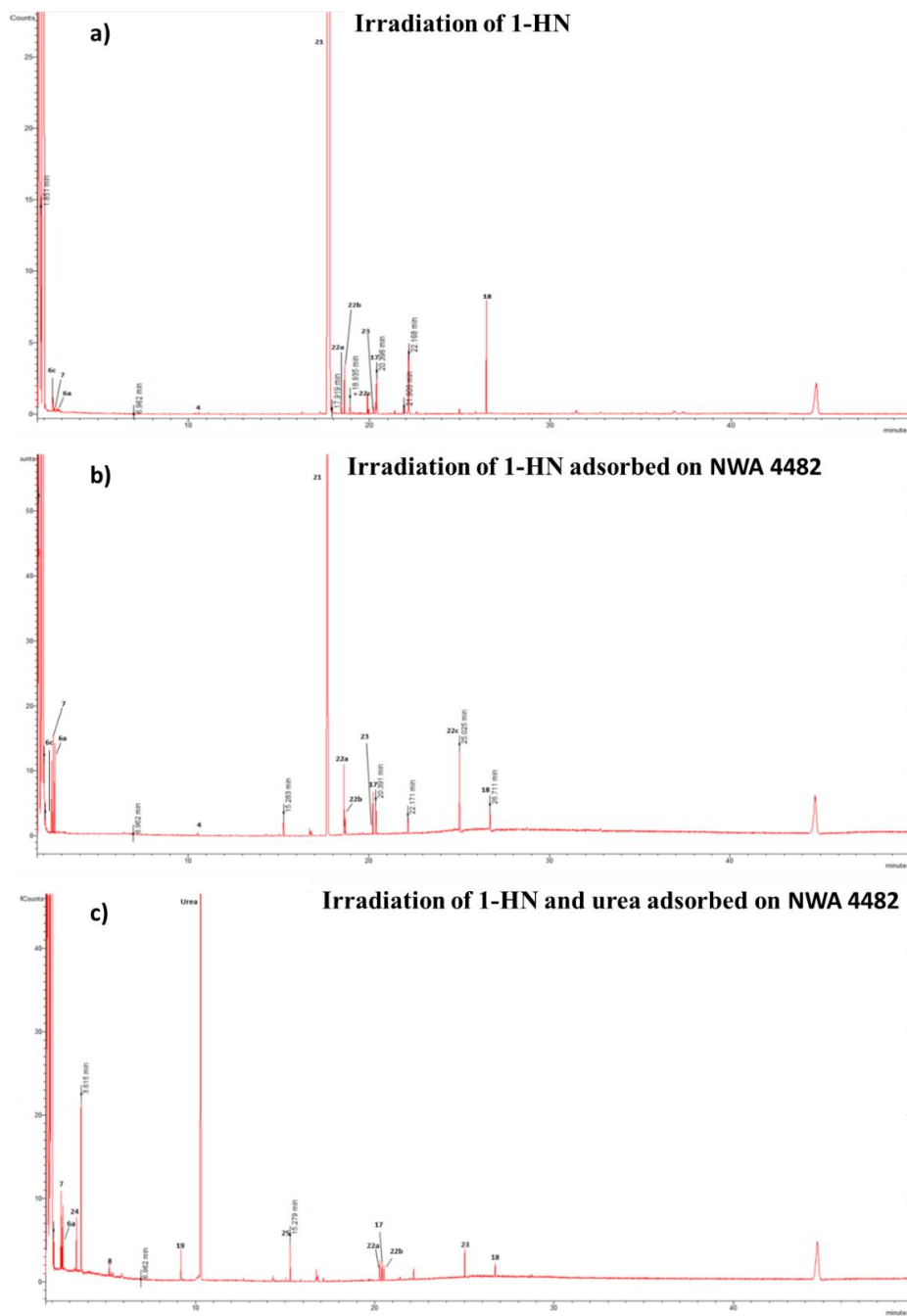
The compounds **22a** and **23** have been previously detected as key intermediates in the laccase-mediated radical oxidative coupling of 1,8-DHN during the formation of melanin in different fungal species.<sup>55,56</sup>

Table 4 (entries 2-4 versus entry 1) displayed that the mass balance of the reaction performed in the presence of meteorites was higher than that measured for the reference.

Moreover, in the reaction conducted with 1,8-DHN, the total yield of products, deriving from oxidation reactions, was significantly lower than 1-HN (Table 4, entries 2-4 versus Table 2, entries 2-4). This finding suggests that high

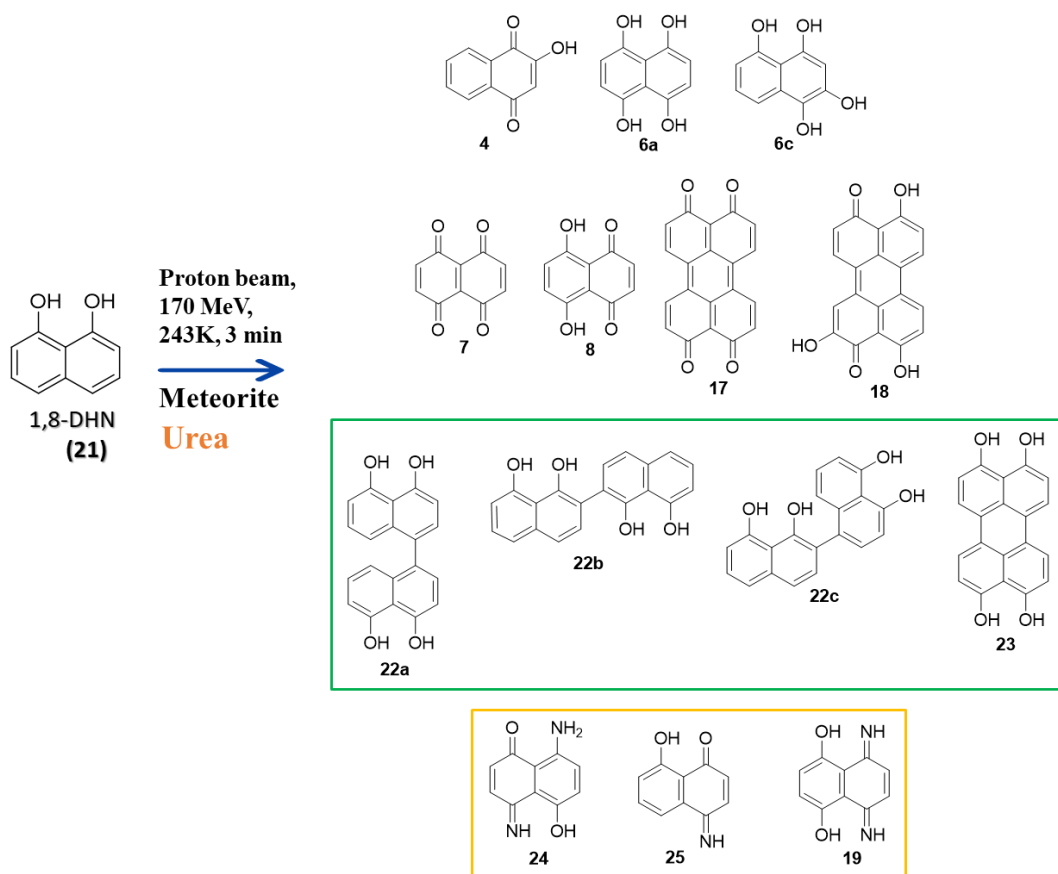
molecular weight oligomerization products prevailed in the case of 1,8-DHN, since the presence of a higher number of reactive hydroxyl groups on the starting naphthalene ring.

Generally, the prevalence of monomeric products with respect to dimeric derivatives (Table 4) was assessed. Moreover, the conversion of starting substrate was increased by the presence of urea in the reaction mixture.



**Figure 6** | Chromatogram of the irradiation of 1,8-dihydroxynaphthalene a) 1,8-dihydroxynaphthalene in presence of NWA 4482 b) 1,8-dihydroxynaphthalene

in presence of NWA 4482 and urea c) with high-energy proton beam. The numbering is referred to assigned compounds



**Scheme 4** | Irradiation of 1,8-dihydroxynaphthalene with high-energy proton beam, in the presence of Northwest Africa NWA 4482, Al Haggunia, and Elephant Moraine EET 96029 meteorite and urea.

**Table 3** | Irradiation of 1,8-dihydroxynaphthalene in the presence of meteorites.

Entry	Meteorite	Conversion (%)	Product	R <sub>t</sub> (min)	Amount <sup>e</sup>	Yield (%) <sup>f</sup>
1	None	63.1	<b>4</b>	10.526 <sup>a</sup>	traces	-
2			<b>6a</b>	2.585 <sup>a</sup>	0.02	0.17
3			<b>6c</b>	2.594	0.07	0.62
4			<b>7</b>	2.560 <sup>a</sup>	traces	-
5			<b>17</b>	20.397 <sup>c</sup>	0.16	0.88
6			<b>18</b>	26.711 <sup>b</sup>	0.75	3.96
7			<b>22a</b>	18.691 <sup>a</sup>	0.03	0.16
8			<b>22b</b>	18.933 <sup>a</sup>	0.17	0.91
9			<b>22c</b>	19.885 <sup>a</sup>	0.08	0.43
10			<b>23</b>	25.025 <sup>b</sup>	0.02	0.11
11	NWA 4482	94 [>99.9] <sup>g</sup>	<b>4</b>	10.526 <sup>a</sup>	0.03	0.30
12			<b>6a</b>	2.619 <sup>a</sup> (2.604 <sup>a</sup> )	0.44 [0.58]	4.44 [4.8]
13			<b>6c</b>	2.595	0.4	3.58
14			<b>7</b>	2.556 <sup>a</sup> (2.512 <sup>a</sup> )	0.48 [0.72]	4.33 [6.08]
15			<b>8</b>	(5.198 <sup>b</sup> )	[0.1]	[0.85]
16			<b>17</b>	20.397 <sup>c</sup> (20.40 <sup>c</sup> )	0.21 [0.13]	1.10 [0.66]
17			<b>18</b>	26.710 <sup>b</sup> (26.712 <sup>b</sup> )	0.18 [0.11]	0.92 [0.53]
18			<b>19</b>	(9.269 <sup>b</sup> )	[0.22]	[1.92]
19			<b>22a</b>	18.711 <sup>a</sup> (20.231)	0.39 [0.14]	2.02 [0.70]
20			<b>22b</b>	20.238 <sup>b</sup> (20.561)	0.18 [0.11]	0.98 [0.55]
21			<b>22c</b>	25.025 <sup>b</sup>	0.41	2.18
22			<b>23</b>	(25.025 <sup>b</sup> )	0.25 [0.21]	1.36 [1.07]
23			<b>24</b>	(3.616 <sup>a</sup> )	[0.38]	[3.24]
24			<b>25</b>	(15.273 <sup>b</sup> )	[0.31]	[2.87]

25	<b>Al-Haggunia</b>	98.6 [>99.99]	<b>6a</b>	2.545 <sup>a</sup> (2.578 <sup>a</sup> )	0.71 [0.85]	6.00 [7.08]		
26			<b>6c</b>	2.512	traces	-		
27			<b>7</b>	2.520 <sup>a</sup> (2.486 <sup>a</sup> )	0.73 [0.95]	6.30 [8.07]		
28			<b>8</b>	(5.44 <sup>b</sup> )	[0.33]	[2.77]		
29			<b>17</b>	20.391 <sup>c</sup> (20.40 <sup>c</sup> )	0.09 [0.20]	0.47 [1.02]		
30			<b>18</b>	(26.850 <sup>b</sup> )	[0.09]	[0.43]		
31			<b>19</b>	(9.270 <sup>b</sup> )	[0.07]	[0.60]		
32			<b>22a</b>	18.724 <sup>a</sup> (18.699 <sup>a</sup> ; 20.193 <sup>b</sup> )	0.71 [0.60]	3.63 [3.01]		
33			<b>22b</b>	18.933 <sup>a</sup> (18.941 <sup>a</sup> ; 20.226 <sup>b</sup> )	0.82 [0.5]	4.18 [2.52]		
34			<b>23</b>	(24.778 <sup>b</sup> )	[0.10]	[0.51]		
35			<b>24</b>	(3.613 <sup>a</sup> )	[0.09]	[0.76]		
36			<b>25</b>	(15.274 <sup>b</sup> )	[0.12]	[1.11]		
37			<b>ETT 96029</b>	95 [>99.9]	<b>6a</b>	2.568 <sup>a</sup> ; 5.068 <sup>b</sup> (2.544 <sup>a</sup> )	0.80 [0.60]	7.01 [5.00]
38					<b>6c</b>	2.535	traces	-
39	<b>7</b>	2.478 <sup>a</sup> (2.477 <sup>a</sup> )			0.68 [0.53]	6.09 [4.50]		
40	<b>8</b>	(5.44 <sup>b</sup> )			[0.33]	[2.77]		
41	<b>17</b>	20.383 <sup>c</sup> (20.40 <sup>c</sup> )			0.35 [0.29]	1.89 [1.48]		
42	<b>19</b>	(9.253 <sup>b</sup> )			[0.11]	[0.94]		
43	<b>22a</b>	18.710 <sup>a</sup> (18.700 <sup>a</sup> ; 19.517 <sup>b</sup> )			0.41 [0.55]	2.16 [2.77]		
44	<b>22b</b>	19.069 <sup>a</sup> (18.942 <sup>a</sup> ; 19.560 <sup>b</sup> )			0.59 [0.53]	3.12 [2.66]		
45	<b>22c</b>	20.230 <sup>b</sup>			0.48	2.55		

[a] Unsilylated derivative. [b] Detected as mono-silylated derivative. [c] Detected as bis-silylated derivative. [d] The retention time value (min) of the reaction with urea is reported in the round brackets. [e] Amount of product is corresponding to mg of product obtained starting from 10 mg of substrate. The data referring to the reaction in the presence of urea are shown in square brackets. [f] Yield is defined as mmol of product relative to mmol of converted substrate. In the case of dimer, the expected mmol of product correspond to half of those of the starting material. [g] The conversion of the reaction in the presence of urea is shown in square brackets.

**Table 4** | Total yield and partial yield of polyhydroxylated naphthalene and perylene derivatives recovered from the proton beam irradiation of 1,8-DHN.

Entry	Conditions	Conversion (%)	Total product yield (%)	Yield of monomeric derivatives(%) <sup>a</sup>	Yield of dimeric derivatives (%) <sup>b</sup>
1	no meteorite	63.1	7.24	0.79	6.45
2	NWA 4482	94	28.71	12.65	8.56
3	Al-Haggunia	98.6	20.58	12.30	8.28
4	ETT 96029	95	22.82	13.1	9.72
5	NWA 4482/urea	>99.9	23.27	19.76	3.51
6	Al-Haggunia/urea	>99.9	27.88	20.39	7.49

[a] Yield of polyhydroxylated naphthalene and naphthoquinone derivatives.

[b] Yield of dihydroxydinaphthyl and perylene derivatives.

## 2.2.4 Mechanistic modelling

In this paragraph, the results deriving from the modelling of the reaction of OH radical with 1-HN were shown. We assumed that the OH radicals can form from the degradation of 1-HN induced by radiation. In this way, the formation of polyhydroxylated naphthalene derivates was justified.

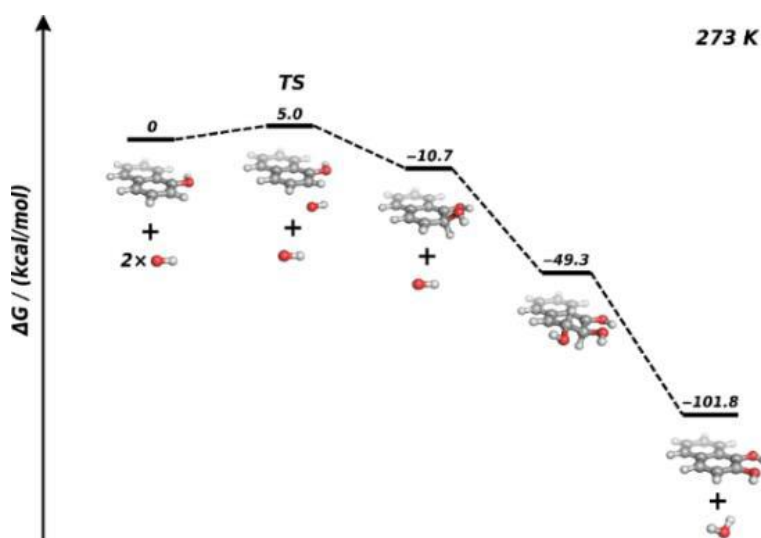


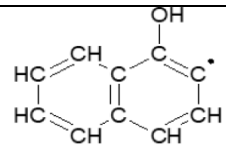
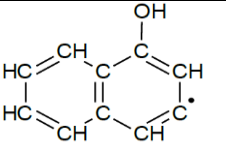
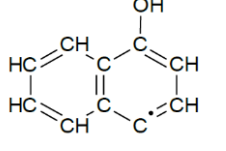
**Figure 7** | B3LYP/6-311++G\*\* free energy ( $\Delta G$ ) profile for the OH radical induced hydroxylation reaction of 1-naphthol. TS: transition state. Color coding: O-red, C-grey, H-white.

The ability of OH radicals to bring about a direct attack on aromatic carbons is well documented.<sup>57</sup> This reaction has been modelled with ab initio quantum chemical calculations at the B3LYP/6-311++G\*\* level of theory (for CCSD(T) benchmark calculations on related systems (for detail, see experimental section). As reported in Figure 7, this reaction proceeds with an almost negligible activation energy of 5 kcal/mol and may be followed by two

additional highly exergonic reaction steps. The first step is a radical recombination reaction leading to 2,3-dihydronaphthalene-1,2,3-triol, which then spontaneously loses water leading to the formation of 1,2-naphthodiol.

In the reactions conducted in presence of urea, the formation of N-substituted products could be ascribable to an analogous chemistry triggered by amino radicals, a dissociation product of urea formed after the irradiation. Table 5 showed that the relative electronic energies computed at B3LYP/6-311++G\*\* and CCSD(T)/6-311++G\*\* levels were in excellent agreement, which justifies the use of the B3LYP/6-311++G\*\* energy data for the evaluation of the reaction mechanism showed before. CCSD(T) calculations were performed with the MOLPRO program package.<sup>58</sup>

**Table 5** | Computed electronic energies (in Hartree) of radicals formed by H-abstraction from 1-naphthol at B3LYP/6-311++G\*\* level and from CCSD(T)/6-311++G\*\* single-point calculations using the DFT-level optimized geometries.

Radical	B3LYP/6-311++G**	CCSD(T)/6-311++G**
	-460.28644	-459.424443
	-460.285285	-459.423616
	-460.283488	-459.421728

## 2.3 Conclusions

The formation and structural modification of oxyPAHs under UV irradiation on minerals have recently been proposed as a possible channel of PAH transformation in astrochemical and prebiotic scenarios of possible relevance for the origin of life.

Herein, proton beam irradiation modelling of the solar wind in the presence of various meteorites, including stony iron, achondrite, and chondrite type, was suggested as a plausible multicomponent scenario for the conversion of oxyPAHs, i.e. 1-HN and 1,8-DHN, into complex mixtures of oxygenated and oligomeric derivatives. Moreover, the catalytic role of meteorites in promoting the synthesis of a broad panel of higher molecular weight reaction products was disclosed. Among these products, cross-coupling dimeric derivatives resembling the 1-3 ring framework characteristic of the pyrolysate of the IOM in chondrite meteorites were detected.<sup>59</sup>

We found that two different reaction pathways dominate the oxyPAH radiative chemistry in the above conditions: 1) the extensive hydroxylation of the naphthalene ring and 2) the dimerization reactions via radical-mediated coupling leading to bis-naphthols and perylene derivatives through the formation of C-C and C-O bonds. Which pathways prevailed depends on the type of meteorite.

The achondrite type, represented by the Al-Haggunia sample, was more active in the synthesis of monomeric derivatives from 1-HN, whereas the chondrite ETT 96029 showed the highest catalytic effect in the formation of dimeric products.

The chondrite ETT 96029 was also the best catalyst for the formation of both monomeric and dimeric products, in the case of oxidation of 1,8-DHN. Thus,

high molecular weight products are mostly expected in chondrites than in the other cases.

In presence of urea, monomeric derivatives prevailed with respect to the dimeric counterpart.

Overall, these data suggested the possibility that the high variability observed in the IOM composition for different sources might be dependent not only on the origin and on the alteration processes experienced by the meteorite but also on the intrinsic catalytic activity associated with its mineralogical composition, which cannot be completely ruled out.

Although the relationship between the localization of IOM in the matrix and the surrounding mineral components is at present under debate,<sup>60</sup> the morphological analyses showed that IOM is adjacent to some mineral components in interplanetary dust particles, as well as in chondrites.<sup>61,62</sup> In principle, these minerals could behave as active catalytic sites for the accretion of organic matter.<sup>63</sup> The catalytic role of phyllosilicates in the late polymerization of pristine soluble organic matter into the second generation of IOM has been also reported, focusing on the role played by the aqueous alteration in the overall composition of the organic matter.<sup>64</sup>

Moreover, the range of discovered species was increased by the addition of urea, a prebiotically-relevant chemical precursor, including, among others, quinone diimines.

In conclusion, in this study emerged two main findings that are worthy of note in the context of emerging prebiotic scenarios:

1) both 1-HN and 1,8-DHN generate naphthoquinones and naphthoquinone imines in significant yields. Given the possible role of these derivatives as early and primitive redox shuttling systems providing chemical and photochemical

energy transduction pathways via reversible electron transfer, these results point to the possible role of naphthoquinones and naphthoquinone imines produced by oxyPAH (irradiation) processing as important mediators in prebiotic processes;

2) the incorporation of nitrogen from urea in reactive naphthoquinone intermediates might explain a possible mechanism for the initial formation of the C-N bond in complex heterocyclic derivatives. Generally, the observed nitrogen transfer from urea to oxyPAHs opens interesting perspectives to the possible generation of nitrogenous building blocks of life from early PAHs nitrogenous precursors. The systematic inventory of the species produced by irradiation of oxyPAHs on various meteorites and the elucidation of the nitrogen transfer capacity of urea as an astrochemical-relevant precursor is expected to delineate an intriguing framework of scaffolds and functionalities that may play a role at different levels and with different modalities in prebiotic processes.

## 2.4 Experimental section

### 2.4.1 Materials and methods

Urea (Merck, > 99%), 1-HN (Merck, > 99%), 1,8-DHN (Merck, > 99%) were used without further purification. NWA 4482 were obtained from Sahara-nayzak, Asnieres sur Seine, France; Al-Haggounia and ETT 96029 from AZ meteorites, Tombstone, Arizona, USA. Gas-chromatography mass-spectrometry (GC-MS) analyses were performed with a GC-MS Varian GC410-320MS equipped with a CP8944 column (WCOT fused silica, film thickness 0.25  $\mu\text{m}$ , stationary phase VF-5ms,  $\text{\O}$  0.25 mm, length 30m). ATR spectra of the powders in transmission mode have been recorded with a Nicolet 5700 spectrometer. The spectra have been scanned on the wave number range of 400-4000  $\text{cm}^{-1}$  with a resolution fixed to 4  $\text{cm}^{-1}$ .

### 2.4.2 Preparation and irradiation of the meteorite samples

Before the irradiation process, any soluble organic matter from the meteorite samples was removed following the next two steps:

1. extraction with sodium hydroxide (1.0 mL, 0.1 N) and chloroform-methanol mixture (3.0 mL, 2:1 v/v, respectively);
2. treatment with sulphuric acid (1.0 mL, 0.1 N) and chloroform-methanol mixture (3.0 mL, of 2:1 v/v, respectively).

The solid material was recovered by centrifugation (6000 rpm, 10 min., Haereus Biofuge) and carefully dried under high vacuum before use.

10 mg of 1-HN and 1,8-DHN were adsorbed on the surface of meteorite powder (2.0 mg) by a casting procedure using a freshly prepared MeOH solution (30mg/mL). Then the mixture was gently homogenized under mild

sonication for a few seconds and the solvent was evaporated in the oven at 40°C.

Then, the meteorite powder coated with 1-HN or 1,8-DHN was further embedded with urea (MeOH solution, 30mg/mL) in equimolar amounts with respect to the substrate (4.2 mg for 1- HN and 3.75 mg for 1,8-DHN) following the previously described casting procedure.

For the irradiation, the appropriate sample was exposed to 170 MeV proton beam in the Phasotron facility of the Joint International Nuclear Institute (JINR; Dubna, Russia) at 243 K for 3.0 min., the uniform proton field being bounded to 10x10 cm<sup>2</sup> by the collimator system (averaged linear energy transfer LET of 0.57 keV/μm, calculated absorbed dose 6 Gy).

After the irradiation process, to recuperate the organic molecules on the meteorite, successive extractions with MeOH (3 x 1.0 mL) were performed. The meteorite powder was removed by centrifugation (6000 rpm, 10 min, HaereusBiofuge). The organic phase was then removed under reduced pressure (40°C, 4x10<sup>-4</sup> barr), and the residue was analyzed by gas-chromatography associated to mass-spectrometry (GC-MS) analysis after derivatization with N,N-bis-trimethylsilyl trifluoroacetamide in pyridine (620 μL) at 60°C for 4 h. The analysis was performed in the presence of betulinic acid [3β-hydroxy-20(29)-lupaene-oic acid] as an internal standard (0.2 mg) using the following program: injection temperature 280°C, detector temperature 280°C, gradient 100 °C x 2min, then 10°C/min for 60 min. First, the spectra were compared with commercially available electron mass spectrum libraries such as NIST (Fison, Manchester, UK). Secondly, GC-MS analysis was repeated with standard compounds. All products have been recognized with a similarity index (S.I.) greater than 98% compared to the reference standards or, in the

alternative, with standard compounds obtained by applying reported synthetic procedures.

### 2.4.3 Mass spectra analysis

The structure of products **1-25** was assigned on the basis of the comparison with commercially available electron mass spectrum libraries such as NIST (Fison, Manchester, UK). The following compounds are commercially available and have been used as standards for the assignment of reaction products: 1-naphthol (**1**) (CAS Registry Number: 90-15-31), 1,4-dihydroxynaphthalene (**2**) (CAS Registry Number: 571-60-8), 2-dihydroxynaphthalene (**3**) (CAS Registry Number: 574-00-5), 2-hydroxynaphthalene-1,4-dione (**4**) (lawsone) (CAS Registry Number: 83-72-7), 5-hydroxynaphthalene-1,4-dione (**5**) (juglone) (CAS Registry Number: 481-39-0), naphthalene-1,4,5,8-tetraone (**7**) (CAS Registry Number: 23077-93-2), 5, 8-dihydroxynaphthalene-1,4-dione (**8**) (naphthazarin) (CAS Registry Number: 475-38-7), perylene-3,10-diol (**13**) (CAS Registry Number: 5796-90-7), perylene-3,10-dione (**14**) (CAS Registry Number: 5796-93-0), 1,8-dihydroxynaphthalene (**21**) (CAS Registry Number: 569-42-6), [1,1'-binaphthalene]-4,4',5,5'-tetraol (**22a-c**) (CAS Registry Number: 111936-76-6), 4,9-dihydroxy-perylene-3,10-quinone (**23**) (CAS Registry Number: 10190-97-3), and 4-Imino-5-hydroxy-8-amino-1(4H)-naphthalenone (**24**) (CAS Registry Number: 6259-68-3). Naphthalene-1,2,4,5,8-pentaol (**9**), dinaphtho[1,2-b:2',3'-d]furan-7-ol (**11**), dibenzo[c,kl]xanthen-3-ol (**12**), Perylen-3-ol (**15**), perylene-1,2,6-triol (**16**), bis-perylene-3,4,9,10-tetraone (**17**), perylene-3,10-dione (**18**), 5,8-diimino-5,8-dihydronaphthalene-1,4-diol (**19**), 5,8-diamino-2-hydroxynaphthalene-1,4-dione (**20**), and 8-hydroxy-4-iminonaphthalen-

1(4H)-one (**25**) were assigned by comparison with authentic samples prepared as reported in references in the main text. The structural isomers 1,4,5,8-tetrahydroxy-naphthalene (**6a**) (CAS No.: 5690-27-7), 1,2,3,4-tetrahydroxy-naphthalene (**6b**) (CAS No.: 5690-26-6), and 1,2,4,8-tetrahydroxy-naphthalene (**6c**) (CAS No.: 5690-27-7) were unambiguously assigned on the basis of the comparison with authentic commercially available samples. The structure of isomers (**10a-c**) was assigned on the basis of data reported in Ref.<sup>22</sup>. The characteristic m/z fragmentation values of the main reaction products are reported in Table 6.

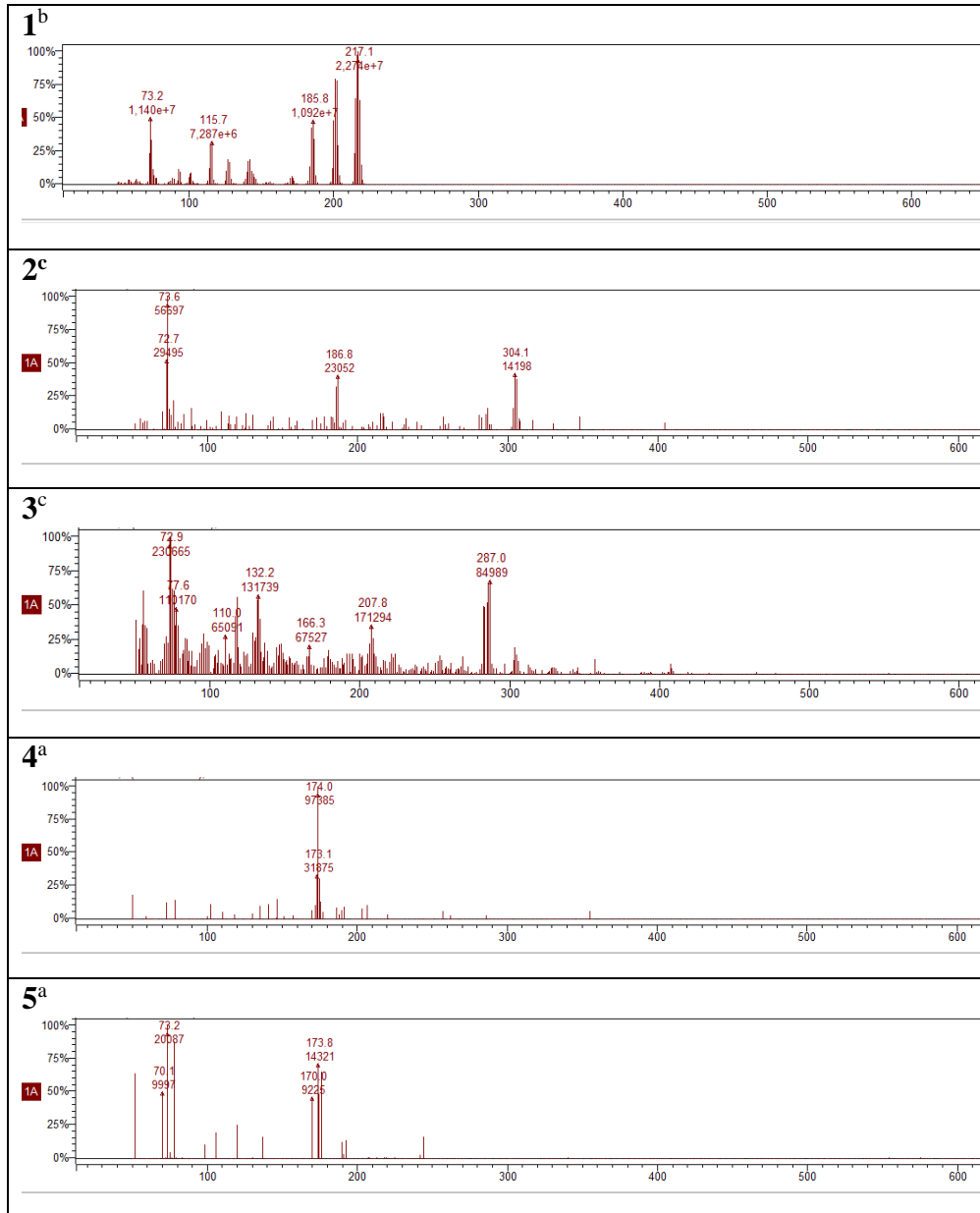
**Table 6** | Ion abundance and MS fragmentation profiles of compounds **1-25**.

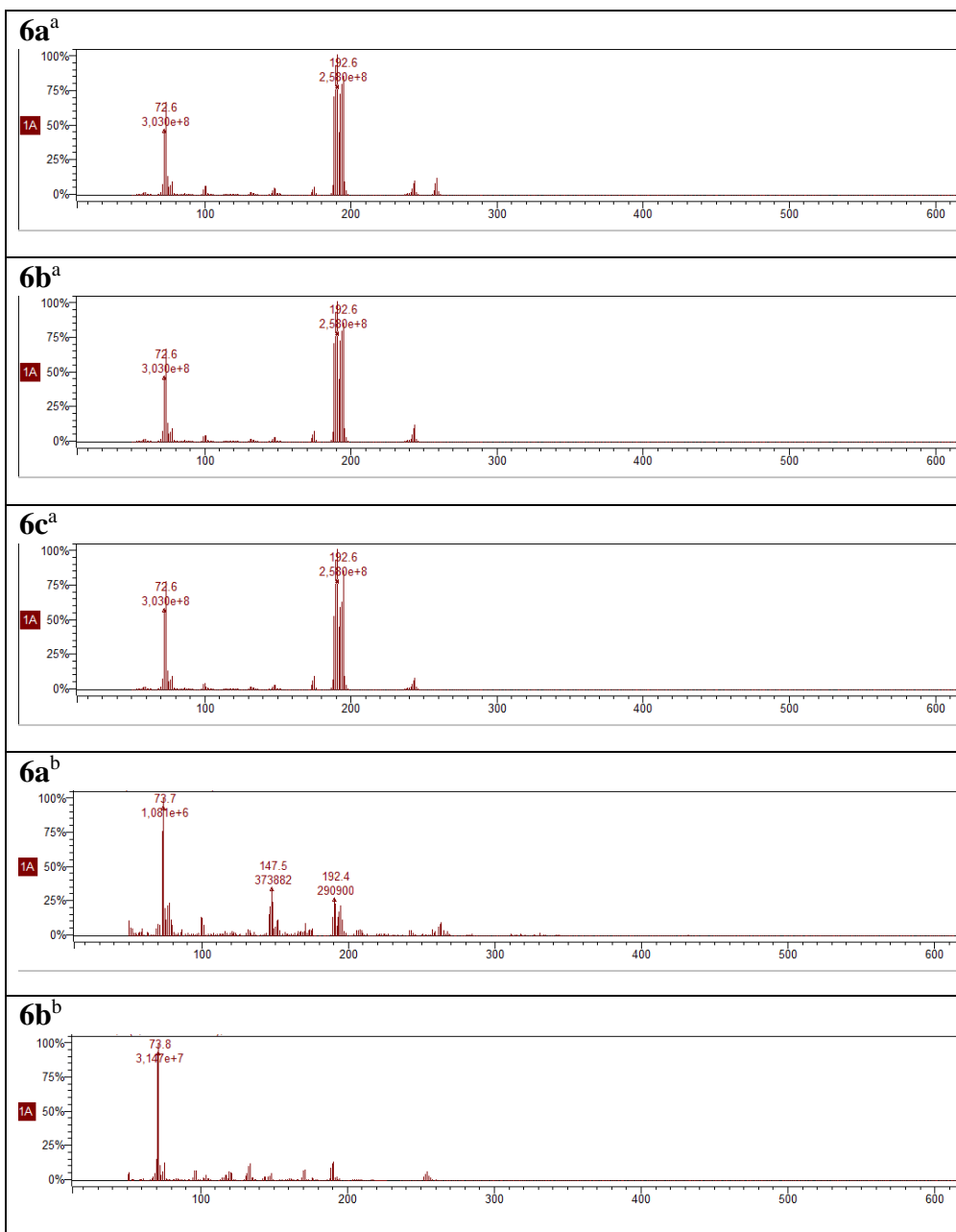
Entry	Product	m/z
	<b>1<sup>b</sup></b>	216 [M+ TMS] (100), 201 [M+ TMS-Me] (75), 186 [M+ TMS-2Me] (50).
	<b>2<sup>c</sup></b>	304[M+ 2 TMS] (3), 287 [M+2TMS-Me] (73).
	<b>3<sup>c</sup></b>	304[M] (40), 287 [M-Me] (12).
	<b>4<sup>a</sup></b>	174 [M] (100), 73 [TMS] (5).
	<b>5<sup>a</sup></b>	174 [M] (75), 73 [TMS] (100).
	<b>6a<sup>a</sup></b>	192 [M] (100), 175 [M-OH] (3), 73 [TMS] (77).
	<b>6b<sup>a</sup></b>	192 [M] (100), 175 [M-OH] (6), 73 [TMS] (80).
	<b>6c<sup>a</sup></b>	192 [M] (100), 175 [M-OH] (4), 73 [TMS] (80).
	<b>6a<sup>b</sup></b>	264 [M] (14); 192 [M-TMS] (20). 73 [TMS] (100).
	<b>6b<sup>b</sup></b>	264 [M] (8), 192 [M-TMS] (18). 73 [TMS] (100).

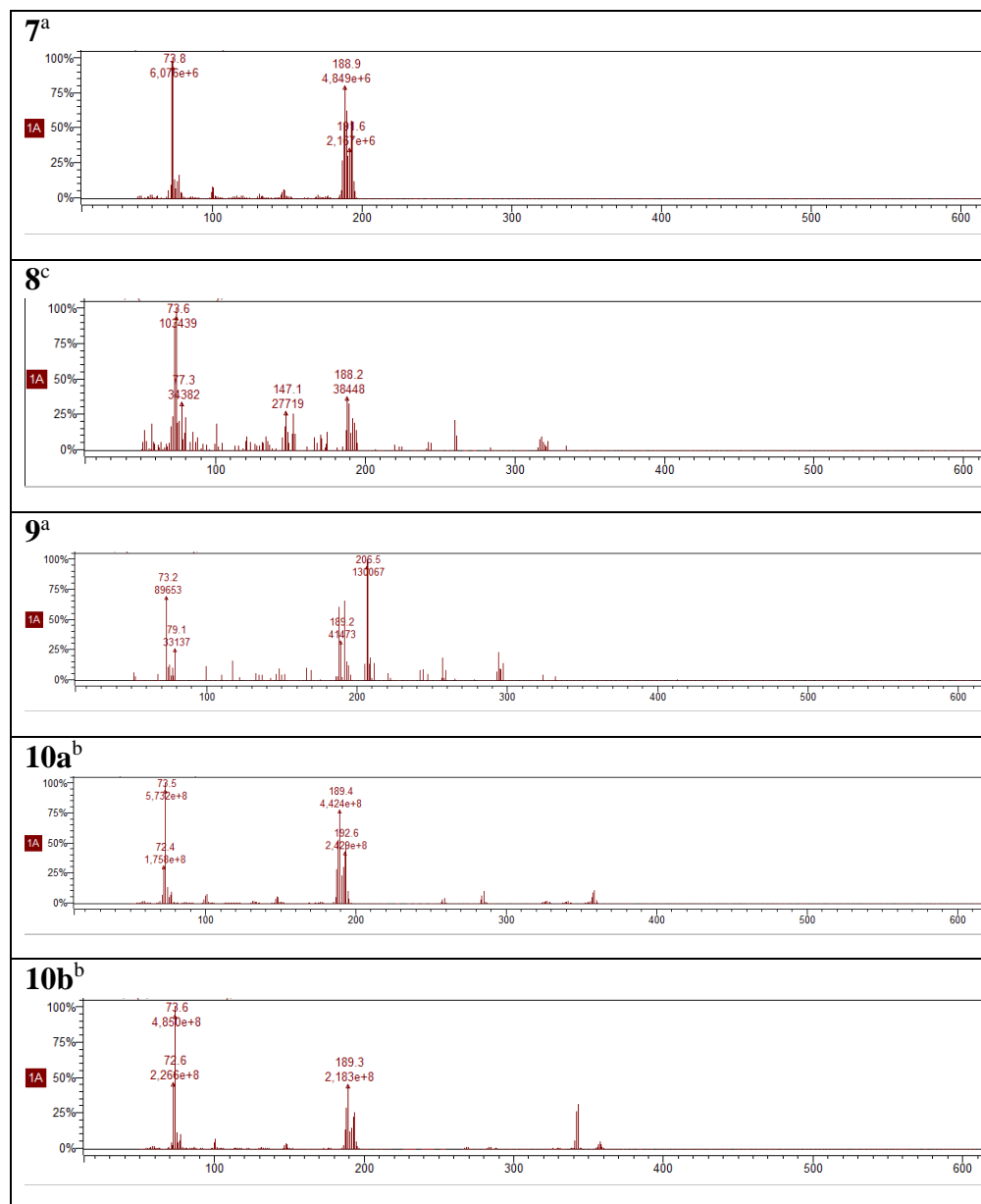
	<b>7<sup>a</sup></b>	188 [M] (75), 73 [TMS] (100).
	<b>8<sup>c</sup></b>	334 [M+ 2 TMS] (3), 319 [M+ 2 TMS-Me] (9), 261 [M+ TMS] (20).
	<b>9<sup>a</sup></b>	208 [M] (26), 191 [M-OH] (26), 179 [M-CHO] (3).
	<b>10a<sup>b</sup></b>	358 [M+ TMS] (25), 343 [M+ TMS-Me] (3), 328 [M+ TMS-2Me] (5), 285 [M-H] (21), 269 [M-OH] (7).
	<b>10b<sup>b</sup></b>	358 [M+ TMS] (10), 343 [M+ TMS-Me] (38), 328 [M+ TMS-2Me] (2), 285 [M-H] (3), 269 [M-OH] (3).
	<b>10c<sup>b</sup></b>	358 [M+ TMS] (25), 343 [M+ TMS-Me] (10), 285 [M-H] (16), 269 [M-OH] (8).
	<b>11<sup>b</sup></b>	356 [M+ TMS] (31), 343 [M+ TMS-Me] (8), 326 [M+ TMS-2Me] (4), 283 [M-H] (30), 267 [M-OH] (5).
	<b>12<sup>b</sup></b>	356 [M+ TMS] (30), 343 [M+ TMS-Me] (11), 326 [M+ TMS-2Me] (8), 283 [M-H] (35), 267 [M-OH] (10).
	<b>13<sup>b</sup></b>	358 [M+ TMS] (26), 343 [M+ TMS-Me] (5), 285 [M-H] (30), 269 [M-OH] (6).
	<b>14<sup>a</sup></b>	282 [M] (24).
	<b>15<sup>b</sup></b>	340 [M+ TMS] (28), 310 [M+ TMS-2Me] (3), 267 [M-H] (10)
	<b>16<sup>b</sup></b>	372 [M+ TMS] (2), 357 [M+TMS-Me] (15), 342

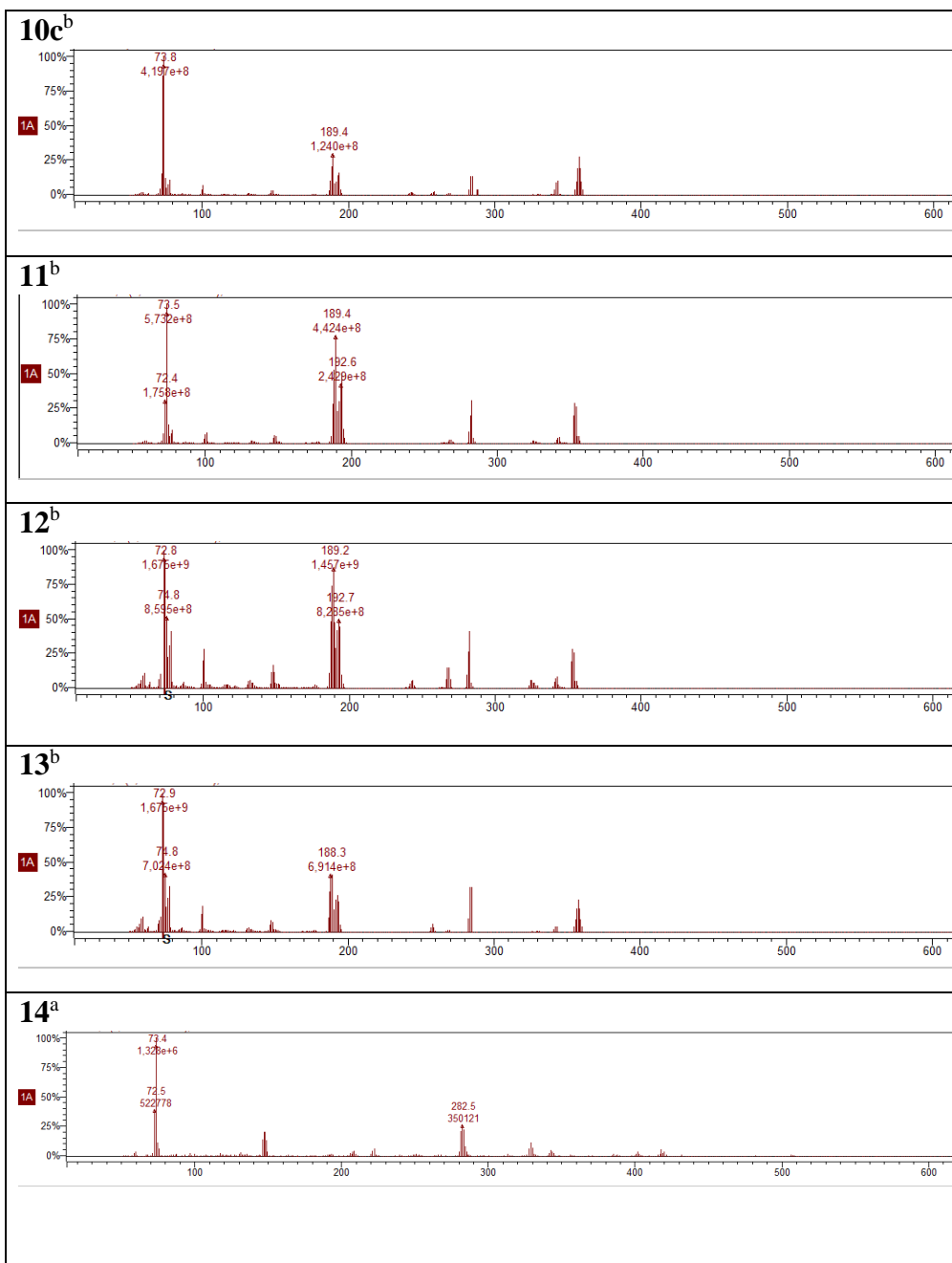
		[M+ TMS-2Me] (5), 299 [M-H] (2).
	<b>17<sup>a</sup></b>	314 [M] (70).
	<b>18<sup>b</sup></b>	402 [M+ TMS] (100), 329 [M-H] (5), 73 [TMS] (80).
	<b>19<sup>c</sup></b>	332 [M+ 2 TMS] (10), 302 [M+ 2TMS-2 Me] (6), 259 [M+TMS-H] (7), 73 [TMS] (100).
	<b>20<sup>c</sup></b>	333 [M+ 2 TMS-Me] (5), 73 [TMS] (100).
	<b>21<sup>c</sup></b>	304 [M] [M+ 2 TMS] (100), 289 [M+ 2TMS-Me] (5), 216 [M+TMS-2 Me] (28), 73 [TMS] (73).
	<b>22a<sup>a</sup></b>	318 [M] (50), 260 [M- 2 CHO] (22).
	<b>22b<sup>a</sup></b>	318 [M] (12), 260 [M- 2 CHO] (61).
	<b>22c<sup>a</sup></b>	318 [M] (12), 260 [M- 2 CHO] (41).
	<b>22a<sup>b</sup></b>	390 [M+ TMS] (33), 317 [M-H] (2), 73 [TMS] (100).
	<b>22b<sup>b</sup></b>	390 [M+ TMS] (13), 317 [M-H] (4), 73 [TMS] (100).
	<b>22c<sup>b</sup></b>	375 [M+ TMS-Me] (100), 73 [TMS] (90).
	<b>23<sup>b</sup></b>	371 [M+ TMS-Me] (50),
	<b>24<sup>a</sup></b>	172 [M-NH <sub>2</sub> ] (100).
	<b>25<sup>b</sup></b>	245 [M+TMS] (100), 73 [TMS] (52).

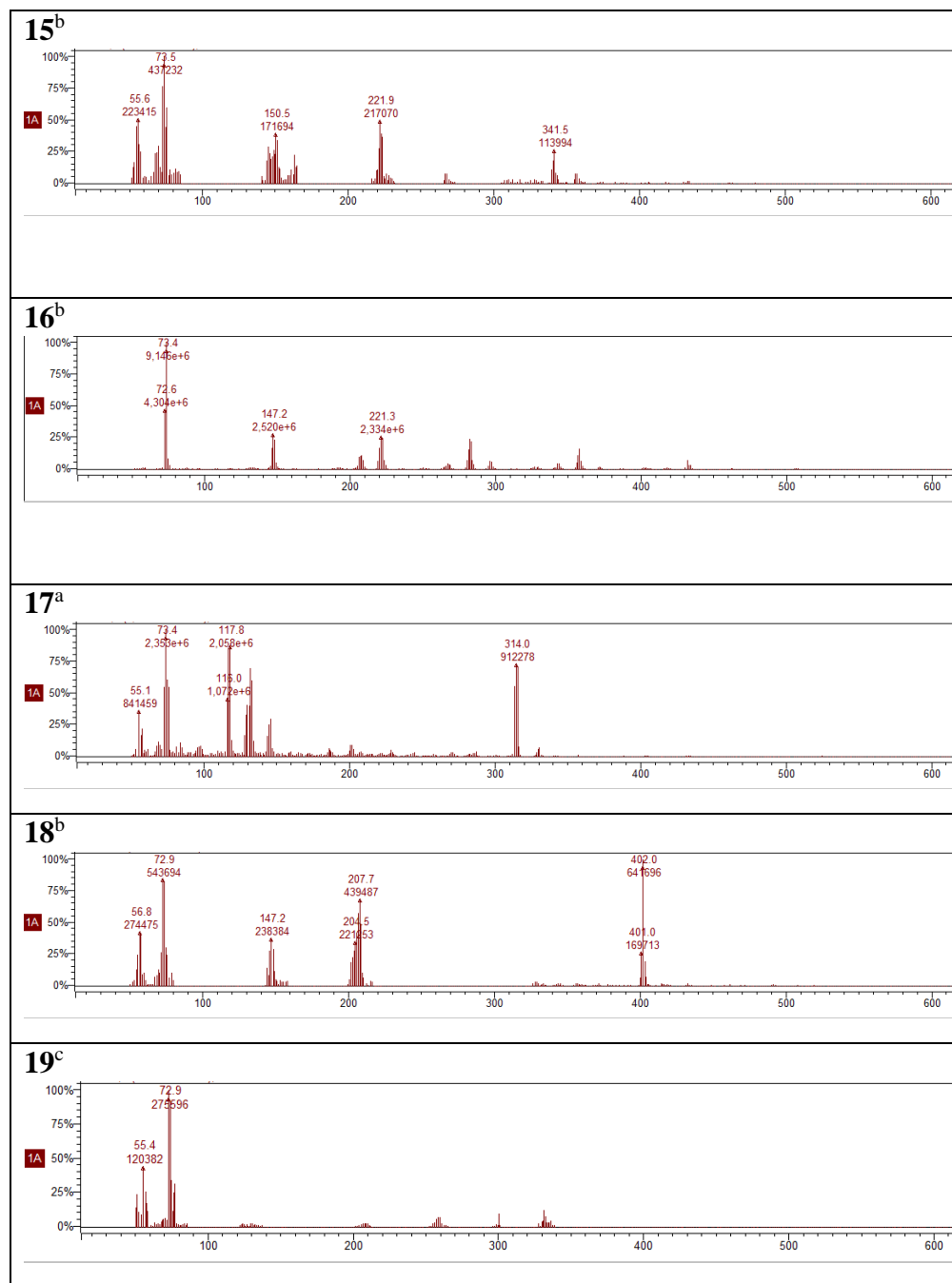
<sup>a</sup>Unsilylated derivative. <sup>b</sup>Detected as mono-silylated derivative. <sup>c</sup>Detected as bis-silylated derivative.

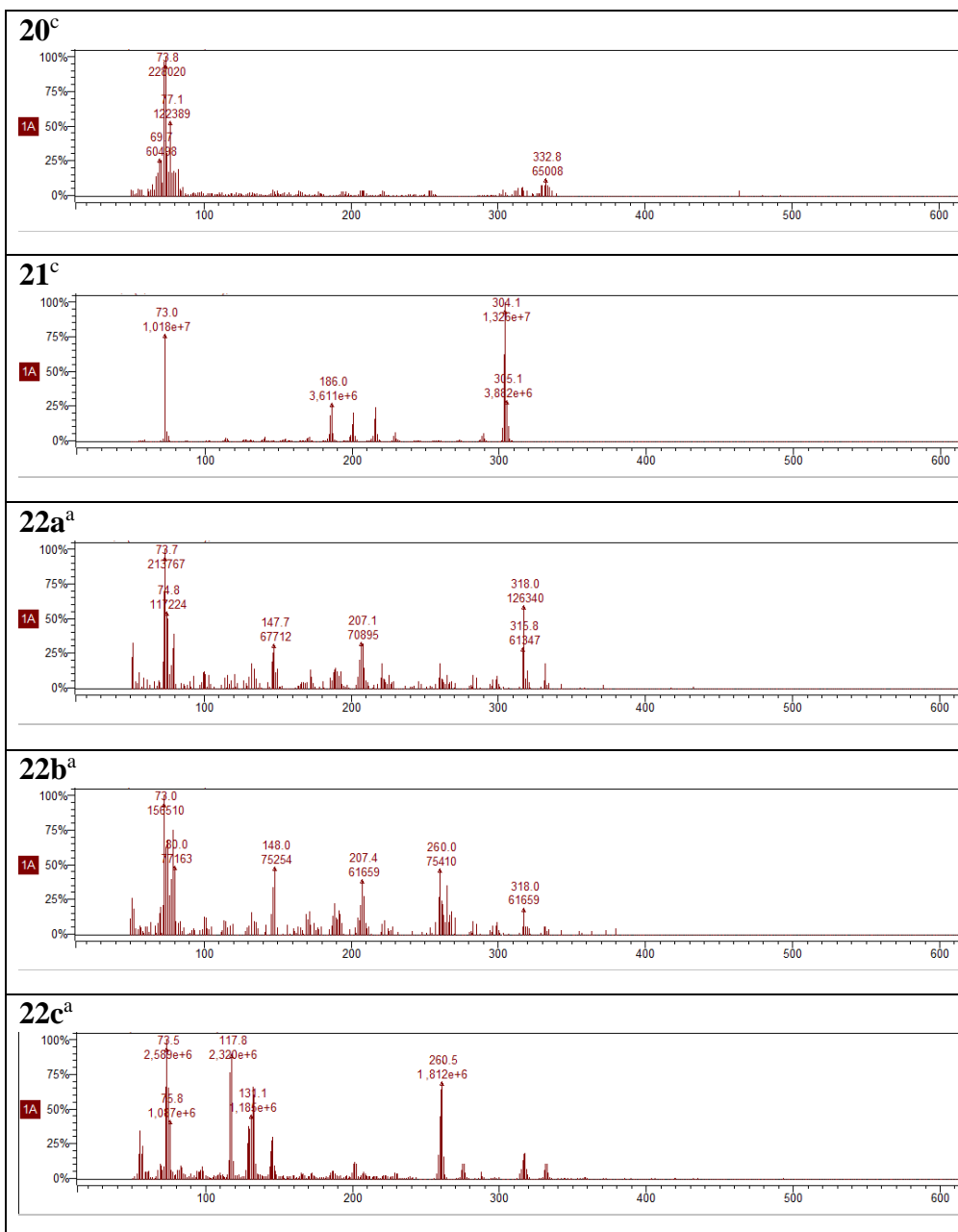












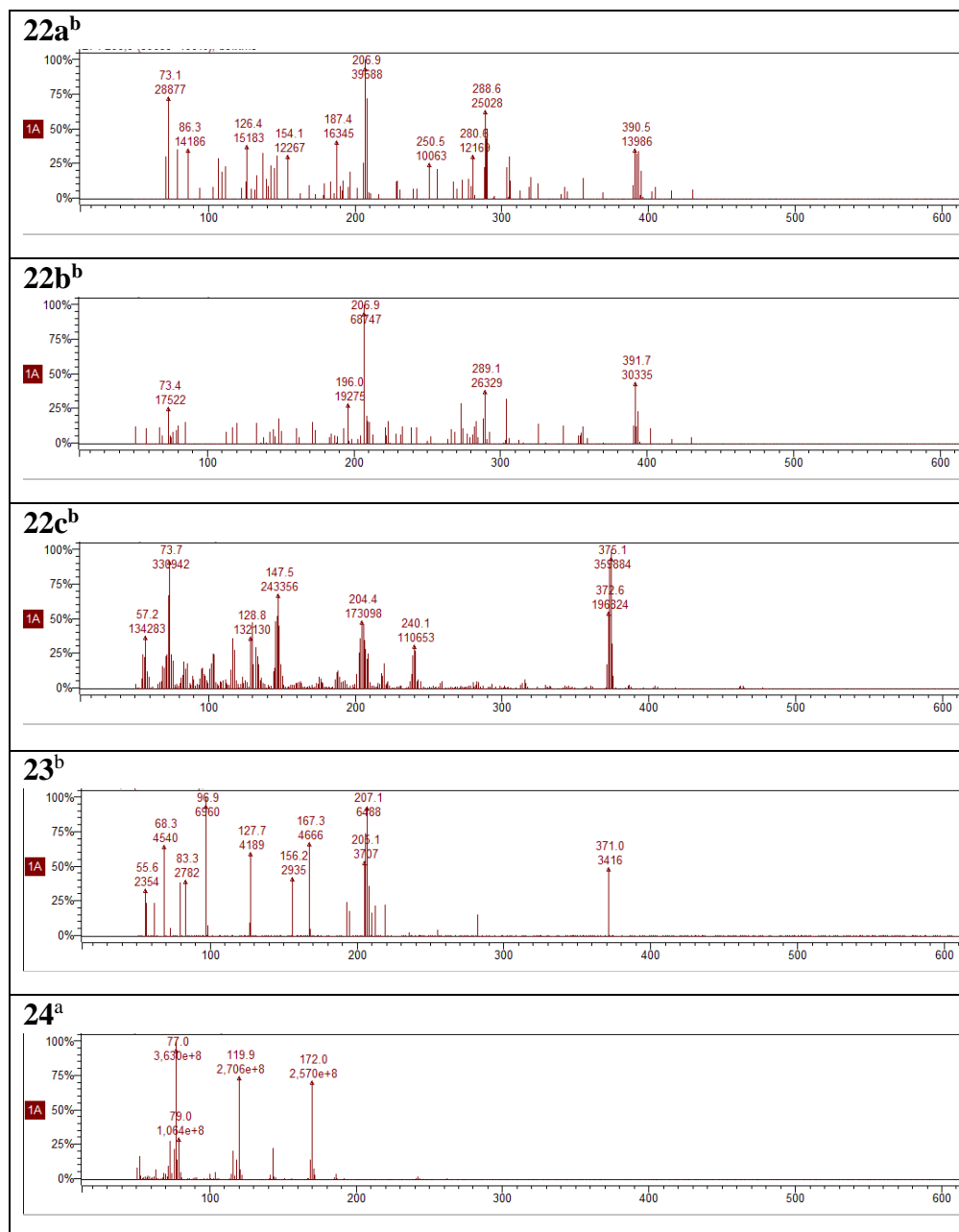


Figure 8 | M/z fragmentation spectra.

#### 2.4.4 Quantum chemical calculations.

Computations were performed at DFT-level of theory using the 6-311++G\*\* basis set of atomic orbitals and Becke's three parameters hybrid functional<sup>65</sup> in combination with Lee-Yang-Parr's correlation functional.<sup>66,67</sup> Free energy data were derived from frequency calculations performed at 273 K in the harmonic approximation. All DFT calculations were carried out in the gas-phase using the ORCA 4.1 program package.<sup>68</sup> In addition, a set of single-point benchmark calculations was performed at CCSD(T)/6-311++G\*\* level for three radicals derived by H-abstraction from 1-naphthol. In these calculations, the B3LYP/6-311++G\*\* geometries were used.

#### 2.4.5 Mineralogical composition, cosmo-origin and historical and terrestrial provenience of selected meteorites

*Northwest Africa NWA 4482.* Class: Pallasite. Group: Main Group Pallasite. Made of large olivine grains (Fa12.2-13.0) (FeO/MnO = 41.1-42.5).<sup>69</sup> Contains iron as iron hydroxides and accessory chromite, scheibersite (Fe, Ni) 3P and metal (both kamacite and tainite  $\gamma$ -[Fe, Ni]).

*Al Haggounia 001.* Class: Aubrite type. Aubrites are brecciated piroxenites made of FeO-free enstatite and reassembled in igneous lithologies. Al Haggounia 001 is a breccia cemented by iron oxide and carbonate.<sup>70</sup> The composition is dominated by enstatite and plagioclase. Contains troilite, graphite, oldhamite CaS, Si-rich kamacite and schreibersite.

*Elephant Moraine EET 96029.* Class: CR2. This meteorite is a CM carbonaceous chondrite with unusually mild aqueous alteration.<sup>71</sup> CM meteorites are among the most primitive bodies carrying out information on

the early history of the Solar System thanks to the presence of materials that have remained unchanged since the accretion from the protoplanetary disc (crystalline and amorphous silicates, oxides, metals, sulphides, organic matter), together with secondary components produced during aqueous alteration of parent body interiors (principally phyllosilicates). A low magnesium/iron ratio value and the presence of glass and quench crystallites in chondrules, associated to gehlenite-bearing calcium- and aluminum-rich inclusion suggested for ET 96029 the occurrence of an unusual low aqueous alteration.<sup>72</sup> Following aqueous alteration, ET 96029 was heated to ~400–600°C by impacts or solar radiation with concomitant amorphisation and dehydroxylation of serpentine, replacement of tochilinite by magnetite, loss of sulfur from the matrix, and modification to the structure of organic matter that includes organic nano-globules.

**REFERENCES:**

1. M.P. Bernstein, J.P. Dworkin, S.A. Sandford, L.J. Allamandola. Ultraviolet irradiation of the polycyclic aromatic hydrocarbon (PAH) naphthalene in H<sub>2</sub>O. Implications for meteorites and biogenesis. *Advances in Space Research* **2002**, 30 (6), 1501–1508.
2. M.P. Bernstein, S.A. Sandford, L.J. Allamandola, et al. UV Irradiation of Polycyclic Aromatic Hydrocarbons in Ices: Production of Alcohols, Quinones, and Ethers. *Science (1979)* **1999**, 283 (5405), 1135–1138.
3. Y.-J. Chen, M. Nuevo, T.-S. Yih, et al. Amino acids produced from the ultraviolet/extreme-ultraviolet irradiation of naphthalene in a H<sub>2</sub>O+NH<sub>3</sub> ice mixture. *Mon Not R Astron Soc* **2008**, 384 (2), 605–610.
4. M. d’Ischia, P. Manini, M. Moracci, et al. Astrochemistry and Astrobiology: Materials Science in Wonderland? *Int J Mol Sci* **2019**, 20 (17), 4079.
5. C.M.O. Alexander, M. Fogel, H. Yabuta, G.D. Cody. The origin and evolution of chondrites recorded in the elemental and isotopic compositions of their macromolecular organic matter. *Geochim Cosmochim Acta* **2007**, 71 (17), 4380–4403.
6. M. d’Ischia, P. Manini, Z. Martins, et al. Insoluble organic matter in chondrites: Archetypal melanin-like PAH-based multifunctionality at the origin of life? *Phys Life Rev* **2021**, 37, 65–93.
7. L. Remusat, S. Derenne, F. Robert, H. Knicker. New pyrolytic and spectroscopic data on Orgueil and Murchison insoluble organic matter: A different origin than soluble? *Geochim Cosmochim Acta* **2005**, 69 (15), 3919–3932.
8. J. Yang, S. Epstein. Interstellar organic matter in meteorites. *Geochim Cosmochim Acta* **1983**, 47 (12), 2199–2216.
9. R. Saladino, E. Carota, G. Botta, et al. Meteorite-catalyzed syntheses of nucleosides and of other prebiotic compounds from formamide under proton irradiation. *Proceedings of the National Academy of Sciences* **2015**, 112 (21).
10. M. Ferus, D. Nesvorný, J. Šponer, et al. High-energy chemistry of formamide: A unified mechanism of nucleobase formation. *Proceedings of the National Academy of Sciences* **2015**, 112 (3), 657–662.
11. G. Cooper, C. Reed, D. Nguyen, M. Carter, Y. Wang. Detection and formation scenario of citric acid, pyruvic acid, and other possible metabolism precursors

- in carbonaceous meteorites. *Proceedings of the National Academy of Sciences* **2011**, 108 (34), 14015–14020.
12. F.S. Brigiano, Y. Jeanvoine, A. Largo, R. Spezia. The formation of urea in space. *Astron Astrophys* **2018**, 610, A26.
  13. F. Ferrari, E. Szuszkiewicz. Cosmic Rays: A Review for Astrobiologists. *Astrobiology* **2009**, 9 (4), 413–436.
  14. R. Saladino, G. Botta, M. Delfino, E. Di Mauro. Meteorites as Catalysts for Prebiotic Chemistry. *Chemistry - A European Journal* **2013**, 19 (50), 16916–16922.
  15. R. Sreekanth, K.P. Prasanthkumar, M.M. Sunil Paul, U.K. Aravind, C.T. Aravindakumar. Oxidation Reactions of 1- and 2-Naphthols: An Experimental and Theoretical Study. *J Phys Chem A* **2013**, 117 (44), 11261–11270.
  16. K. Klotz, B.K. Schindler, J. Angerer. 1,2-Dihydroxynaphthalene as biomarker for a naphthalene exposure in humans. *Int J Hyg Environ Health* **2011**, 214 (2), 110–114.
  17. M.R. Xavier, M.M.S. Santos, M.G. Queiroz, et al. Lawsonone, a 2-hydroxy-1,4-naphthoquinone from *Lawsonia inermis* (henna), produces mitochondrial dysfunctions and triggers mitophagy in *Saccharomyces cerevisiae*. *Mol Biol Rep* **2020**, 47 (2), 1173–1185.
  18. L. Guo, A. Wang, P. Hu, et al. Renewable juglone nanowires with size-dependent charge storage properties. *RSC Adv* **2018**, 8 (4), 2077–2081.
  19. A. Kassam, D.J. Burnell, J.R. Dahn. Lithiated 1,4,5,8-Naphthalenetetraol Formaldehyde Polymer, An Organic Cathode Material. *Electrochemical and Solid-State Letters* **2011**, 14 (2), A22.
  20. K. Zahn, P. Ochwat. Zur Konstitution und Reaktionsweise mehrkerniger Polyoxy-chinone. Über Naphtazarin und Chinizarin. *Justus Liebigs Ann Chem* **1928**, 462 (1), 72–97.
  21. N.K. Utkina, N.D. Pokhilo, L.N. Atopkina. Antiradical Activity of Naphthazarin-Carbohydrate Nonglycoside Conjugates. *Nat Prod Commun* **2019**, 14 (5), 1934578X1984817.
  22. D. Klotz, T.H. Jülich, G. Wax, H. B. Stegmann. Group II Molecules and Radicals (Semidiones and Semiquiones, and Related Species); Springer-Verlag Berlin Heidelberg, **1989**; Vol. 17G.

23. M. Montesinos-Magraner, C. Vila, G. Blay, J. Pedro. Catalytic Enantioselective Friedel–Crafts Reactions of Naphthols and Electron-Rich Phenols. *Synthesis (Stuttg)* **2016**, 48 (14), 2151–2164.
24. Z. Sheikh, J. Doležal, J. Zýka. Oxidation of hydroxynaphthalenes by means of Co(III) acetate. *Microchemical Journal* **1971**, 16 (4), 548–556.
25. P. Manini, M. Bietti, M. Galeotti, et al. Characterization and Fate of Hydrogen-Bonded Free-Radical Intermediates and Their Coupling Products from the Hydrogen Atom Transfer Agent 1,8-Naphthalenediol. *ACS Omega* **2018**, 3 (4), 3918–3927.
26. J.D. Edwards, J.L. Cashaw. Studies in the Naphthalene Series. I. Oxidative Coupling of 1-Naphthol. *J Am Chem Soc* **1954**, 76 (23), 6141–6143.
27. T. Berndt, O. Böge. Gas-phase reaction of OH radicals with phenol. *Phys. Chem. Chem. Phys.* **2003**, 5 (2), 342–350.
28. M. Cocivera, M. Tomkiewicz, A. Groen. Electron paramagnetic resonance and nuclear spin polarization study of the photooxidation of phenol in water. *J Am Chem Soc* **1972**, 94 (19), 6598–6604.
29. G. Dobson, L.I. Grossweiner. Flash photolysis of aqueous phenol and cresols. *Transactions of the Faraday Society* **1965**, 61, 708.
30. V. Maurino, D. Borghesi, D. Vione, C. Minero. Transformation of phenolic compounds upon UVA irradiation of anthraquinone-2-sulfonate. *Photochemical & Photobiological Sciences* **2008**, 7 (3), 321–327.
31. R.L. Hudson. N<sub>2</sub> Chemistry in Interstellar and Planetary Ices: Radiation-driven Oxidation. *Astrophys J* **2018**, 867 (2), 160.
32. J. Vondráček, K. Chramostová, M. Plíšková, et al. Induction of aryl hydrocarbon receptor-mediated and estrogen receptor-mediated activities, and modulation of cell proliferation by dinaphthofurans. *Environ Toxicol Chem* **2004**, 23 (9), 2214.
33. K. Reddi Mohan Naidu, B. Satheesh Krishna, M. Anil Kumar, et al. Design, Synthesis and Antiviral Potential of 14-Aryl/Heteroaryl-14H-dibenzo[a,j]xanthenes Using an Efficient Polymer-Supported Catalyst. *Molecules* **2012**, 17 (6), 7543–7555.
34. A.A. Bell, M.H. Wheeler. Biosynthesis and Functions of Fungal Melanins. *Annu Rev Phytopathol* **1986**, 24 (1), 411–451.

35. E. Clar. Polycyclic Hydrocarbons; Springer-Verlag BerlinHeidelberg, **1964**; Vol. 2.
36. P. Sotero, R. Arce. Major products in the photochemistry of perylene adsorbed in models of atmospheric particulate matter. *J Photochem Photobiol A Chem* **2008**, 199 (1), 14–22.
37. Y. Hirao, T. Okuda, Y. Hamamoto, T. Kubo. Formation of Perylenes by Oxidative Dimerization of Naphthalenes Bearing Radical Sources. *Chempluschem* **2020**, 85 (1), 101–109.
38. C.A. Mulrooney, E.M. O'Brien, B.J. Morgan, M.C. Kozlowski. Perylenequinones: Isolation, Synthesis, and Biological Activity. *European J Org Chem* **2012**, 2012 (21), 3887–3904.
39. U. Weiss, L. Merlini, G. Nasini. Naturally Occurring Perylenequinones; **1987**; pp 1–71.
40. T. Miersch, H. Czech, A. Hartikainen, et al. Impact of photochemical ageing on Polycyclic Aromatic Hydrocarbons (PAH) and oxygenated PAH (Oxy-PAH/OH-PAH) in logwood stove emissions. *Science of The Total Environment* **2019**, 686, 382–392.
41. Z. Zhu. Retrospective Theses and Dissertations, **1995**.
42. I. Fourré, L. Rosset, H. Chevreau, Y. Ellinger. About the detection of urea in the interstellar medium: the energetic aspect. *A. & A.* **2016**, 589, A18.
43. G. Schlesinger, S.L. Miller. Prebiotic synthesis in atmospheres containing CH<sub>4</sub>, CO, and CO<sub>2</sub>. *J Mol Evol* **1983**, 19 (5), 383–390.
44. M. Colín-García, A. Negrón-Mendoza, S. Ramos-Bernal. Organics Produced by Irradiation of Frozen and Liquid HCN Solutions: Implications for Chemical Evolution Studies. *Astrobiology* **2009**, 9 (3), 279–288.
45. R. Saladino, G. Botta, B.M. Bizzarri, E. di Mauro, J.M. Garcia Ruiz. A Global Scale Scenario for Prebiotic Chemistry: Silica-Based Self-Assembled Mineral Structures and Formamide. *Biochemistry* **2016**, 55 (19), 2806–2811.
46. R. Saladino, G. Botta, S. Pino, G. Costanzo, E. di Mauro. Genetics first or metabolism first? The formamide clue. *Chem Soc Rev* **2012**, 41 (16), 5526.
47. A.E. Abigail E. Cruz-Hernández, M. Colin-Garcia, A. Heredia-Barbero, A. Negrón-Mendoza, S. Ramos-Bernal. Heterogeneous radiolysis of urea. Implications in astrobiology and prebiotic chemistry. *Open Chem* **2015**, 13 (1).

48. S. Okada, O. Tamemasa. Antibiological Actions of 2-Amino-1, 4-naphthoquinone Imine. *Chem Pharm Bull (Tokyo)* **1969**, 17 (7), 1432–1437.
49. R.L. Reeves, L.K.J. Tong. The Mechanism of Bleaching of Naphthoquinone Imine Dyes in Alkaline Solution. *J Org Chem* **1965**, 30 (1), 237–242.
50. R. Navarro-González, A. Negrón-Mendoza, E. Chacón. The  $\gamma$ -irradiation of aqueous solutions of urea. Implications for chemical evolution. *Origins of Life and Evolution of the Biosphere* **1989**, 19 (2), 109–118.
51. M.-J. Cheng, M.-D. Wu, S.-Y. Hsieh, I.-S. Chen, G.-F. Yuan. Secondary metabolites isolated from the fungus *Biscogniauxia cylindrospora* BCRC 33717. *Chem Nat Compd* **2011**, 47 (4), 527–530.
52. K. Ono, H. Yamaguchi, K. Taga, et al. Synthesis and properties of BF<sub>2</sub> complexes to dihydroxydiones of tetracene and perylene: novel electron acceptors showing n-type semiconducting behavior. *Org Lett* **2009**, 11 (1), 149–152.
53. A. Riffel, L.F. Medina, V. Stefani, et al. In vitro antimicrobial activity of a new series of 1,4-naphthoquinones. *Brazilian Journal of Medical and Biological Research* **2002**, 35 (7), 811–818.
54. A.A. de Aguiar, Al.G. Bayer. Zur Geschichte des Naphtazarins. *Berichte der deutschen chemischen Gesellschaft* **1871**, 4 (1), 251–253.
55. D. Robeson, G. Strobel, G.K. Matusumoto, et al. Alteichin: an unusual phytotoxin from *Alternaria eichorniae*, a fungal pathogen of water hyacinth. *Experientia* **1984**, 40 (11), 1248–1250.
56. W. B. Turner, D. C. Aldridge. *Fungal Metabolites*; **1983**; Vol. 2, p 631.
57. R. Atkinson, J. Arey. Mechanisms of the Gas-Phase Reactions of Aromatic Hydrocarbons and PAHs with OH and NO<sub>3</sub> Radicals. *Polycycl Aromat Compd* **2007**, 27 (1), 15–40.
58. H.J. Werner, P.J. Knowles, G. Knizia, F.R. Manby, M. Schütz. Molpro: a general-purpose quantum chemistry program package. *Wiley Interdiscip Rev Comput Mol Sci* **2012**, 2 (2), 242–253.
59. C.M.O. Alexander, G.D. Cody, B.T. De Gregorio, L.R. Nittler, R.M. Stroud. The nature, origin and modification of insoluble organic matter in chondrites, the major source of Earth's C and N. *Geochemistry* **2017**, 77 (2), 227–256.
60. L. Remusat, Y. Guan, Y. Wang, J.M. Eiler. Accretion and Preservation of D-rich Organic Particles in Carbonaceous Chondrites: Evidence for Important

- Transport in the Early Solar System Nebula. *Astrophys J* **2010**, 713 (2), 1048–1058.
61. S. Messenger, L.P. Keller, D.S. Lauretta. Supernova Olivine from Cometary Dust. *Science (1979)* **2005**, 309 (5735), 737–741.
  62. V.K. Pearson, A.T. Kearsley, M.A. Sephton, I. Gilmour. The labelling of meteoritic organic material using osmium tetroxide vapour impregnation. *Planet Space Sci* **2007**, 55 (10), 1310–1318.
  63. Y. Kebukawa, A.L. David Kilcoyne, G.D. Cody. Exploring the Potential Formation of Organic Solids in Chondrites and Comets through Polymerization of Interstellar Formaldehyde. *Astrophys J* **2013**, 771 (1), 19.
  64. C. le Guillou, S. Bernard, A.J. Brearley, Evolution of organic matter in Orgueil, Murchison and Renazzo during parent body aqueous alteration: In situ investigations. *Geochim Cosmochim Acta* **2014**, 131, 368–392.
  65. A.D. Becke. Density-functional thermochemistry. III. The role of exact exchange. *J Chem Phys* **1993**, 98 (7), 5648–5652.
  66. C. Lee, W. Yang, R.G. Parr. Development of the Colle-Salvetti correlation-energy formula into a functional of the electron density. *Phys Rev B* **1988**, 37 (2), 785–789.
  67. B. Miehlich, A. Savin, H. Stoll, H. Preuss. Results obtained with the correlation energy density functionals of Becke and Lee, Yang and Parr. *Chem Phys Lett* **1989**, 157 (3), 200–206.
  68. F. Neese. The ORCA program system. *WIREs Computational Molecular Science* **2012**, 2 (1), 73–78.
  69. A. Irving, S. Kuehner. *J. Meteoritical Bulletin MAPS* 42; **2007**.
  70. H.C. Connolly, C. Smith, G. Benedix, L. Folco, K. Righter, J. Zipfel, A. Yamaguchi, A. H. Chennaoui. The Meteoritical Bulletin, No. 92, 2007 September. *Meteorit Planet Sci* **2007**, 1647–1694.
  71. K.T. Howard, C.M.O. Alexander, D.L. Schrader Classification of hydrous meteorites by phyllosilicate fraction: PSD-XRD modal mineralogy and planetesimal environments. *Geochim Cosmochim Acta* **2015**, 149, 206–222.
  72. M.R. Lee, P. Lindgren, A.J. King, et al. Elephant Moraine 96029, a very mildly aqueously altered and heated CM carbonaceous chondrite: Implications for the drivers of parent body processing. *Geochim Cosmochim Acta* **2016**, 187, 237–259.

# CHAPTER 3

## PHOTO-PROCESSING AND THERMAL DESORPTION OF PA(N)HS AND COMs ON ICE DUST GRAINS

*“All my life I have wondered about the possibility of life elsewhere. What would it be like? Of what would it be made? ...Is extraterrestrial life, if it exists, based on the same organic molecules as life on Earth? Do the beings of other worlds look much like life on Earth? ... What else is possible? The nature of life on Earth and the search for life elsewhere are two sides of the same question - the search for who we are.”*

— Carl Sagan’s Cosmos

### 3.1 Introduction

For many years the ISM has been considered an “inhospitable” environment in which the low temperature and density together with the intense ionizing radiations may prevent any kind of chemical reactivity. Nowadays we know that the space between the stars hosts a rich palette of molecular species, with the identification of more than 250 individual species, excluding isotopologues. About 50 of these contain 6 or more atoms. These molecules have been defined by astronomers as interstellar complex organic molecules (iCOMs)<sup>1</sup>

An increasing number of iCOMs, in a large variety of star-forming sites, have been discovered by millimeter and centimeter observations. The advent of large interferometers in the (sub-)mm range, such as IRAM-NOEMA and ALMA, have revealed the presence of iCOMs in all the stages of the Solar-like star formation process: from the earliest stages of star formation,<sup>2</sup> i.e. in pre-stellar dense cores,<sup>3,4</sup> in hot corinos around protostars,<sup>5,6</sup> and in the associated jets and outflows,<sup>7-10</sup> to protoplanetary disks. In particular, protoplanetary disks are extremely interesting because are the place where planets form, inheriting their chemical complexity. Nevertheless, the region in which the dust temperature is high enough to allow the thermal desorption of water ice and iCOMs ( $T > 100$  K) is very small ( $\leq 5$  AU) for Solar-like stars,<sup>11</sup> making the so COMs detection very hard (see sketch reported in panel a in Figure 1).

Only methanol,<sup>12,13</sup> acetonitrile,<sup>14</sup> and formic acid<sup>15</sup> have been observed so far. A new fascinating perspective was recently provided by FU Ori objects in which the young central star undergoes a strong accretion burst and hence a sudden increase in brightness which leads to heating of the surrounding disk and to a quick expansion of the molecular snow lines to larger radii (see sketch reported in panel b in Figure 1). This phenomenon was first observed in V883 Ori by Cieza et al. in 2016.<sup>11</sup> The increase in brightness, according to the latter authors, extended the water snow line up to 42 AU. Methanol has been detected in this disk by Hoff et al. in 2018: the transitions observed suggest the thermal desorption of methanol from dust grains from the surface layers beyond or within the water snow line, which would therefore have extended up to 100 AU.<sup>16</sup> Thanks to the increase in temperature of the disk, five iCOMs thermally

desorbed from the disk were later detected: methanol, acetone, acetonitrile, acetaldehyde and methyl formate.<sup>17</sup>

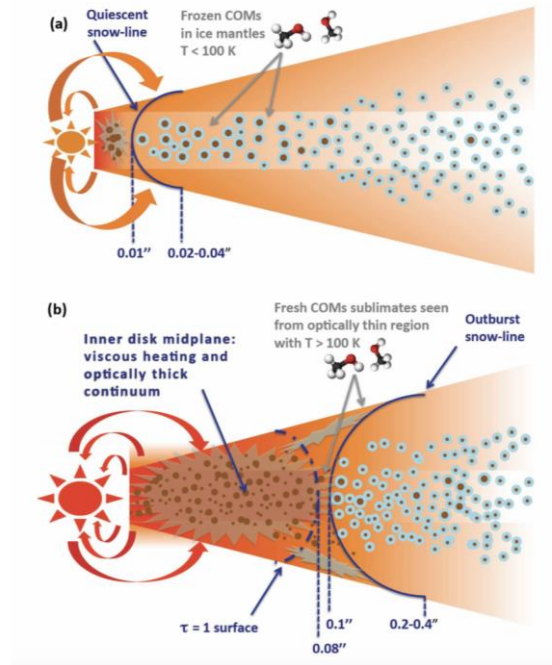


**Figure 1** | The sketches shown in Figure reveal the differences between a protoplanetary disk around a Solar-like star (a) and a FuOri object (b). Sketch (a) shows that in a protoplanetary disk around a Solarlike star, the region where the dust temperature is high enough to let the water and iCOMs thermal desorption ( $>100$  K) is very small. At a distance from the central star greater than  $0.01''$  ( $\sim 5$  AU), the dust temperature is lower than 100 K and the iCOMs are frozen in the ice mantles. Sketch (b) shows what happens in a FuOri object. The central star undergoes a sudden accretion burst which leads to the heating of the surrounding disk and to a quick expansion of the molecular snow lines to larger radii ( $0.08'' \sim 100$  AU). Image adapted from Ref.<sup>17</sup>.

Acetonitrile ( $\text{CH}_3\text{CN}$ ) was found in many regions both within and outside the Solar System: in the Titan atmosphere,<sup>18-20</sup> in the comet 67P / Churyumov-Gerasimenko,<sup>21</sup> in the cometary coma of Hale - Bopp,<sup>22</sup> in the molecular cloud SgrB2(N),<sup>23</sup> in the high and low mass protostars,<sup>24,25</sup> in hot cores,<sup>26</sup> in protoplanetary disks;<sup>14,27</sup> moreover, it is among the most commonly detected organic molecules in disks.<sup>28</sup>

Many works invoked chemical reactions occurring on the surface of the grains triggered by atoms, UV light, cosmic rays, or thermal processing,<sup>29,30</sup> to explain the large abundance observed in the gas phase of acetonitrile.

The nitrile species are of particular interest for their involvement in the processes for the formation of prebiotic molecules.

Acetaldehyde ( $\text{CH}_3\text{COH}$ ) was also observed in the interstellar medium, in low- and high-mass protostars,<sup>31,32</sup> in hot corinos<sup>33,34</sup> and comets<sup>35</sup>. The reaction pathways involving the iCOMs described by the  $\text{C}_2\text{H}_n\text{O}$  formula, such as acetaldehyde ( $\text{CH}_3\text{COH}$ ), are still a matter of debate.<sup>36</sup> Many works show how acetaldehyde can be synthesized directly on the grain surfaces<sup>37,38</sup> starting from HCO and  $\text{CH}_3$  radicals on CO-rich ices<sup>39</sup> or through surface chemistry at 10 K on  $\text{C}_2\text{H}_2$  ices with H-atoms and OH radicals,<sup>36</sup> or through UV photoprocessing of interstellar ice analogs.<sup>40</sup> Other works claimed that it is not clear whether acetaldehyde is formed on the icy surfaces of interstellar grains or through gas phase reactions.<sup>41</sup>

Polycyclic aromatic hydrocarbons (PAHs) are another family of compounds of particular interest because they are among the most diffuse interstellar polyatomic molecules known in the gas phase and are thought to account for up 30 % of the molecular carbon in the universe.

Their widespread presence is evidenced by their strong and ubiquitous mid-infrared (mid-IR) emission features at 3.3, 6.2, 7.7, 8.6, 11.3, 12.7 and 17  $\mu\text{m}$ , commonly known as unidentified infrared (UIR) bands.<sup>42–45</sup>

These bands can be seen in various ISM environments, including reflection nebulae, planetary nebulae, photodissociation regions, HII regions, asymptotic giant branch (AGB) objects, young stellar objects, active star formation regions, diffuse interstellar regions and external galaxies.<sup>46–53</sup>

The PAH hypothesis developed by Leger and Puget in 1984 states<sup>54</sup> that the mid-IR fluorescence emission bands result from the excitation of gas-phase PAH molecules by energetic ultraviolet (UV) photons from young stars.<sup>45,54,55</sup>

The broad features of the mid-IR bands have been ascribed to the simultaneous presence of a series of PAH-related species, such as:

- heteroatom substituted PAHs. For example, in the case of PANHs, one or more carbon atoms are replaced with nitrogen atoms;<sup>48,56,57</sup>
- PAH-metal complexes. Metal is placed either below or above the aromatic carbon rings skeleton;<sup>56–59</sup>
- PAH oligomers, such as dimers or trimers;<sup>60,61</sup>
- mixture of PAHs of different size;
- mixture of aromatic and aliphatic components ratio.<sup>62–69</sup>

PAHs are commonly thought to be produced in the circumstellar shells and outflows of late-type carbon stars, including AGB stars, via gas-phase radical reactions involving the polymerization of acetylene.<sup>70</sup> Nevertheless, “Top-down” cleavage reactions are considered as another possible formation pathways.

Smaller size PAHs, ranging from 10 (naphthalene) to 24 carbon atoms (coronene) are also found in at least 20 carbonaceous chondrites (CCs).<sup>71–74</sup>

After the explosion of a supernova, PAHs could be ejected in the ISM where they condense onto very cold grains made of silicates ( $T = 10$  K) and being incorporated in the interstellar water-rich icy grains mantles. Mid-IR absorption features in the spectra of stars embedded within dense clouds emphasize the occurrence of PAHs in these ices.<sup>75–79</sup>

The gravitational collapse of material onto a central dense core feeds the growth of a nascent protostar, which heats the inner regions of its surrounding envelope, thus creating the ‘‘hot’’ ( $T = 100$  K) conditions. As the temperature gradually increases, the frozen molecules in grain mantles acquire mobility and the desorption into the gas phase may occur thermally.

PAHs may play an active role at this stage, conducting to the formation of a set of PAH-related molecules and/or fragments to be released in the gas phase, which may contribute to the high chemical diversity of ISM.

Polycyclic aromatic nitrogen heterocycles (PANHs), which can be formally derived from PAHs by replacing a methylidyne (CH) moiety with an isoelectronic nitrogen atom (N), are also supposed to be present in the ISM. The interest in this class of molecules derives from the high abundance of nitrogenated compounds in the ISM and on different celestial bodies. Indeed, nitrogen-containing aromatic heterocycles, such as nucleobases, have been detected on comets and meteorites and many small building blocks, such as formamide, cyanoacetylene and cyanamide, have been observed in the ISM and strictly associated with the processes that may have led to the formation of the molecules of life.

Recently, PAH nitriles, including benzonitrile ( $C_6H_5CN$ ), 1-cyano-1,3-cyclopentadiene ( $C_5H_6CN$ ), and 1- and 2-cyano-naphthalene ( $C_{11}H_7CN$ ) have also been detected in a cold molecular cloud.<sup>80–82</sup>

The photo-processing of interstellar icy mantles through low-energy cosmic rays,<sup>83</sup> X-ray,<sup>84</sup> and UV<sup>85</sup> photons irradiation, is another aspect to take into account.

In particular, UV radiations are responsible for the chemical evolution in space, promoting photochemical reactions on surfaces of dust grains. Laboratory experiments simulating the thermal and energetic processing of interstellar ice analogue showed how new molecules, radicals and fragments are produced by the ice photoprocessing.<sup>86-91</sup>

The photo-processing can take place in different protostellar regions, around young stellar objects<sup>92,93</sup> or in the outer regions of the circumstellar environments, where there are UV photons scattered by dust in the bipolar outflow cavities around protostars.<sup>94,95</sup>

In 2018 Taha et al. reported on the observation of the emission of PAHs in the disk around the Herbig star HD 179218.<sup>96</sup> Using the radiative transfer (RT) model of the continuum, it was found that PAH molecules extend along the surface of the disk and are excited and ionized by stellar UV photons even at large distances. So, they are in a state of ionized charge due to the strong UV radiation field. Finally, Muñoz Caro et al.,<sup>87</sup> calculated that at 100 AU from the central star in a disk of the T Tauri phase with a UV field of intensity  $10^{12}$  photons $\cdot$ cm<sup>-2</sup> $\cdot$ sec<sup>-1</sup><sup>97</sup> and for a UV cross-section of  $10^{-18}$  cm<sup>2</sup>, a molecule absorbs about 1 UV photon per week inside the ice mantle, enough to convert ~10% of the carbon in the ice into iCOMs;

moreover, relatively high abundances of iCOMs, such as acetonitrile and acetaldehyde, and PAHs are observed in photon-dominated regions (PDRs) and in the UV-exposed atmospheres of planet-forming disks.<sup>28</sup>

In this context, laboratory studies are crucial to study the evolution and preservation of processed complex organic molecules in harsh astronomical environments.

In this Chapter we will discuss about the results obtained from the photo-processing and thermal desorption experiments carried out on ices made up of acetaldehyde, acetonitrile, NAPH and QUIN, these two latter selected as representative molecules of the PAHs and PANHs family (chemical structures in Figure 2).

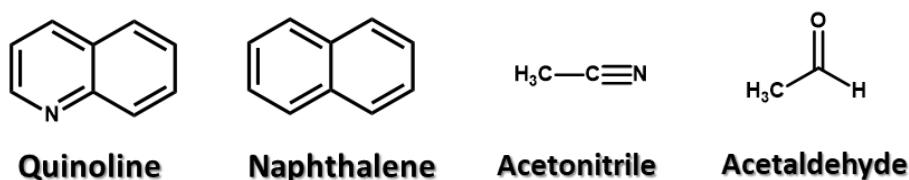


**Figure 2** | Chemical structures of investigated molecules.

The main focus of this research line is to shed more light on the mechanisms responsible for the release of tested molecules in the gas phase and understand the effect both of dust grains and UV irradiation on the thermal desorption processes and on the formation of new species. As a matter of fact, the mineral surface can drive the orientation of adsorbed molecules and act as a template, adsorbing selectively molecules and favouring their concentration. Therefore, the presence of minerals can influence the desorption of molecules so that grain–molecule interaction cannot be neglected.

A very useful experimental setup that simulates quite well the environmental conditions of ice dust grains is the ultrahigh vacuum (UHV) chamber (Figure 3).

The gas mixtures of selected molecules were prepared in the prechamber following the partial pressures and were deposited through a valve system inside the UHV chamber on a smooth nickel plate cooled at 11 K (cold finger). The condensation of the gas mixtures could occur also on mineral grains with a size smaller than 5  $\mu\text{m}$ , such as olivine, deposited on the cold finger.

The UHV chamber was equipped with quadrupole mass spectrometer (QMS) and with a Xenon lamp (wavelength range 200 - 300 nm, 4-6 eV) that simulate the radiation of solar-like stars. The UV radiation emitted by the lamp was collimated through an optical system towards an optical fiber focused on the cold finger.

After condensation, the sample was heated with a linear temperature ramp. As the cold finger warmed, the condensed molecules desorbed, entered the mass spectrometer where were discriminated by their  $m/z$  value.

The composition of the desorbed gas monitored by mass analysis was monitored in the mass range 1-300 a.m.u. by varying the temperature with the time according to a temperature-programmed desorption (TPD) curve. For a given mass, the TPD was analyzed by using the Polanyi-Wigner equation:

$$r_{des} = - \frac{d\theta}{dT} = \frac{A}{h_r} \cdot \theta^m \cdot e^{-\frac{E_{des}}{k_b T}} \quad \mathbf{3.1.1}$$

The TPD technique is very powerful in investigating the desorption process of organic molecules from the surface of dust grains. The TPD technique allows to obtain useful parameters including thermal desorption temperatures and energies.

Up to now, TPD experiments have been carried out mainly from graphite and amorphous water ice surfaces.<sup>98-101</sup>

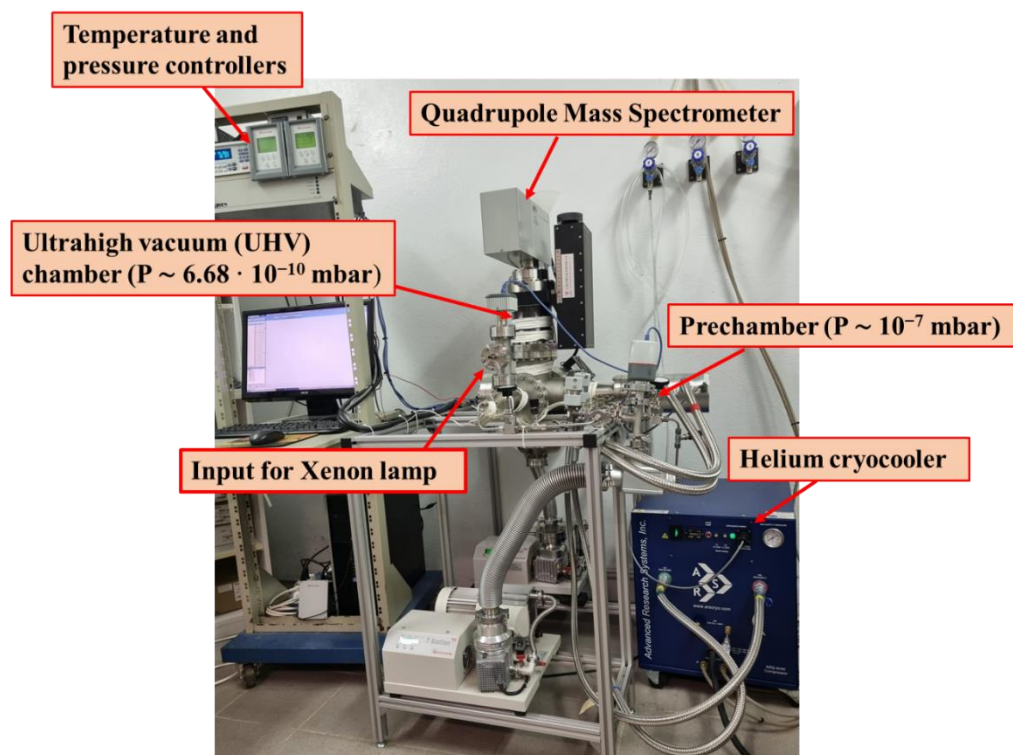


**Figure 3** | Experimental setup for TPD and mass spectra measurements.

Molecules can interact on the mineral surface by means of Van der Waals-like forces and dipole-dipole interactions, as demonstrated through vibrational spectroscopic methods such as infrared and Raman spectroscopy.<sup>102</sup>

Moreover, molecules can diffuse inside the grains when the submicron interstellar grains begin to accrete into hundreds of microns of fluffy dust.

Because silicates are ubiquitous in space, their choice as analogue samples is quite straightforward. There is evidence of silicates from comets, observed from both ground observations<sup>103–105</sup> and from space missions,<sup>106,107</sup> to protoplanetary disks.<sup>108–112</sup> Silicates were also found in the cometary coma of

Hale Bopp,<sup>108</sup> in circumstellar envelopes around young stars<sup>113</sup> and in evolved stars and planetary nebulae.<sup>114</sup>

Olivine is an isomorphic mixture of forsterite ( $\text{Mg}_2\text{SiO}_4$ ) and fayalite ( $\text{Fe}_2\text{SiO}_4$ ). In our experiments, we used olivine made up of 80% forsterite and 20% fayalite.

Forsterite is the magnesium-rich end member of the olivine group and is one of the most abundant silicate minerals in the Solar System. It has been found in meteorites,<sup>115</sup> cometary dust,<sup>116</sup> and in protoplanetary disk.<sup>117</sup> Furthermore, Mg-containing minerals are important because magnesium is supposed to have played a key role in prebiotic geochemistry.

Fayalite, the iron end-member of the olivine group, was found in the interstellar medium and meteorite.<sup>118</sup>

Olivine is one of the most common silicate grains in space: through IRAS low-resolution spectra, olivine dust was detected as a common material in the circumstellar disks or/and shells of Herbig Ae/Be stars<sup>119</sup> and around T Tauri stars.<sup>120</sup> More recently, the mid-infrared spectrum obtained through Spitzer Space Telescope revealed the presence of crystalline silicate in a cold, infalling protostellar envelope of the Orion A protostar HOPS-68.<sup>121</sup> Protostar EX Lupi is the prototype of EXORs like objects, that are similar to FUORs objects mentioned above but their outbursts are shorter and recursive in time, and it underwent its most important explosion in 2008, when its brightness increased by a factor of 30 for six months, due to the high accretion from the circumstellar disk on the star. Ábrahám et al.<sup>122</sup> observed the system during the explosion and discovered the crystallization of the amorphous silicate grains due to the heating of the disk. In particular, they observed silicates of the order of micrometer size.

Starting from this background, TPD experiments were carried out both on acetonitrile and acetaldehyde, in pure form and in water ice mixtures, both on naphthalene and quinoline, all condensed at 11 K on micrometric grains of silicate olivine ((Mg,Fe)<sub>2</sub>SiO<sub>4</sub>). The effects of UV irradiation on the ice mixtures were also investigated to disclose possible photo-processes.

The work reported in this Chapter has been carried out at INAF Arcetri Astrophysical Observatory (Florence) in collaboration with Prof. Robert John Brucato.

## 3.2 Results and discussion

The experimental activity reported in this Chapter can be divided into two main blocks:

- 1) The photochemistry of acetaldehyde ( $\text{CH}_3\text{COH}$ )/acetonitrile ( $\text{CH}_3\text{CN}$ ) on ice dust grains;
- 2) The photochemistry of naphthalene (NAPH)/quinoline (QUIN) on ice dust grains.

In both cases the ultra-high vacuum chamber reported in Figure 4 has been used. The experimental setup allowed for:

- a) the deposition of ice layers with a controlled composition over a nickel surface (cold finger) under a pressure of  $10^{-10}$  mbar and a temperature of 11 K;
- b) the investigation of the interaction of the selected compounds with the surface simulating the dust grains by means of TPD experiments;
- c) the analysis of the compounds desorbed in the gas phase by mass spectrometry (electron impact ionization mode);
- d) the irradiation of the ices with UV light (200 - 300 nm, 4 - 6 eV).

In the Chapter 1 we underlined how photo-processing is one of the mechanisms responsible for chemical evolution in space promoting photochemical reactions, particularly on surfaces of dust grains that can act as catalysts.

In this Chapter, by means of TPD experiments carried out on the ice mixtures of acetaldehyde, acetonitrile, naphthalene and quinoline from micrometric grains of olivine, we studied first how solid-phase interactions between molecules and grain surfaces can influence the desorption process and, hence, the presence and abundance of molecular species in the gas phase. Then, by applying a flux of UV radiations, we have investigated the possible

mechanisms of formation of complex molecules identified by mass spectrometric analysis.

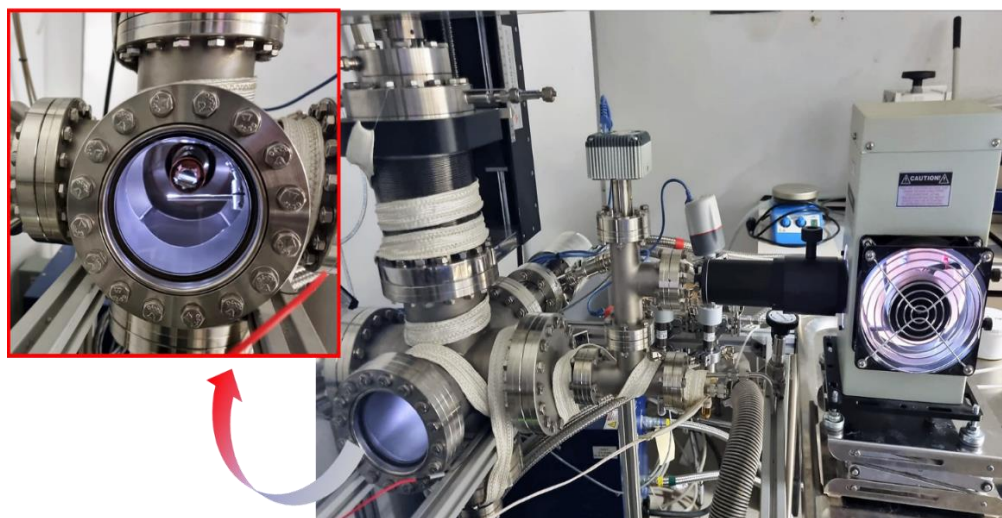


**Figure 4** | Experimental setup used for in situ UV irradiation experiments.

### **3.2.1 Photo-processing and thermal desorption of acetaldehyde and acetonitrile on ice dust grains**

The photo-processing of acetonitrile and acetaldehyde ice mixtures by UV irradiation was performed to study the formation of complex molecules through TPD experiments and mass spectra analysis. To this aim a ternary ice mixture composed by  $\text{CH}_3\text{CN}:\text{CH}_3\text{COH}:\text{H}_2\text{O}$  (1:1:3) was prepared and deposited as monolayer on the bare cold finger or on the surface of micrometric olivine grains on the cold finger at 11 K within the UHV chamber ( $P \sim 6.68 \cdot 10^{-10}$  mbar). In such a composition the ice will simulate the astrophysical environment of the star-forming regions where water is the most abundant ice component. For comparative purposes, the same analyses were also carried out

on monolayers of pure  $\text{CH}_3\text{COH}$ , pure  $\text{CH}_3\text{CN}$  and of the binary mixture of  $\text{CH}_3\text{CN}:\text{CH}_3\text{COH}$  (1:6).

To assess the effect of UV radiations in promoting the formation of new molecular species, we compared the mass peak intensities recorded with and without UV irradiation and considered only the peaks showing the highest intensity after UV irradiation. The structural assignment for the main peaks detected in the mass spectra has been performed by matching with the data reported in the NIST Web Book and on the basis of literature data.

### 3.2.1.1 Pure acetaldehyde ice

Figure 5 shows the TPD curves of acetaldehyde ( $m/z$  44) desorbed from the bare cold finger in the non-irradiated case (blue line) and after 8 hours of UV irradiation (purple line).

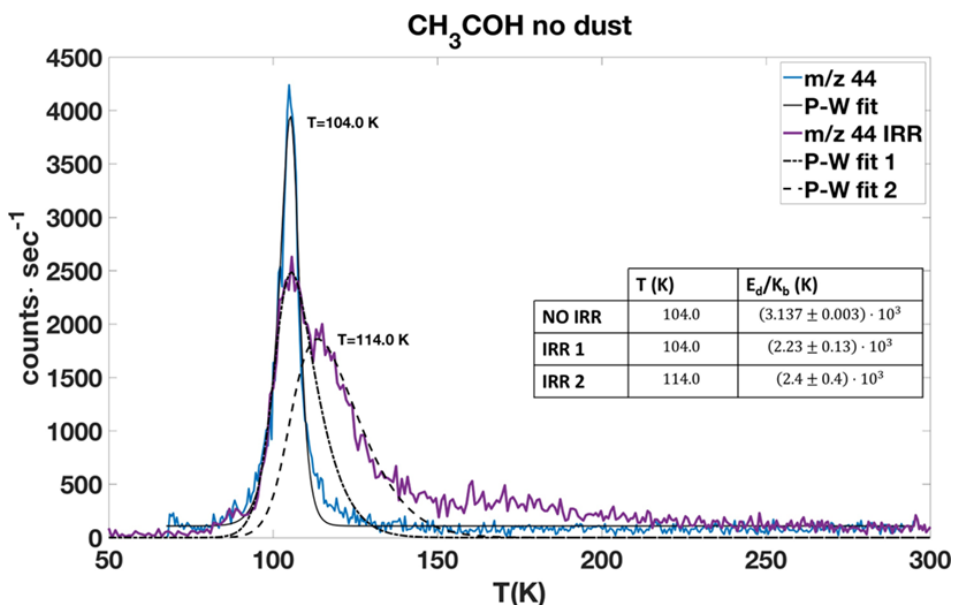


**Figure 5** | TPD curves of  $\text{CH}_3\text{COH}$  (44  $m/z$ ) before (blue line) and after (purple line) 8 hours of UV irradiation.

The TPD curves were fitted with different Polanyi-Wigner equations. When no irradiation was performed, a single peak, centered at 104 K (4500 counts per second (c/s)) and associated with a binding energy of  $E_d/K_b$  of 3137 K, was detected in good agreement with previously obtained results.<sup>123</sup> After exposure to UV radiations, the intensity of the signal at 104 K was 40% lower (2700 c/s and a binding energy of 2230 K), despite the same amount of acetaldehyde was deposited, with a broadening at higher temperatures and a second desorption peak at 114 K (binding energy of 2400 K).

Mass spectra of desorbed acetaldehyde were registered in the  $m/z$  1-300 range. Selected data collected in the 92-138 K temperature range are reported in Figure 6 and summarized in Table 1. In this latter, the main peaks detected during the thermal desorption of  $\text{CH}_3\text{COH}$  from the bare cold finger and from the olivine grains with or without UV irradiation were shown.

The mass spectra obtained after irradiating pure acetaldehyde ice deposited on bare cold finger or olivine grains revealed the presence of three major clusters of peaks around  $m/z$  15, 29, and 46. (Figure 6). In particular, a considerable increase due to the effect of UV irradiation was observed in the case of the peaks at  $m/z$  15 and 29 relative to the methyl ( $\text{CH}_3$ ) and formyl ( $\text{HCO}$ ) radicals,  $m/z$  16 relative to methane ( $\text{CH}_4$ ), and  $m/z$  46 relative to formic acid ( $\text{HCOOH}$ ) (Figure 6, red bars). This effect proved to be more evident in the case of acetaldehyde ice deposited on olivine grains (Figure 6B) suggesting the catalytic role of the mineral in the photodegradation processes.

By comparison with the spectra reported in the NIST Web Book it was possible to assign the structures of the compounds listed in Table 2 to the main peaks detected after UV irradiation.

**Table 1** | Mass spectra data registered for pure CH<sub>3</sub>COH deposited on bare cold finger or on olivine grains with or without UV irradiation. Only main clusters around  $m/z$  15, 29, 44 and the most significant peaks above  $m/z$  50 are reported. Among these, only values with an intensity of at least 60 c/s are reported.

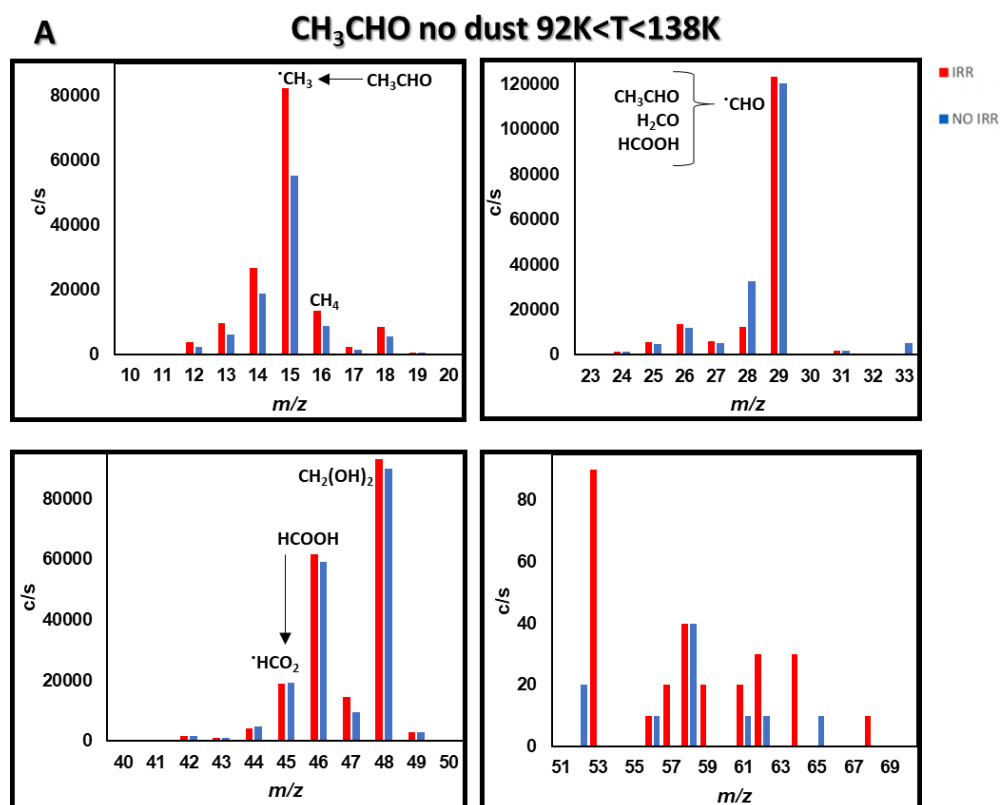
$m/z$	Peak Intensity (c/s)				$m/z$	Peak Intensity (c/s)			
	CH <sub>3</sub> COH <sup>a</sup>								
	Bare finger		Olivine grains			Bare finger		Olivine grains	
	NO UV	UV	NO UV	UV		NO UV	UV	NO UV	UV
<b>15</b>	6·10 <sup>4</sup>	8·10 <sup>4</sup>	8·10 <sup>4</sup>	1·10 <sup>5</sup>	<b>42</b>	2·10 <sup>3</sup>	2·10 <sup>3</sup>	2·10 <sup>3</sup>	2·10 <sup>3</sup>
<b>16</b>	9·10 <sup>3</sup>	1·10 <sup>4</sup>	1·10 <sup>4</sup>	2·10 <sup>4</sup>	<b>43</b>	9·10 <sup>2</sup>	9·10 <sup>2</sup>	8·10 <sup>2</sup>	2·10 <sup>3</sup>
<b>17</b>	1·10 <sup>3</sup>	2·10 <sup>3</sup>	6·10 <sup>3</sup>	1·10 <sup>3</sup>	<b>44</b>	5·10 <sup>3</sup>	3·10 <sup>3</sup>	9·10 <sup>3</sup>	6·10 <sup>3</sup>
<b>18</b>	6·10 <sup>3</sup>	9·10 <sup>3</sup>	2·10 <sup>4</sup>	4·10 <sup>3</sup>	<b>45</b>	2·10 <sup>4</sup>	2·10 <sup>4</sup>	3·10 <sup>4</sup>	3·10 <sup>4</sup>
<b>26</b>	1·10 <sup>4</sup>	1·10 <sup>4</sup>	2·10 <sup>4</sup>	2·10 <sup>4</sup>	<b>46</b>	6·10 <sup>4</sup>	6·10 <sup>4</sup>	8·10 <sup>4</sup>	1·10 <sup>3</sup>
<b>27</b>	5·10 <sup>3</sup>	6·10 <sup>3</sup>	7·10 <sup>3</sup>	8·10 <sup>3</sup>	<b>48</b>	9·10 <sup>4</sup>	9·10 <sup>4</sup>	2·10 <sup>5</sup>	1·10 <sup>5</sup>
<b>28</b>	3·10 <sup>4</sup>	1·10 <sup>4</sup>	1·10 <sup>4</sup>	1·10 <sup>4</sup>	<b>50</b>	--	3·10 <sup>2</sup>	5·10 <sup>2</sup>	5·10 <sup>2</sup>
<b>29</b>	1·10 <sup>5</sup>	1·10 <sup>5</sup>	2·10 <sup>5</sup>	2·10 <sup>5</sup>	<b>62</b>	--	--	2·10 <sup>2</sup>	--
<b>30</b>	--	--	9·10 <sup>2</sup>	2·10 <sup>3</sup>	<b>65</b>	--	--	6·10 <sup>2</sup>	--
<b>31</b>	--	2·10 <sup>3</sup>	9·10 <sup>2</sup>	2·10 <sup>3</sup>	<b>81</b>	--	--	1·10 <sup>2</sup>	--
<b>32</b>	--	4·10 <sup>2</sup>	4·10 <sup>2</sup>	7·10 <sup>2</sup>	<b>82</b>	--	--	1·10 <sup>2</sup>	--

<sup>a</sup> Data refer to compounds desorbed in the temperature range 92-138 K;

These data enabled us to describe the main processes taking place on the acetaldehyde ice. In detail, UV radiation (photons with energies ranging from 4-6 eV) can promote the dissociation of the CH<sub>3</sub>-CHO bond (bond dissociation energy = 3.2 eV for the reaction CH<sub>3</sub>-CHO → CH<sub>3</sub> + CHO) and

resulting in the formation of the methyl ( $\text{CH}_3$ ,  $m/z$  15) and formyl ( $\text{HCO}$ ,  $m/z$  29) radicals.

The first one may undergo hydrogen addition, resulting in methane ( $\text{CH}_4$ ,  $m/z$  16) formation, whereas the second one may undergo hydrogen addition, resulting in the formation of formaldehyde ( $\text{H}_2\text{CO}$ ,  $m/z$  29), or can recombine with the hydroxyl radicals generated by the photodissociation of water forming formic acid ( $\text{HCOOH}$ ,  $m/z$  46). In any case, no significant signal was observed beyond  $m/z$  50.



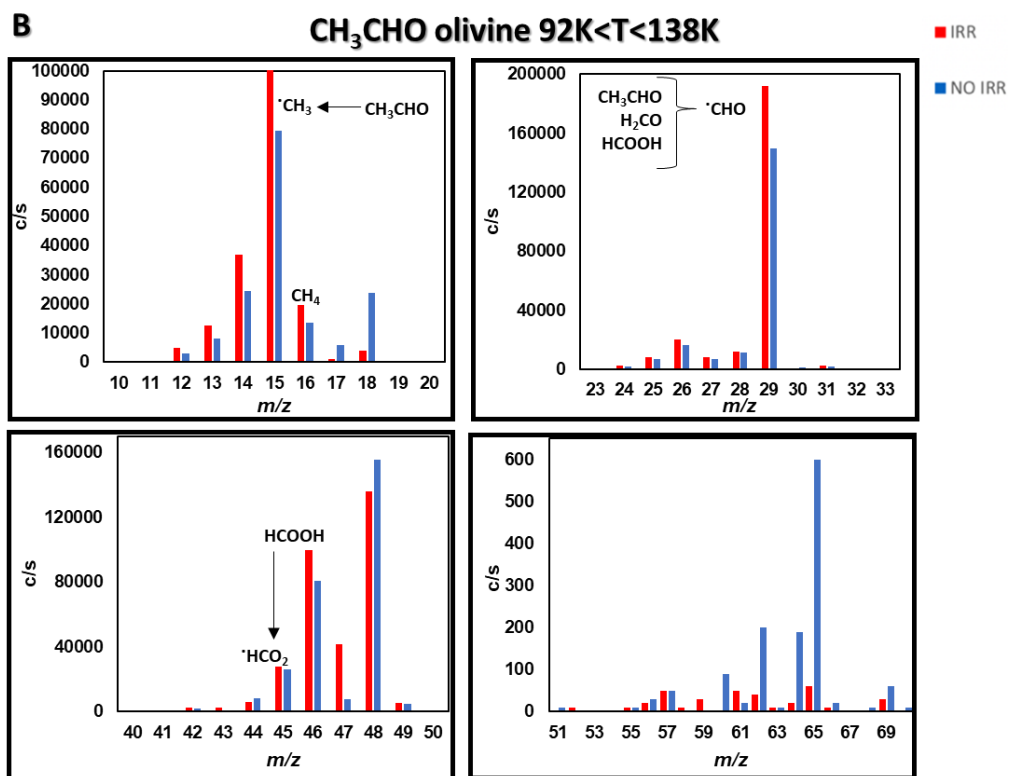


**Figure 6** | Expanded regions of main clusters of mass spectra registered in the range  $m/z$  1-70 for experiments carried out on acetaldehyde ice condensed on the bare cold finger (panel A) or on olivine (panel B). Data refer to compounds desorbed in the temperature range 92-138 K. Red bars refer to experiments carried out on irradiated ices, blue bars refer to experiments carried out on non-irradiated ices.

**Table 2** | Tentative assignments of the main peaks detected in the mass spectra of acetaldehyde ice deposited on bare cold finger or on olivine grains after UV irradiation.

UV irradiation CH <sub>3</sub> COH ice <sup>a</sup>				
<i>m/z</i>	Elemental composition	Proposed molecular species	Bare finger	Olivine grains
			Name	
2	H <sub>2</sub>	H <sub>2</sub>	Hydrogen (molecular)	
16	CH <sub>4</sub>	CH <sub>4</sub>	Methane	
29, 15	C <sub>2</sub> H <sub>4</sub> O	CH <sub>3</sub> COH	Acetaldehyde	
29	CH <sub>2</sub> O	H <sub>2</sub> CO		Formaldehyde
46, 45, 29	CH <sub>2</sub> O <sub>2</sub>	HCOOH		Formic acid
48	CH <sub>4</sub> O <sub>2</sub>	CH <sub>2</sub> (OH) <sub>2</sub>	Methanediol	

<sup>a</sup>Mass peaks have been assigned based on the mass spectra reported in the NIST Chemistry Web Book.

### 3.2.1.2 Pure acetonitrile ice

Figure 7 shows the thermal desorption profile of the acetonitrile ice with (dashed lines) or without (continuous lines) UV irradiation.

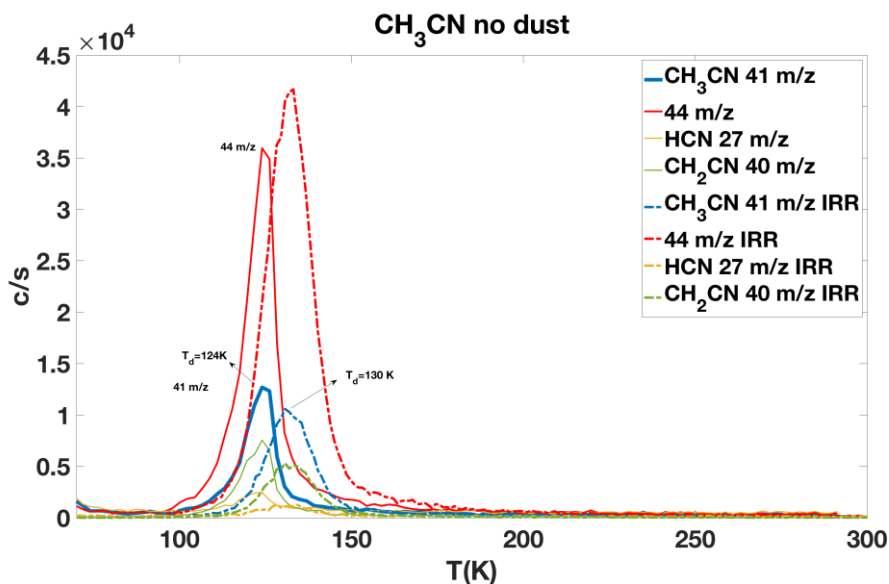


**Figure 7** | TPD curves at 41  $m/z$  (blue curves -  $\text{CH}_3\text{CN}$ ), 44  $m/z$  (red curves – a possible interpretation for this 44  $m/z$  signal is that it could be associated with the cracking in the mass spectrometer of ethylamine  $\text{CH}_3\text{-CH}_2\text{-NH}_2$  which presence could be due to acetonitrile hydrogenation), 40  $m/z$  (green curves -  $\text{CH}_2\text{CN}$ ), and 27  $m/z$  (yellow curves -  $\text{HCN}$ ) before (continuous curves) and after (dashed curves) 8 hours of UV irradiation.

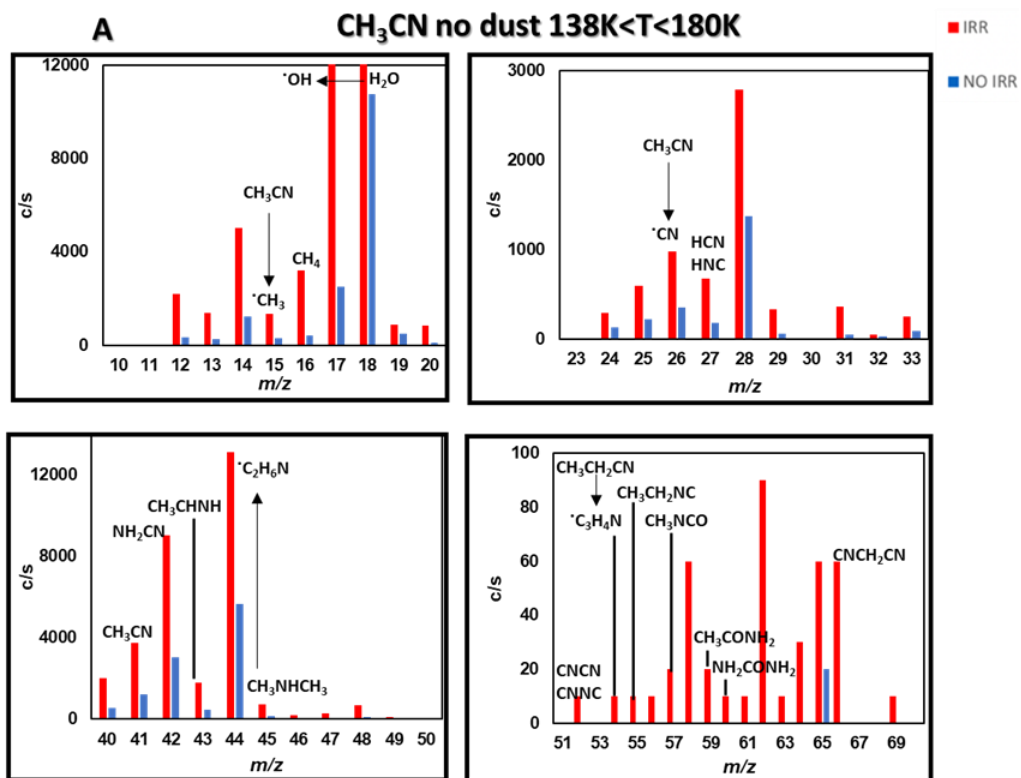
In the latter case, four peaks centered at 124 K were clearly detected: the more intense associated with a  $m/z$  value of 44 ascribable to dimethylamine ( $\text{CH}_3\text{NHCH}_3$ ) deriving from the hydrogenation of acetonitrile,<sup>123,124</sup> then the other ones relative to acetonitrile ( $m/z$  41) and to the  $\text{CH}_2\text{CN}$  radical ( $m/z$  40) and to  $\text{HCN}$  ( $m/z$  27), both deriving from the fragmentation of acetonitrile. After UV irradiation, the same four peaks associated with  $m/z$  41, 44, 40, and 27 were detected but centered at a higher desorption temperature (130 K) with respect to the non-irradiated ice. Also for the acetonitrile ice the mass spectra in the  $m/z$  1-300 range were recorded during the thermal desorption, both in

the non-irradiated and irradiated cases. We selected data in the 138-180 K temperature range (Figure 8, Table 3) where we observed the higher signal intensities.

**Table 3** | Mass spectra data registered for pure CH<sub>3</sub>CN ices deposited on bare cold finger or on olivine grains with or without UV irradiation. Only main clusters around  $m/z$  15, 29, 44 and the most significant peaks above  $m/z$  50 are reported. Among these, only values with an intensity of at least 60 c/s are reported.

$m/z$	Peak Intensity (c/s)				$m/z$	Peak Intensity (c/s)			
	CH <sub>3</sub> CN <sup>b</sup> <td></td>								
	Bare finger		Olivine grains			Bare finger		Olivine grains	
	NO UV	UV	NO UV	UV		NO UV	UV	NO UV	UV
15	1·10 <sup>2</sup>	1·10 <sup>3</sup>	3·10 <sup>2</sup>	1·10 <sup>3</sup>	40	6·10 <sup>2</sup>	2·10 <sup>3</sup>	--	--
16	4·10 <sup>2</sup>	3·10 <sup>3</sup>	5·10 <sup>2</sup>	1·10 <sup>3</sup>	41	1·10 <sup>3</sup>	4·10 <sup>3</sup>	7·10 <sup>2</sup>	5·10 <sup>3</sup>
17	3·10 <sup>3</sup>	5·10 <sup>3</sup>	2·10 <sup>3</sup>	2·10 <sup>3</sup>	42	3·10 <sup>3</sup>	9·10 <sup>3</sup>	1·10 <sup>3</sup>	1·10 <sup>4</sup>
18	1·10 <sup>3</sup>	2·10 <sup>4</sup>	8·10 <sup>3</sup>	1·10 <sup>4</sup>	43	4·10 <sup>2</sup>	2·10 <sup>3</sup>	3·10 <sup>2</sup>	4·10 <sup>3</sup>
26	4·10 <sup>2</sup>	1·10 <sup>3</sup>	2·10 <sup>2</sup>	1·10 <sup>3</sup>	44	6·10 <sup>3</sup>	1·10 <sup>4</sup>	2·10 <sup>3</sup>	2·10 <sup>4</sup>
27	2·10 <sup>2</sup>	7·10 <sup>2</sup>	2·10 <sup>2</sup>	1·10 <sup>3</sup>	45	2·10 <sup>2</sup>	7·10 <sup>2</sup>	1·10 <sup>2</sup>	7·10 <sup>2</sup>
28	1·10 <sup>3</sup>	3·10 <sup>3</sup>	6·10 <sup>2</sup>	4·10 <sup>3</sup>	46	--	2·10 <sup>2</sup>	90	4·10 <sup>2</sup>
29	--	3·10 <sup>2</sup>	3·10 <sup>2</sup>	5·10 <sup>2</sup>	48	2·10 <sup>2</sup>	7·10 <sup>2</sup>	2·10 <sup>2</sup>	2·10 <sup>3</sup>
31	--	4·10 <sup>2</sup>	--	3·10 <sup>2</sup>	50	--	--	--	1·10 <sup>2</sup>
32	--	--	--	1·10 <sup>2</sup>	62	--	90	--	1·10 <sup>2</sup>
33	--	3·10 <sup>2</sup>	3·10 <sup>2</sup>	3·10 <sup>2</sup>	65	--	65	--	2·10 <sup>2</sup>

<sup>b</sup> Data refer to compounds desorbed in the temperature range 138-180 K;



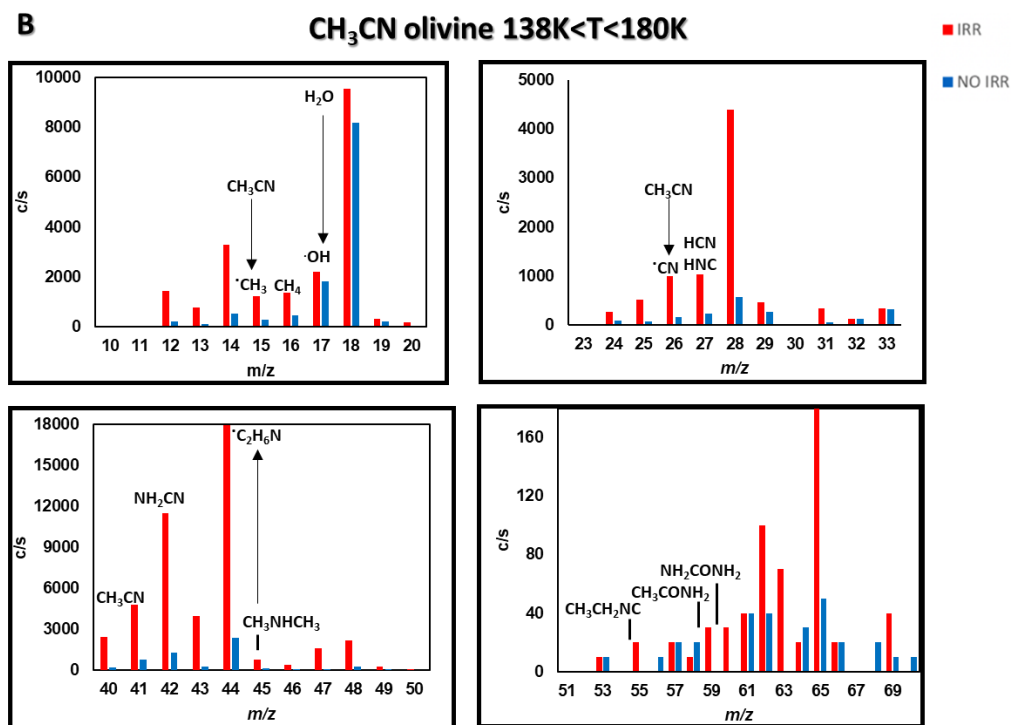


**Figure 8** | Mass spectra registered in the range  $m/z$  1-70 for experiments carried out on acetonitrile ice condensed on the bare cold finger (panel A) or on olivine (panel B). Expanded regions are reported in the insights. Data refer to compounds desorbed in the temperature range 138-180 K. Red bars refer to experiments carried out on irradiated ices, blue bars refer to experiments carried out on non-irradiated ices.

Main peaks detected were assigned to methane ( $\text{CH}_4$ ,  $m/z$  16) and ethane ( $\text{CH}_3\text{CH}_3$ ,  $m/z$  28), deriving from radical recombination processes, ethaneimine ( $\text{CH}_3\text{CH}=\text{NH}$ ,  $m/z$  43) and dimethylamine ( $\text{CH}_3\text{NHCH}_3$ ,  $m/z$  45, 44), deriving from hydrogen addition processes, and cyanamide ( $\text{NH}_2\text{CN}$ ,  $m/z$

42), deriving from both hydrogen addition and radical recombination processes (Figure 8 and Table 4).

**Table 4** | Tentative assignments of the main peaks detected in the mass spectra of acetonitrile ice deposited on the bare cold finger or on olivine grains after UV irradiation.

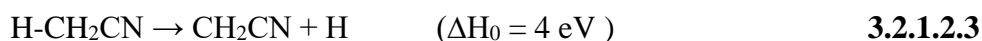
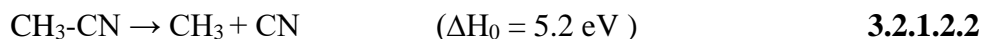
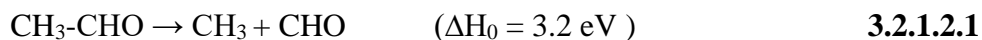
UV irradiation CH <sub>3</sub> CN ice <sup>a</sup>				
<i>m/z</i>	Elemental composition	Proposed molecular species	Bare finger	Olivine grains
			Name	
2	H <sub>2</sub>	H <sub>2</sub>	Hydrogen (molecular)	
16	CH <sub>4</sub>	CH <sub>4</sub>	Methane	
27	HCN	HCN/HNC	Hydrogen cyanide/Hydrogen isocyanide	
41	C <sub>2</sub> H <sub>3</sub> N	CH <sub>3</sub> CN/CH <sub>3</sub> NC	Acetonitrile/Methyl isocyanide	
42	CH <sub>2</sub> N <sub>2</sub>	NH <sub>2</sub> CN	Cyanamide	
43 <sup>b</sup>	C <sub>2</sub> H <sub>5</sub> N	CH <sub>3</sub> CHNH	Ethaneimine	
45,	C <sub>2</sub> H <sub>7</sub> N	CH <sub>3</sub> NHCH <sub>3</sub>	Dimethylamine	
44 <sup>b</sup>				
52	C <sub>2</sub> N <sub>2</sub>	CNCN/CNNC	Cyanogen/isocyanogen	
54	C <sub>3</sub> H <sub>5</sub> N	CH <sub>3</sub> CH <sub>2</sub> CN	Propionitrile	
55	C <sub>3</sub> H <sub>5</sub> N	CH <sub>3</sub> CH <sub>2</sub> NC	Ethyl isocyanide	
57	C <sub>2</sub> H <sub>3</sub> NO	CH <sub>3</sub> NCO	Methyl isocyanate	
59	C <sub>2</sub> H <sub>5</sub> NO	CH <sub>3</sub> CONH <sub>2</sub>		Acetamide
60,	CH <sub>4</sub> N <sub>2</sub> O	NH <sub>2</sub> CONH <sub>2</sub>	Urea	
44,				
17				
60,	C <sub>2</sub> H <sub>4</sub> O <sub>2</sub>	CH <sub>3</sub> COOH	Acetic acid	
43				
66	C <sub>2</sub> H <sub>2</sub> N <sub>2</sub>	CNCH <sub>2</sub> CN	Malononitrile	

<sup>a</sup>Mass peaks have been assigned based on the mass spectra reported in the NIST Chemistry Web Book. <sup>b</sup>Mass peak assigned based on Bulak et al.<sup>125</sup>

All these signals proved to be more intense after UV irradiation and when carried out at the interface of olivine grains.

By comparing the peaks detected from acetonitrile and acetaldehyde ices, is evident that the intensities in the first case were significantly lower (up to two orders of magnitude).

This suggested that acetonitrile has a lower ionization cross-section than acetaldehyde. In fact, the signals in the acetaldehyde mass spectra are higher because a larger ionization cross-section allows for the ionization of more molecules, resulting in a larger signal. Indeed, in the case of acetonitrile, the relative intensity of  $m/z$  41 peak with respect to  $m/z$  15 is greater than the relative intensity of  $m/z$  44 with respect to  $m/z$  15 of acetaldehyde. This evidence suggests that acetonitrile is more stable than acetaldehyde,<sup>126</sup> which can be explained by the higher values of bond dissociation energy measured for  $\text{CH}_3\text{CN}$ ,<sup>127</sup> as reported in the following equations:



The dissociation of acetonitrile leads to the formation methyl ( $\text{CH}_3$ ,  $m/z$  15), cyano ( $\text{CN}$ ,  $m/z$  26), and cyanomethyl ( $\text{CH}_2\text{CN}$ ,  $m/z$  40) radicals. The methyl radical can recombine with itself to form ethane ( $\text{CH}_3\text{CH}_3$ ,  $m/z$  28), or can recombine with cyano radicals to form methyl isocyanide ( $\text{CH}_3\text{NC}$ ,  $m/z$  41). The methyl and cyano radicals can recombine with hydrogen to form methane ( $\text{CH}_4$ ,  $m/z$  16), hydrogen cyanide/hydrogen isocyanide ( $\text{HCN}/\text{HNC}$ ,  $m/z$  27). The cyano radical can recombine with itself to form cyanogen/isocyanogen ( $\text{CNCN}/\text{CNNC}$ ,  $m/z$  52) or with the cyanomethyl radical to form malononitrile

( $\text{CNCH}_2\text{CN}$ ,  $m/z$  66). Hydrogen addition can result in the formation of ethaneimine ( $\text{CH}_3\text{CH}=\text{NH}$ ,  $m/z$  43) and dimethylamine ( $\text{CH}_3\text{NHCH}_3$ ,  $m/z$  45, 44) from acetonitrile and methyl isocyanide. By combined hydrogen addition and radical recombination processes cyanamide ( $\text{NH}_2\text{CN}$ ,  $m/z$  42) can be formed.

### 3.2.1.3 Ice mixture $\text{CH}_3\text{CN}:\text{CH}_3\text{COH}$ (1:6)

The thermal desorption of the binary ice mixture composed by  $\text{CH}_3\text{CN}:\text{CH}_3\text{COH}$  (1:6) from the bare cold finger is reported in Figure 9.

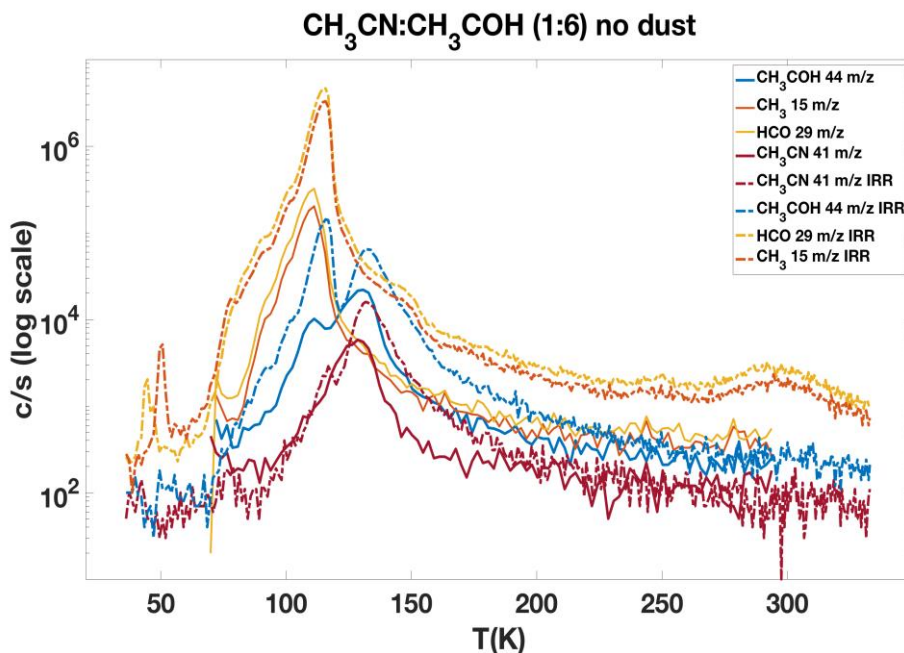


**Figure 9** | TPD curves at  $m/z$  44 (blue curves), 41 (bordeaux curves), 29 (yellow curves), and 15 (orange curves) before (continuous curves) and after (dashed curves) 8 hours of UV irradiation.

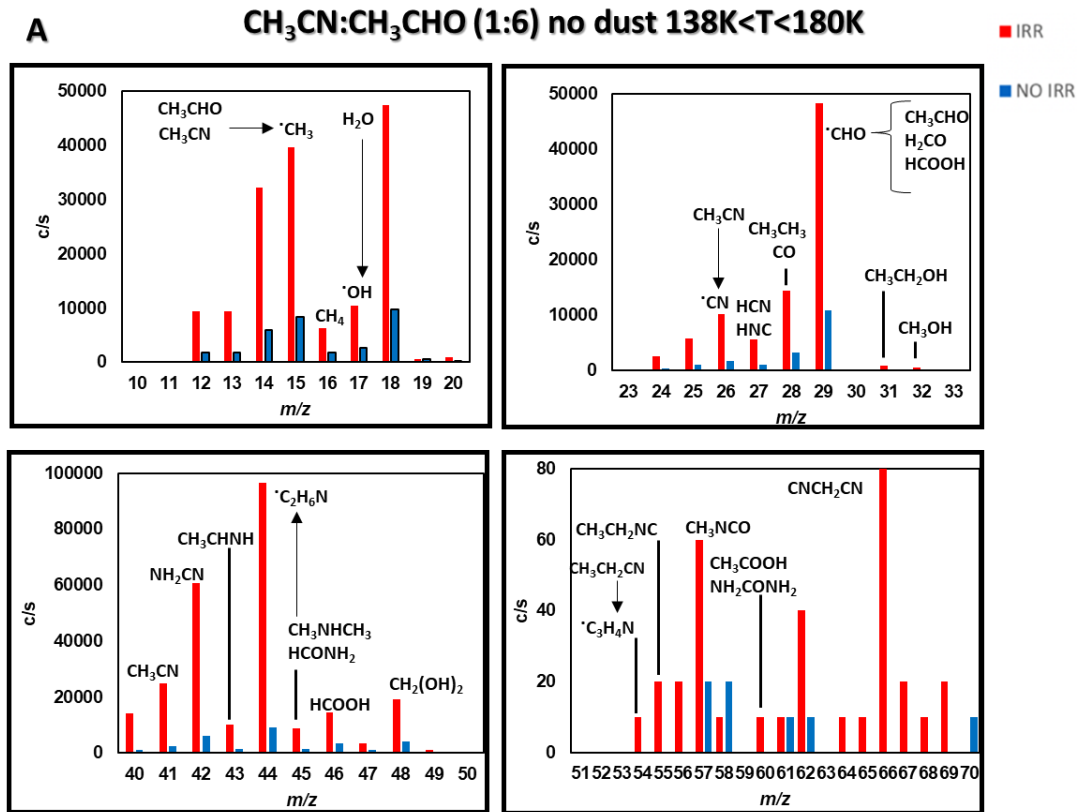
The TPD curves at  $m/z$  44 revealed the presence of two peaks, one at around 100 K (the temperature of sublimation for acetaldehyde) and a second one at around 120 K. A peak centered at 100 K was also visible in the TPD curves of the two acetaldehyde radicals HCO ( $m/z$  29 - yellow curves) and CH<sub>3</sub> ( $m/z$  15 - orange curves), while acetonitrile ( $m/z$  41 - bordeaux curves) had a peak centered at 120 K. The TPD curves of the irradiated mixture show that the desorption temperatures did not change after irradiation, but the curves are wider due to the convolution of multiple desorption contributions that occurred over a wider temperature range.

During thermal desorption, we recorded the entire mass spectrum in the  $m/z$  range of 1 to 300. Figure 10 and Table 5 summarize selected data collected in the 92 - 180 K temperature range, which covers the temperature desorption range of both acetaldehyde and acetonitrile. Table 5 describe the desorption of a CH<sub>3</sub>CN:CH<sub>3</sub>COH (1:6) mixture from a bare cold finger and olivine grains, respectively.

**Table 5** | Mass spectra data registered for CH<sub>3</sub>CN:CH<sub>3</sub>COH (1:6) ice mixtures deposited on bare cold finger or on olivine grains with or without UV irradiation. Only main clusters around  $m/z$  15, 29, 44 and the most significant peaks above  $m/z$  50 are reported. Among these, only values with an intensity of at least 60 c/s are reported.

$m/z$	Peak Intensity (c/s)				$m/z$	Peak Intensity (c/s)			
	CH <sub>3</sub> CN:CH <sub>3</sub> COH (1:6) <sup>c</sup>								
	Bare finger		Olivine grains			Bare finger		Olivine grains	
	NO UV	UV	NO UV	UV		NO UV	UV	NO UV	UV
<b>15</b>	6·10 <sup>4</sup>	2·10 <sup>5</sup>	5·10 <sup>3</sup>	1·10 <sup>5</sup>	<b>40</b>	1·10 <sup>3</sup>	1·10 <sup>4</sup>	1·10 <sup>2</sup>	2·10 <sup>3</sup>
<b>16</b>	9·10 <sup>3</sup>	3·10 <sup>4</sup>	7·10 <sup>3</sup>	2·10 <sup>4</sup>	<b>41</b>	2·10 <sup>3</sup>	3·10 <sup>4</sup>	3·10 <sup>2</sup>	3·10 <sup>3</sup>
<b>17</b>	3·10 <sup>3</sup>	1·10 <sup>4</sup>	7·10 <sup>2</sup>	2·10 <sup>3</sup>	<b>42</b>	6·10 <sup>3</sup>	6·10 <sup>4</sup>	1·10 <sup>3</sup>	8·10 <sup>3</sup>
<b>18</b>	1·10 <sup>4</sup>	5·10 <sup>4</sup>	3·10 <sup>3</sup>	7·10 <sup>4</sup>	<b>43</b>	2·10 <sup>3</sup>	1·10 <sup>4</sup>	1·10 <sup>3</sup>	1·10 <sup>3</sup>
<b>26</b>	1·10 <sup>4</sup>	3·10 <sup>4</sup>	5·10 <sup>3</sup>	2·10 <sup>4</sup>	<b>44</b>	9·10 <sup>3</sup>	1·10 <sup>5</sup>	3·10 <sup>3</sup>	2·10 <sup>4</sup>
<b>27</b>	5·10 <sup>3</sup>	2·10 <sup>4</sup>	4·10 <sup>3</sup>	7·10 <sup>3</sup>	<b>45</b>	2·10 <sup>4</sup>	3·10 <sup>4</sup>	9·10 <sup>3</sup>	1·10 <sup>4</sup>
<b>28</b>	3·10 <sup>4</sup>	3·10 <sup>4</sup>	5·10 <sup>3</sup>	1·10 <sup>5</sup>	<b>46</b>	6·10 <sup>4</sup>	1·10 <sup>5</sup>	3·10 <sup>4</sup>	5·10 <sup>4</sup>
<b>29</b>	1·10 <sup>5</sup>	3·10 <sup>3</sup>	8·10 <sup>4</sup>	1·10 <sup>5</sup>	<b>48</b>	8·10 <sup>4</sup>	2·10 <sup>5</sup>	4·10 <sup>4</sup>	7·10 <sup>4</sup>
<b>30</b>	3·10 <sup>2</sup>	8·10 <sup>2</sup>	3·10 <sup>2</sup>	7·10 <sup>2</sup>	<b>50</b>	3.7·10 <sup>2</sup>	5·10 <sup>2</sup>	1·10 <sup>2</sup>	2·10 <sup>2</sup>
<b>31</b>	1·10 <sup>3</sup>	4·10 <sup>3</sup>	1·10 <sup>3</sup>	2·10 <sup>3</sup>	<b>62</b>	--	--	--	2·10 <sup>2</sup>
<b>32</b>	3·10 <sup>2</sup>	1·10 <sup>3</sup>	2·10 <sup>2</sup>	6·10 <sup>2</sup>	<b>65</b>	--	--	--	2·10 <sup>2</sup>
<b>33</b>	5·10 <sup>3</sup>	6·10 <sup>2</sup>	1·10 <sup>2</sup>	3·10 <sup>2</sup>	<b>82</b>	--	--	--	90

<sup>c</sup> Data refer to compounds desorbed in the temperature range 92-180 K



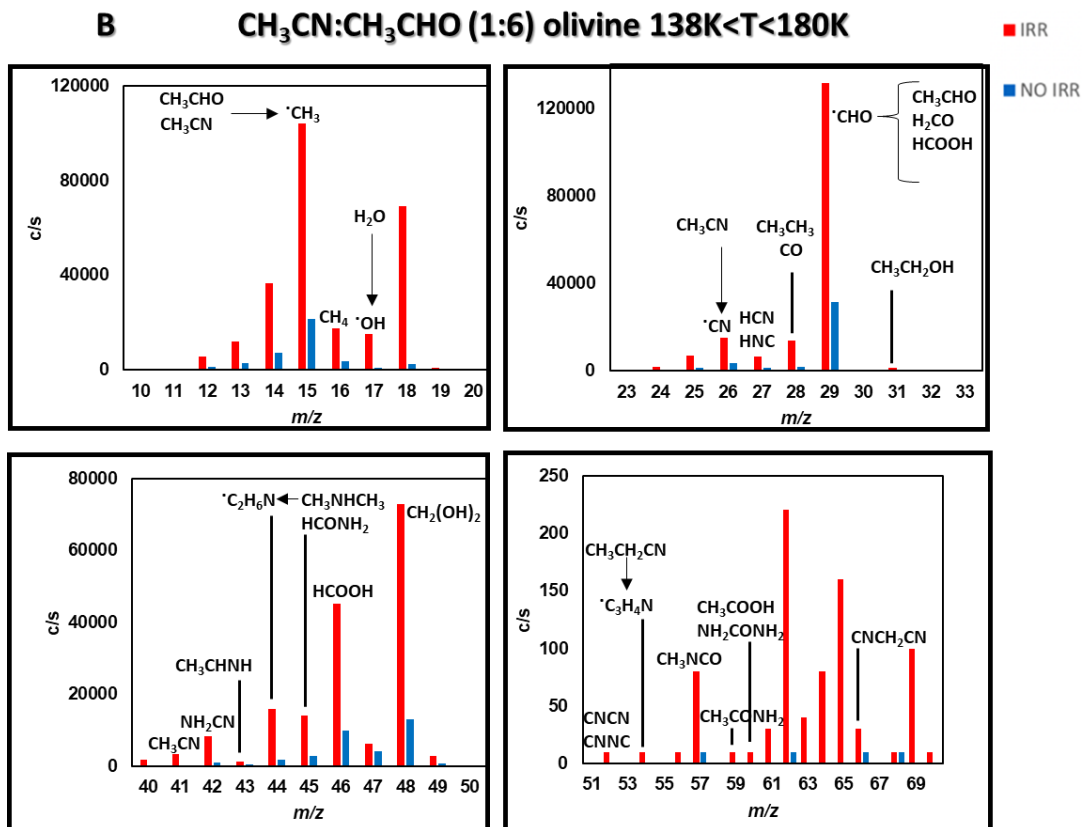


**Figure 10** | Mass spectra registered in the range  $m/z$  1-70 for experiments carried out on  $\text{CH}_3\text{CN}:\text{CH}_3\text{COH}$  (1:6) ice mixture condensed on the bare cold finger (panel A) or on olivine (panel B). Expanded regions are reported in the insights. Data refer to compounds desorbed in the temperature range 92-180 K. Red bars refer to experiments carried out on irradiated ices, blue bars refer to experiments carried out on non-irradiated ices.

The mass spectra recorded after UV irradiation of the  $\text{CH}_3\text{CN}:\text{CH}_3\text{COH}$  (1:6) ice mixture revealed a combination of pure ice results, with main peaks found in four clusters around  $m/z$  15, 29, 44, and 60.

The number of compounds tentatively assigned to the peaks detected in the

mass spectra is quite high, as expected, and includes compounds previously reported for pure ices as well as compounds derived from the crossed recombination of radicals from the acetonitrile and acetaldehyde fragmentation processes (Table 6). This is the case, for example, of formamide ( $\text{HCONH}_2$ ,  $m/z$  45), methyl isocyanate ( $\text{CH}_3\text{NCO}$ ,  $m/z$  57), acetamide ( $\text{CH}_3\text{CONH}_2$ ,  $m/z$  59), and urea ( $\text{NH}_2\text{CONH}_2$ ,  $m/z$  60).

#### 3.2.1.4 Ice mixture $\text{CH}_3\text{CN}:\text{CH}_3\text{COH}:\text{H}_2\text{O}$ (1:1:3)

To simulate a more realistic astrophysical context and considering that water is the most abundant molecule in interstellar ice with abundances up to 1000 and 10000 times greater than acetaldehyde and acetonitrile, respectively,<sup>128,129</sup> we decided to investigate also the icy ternary mixture constituted by  $\text{CH}_3\text{CN}:\text{CH}_3\text{COH}:\text{H}_2\text{O}$  (1:1:3),

In Figure 11 and Table 7, the data relative to the mass spectra registered during the thermal desorption at temperatures ranging from 138 to 220 K are reported. What emerged is that, both on the bare finger and on the olivine grains, UV radiations primarily promoted water molecule dissociation, with the very intense peak at  $m/z$  17 and 18 assigned to OH radicals and  $\text{H}_2\text{O}$ .

In the case of the bare finger, the cluster of peaks in the  $m/z$  23-33 proved to be less intense in the case of UV photoirradiation, whereas higher peaks were detected in the  $m/z$  40-50. The situation was completely opposite when analyzing the mass spectra on olivine grains.

Worthy of note are the assignments to the following peaks: hydrogen cyanide (27  $m/z$ ), ethane (30  $m/z$ ), methanol (32  $m/z$ ), hydroxylamine (33  $m/z$ ), formamide (45  $m/z$ ), formic acid (46  $m/z$ ), cyanamide (42  $m/z$ ).

**Table 6** | Tentative assignments of the main peaks detected in the mass spectra of CH<sub>3</sub>CN:CH<sub>3</sub>COH (1:6) ice mixture deposited on bare cold finger or on olivine grains after UV irradiation.

UV irradiation CH <sub>3</sub> CN:CH <sub>3</sub> COH (1:6) ice mixture <sup>a</sup>				
<i>m/z</i>	Elemental composition	Proposed molecular species	Bare finger	Olivine grains
			Name	
2	H <sub>2</sub>	H <sub>2</sub>	Hydrogen (molecular)	
16	CH <sub>4</sub>	CH <sub>4</sub>	Methane	
27	HCN	HCN/HNC	Hydrogen cyanide/hydrogen isocyanide	
28	C <sub>2</sub> H <sub>6</sub>	CH <sub>3</sub> CH <sub>3</sub>	Ethane	
	CO	CO	Carbon monoxide	
29, 15	C <sub>2</sub> H <sub>4</sub> O	CH <sub>3</sub> COH	Acetaldehyde	
29	CH <sub>2</sub> O	H <sub>2</sub> CO	Formaldehyde	
31	C <sub>2</sub> H <sub>6</sub> O	CH <sub>3</sub> CH <sub>2</sub> OH	Ethanol	
32	CH <sub>4</sub> O	CH <sub>3</sub> OH	Methanol	
41	C <sub>2</sub> H <sub>3</sub> N	CH <sub>3</sub> CN/CH <sub>3</sub> NC	Acetonitrile/Methyl isocyanide	
42	CH <sub>2</sub> N <sub>2</sub>	NH <sub>2</sub> CN	Cyanamide	
43 <sup>b</sup>	C <sub>2</sub> H <sub>5</sub> N	CH <sub>3</sub> CHNH	Ethaneimine	
45, 44 <sup>b</sup>	C <sub>2</sub> H <sub>7</sub> N	CH <sub>3</sub> NHCH <sub>3</sub>	Dimethylamine	
45	CH <sub>3</sub> NO	HCONH <sub>2</sub>	Formamide	
46, 45, 29	CH <sub>2</sub> O <sub>2</sub>	HCOOH	Formic acid	
48	CH <sub>4</sub> O <sub>2</sub>	CH <sub>2</sub> (OH) <sub>2</sub>	Methandiol	
52	C <sub>2</sub> N <sub>2</sub>	CNCN/CNNC	Cyanogen/Isocyanogen	
54	C <sub>3</sub> H <sub>5</sub> N	CH <sub>3</sub> CH <sub>2</sub> CN	Propionitrile	
55	C <sub>3</sub> H <sub>5</sub> N	CH <sub>3</sub> CH <sub>2</sub> NC	Ethyl isocyanide	
57	C <sub>2</sub> H <sub>3</sub> NO	CH <sub>3</sub> NCO	Methyl isocyanate	

<b>59,</b>	$C_2H_5NO$	$CH_3CONH_2$	Acetamide
<b>44</b>		$CH_3NHCHO$	
<b>60,</b>	$CH_4N_2O$	$NH_2CONH_2$	Urea
<b>44,</b>	$C_2H_4O_2$	$CH_3COOH$	Acetic acid
<b>17</b>			
<b>60,</b>			
<b>43</b>			
<b>66</b>	$C_3H_2N_2$	$CNCH_2CN$	Malononitrile

<sup>a</sup>Mass peaks have been assigned based on the mass spectra reported in the NIST Chemistry Web Book. <sup>b</sup>Mass peak assigned based on Bulak et al.<sup>125</sup>

In the case of olivine grains, the peaks detected in the  $m/z$  50-60 range are more intense, implying that the mineral may play a role in promoting the recombination of radicals formed after UV irradiation. A clear example is given by the signal  $m/z$  65, due to the loss of a hydrogen atom by the malononitrile  $CNCH_2CN$ ,  $m/z$  66. This molecule is the result of the recombination of the radicals  $CH_2CN$  ( $m/z$  40) and  $CN$  ( $m/z$  26) due to the photodissociation of acetonitrile.

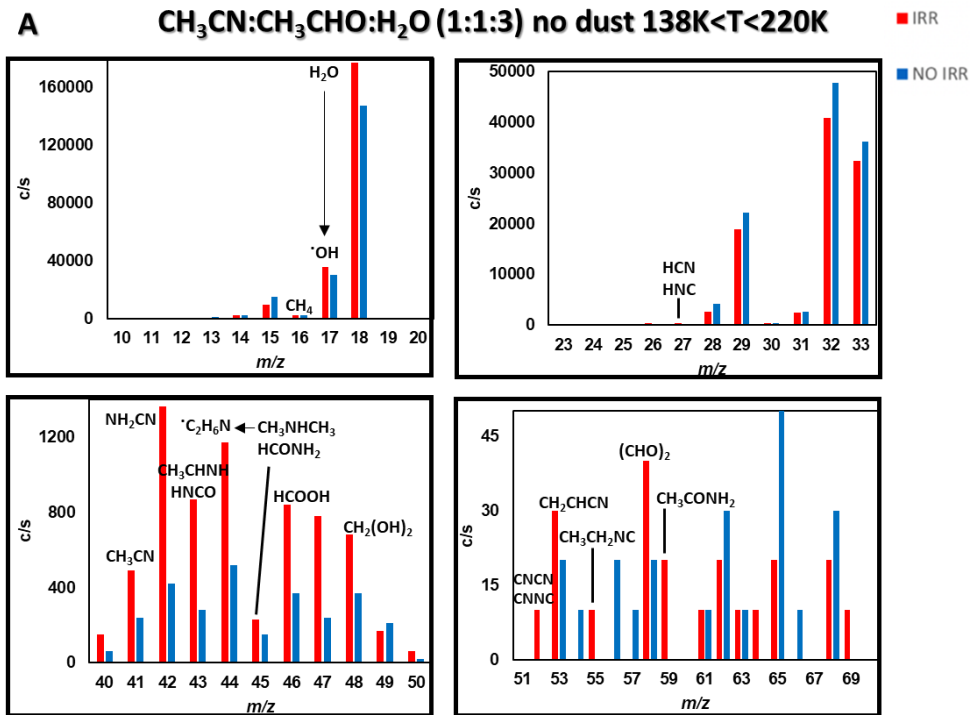
Overall, from the results obtained a complete picture of the complex sequence of processes that occur as a result of the combined action of UV irradiation and olivine grains in the  $CH_3CN:CH_3COH:H_2O$  (1:1:3) ice mixture is reported in Figure 12. Despite its complexity, the scheme clearly shows that the following processes are involved in the UV photoprocessing of the  $CH_3CN:CH_3COH:H_2O$  (1:1:3) ice mixture: 1) bond dissociation; 2) radical recombination; 3) hydrogen addition; and 4) isomerization. Figure 12 shows that, besides the plethora of compounds previously reported in Table 6 and deriving from the reactivity of the pure acetaldehyde and acetonitrile, in the case of the UV irradiation of  $CH_3CN:CH_3COH:H_2O$  (1:1:3) ice mixture we can observe the formation of quite intense peaks deriving from recombination

processes involving the hydroxyl radical: methanol ( $\text{CH}_3\text{OH}$ ,  $m/z$  32), hydroxylamine ( $\text{NH}_2\text{OH}$ ,  $m/z$  33) and acetic acid ( $\text{CH}_3\text{COOH}$ ,  $m/z$  60).

**Table 7** | Mass spectra data registered for  $\text{CH}_3\text{CN}:\text{CH}_3\text{COH}:\text{H}_2\text{O}$  (1:1:3) ice mixtures deposited on bare cold finger or on olivine grains with or without UV irradiation. Only main clusters around  $m/z$  15, 29, 44 and the most significant peaks above  $m/z$  50 are reported. Among these, only values with an intensity of at least 60 c/s are reported.

$m/z$	Peak Intensity (c/s)				$m/z$	Peak Intensity (c/s)			
	$\text{CH}_3\text{CN}:\text{CH}_3\text{COH}:\text{H}_2\text{O}$ (1:1:3) <sup>d</sup>								
	Bare finger		Olivine grains			Bare finger		Olivine grains	
	NO	UV	NO	UV		NO	UV	NO	UV
<b>15</b>	$2 \cdot 10^4$	$9 \cdot 10^3$	$8 \cdot 10^2$	$1 \cdot 10^3$	<b>40</b>	--	$2 \cdot 10^2$	$3 \cdot 10^2$	$3 \cdot 10^2$
<b>16</b>	$2 \cdot 10^3$	$3 \cdot 10^3$	$3 \cdot 10^2$	$1 \cdot 10^3$	<b>41</b>	$2 \cdot 10^2$	$5 \cdot 10^2$	$4 \cdot 10^2$	$5 \cdot 10^2$
<b>17</b>	$3 \cdot 10^4$	$4 \cdot 10^4$	$1 \cdot 10^3$	$7 \cdot 10^3$	<b>42</b>	$4 \cdot 10^2$	$1 \cdot 10^3$	$1 \cdot 10^3$	$9 \cdot 10^2$
<b>18</b>	$1 \cdot 10^5$	$2 \cdot 10^5$	$7 \cdot 10^3$	$3 \cdot 10^4$	<b>43</b>	$3 \cdot 10^2$	$9 \cdot 10^2$	$2 \cdot 10^2$	--
<b>26</b>	$2 \cdot 10^2$	$4 \cdot 10^2$	$2 \cdot 10^2$	$4 \cdot 10^2$	<b>44</b>	$5 \cdot 10^2$	$1 \cdot 10^3$	$2 \cdot 10^3$	$2 \cdot 10^3$
<b>27</b>	$3 \cdot 10^2$	$4 \cdot 10^2$	$2 \cdot 10^2$	$3 \cdot 10^2$	<b>45</b>	$2 \cdot 10^2$	$2 \cdot 10^2$	$2 \cdot 10^2$	$3 \cdot 10^2$
<b>28</b>	$4 \cdot 10^3$	$3 \cdot 10^3$	$7 \cdot 10^2$	$2 \cdot 10^3$	<b>46</b>	$4 \cdot 10^2$	$8 \cdot 10^2$	$5 \cdot 10^2$	$5 \cdot 10^2$
<b>29</b>	$2 \cdot 10^4$	$2 \cdot 10^4$	$1 \cdot 10^3$	$2 \cdot 10^3$	<b>48</b>	$4 \cdot 10^2$	$7 \cdot 10^2$	$7 \cdot 10^2$	$2 \cdot 10^3$
<b>30</b>	--	--	--	--	<b>62</b>	--	--	--	90
<b>31</b>	$3 \cdot 10^3$	$2 \cdot 10^3$	--	--	<b>65</b>	--	--	--	$1 \cdot 10^2$
<b>32</b>	$5 \cdot 10^4$	$4 \cdot 10^4$	$1 \cdot 10^2$	$1 \cdot 10^2$	<b>81</b>	--	--	$1 \cdot 10^2$	--
<b>33</b>	$4 \cdot 10^4$	$3 \cdot 10^4$	$1 \cdot 10^2$	$2 \cdot 10^2$	<b>82</b>	--	--	$3 \cdot 10^2$	--

<sup>d</sup> Data refer to compounds desorbed in the temperature range 138-220 K.



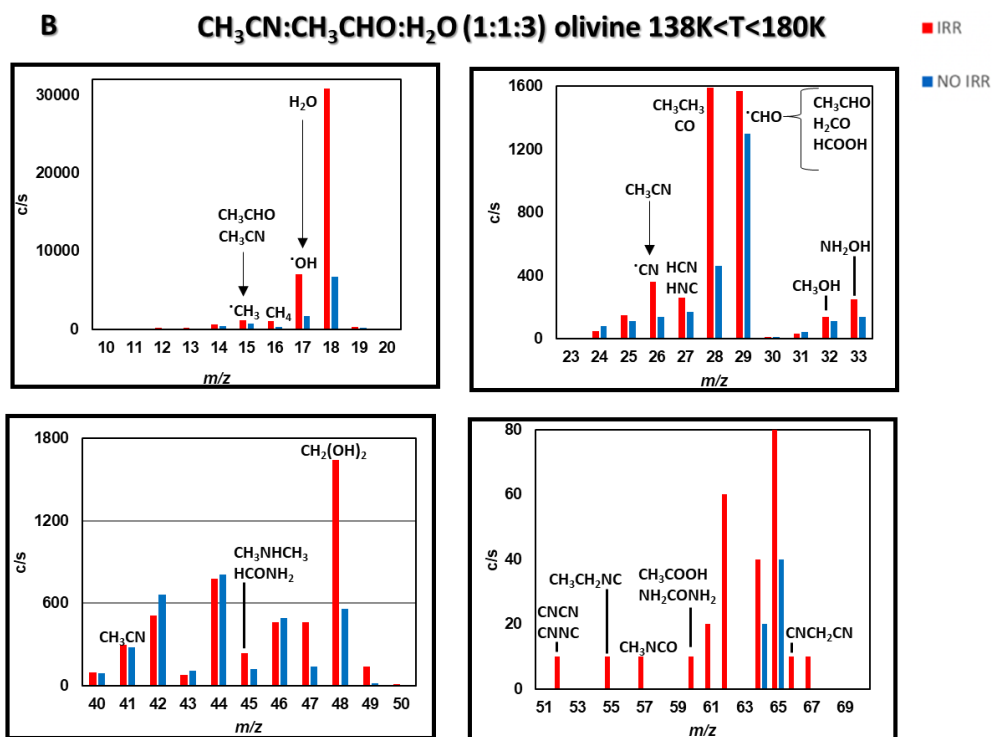


**Figure 11** | Mass spectra registered in the range  $m/z$  1-70 for experiments carried out on  $\text{CH}_3\text{CN}:\text{CH}_3\text{COH}:\text{H}_2\text{O}$  (1:1:3) ice mixture condensed on the bare cold finger (panel A) or on olivine (panel B). Data refer to compounds desorbed in the temperature range 138-220 K. Expanded regions are reported in the insights. Red bars refer to experiments carried out on irradiated ices, blue bars refer to experiments carried out on non-irradiated ices.

Methanol, as shown in the figure, is produced by the recombination of hydroxyl OH and the radical  $\text{CH}_3$ , which can be supplied by both acetaldehyde and acetonitrile. Acetic acid is formed by the recombination of hydroxyl OH and acetaldehyde, whereas hydroxylamine is formed by the recombination of hydroxyl OH and the radical  $\text{NH}_2$ , which is supplied by acetonitrile via hydrogen addition reactions and photodissociation. The formation of

hydroxylamine is of particular interest due to its potential role as amino acid precursor. It was discovered in the interstellar medium for the first time<sup>130</sup> in 2020 and has yet to be discovered in hot corinos and low mass protostars.<sup>131</sup> However, we can infer its presence, from our experiments, in star-forming regions beaten by UV photons in the presence of acetonitrile and silicates. The amount of H<sub>2</sub>O relative to other species in interstellar ices is much higher than the 1:1:3 ratio used in our experiments: through spectroscopic investigations, CH<sub>3</sub>CN has been detected in more than 10 comets and its molecular abundance relative to water is 0.01%,<sup>129</sup> while the molecular abundance of acetaldehyde relative to water in comet Lovejoy is 0.1%.<sup>128,129</sup> Laboratory irradiation experiments on olivine grains with the 1:1:3 mixtures revealed that the observed intense hydroxylamine peaks are caused by the reaction of water and acetonitrile photoproducts. As a result, such a process must take place in space, even though the abundance of water is thousands of times greater than that of molecules like acetonitrile.

The majority of the reaction pathways depicted in Figure 12 have previously been reported in the literature for UV photoprocessing experiments on pure acetonitrile ice, CH<sub>3</sub>CN:H<sub>2</sub>O and CH<sub>3</sub>COH:H<sub>2</sub>O ice mixtures. As a matter of fact, formaldehyde ( $m/z$  30 H<sub>2</sub>CO), methanol ( $m/z$  32 CH<sub>3</sub>OH) and acetic acid ( $m/z$  60 CH<sub>3</sub>COOH) have been previously detected by Kleimeier et al.,<sup>132</sup> whereas methane ( $m/z$  16 CH<sub>4</sub>), hydrogen (iso)cyanide ( $m/z$  27 HCN/HNC), hydroxylamine ( $m/z$  33 NH<sub>2</sub>OH), ethaneimine ( $m/z$  42 CH<sub>3</sub>CHNH), ethylamine ( $m/z$  45 CH<sub>3</sub>CH<sub>2</sub>NH<sub>2</sub>), (iso)cyanogen ( $m/z$  52 CNCN/CNNC), 2-propenitrile ( $m/z$  54 CH<sub>3</sub>CHCN) and ethyl isocyanide ( $m/z$  55 CH<sub>3</sub>CH<sub>2</sub>NC) have been reported by Bulak et al.<sup>125</sup>

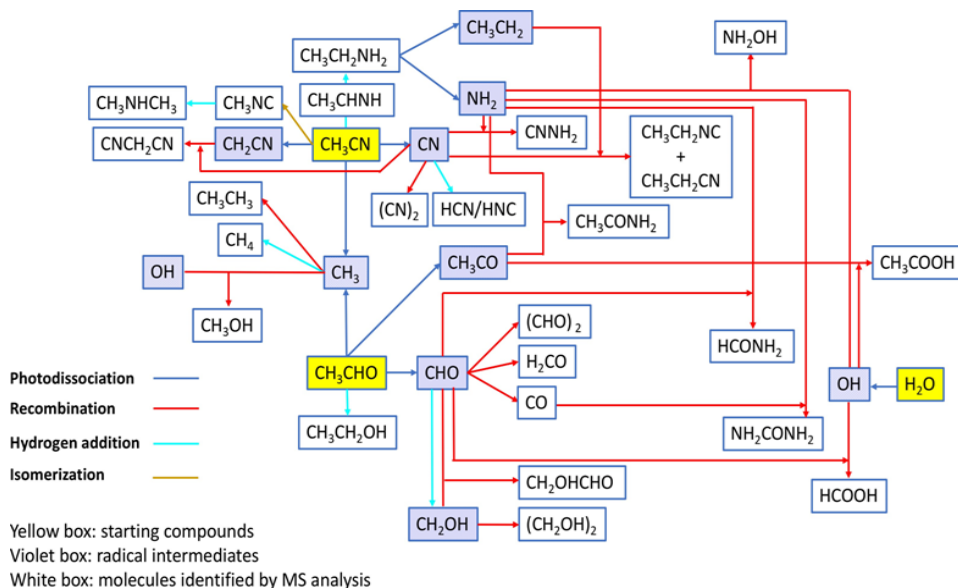


**Figure 12** | Photodissociation, recombination, isomerization, and hydrogen addition reactions involved in the formation of the peaks revealed by the mass analysis of the UV irradiated  $\text{CH}_3\text{CN}:\text{CH}_3\text{COH}:\text{H}_2\text{O}$  (1:1:3) ice mixture on olivine grains.

What emerges for the first time from UV photoprocessing of the ternary ice mixture  $\text{CH}_3\text{CN}:\text{CH}_3\text{COH}:\text{H}_2\text{O}$  (1:1:3) is that, despite the presence of water, cross-recombination processes involving only the radicals generated by the photodissociation of acetaldehyde and acetonitrile can still occur, enhanced by the presence of olivine grains.

These processes resulted in the formation in the solid phase of COMs responsible for the development of prebiotic chemistry, such as formamide ( $\text{HCONH}_2$ ,  $m/z$  44), acetamide ( $\text{CH}_3\text{CONH}_2$ ,  $m/z$  45) and urea ( $\text{NH}_2\text{CONH}_2$ ,  $m/z$  60), as shown in Figure 12. However, in space environments where water condensed on dust is the most abundant molecule, the likelihood that the radicals of the two target molecules interact and recombine giving rise to

prebiotic molecules such as formamide or urea, is lower than in our experiment.

**Table 8** | Tentative assignments of the main peaks detected in the mass spectra of CH<sub>3</sub>CN:CH<sub>3</sub>COH:H<sub>2</sub>O (1:1:3) ice mixture deposited on bare cold finger or on olivine grains after UV irradiation.

UV irradiation CH <sub>3</sub> CN:CH <sub>3</sub> COH:H <sub>2</sub> O (1:1:3) ice mixture <sup>a</sup>				
<i>m/z</i>	Elemental composition	Proposed molecular species	Bare finger	Olivine grains
			Name	
2	H <sub>2</sub>	H <sub>2</sub>	Hydrogen (molecular)	
16	CH <sub>4</sub>	CH <sub>4</sub>	Methane	
18	H <sub>2</sub> O	H <sub>2</sub> O	Water	
27	HCN	HCN/HNC	Hydrogen cyanide/Hydrogen isocyanide	
28	C <sub>2</sub> H <sub>6</sub>	CH <sub>3</sub> CH <sub>3</sub>	Ethane	
	CO	CO	Carbon monoxide	
29, 15	C <sub>2</sub> H <sub>4</sub> O	CH <sub>3</sub> COH	Acetaldehyde	
29	CH <sub>2</sub> O	H <sub>2</sub> CO	Formaldehyde	
32	CH <sub>4</sub> O	CH <sub>3</sub> OH	Methanol	
33	NH <sub>3</sub> O	NH <sub>2</sub> OH	Hydroxylamine	
41	C <sub>2</sub> H <sub>3</sub> N	CH <sub>3</sub> CN/CH <sub>3</sub> NC	Acetonitrile/methyl isocyanide	
42	CH <sub>2</sub> N <sub>2</sub>	NH <sub>2</sub> CN	Cyanamide	
43 <sup>b</sup>	C <sub>2</sub> H <sub>5</sub> N	CH <sub>3</sub> CHNH	Ethaneimine	
	CNOH	HNCO/HOCN/HCNO	Cyanic acid/Isocyanic acid/Fulminic acid	
45, 44 <sup>b</sup>	C <sub>2</sub> H <sub>7</sub> N	CH <sub>3</sub> NHCH <sub>3</sub>	Dimethylamine	
45	CH <sub>3</sub> NO	HCONH <sub>2</sub>	Formamide	
46, 45, 29	CH <sub>2</sub> O <sub>2</sub>	HCOOH	Formic acid	
48	CH <sub>4</sub> O <sub>2</sub>	CH <sub>2</sub> (OH) <sub>2</sub>	Methanediol	
52	C <sub>2</sub> N <sub>2</sub>	CNCN/CNNC	Cyanogen/isocyanogen	

53	C <sub>3</sub> H <sub>3</sub> N	CH <sub>2</sub> CHCN	2-Propenitrile	Ethyl isocyanide
55	C <sub>3</sub> H <sub>5</sub> N	CH <sub>3</sub> CH <sub>2</sub> NC		
57	C <sub>2</sub> H <sub>3</sub> NO	CH <sub>3</sub> NCO	Glyoxal	Methyl isocyanate
58	C <sub>2</sub> H <sub>2</sub> O <sub>2</sub>	CHOCHO		
59, 44	C <sub>2</sub> H <sub>5</sub> NO	CH <sub>3</sub> CONH <sub>2</sub> CH <sub>3</sub> NHCHO		
60, 44, 17	CH <sub>4</sub> N <sub>2</sub> O	NH <sub>2</sub> CONH <sub>2</sub>	Urea	Acetic acid
60, 43	C <sub>2</sub> H <sub>4</sub> O <sub>2</sub>	CH <sub>3</sub> COOH		
66	C <sub>3</sub> H <sub>2</sub> N <sub>2</sub>	CNCH <sub>2</sub> CN		

<sup>a</sup>Mass peaks have been assigned based on the mass spectra reported in the NIST Chemistry Web Book. <sup>b</sup>Mass peak assigned based on Bulak et al. <sup>125</sup>

### 3.2.2 Photo-processing and thermal desorption of naphthalene and quinoline on ice dust grains

#### 3.2.2.1 TPD measurements of naphthalene and quinoline on ice dust grains

To investigate the thermal desorption processes of NAPH and QUIN when deposited as water ice on micrometric grains of silicates, the 1:10000 gas mixtures with water were prepared in the prechamber and then deposited inside the UHV chamber on the cold finger of the cryostat or on olivine grains at 11K. In Figures 13-14 the TPD curves relative to NAPH ( $m/z$  128), QUIN ( $m/z$  129) and water ( $m/z$  18) after the thermal treatment of the ices when deposited on the cold finger (blue traces) or on the olivine grains (red traces) are reported. By means of the fitting of the curves with the Polanyi-Wigner equation, it has been

possible to obtain the desorption temperature ( $T_d$ ) and energy values ( $E_d/K_b$ ); the data are reported in Table 9.

As expected, the curves reported in Figure 13 indicate that the desorption process is strongly influenced by the nature of the substrate on which the ice is deposited. Indeed, if the desorption of molecules occurred directly from the cold finger of the cryostat or from the olivine grains, different profiles were registered with different desorption temperatures.

**Table 9** | Best -fit Values of TPD Curves

	<b>Bare finger</b>		<b>OLIVINE GRAINS</b>	
<b>Molecules</b>	<b>T<sub>des</sub>(fitting) (K)</b>	<b>E<sub>des</sub>/K<sub>b</sub> (K)</b>	<b>T<sub>des</sub>(fitting) (K)</b>	<b>E<sub>des</sub>/K<sub>b</sub> (K)</b>
H <sub>2</sub> O with NAPH or QUIN	166.40±0.05	(2.12 ± 0.07) * 10 <sup>3</sup>	156.6± 0.1	(2.989 ± 0.004) * 10 <sup>3</sup>
			168.5 ± 0.4	(3.154 ± 0.007) * 10 <sup>3</sup>
Pure H <sub>2</sub> O	141.2	(3.80± 0.01) * 10 <sup>3</sup>	128.5	(3.56 ± 0.02) * 10 <sup>3</sup>
			166.4	(4.04 ± 0.06) * 10 <sup>3</sup>
<b>Mixture NAPH:H<sub>2</sub>O</b>				
NAPH	219.70±0.15	(6.0 ± 0.8) * 10 <sup>3</sup>	142.9 ± 0.7	(3.996 ± 0.016) * 10 <sup>3</sup>
<b>Mixture QUIN:H<sub>2</sub>O</b>				
QUIN	176.5± 0.4	(3.3 ± 0.2) * 10 <sup>3</sup>	174.9 ± 0.9	(3.9 ± 0.3) * 10 <sup>3</sup>
			186.3 ± 0.9	(5.158 ± 0.018) * 10 <sup>3</sup>

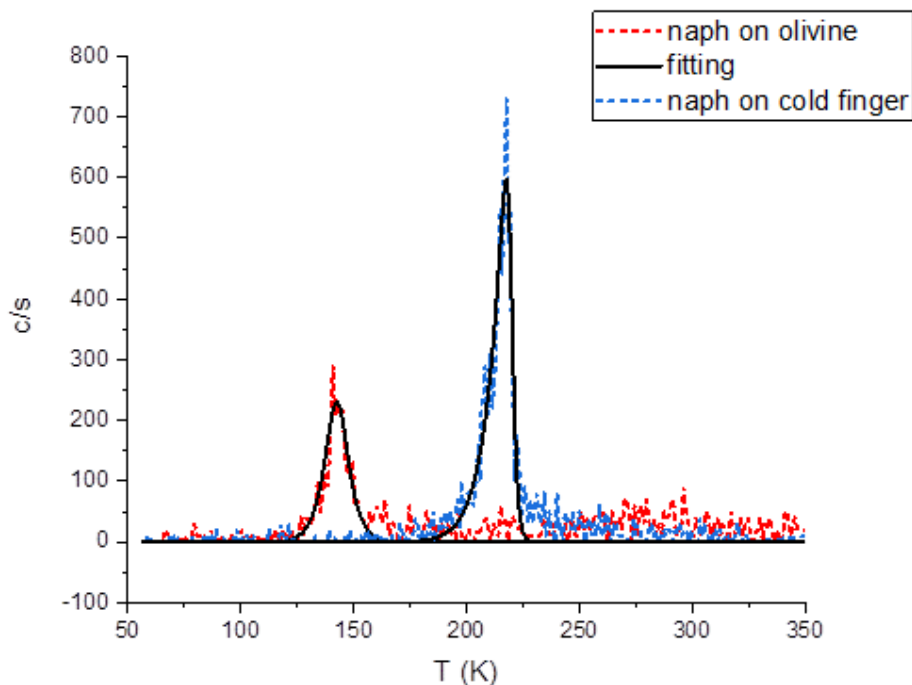


**Figure 13** | TPD curves of naphthalene desorbed from the cold finger of cryostat (blue dotted line) and from olivine (red dotted line). Black lines represent the TPD curves fitted through the Polanyi - Wigner equation.

In Figure 13 the TDP curve relative to the desorption of NAPH from the cold finger of the cryostat (blue trace) revealed a single peak centered at 218 K as intense as 700 c/s. When the same analysis was performed with NAPH deposited on olivine grains (red trace), the desorption process started earlier, at 125 K, and reached a maximum value at 140 K with a peak less intense (300 c/s) than the previous case; moreover, by raising the temperature up to 300 K a sort of NAPH leaching from the substrate was observed, with the mass counts remained always higher than the initial value. This unusual profile indicates

that most of the adsorbed NAPH got stuck inside the grains, being slowly released at high temperatures, whereas a small amount remains adsorbed on the grain surface by establishing weaker  $\pi$ -stacking interactions due to steric hindrance.

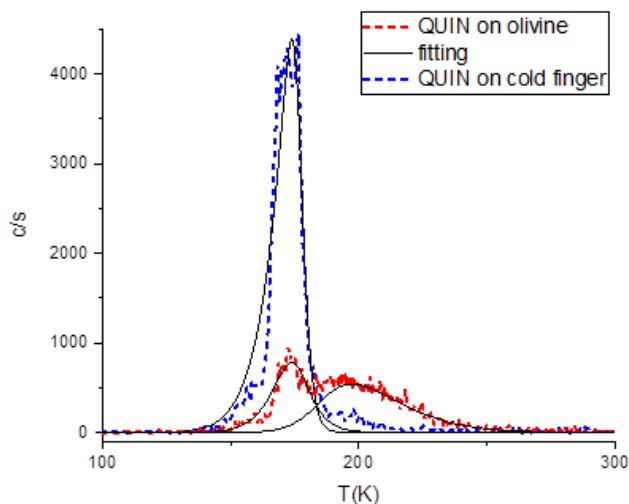


**Figure 14** | TPD curves of quinoline desorbed from the cold finger of cryostat (blue dotted line) and from olivine (red dotted line). Black lines represent the TPD curves fitted through the Polanyi - Wigner equation.

As reported in Figure 14, different profiles were registered when the TPD measurements were performed on QUIN adsorbed on the cold finger of the cryostat (blue trace) or on olivine grains (reed trace). In particular, a quite intense ( $4.4 \times 10^3$  counts/s) single peak centered at 170 K was detected in the first case, whereas two less intense peaks were detected in the second case, centered at 170 K (950 counts/s) and 197 K (620 counts/s). This suggested that large amounts of QUIN were retained by olivine grains by establishing strong interactions.

The comparative analysis of the data obtained from NAPH and QUIN revealed that: a) NAPH can establish more effective interactions with the cold finger with respect to QUIN as denoted by the higher desorption temperatures. This evidence is supported by theoretical calculations previously reported in the literature revealing higher values of absorption energy for NAPH on platinum clusters.<sup>133</sup> b) the interaction of NAPH and QUIN with olivine grains proved to be quite different.

The presence of nitrogen in the QUIN backbone allowed for the formation of hydrogen bonds involving the -SiOH groups of silicates and the water molecules. Moreover, QUIN molecules can interact with each other through  $\pi$ -stacking interactions. Since the first desorption peak was also visible in the absence of olivine grains, it is likely that it is strictly correlated with the breaking of interactions that did not involve the grains, while the second peak, due essentially to the interactions with olivine, was probably ascribable to the molecules situated nearest the dust and retained by the hydrogen bonds. In the case of NAPH, the only interactions with the mineral were ascribable to weak van der Waals bonds through its carbon atoms, while the naphthalene interacted with itself by means of  $\pi$ -stacking interactions. In this case the microporous structure of the grains can become determinant in the entrapment of the molecules inside their structure. Thus, the first peak can account for the desorption of molecules on the surface of olivine grains bonded by means of  $\pi$ -stacking interactions and the second one, less intense, to the desorption of molecules adsorbed deeper inside the mineral.

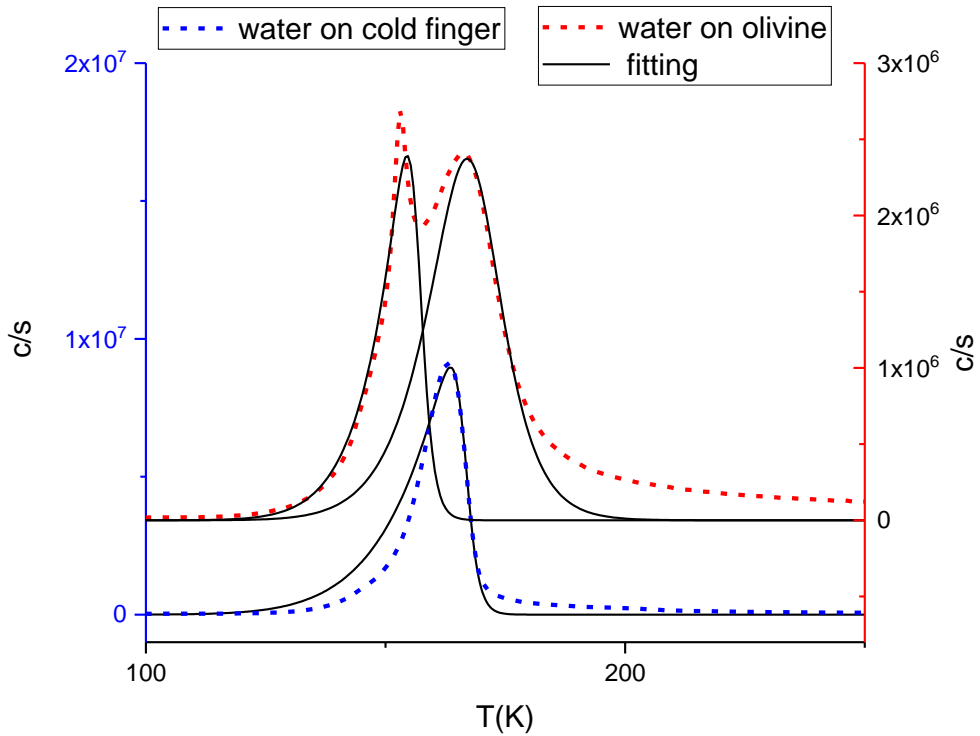


**Figure 15** | TPD curves of water mixed with naphthalene or quinoline desorbed from the cold finger of cryostat (blue dotted line) and from olivine (red dotted line). Black lines represent the TPD curves fitted through the Polanyi - Wigner equation.

The same ices deposited both on the cold finger and on dust grains starting from the 1:10000 gas mixtures of NAPH and water and QUIN and water have been analyzed in terms of water desorption ( $m/z$  18). The TPD curves reported in Figure 15 display a single peak at 166 K ( $8.9 \cdot 10^6$  counts/s) in the case of water desorption from the cold finger, and two peaks at 156 K ( $2.7 \cdot 10^6$  counts/s) and 168 K ( $2.4 \cdot 10^6$  counts/s) in the case of desorption from dust grains.

All these results highlighted that in presence of olivine grains the water molecules were in part adsorbed on the external surface of the mineral in a less effective manner, so desorbed at lower temperatures, and in part trapped inside the vacancies of the grains, therefore desorbed at higher temperatures. A more uniform adsorption type was evident in the case of the cold finger, with a single desorption peak.

The same behaviour was observed when the TPD analysis was carried out on a pure water ice layer deposited on the cold finger or on olivine grains, with a single peak at 141 K registered on the cold finger and two peaks at 128 and 166 K on the olivine grains (Figure 16).

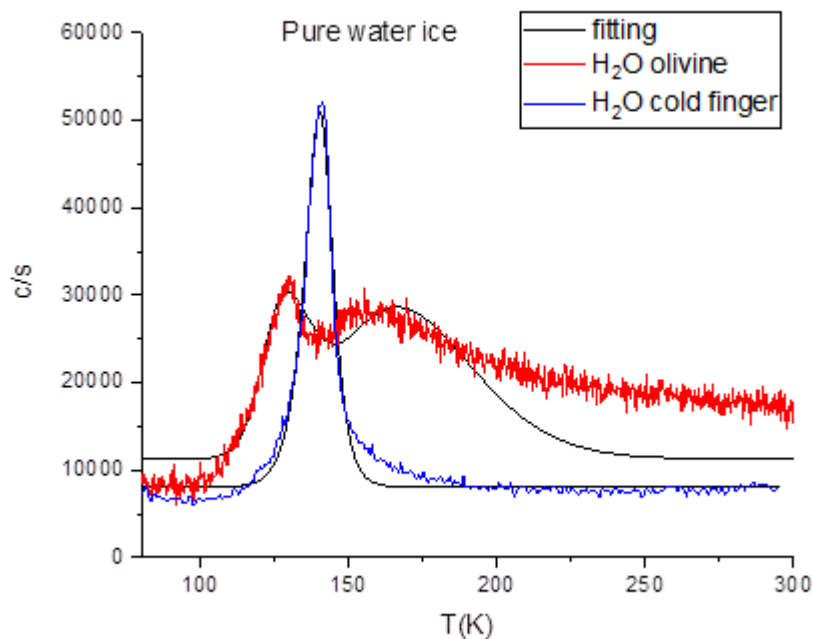


**Figure 16** | TPD curves of pure water ice desorbed from the cold finger of cryostat (blue dotted line) and from olivine (red dotted line). Black lines represent the TPD curves fitted through the Polanyi - Wigner equation.

### 3.2.2.2 UV radiation effects on naphthalene and quinoline adsorbed on cold finger and olivine: mass spectrometry analysis

In this study, the effects of UV radiations on naphthalene and quinoline ice layer deposited on a cold finger or on olivine grains were investigated. By means of mass spectrometry analysis, the structural modifications occurring on the PAH ring system were examined, shedding light on the intricate interplay between UV irradiation and these aromatic compounds.

This exploration contributes valuable data to the understanding of surface-mediated chemical processes and their implications for astrochemical studies.

#### 3.2.2.2.1 Naphthalene

In Figure 17, the mass spectra resulting from the desorption of naphthalene from a cold finger, both before and after exposure to UV irradiation, are shown. Two temperature ranges were selected for analysis: 139-181 K and 181-220 K. Notably, the latter range also corresponds to the desorption temperature of naphthalene. According to the NIST library, the mass spectrum of naphthalene reveals the presence of a main peak centered at  $m/z$  128 and a series of less intense peak clusters centered at  $m/z$  102, 76, 64 and 51.

Comparing the mass spectra obtained before and after the exposure to UV radiations a notable trend emerges: the intensity of almost all the peaks in the  $m/z$  range 50-170 desorbed in the 181-220 K interval of temperature tends to decrease whereas a general increase in the intensity of peaks with lower molecular weight (0-50  $m/z$ ) desorbed in the 139-181 K interval of temperature was observed.

This outcome suggests that naphthalene adsorbed on a cold finger tends to undergo fragmentation in response to UV irradiation.

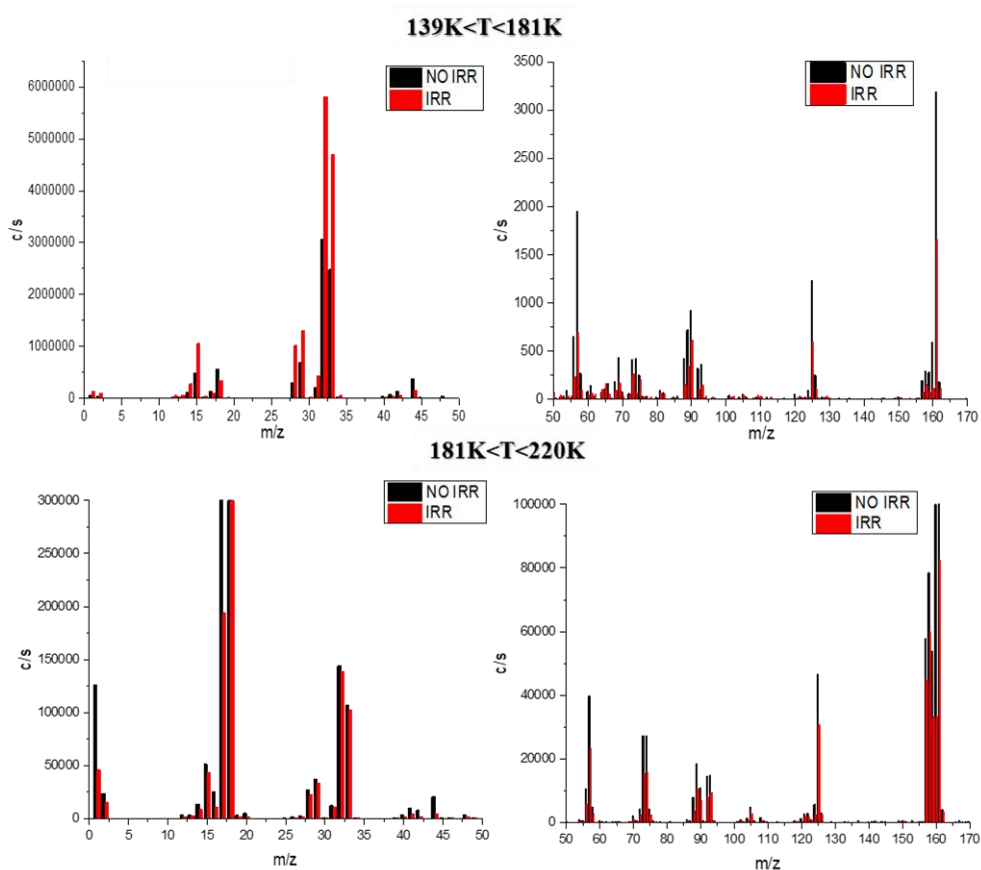


**Figure 17** | Mass spectra registered for experiments carried out on NAPH:H<sub>2</sub>O condensed on the bare cold finger. Data refer to compounds desorbed in the temperature range 139-181K and 181-220 K. Red bars refer to experiments carried out on irradiated ices, black bars refer to experiments carried out on non-irradiated ices.

Figure 18 showed the mass spectra of naphthalene adsorbed on olivine before and after UV irradiation, focusing on three distinct temperature ranges: 139-180 K, 220-259 K, and 259-295 K. In all the spectra is evident a notable increase in the intensity of almost all peaks after exposure to UV irradiation.

A more detailed analysis of the lower temperature range (139-180 K), presumed to correspond to the desorption temperatures of lower molecular weight species, revealed a significant rise in the intensity of peaks with  $m/z$  values between 20 and 100 after UV radiation exposure. This trend continued even with higher molecular weight species when considering elevated temperature ranges. These findings suggest that UV irradiation of naphthalene adsorbed on olivine not only induces molecular fragmentation, as observed on a cold finger, but also stabilizes the newly formed compounds.

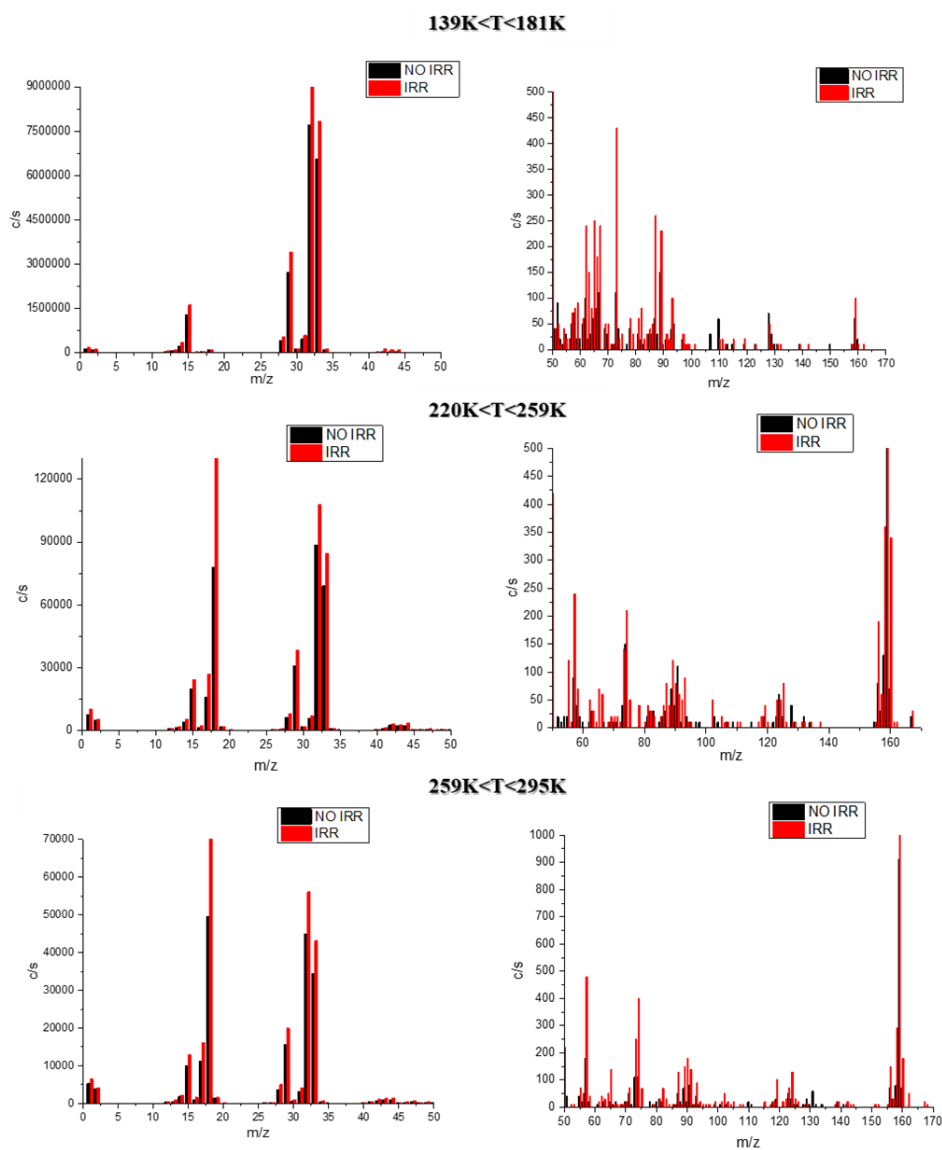


**Figure 18** | Mass spectra registered for experiments carried out on NAPH:H<sub>2</sub>O condensed on olivine dust grains. Data refer to compounds desorbed in the temperature range 139-181K, 220-259 and 259-295K. Red bars refer to experiments carried out on irradiated ices, black bars refer to experiments carried out on non-irradiated ices.

Table 10 shows the data relative to the intensity (counts/seconds) of the peaks detected in the mass spectra of NAPH:H<sub>2</sub>O ice mixtures deposited on bare cold finger or on olivine grains with or without UV irradiation. For the thermal desorption of both substrates, the bare finger and olivine grains, temperatures ranging from 139-180 K are considered.

**Table 10** | Mass spectra data registered for NAPH:H<sub>2</sub>O ice mixtures deposited on bare cold finger with or without UV irradiation. Tentative assignments of the main peaks detected after UV irradiation are provided in the last column.

m/z	Peak Intensity (c/s) naphthalene:water ice		
	Bare Finger		Proposed molecular species
	NO IRR	IRR	
<b>139K&lt;T&lt;180K</b>			
1	6.6 x10 <sup>4</sup>	1.3 x10 <sup>5</sup>	H
2	4.2 x10 <sup>4</sup>	9.5 x10 <sup>4</sup>	H <sub>2</sub>
15	4.8 x10 <sup>5</sup>	1.1 x10 <sup>6</sup>	CH <sub>3</sub>
16	3.9 x10 <sup>4</sup>	6.2 x10 <sup>4</sup>	CH <sub>4</sub>
28	3.1 x10 <sup>5</sup>	1.1 x10 <sup>6</sup>	C <sub>2</sub> H <sub>4</sub> <sup>+</sup> /CO
29	6.8 x10 <sup>5</sup>	1.3 x10 <sup>6</sup>	CHO (Acetaldehyde, formic acid)
32	3.1 x10 <sup>6</sup>	5.8 x10 <sup>6</sup>	CH <sub>3</sub> OH Methanol
33	2.5 x10 <sup>6</sup>	4.7x10 <sup>6</sup>	OOH
34	2.7 x10 <sup>4</sup>	5.3 x10 <sup>4</sup>	H <sub>2</sub> O <sub>2</sub>
128	1.0 x10 <sup>2</sup> *	50*	C <sub>10</sub> H <sub>8</sub> <sup>+</sup> Naphthalene
129	1.5 x10 <sup>2</sup> *	30*	C <sub>10</sub> H <sub>9</sub> <sup>+</sup>

\*180K<T<220K

**Table 11** | Mass spectra data registered for NAPH:H<sub>2</sub>O ice mixtures deposited on olivine grains with or without UV irradiation. Tentative assignments of the main peaks detected after UV irradiation are provided in the last column.

m/z	Peak Intensity (c/s) naphthalene:water ice		
	Olivine grains		Proposed molecular species
	NO IRR	IRR	
	<b>139K&lt;T&lt;180K</b>		
1	1.4 x10 <sup>5</sup>	1.9 x10 <sup>5</sup>	H
2	1.0 x10 <sup>5</sup>	1.3 x10 <sup>5</sup>	H <sub>2</sub>
15	1.3 x10 <sup>6</sup>	1.6 x10 <sup>6</sup>	CH <sub>3</sub>
16	2.6 x10 <sup>4</sup>	3.2 x10 <sup>4</sup>	CH <sub>4</sub>
17	4.7 x10 <sup>4</sup>	5.6 x10 <sup>4</sup>	OH
18	1.1x10 <sup>5</sup>	1.2 x10 <sup>5</sup>	H <sub>2</sub> O
25	2.0 x10 <sup>3</sup>	9.0 x10 <sup>3</sup>	C <sub>2</sub> H <sup>+</sup>
26	2.8 x10 <sup>3</sup>	1.3 x10 <sup>4</sup>	C <sub>2</sub> H <sub>2</sub> <sup>+</sup>
27	3.1 x10 <sup>3</sup>	1.5 x10 <sup>4</sup>	C <sub>2</sub> H <sub>3</sub> <sup>+</sup>
28	4.1 x10 <sup>5</sup>	5.4 x10 <sup>5</sup>	C <sub>2</sub> H <sub>4</sub> <sup>+</sup> /CO
29	2.7 x10 <sup>6</sup>	3.4 x10 <sup>6</sup>	CHO (Acetaldehyde, formic acid)
32	7.7 x10 <sup>6</sup>	9.3 x10 <sup>6</sup>	CH <sub>3</sub> OH Methanol
33	6.6 x10 <sup>6</sup>	7.8 x10 <sup>6</sup>	OOH
34	1.2 x10 <sup>5</sup>	1.5 x10 <sup>5</sup>	H <sub>2</sub> O <sub>2</sub>
39	90	1.7 x10 <sup>2</sup>	C <sub>3</sub> H <sub>3</sub> <sup>+</sup>
44	3.6 x10 <sup>4</sup>	1.2 x10 <sup>5</sup>	CH <sub>3</sub> CHO Acetaldehyde
46	1.6 x10 <sup>3</sup>	2.8 x10 <sup>3</sup>	HCCOH Formic acid
63	20	1.5 x10 <sup>2</sup>	C <sub>3</sub> H <sub>5</sub> <sup>+</sup>
74	70*	1 x10 <sup>2</sup> *	C <sub>6</sub> H <sub>2</sub> <sup>6+</sup>
75	0	30	C <sub>6</sub> H <sub>3</sub> <sup>5+</sup>
78	40	60	C <sub>6</sub> H <sub>6</sub> <sup>2+</sup>
128	70	50	C <sub>10</sub> H <sub>8</sub> <sup>+</sup> Naphthalene
129	30	10	C <sub>10</sub> H <sub>9</sub> <sup>+</sup>
158	1.3 x10 <sup>2</sup> **	3.6 x10 <sup>2</sup> **	Naphthoquinone
160	70**	3.4 x10 <sup>2</sup> **	Dihydroxynaphthalene

\* 180<T<220K

\*\* 220<T<259K

As observed from the Tables 10-11, UV irradiation induces the formation of photo-products resulting from the fragmentation of the water molecule (e.g. OH, OOH, H<sub>2</sub>O<sub>2</sub>) those arising from the fragmentation of naphthalene (e.g. C<sub>2</sub>H<sub>3</sub><sup>+</sup>, C<sub>2</sub>H<sub>2</sub><sup>+</sup>, C<sub>2</sub>H<sub>4</sub><sup>+</sup>, C<sub>3</sub>H<sub>3</sub><sup>+</sup>) and products resulting from the combination of both, such as acetaldehyde, formic acid, methanol, and dihydroxynaphthalene. This effect is more evident when desorption occurs from olivine grains, suggesting the catalytic action of the grain and a more stability of naphthalene on cold finger.

The photostability of naphthalene has been extensively investigated in previous studies employing high-energy electron impact.<sup>134-136</sup> Key findings from these works reveal that the primary dissociation channels of naphthalene upon electronic excitation involve hydrogen or acetylene loss (C<sub>2</sub>H<sub>2</sub><sup>+</sup>). Additionally, signals at  $m/z = 72-78$  were identified, corresponding to a benzene cation and several dehydrogenated forms. Peaks at  $m/z = 39$  amu and  $m/z = 63$  were attributed to species with molecular formulas C<sub>3</sub>H<sub>3</sub><sup>+</sup> and C<sub>5</sub>H<sub>3</sub><sup>+</sup>, respectively.

These outcomes align with those obtained through UV irradiation. Furthermore, the study by Bernstein et al. demonstrated the presence of naphthoquinone and dihydroxynaphthalene following UV photolysis of NAPH in ice at 15K.<sup>137</sup>

This study provides valuable insights into the intricate interplay between UV radiation and naphthalene on olivine surfaces. The dual effect of fragmentation and the generation of larger molecular species underscores the complexity of molecular transformations induced by UV irradiation. Further exploration into the underlying mechanisms promises to contribute to our understanding of surface-mediated chemical processes under UV exposure.

### 3.2.2.2.2 Quinoline

In Figures 19 and 20, the mass spectra resulting from the desorption of quinoline from a cold finger and olivine grains, both before and after exposure to irradiation, are shown. Three temperature ranges were selected for analysis: 139-181 K, 181-220 K, 256-295K. The first one also corresponds to desorption temperature of quinoline.

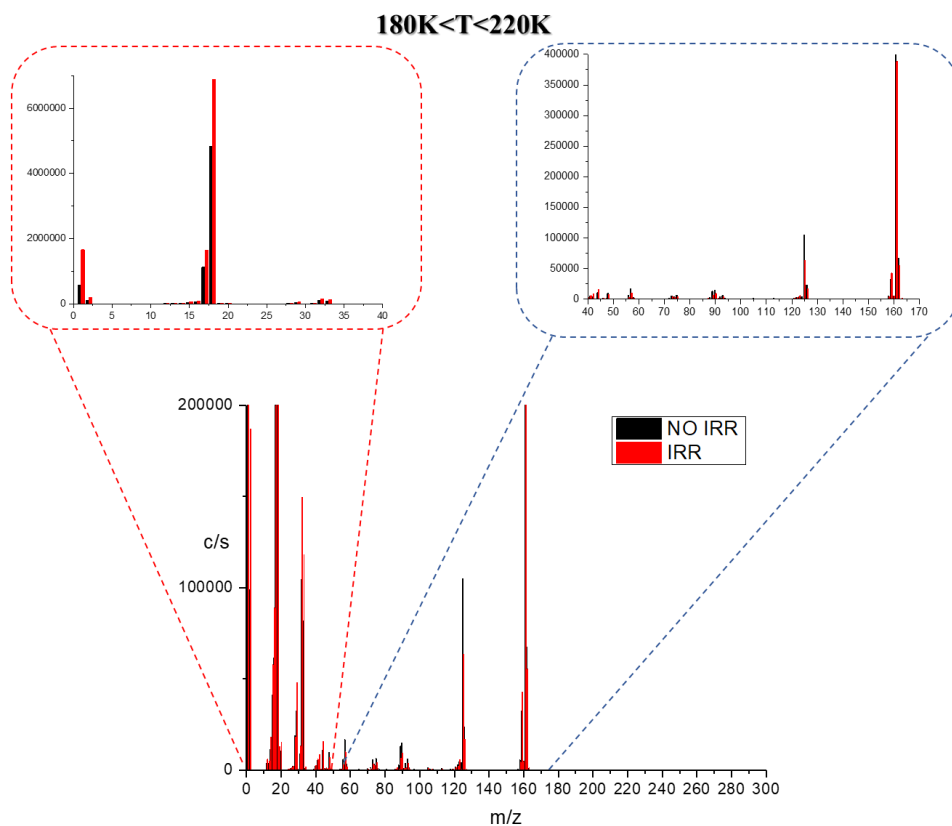


**Figure 19** | Mass spectra registered in the range  $m/z$  1-300 for experiments carried out on QUIN:H<sub>2</sub>O condensed on the bare cold finger. Data refer to compounds desorbed in the temperature range 180-220 K. Red bars refer to

experiments carried out on irradiated ices, black bars refer to experiments carried out on non-irradiated ices.

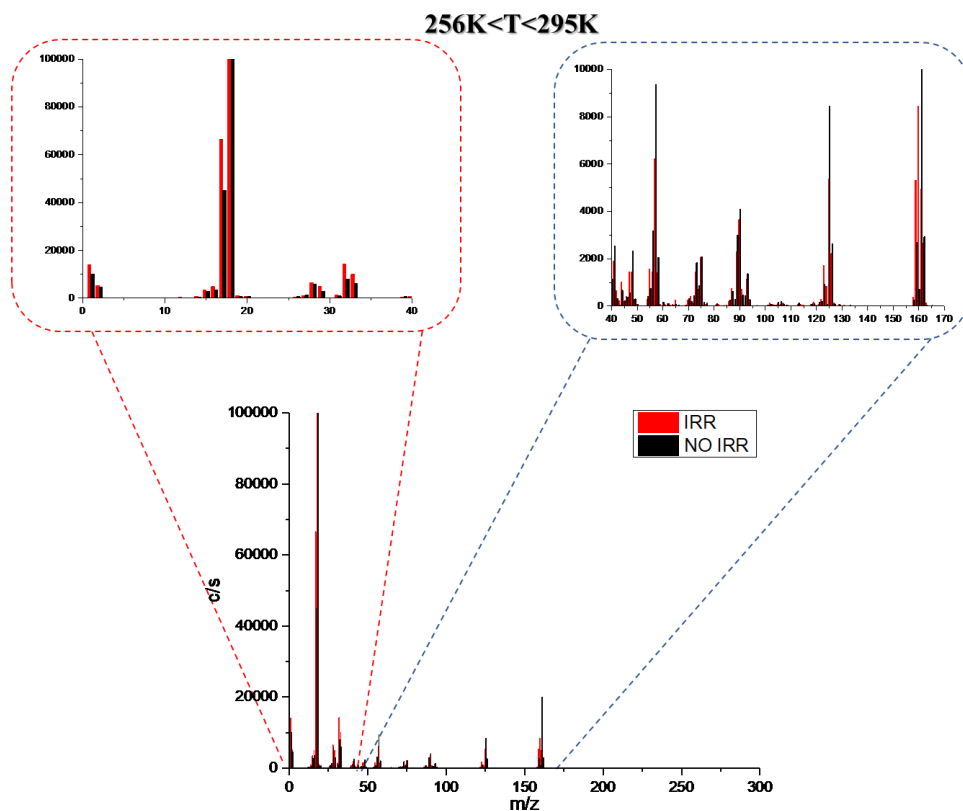


**Figure 20** | Mass spectra registered in the range  $m/z$  1-300 for experiments carried out on QUIN:H<sub>2</sub>O condensed on the olivine dust grains. Data refer to compounds desorbed in the temperature range 256-295 K. Red bars refer to experiments carried out on irradiated ices, black bars refer to experiments carried out on non-irradiated ices.

According to the NIST library, quinoline fragments generate peak clusters with values around 129 $m/z$ , 102 $m/z$ , 76 $m/z$ , and 51 $m/z$ . These peaks, arising from quinoline fragmentation inside the mass spectrometer, are expected in the

temperature range of 139-181 K, consistent with quinoline desorption at approximately 176 K from a cold finger and 176-186 K from olivine. Therefore, the presence of peaks due to new molecules is expected in the temperature range of 181-220 K for desorption from a cold finger and 256-295 K for desorption from olivine grains.

Analysis of the mass spectra obtained during quinoline desorption without irradiation reveals the presence of intense peaks at these temperatures, both on the cold finger and olivine. The notable water content in the ices could be enough to trigger chemical reactions.

Following 8 hours of UV irradiation, a simultaneous decrease in the intensity of peaks with  $m/z$  values greater than 50 and an increase in those with  $m/z$  values less than 50 were observed. This suggests that UV irradiation induced the fragmentation of molecules with  $m/z > 50$  or triggered further reactions leading to the consumption of these species and, consequently, a decrease in the intensity of their peaks. Additionally, the peaks at 159  $m/z$  and 160  $m/z$  exhibited increased intensity after irradiation, while the 161  $m/z$  tended to decrease. Accordingly, the 160  $m/z$  peak was also monitored via TPD, confirming this trend for both the cold finger and olivine (Figure 21).

It is evident that the TPD curve of the 160  $m/z$  peak reaches higher counts within the temperature range consistent with those considered in the mass spectra. Furthermore, it is noteworthy that the TPD curve is significantly broader when the desorption process occurs from olivine compared to the cold finger, suggesting a more gradual release of molecules in the latter case.

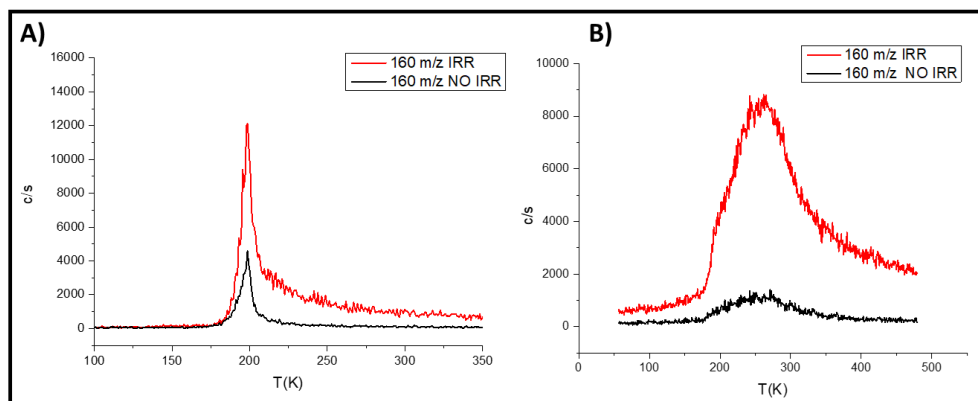


**Figure 21** | The figure shows two experiments: A) TPD desorption from the cold finger and B) TPD desorption from olivine grains. In both experiments, the same amount of quinoline was deposited in the UHV chamber at 11 K. The red curve represents the signal detected at 160 m/z after irradiation, while the black curve represents the signal before irradiation.

Tables 12-13 show the data relative to the mass spectra recorded for QUIN:H<sub>2</sub>O ice mixture deposited on bare cold finger or on olivine grains with or without UV irradiation. For thermal desorption from the bare finger, temperatures ranging from 180 to 220 K were considered, while for thermal desorption from olivine grains, temperatures from 180 to 220 K were considered for 0-50 m/z values, and temperatures from 256 to 295 K for 50-170 m/z values.

**Table 12** | Mass spectra data registered for QUIN:H<sub>2</sub>O ice mixtures deposited on bare cold finger with or without UV irradiation. Tentative assignments of the main peaks detected after UV irradiation was provided in the last column.

m/z	Peak Intensity (c/s) QUIN:water ice		
	NO IRR	IRR	Bare Finger Proposed molecular species
<b>180K&lt;T&lt;220K</b>			
1	5.7x10 <sup>5</sup>	1.7x10 <sup>6</sup>	H
2	9.9x10 <sup>4</sup>	1.9x10 <sup>5</sup>	H <sub>2</sub>
15	4.1x10 <sup>4</sup>	5.8x10 <sup>4</sup>	CH <sub>3</sub>
16	6.1x10 <sup>4</sup>	8.9x10 <sup>4</sup>	CH <sub>4</sub>
17	1.1x10 <sup>6</sup>	1.6x10 <sup>6</sup>	OH/NH <sub>3</sub>
18	4.8x10 <sup>6</sup>	6.9x10 <sup>6</sup>	H <sub>2</sub> O
25	3.5x10 <sup>2</sup>	7.2x10 <sup>2</sup>	C <sub>2</sub> H <sup>+</sup>
26	1x10 <sup>3</sup>	1.4 x10 <sup>3</sup>	C <sub>2</sub> H <sub>2</sub> <sup>+</sup> /CN
29	3.2x10 <sup>4</sup>	4.8x10 <sup>4</sup>	HCO (Acetaldehyde, formic acid)
32	1x10 <sup>5</sup>	1.5x10 <sup>5</sup>	CH <sub>3</sub> OH Methanol
33	8.2x10 <sup>4</sup>	1.2x10 <sup>5</sup>	OOH
44	1.1x10 <sup>4</sup>	1.6x10 <sup>4</sup>	CH <sub>3</sub> CHO Acetaldehyde
46	1x10 <sup>3</sup>	1.1x10 <sup>3</sup>	HCOOH Formic acid
47	6.1x10 <sup>2</sup>	1.1x10 <sup>3</sup>	NH <sub>2</sub> CH <sub>2</sub> OH Aminomethanol
127	2.4x10 <sup>2</sup>	3.3x10 <sup>2</sup>	QUIN-H <sub>2</sub>
129	2.9 x10 <sup>2</sup> *	2.4 x10 <sup>2</sup> *	C <sub>9</sub> H <sub>7</sub> N <sup>+</sup> Quinoline
159	5.7x10 <sup>2</sup> **	1.5x10 <sup>3</sup> **	Quinoline-quinone
160	1.4x10 <sup>2</sup> **	2x10 <sup>2</sup> **	Dihydroxyquinoline-H

\*139K<T<180K

\*\*256K<T<295K

**Table 13** | Mass spectra data registered for QUIN:H<sub>2</sub>O ice mixtures deposited on olivine grains with or without UV irradiation. Tentative assignments of the main peaks detected after UV irradiation was provided in the last column.

m/z	Peak Intensity (c/s) QUIN:water ice		
	NO IRR	IRR	Olivine grains Proposed molecular species
<b>180K&lt;T&lt;220K</b>			
1	2.3x10 <sup>5</sup>	4.3x10 <sup>5</sup>	H
2	4.3x10 <sup>4</sup>	5.8x10 <sup>4</sup>	H <sub>2</sub>
15	3.2x10 <sup>4</sup>	4.0x10 <sup>4</sup>	CH <sub>3</sub>
16	4.2x10 <sup>4</sup>	6.2x10 <sup>4</sup>	CH <sub>4</sub>
17	7.4x10 <sup>5</sup>	1.1x10 <sup>6</sup>	OH/NH <sub>3</sub>
18	3.3x10 <sup>6</sup>	4.7x10 <sup>6</sup>	H <sub>2</sub> O
25	2.1x10 <sup>2</sup>	3.4x10 <sup>2</sup>	C <sub>2</sub> H <sup>+</sup>
29	3.3x10 <sup>4</sup>	4.8x10 <sup>4</sup>	HCO (Acetaldehyde, formic acid)
32	9.9x10 <sup>4</sup>	1.3x10 <sup>5</sup>	CH <sub>3</sub> OH Methanol
33	7.5x10 <sup>4</sup>	9.9x10 <sup>4</sup>	OOH
44	1.0x10 <sup>4</sup>	1.1x10 <sup>4</sup>	CH <sub>3</sub> CHO Acetaldehyde
46	1.3x10 <sup>4</sup>	1.4x10 <sup>4</sup>	HCOOH Formic acid
45	9.1x10 <sup>2</sup>	9.2x10 <sup>2</sup>	HCONH <sub>2</sub> Formamide
47	1.8x10 <sup>4</sup>	5.0x10 <sup>4</sup>	NH <sub>2</sub> CH <sub>2</sub> OH Aminomethanol
<b>256&lt;T&lt;295</b>			
102	80	1.3x10 <sup>2</sup>	Quin-HCN
103	30	70	Benzonitrile
127	2.4x10 <sup>2</sup>	3.3x10 <sup>2</sup>	QUIN-H <sub>2</sub>
129	8.0x10 <sup>2</sup> *	5.1x10 <sup>2</sup> *	C <sub>9</sub> H <sub>7</sub> N <sup>+</sup> Quinoline
159	2.7x10 <sup>4</sup>	5.3x10 <sup>4</sup>	Quinoline-quinone
160	7.2x10 <sup>2</sup>	8.5x10 <sup>3</sup>	Dihydroxyquinoline-H

\*180K<T<220K

In this investigation, three principal pathways for the formation of photo-products are discerned upon UV irradiation of quinoline, whether desorption occurs from the cold finger or olivine grains. Specifically, species resulting from the fragmentation of water, those arising from the fragmentation of

quinoline, and species resulting from the combination of both photo-products were observed.

Notably, in comparison to the latter scenario, the formation of quinoline-quinone and hydroxyquinoline is highlighted. These results align with findings from experiments conducted by Elsila et al.,<sup>138</sup> utilizing high-performance liquid chromatography (HPLC) analysis to detect species formed after UV irradiation of quinoline frozen in astrophysically relevant H<sub>2</sub>O-dominated ices. Additionally, the presence of aminomethanol (NH<sub>2</sub>CH<sub>2</sub>OH) was observed, a compound whose formation at low temperatures from the H<sub>2</sub>O:NH<sub>3</sub>:H<sub>2</sub>CO ice mixture has been systematically studied by J.B. Bossa et al.<sup>139</sup> Furthermore, this study underscores the emergence of formamide (HCONH<sub>2</sub>) resulting from the photolysis of aminomethanol under vacuum ultraviolet (VUV) irradiation. This outcome is attributed to a dehydrogenation process depicted as  $\text{NH}_2\text{CH}_2\text{OH} + h\nu \rightarrow \text{HCONH}_2 + \text{H}_2$ , as elucidated by previous studies.

In another study, the gamma irradiation of quinoline in an aqueous solution was investigated.<sup>140</sup> Upon exposure to gamma irradiation, hydroxyquinoline and formic acid were detected. The proposed mechanism suggests that the degradation of quinoline initiates with a hydroxylation reaction, followed by a series of ring-opening and backbone-fragmentation processes.

Overall, Figure 21 shows the main fragmentation pattern deriving from photo-irradiation of naphthalene or quinoline in water ice at 11K.

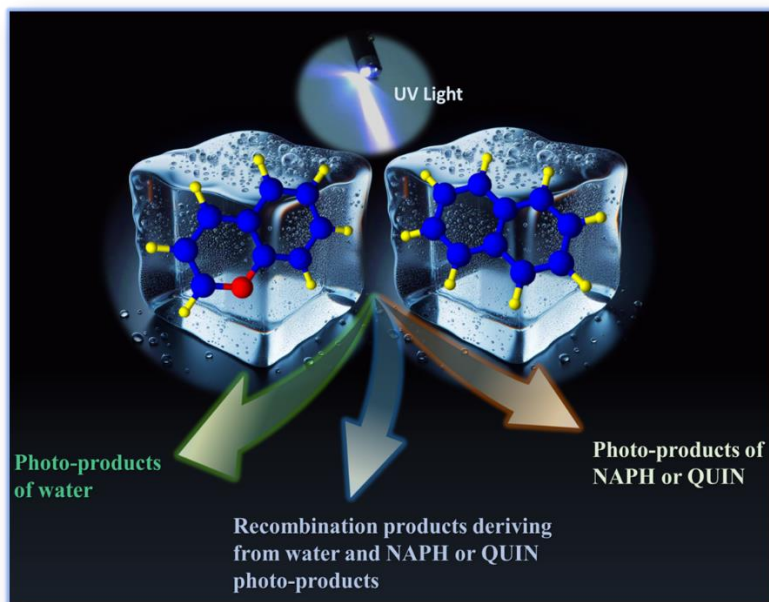


**Figure 21** | Formation pathways of main photo-products formed after UV irradiation of a naphthalene or quinoline water ice mixture.

### 3.3 Conclusions

In this Chapter, TPD experiments on water ice mixtures of acetonitrile and acetaldehyde, both pure and mixed with water, naphthalene and quinoline, condensed at 11 K on micrometric grains of silicate olivine ((Mg,Fe)<sub>2</sub>SiO<sub>4</sub>), were carried out. Ice mixtures were subjected to in situ UV irradiation to study the results of photo- processes monitored by means of both the analysis of TPD curves of the irradiated molecules and of the mass spectra.

To the best of our knowledge, in the literature TPD experiments of ices have been performed only from graphite and amorphous water ice surfaces. TPD studies from olivine grain surfaces are lacking.

The experiments carried out both for pure ices and mixtures of CH<sub>3</sub>CN and CH<sub>3</sub>COH showed that the presence of olivine does not significantly affect the distribution of the peaks in the mass spectra.

Through careful examination of the products formed from pure ices of acetaldehyde and acetonitrile, binary and ternary ice mixtures with water, four main reaction pathways due to the combined action of UV irradiation and olivine grains have been identified: photodissociation, radical recombination, isomerization and hydrogen addition.

Under UV irradiation of the mixture with water (1:1:3), high levels of hydroxyl radicals were produced as denoted by the mass spectra. Moreover, peaks relative to methanol (CH<sub>3</sub>OH, *m/z* 32), hydroxylamine (NH<sub>2</sub>OH, *m/z* 33) and acetic acid (CH<sub>3</sub>COOH, *m/z* 60) deriving from recombination processes involving the hydroxyl radical were discovered. These latter molecules may be detected in star-forming regions containing acetaldehyde, acetonitrile, UV radiation and silicates. In fact, the amount of water relative to the other species in interstellar ices is much higher than the 1:1:3 ratio used in these experiments,

so we can expect that more of the hydroxyl OH is responsible for the formation of these molecules. Hydroxylamine, an amino acid precursor that has yet to be detected in hot corinos and low-mass corinos, is of particular interest.

Interestingly, despite the presence of water, in the ternary mixture cross-recombination processes involving only the radicals generated by the photodissociation of acetaldehyde and acetonitrile can still occur in the laboratory, leading to the formation in the solid phase of COMs responsible for the development of prebiotic chemistry, such as formamide ( $\text{HCONH}_2$ ,  $m/z$  45), acetamide ( $\text{CH}_3\text{CONH}_2$ ,  $m/z$  59) and urea ( $\text{NH}_2\text{CONH}_2$ ,  $m/z$  60). A complete picture of the photodissociation, recombination, isomerization, and hydrogen addition reactions was provided, which could represent the possible pathway for assigning the peaks revealed by the mass analysis of the UV irradiated  $\text{CH}_3\text{CN}:\text{CH}_3\text{COH}:\text{H}_2\text{O}$  (1:1:3) ice mixture on olivine grains.

The inspection of this scheme revealed a very important point: the origin in the solid phase of a series of key molecules, including prebiotic molecules (i.e., formamide, urea) and molecules detected in the interstellar medium (i.e., hydroxylamine, hydrogen cyanide).

Complex organic molecules, such as those detected in our mass spectra, are expected to form in the solid phase and then be released in the gas phase of various interstellar environments via the combined action of the grain surface, which acts as a catalyst for recombination reactions between the various radicals, and energetic processes involving photons, electrons, ions, and atoms. Moreover, for the first time, the thermal desorption of water mixtures of naphthalene and quinoline deposited on a 100  $\mu\text{m}$  thick layer of olivine grains smaller than 5  $\mu\text{m}$  was simulated.

In the presence of olivine grains, two different peaks were displayed in the TPD spectrum, suggesting that two desorption processes occurred. We can argue that the first peak corresponds to the desorption of molecules placed on the surface, while molecules placed deeper inside the layer of olivine underwent delayed desorption, producing the second wider peak. In particular, in the case of quinoline, the grains involved a gradual release of the molecules from the grains to the gas phase. Indeed, as soon as the temperature reached 150 K, the desorption process started and continued up to 250 K, in contrast with the desorption process from the cold finger that occurred in the temperature range between 150-210 K.

The investigation of naphthalene and quinoline desorption from different substrates UV irradiation unveils a complex interplay of chemical reactions. Notably, the simultaneous decrease and increase in peak intensities post-UV irradiation indicate a dynamic interplay of fragmentation and formation of larger molecular species.

This study contributes crucial insights into the molecular processes occurring in astrophysically relevant environments, shedding light on the intricate chemistry of polycyclic aromatic hydrocarbons under the influence of UV radiation.

Overall, these types of experiments are increasingly interesting in view of the new discoveries of organic molecules that we expect from the recent successful launch of the James Webb Space Telescope (JWST), which will be able to visualize disks around young stars and to study organic molecules important for the development of life.

## 3.4 Experimental section

### 3.4.1 Experimental Setup and Thermal Desorption Diagnostic

The thermal desorption experiments were performed in an ultrahigh vacuum (UHV) chamber ( $P \sim 6.68 \cdot 10^{-10}$  mbar) with feedthroughs for gas-phase deposition from a prechamber ( $P \sim 10^{-7}$  mbar).

The UHV chamber was equipped with the Hidden Analytical 3F RC 301 PicQuadrupole Mass Spectrometer (HAL 3F RC) for mass spectrometry. The ion source is an electron impact ionizer with twin-oxide-coated iridium filaments, and the detector is a pulse ion counting single channel electron multiplier, which allows us to analyze masses from 1 to 300 a.m.u. The chamber interfaces with an ARS closed-cycle helium cryocooler able to get a temperature of 11 K.

The UHV chamber was equipped also with a 300 W UV-enhanced Newport Xenon lamp with purified Xenon at 5-20 bar (wavelength range 185 - 2000 nm) to simulate the radiation of solar-like stars. The UV radiation emitted by the lamp was collimated through an optical system towards an optical fiber. The photon flux measured by the Optics Laboratory of the National Research Council (CNR) is  $2.48 \cdot 10^{16}$  photons $\cdot$ sec $^{-1}$  $\cdot$ cm $^{-2}$ . This value is the incident flux of UV radiation coming out from the optical fiber per unit area in the range of 200 - 300 nm (6 - 4 eV). The chamber is equipped with a closed-cycle helium cryocooler able to get a temperature of 11 K.

### 3.4.2 Preparation of ice mixtures

The CH<sub>3</sub>COH, CH<sub>3</sub>CN, naphthalene and quinoline molecules were purchased from Sigma Aldrich, Merck Corporation, with a purity of 99.5%.

To prepare ice mixtures of pure H<sub>2</sub>O, CH<sub>3</sub>CN, CH<sub>3</sub>COH, and mixtures CH<sub>3</sub>CN:H<sub>2</sub>O (1:2), CH<sub>3</sub>COH:H<sub>2</sub>O (1:2), CH<sub>3</sub>CN:CH<sub>3</sub>COH (1:6), and CH<sub>3</sub>CN:CH<sub>3</sub>COH:H<sub>2</sub>O (1:1:3), NAPH:water (1:10000) and QUIN:water (1:10000), the gas mixing was controlled by their partial pressures inside the prechamber.

The thermal desorption of these samples was performed by condensing the mixtures both on micrometric grains of olivine, to better simulate the desorption process that occurred in the hot star-forming regions, and directly on the cold finger of the cryostat made with a smooth nickel plate, at 11 K, used as a reference.

For this aim, a hundreds-micron-thick layer of olivine grains with a size smaller than 5 μm, was employed to cover the cold finger.

The natural olivine mineral was ground using a planetary mill, Retsch PM 100, obtaining grains of different sizes. To select micrometric grains, two procedures were carried out: dry sieving to select grains with size  $d < 20 \mu\text{m}$  and then a methanol sedimentation procedure to select grains with even smaller dimensions. The methanol solvent was used both to remove organic contamination from the natural mineral and for its volatility.

Grains with dimensions  $d < 5 \mu\text{m}$  were selected by means of sedimentation. The grain size measurement was confirmed with the Bruker Hyperion 1000 microscope.

Figure 22 shows the image of micrometric olivine dust.

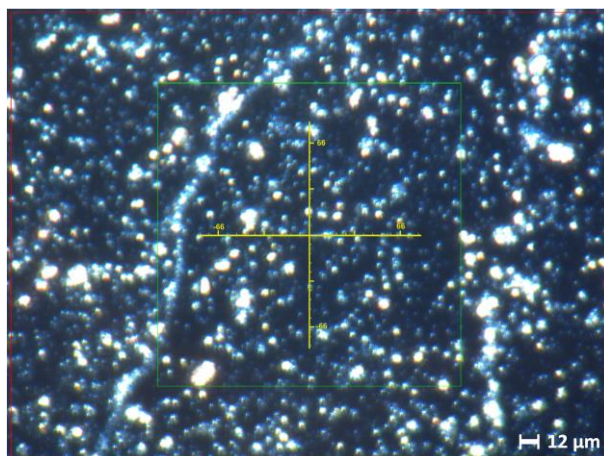


**Figure 22** | Olivine grains smaller than  $5\mu\text{m}$ . The image was obtained with the Hyperion microscope.

### 3.4.3. TPD Experiments and Analysis

The gas mixture of PA(N)Hs and iCOMs with water was prepared in the prechamber following the partial pressures and was deposited through a valve system inside the UHV chamber on the cold finger of the cryostat cooled at 11 K, with and without the olivine grains.

In all measurements during the gas mixtures deposition, the pressure in the UHV chamber increased from  $6.68 \cdot 10^{-10}$  mbar without ever exceeding a maximum pressure of  $10^{-6}$  mbar, for PA(N)Hs and  $10^{-8}$  mbar, for iCOMs.

In the case of naph:water mixture, the naphthalene and water partial pressure of 3 mbar and 0.4 mbar, respectively, were deposited in the UHV chamber.

The quin: water mixture was prepared, mixing in the prechamber 0.4 mbar of water and 3 mbar of quinoline, as partial pressure. In this case, the deposition process continued until the pressure in the prechamber reached 2.4 mbar.

The pressure maintained this maximum value for about 1 s. The surface exposure to gas is generally measured by the Langmuir unit (L). Assuming a

sticking coefficient equal to 1, i.e., each gas molecule that reaches the surface sticks to it, 1 L (1 L =  $10^{-6}$  mbar s) results in the formation of a monolayer of gas molecules adsorbed on the surface. Because during the deposit the maximum pressure in the UHV chamber was  $10^{-6}$  mbar or  $10^{-8}$  for 1 s, we can assume that the formation of a monolayer of gas molecules adsorbed on the surface occurred. The amounts of the molecules adsorbed on the surface were expressed in partial pressure instead of L units because the first one is a direct measure in our experimental apparatus. After condensation, the sample was heated at a constant rate of  $1.21 \text{ K s}^{-1}$ . As the cold finger warmed, the condensed molecules desorbed, entered the mass spectrometer, and were detected. We followed the signal detected by the mass spectrometer as the temperature increased for selected masses from 1 to 300 a.m.u. and so, the TPD curves were obtained. The same procedure was followed after the UV irradiation of ice mixtures for 8 hours and the resulting TPD curves and mass spectra masses from 1 to 300 a.m.u. provided information on how UV irradiation affected the initial molecules. The desorption temperature ( $T_d$ ) and the desorption energy ( $E_d$ ) were calculated by fitting the TPD curves with the Polanyi–Wigner equation<sup>141</sup> with preexponential factors ranging between  $10^{12}$  and  $10^{15} \text{ s}^{-1}$ , found as the best-fit values. To assess if the interactions between photons and the olivine surface affected the data obtained, the mass spectrum of olivine before and after eight hours of UV irradiation was recorded (Figure 23). No differences between the irradiated and non-irradiated bare olivine are shown.

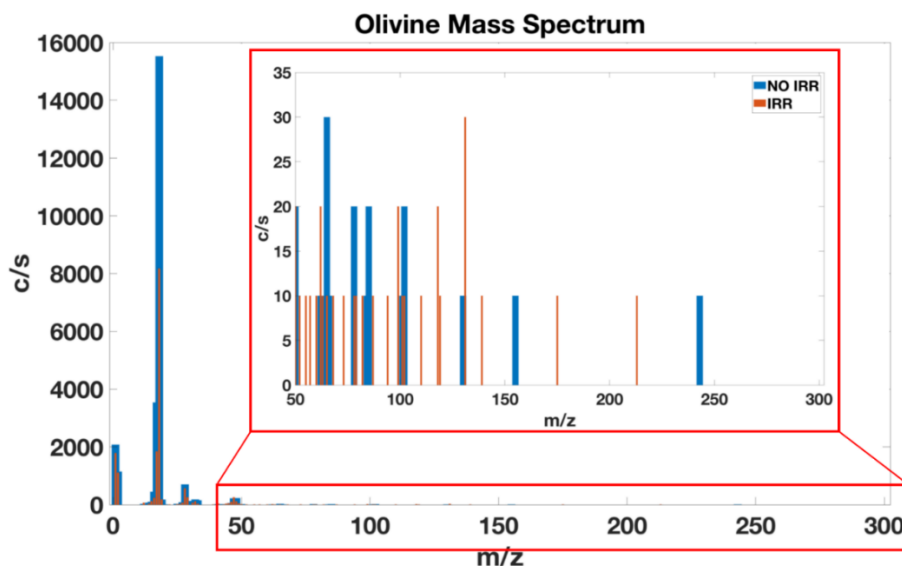


**Figure 23** | Two experiments are reported. For both experiments, the figures show the complete olivine mass spectrum when the temperature was rising from 256 to 293 K. The blue histograms show the olivine mass spectrum without the effects of UV irradiation, while the red histograms show how the olivine mass spectrum changed after 8 hours of UV irradiation.

#### 3.4.4 TPD curves and the Polanyi-Wigner equation

In a TPD experiment, the molecules are deposited in a UHV chamber ( $P \sim 10^{-10}$  mbar) on a surface. Once the surface is heated with a constant heating rate  $hr$  given by the equation  $x$ , the molecules desorb, enter the mass spectrometer, and are discriminated by their  $m/z$  ratio. For a given mass, the TPD curve is the figure describing the thermal desorption which is generally analyzed using the Polanyi-Wigner equation<sup>141</sup> :

$$r_{des} = - \frac{d\theta}{dT} = \frac{A}{h_r} \cdot \theta^m \cdot e^{-\frac{E_{des}}{K_b T}} \quad 3.4.4.1$$

where

- A is the pre-exponential factor in  $\text{sec}^{-1}$ ,
- $\theta^m$  is the surface coverage of order m,
- $E_{des}$  is the desorption energy,
- $K_b$  is the Boltzmann's constant.

A TPD curve and the Polanyi - Wigner equation give us information on the desorption rate,  $r_{des}$ , and on the desorption energy,  $E_{des}$  (see equation 3.4.4.1).

Now, we will briefly outline the steps to get the Polanyi - Wigner equation.

The principle of microscopic reversibility requires that a reaction goes through the same states regardless of whether it proceeds forward or backward. So, adsorption and desorption can be described by the same rate equation. The desorption rate is usually written as a rate law of  $m^{\text{th}}$  order:

$$r_{des} = - \frac{d\theta}{dT} = K_d \cdot \theta^m \quad 3.4.4.2$$

where

- $\theta^m$  is the surface coverage,
- $K_d$  is the desorption rate constant,
- m is the kinetic desorption order.

Adsorption is an activated process that obeys the Arrhenius equation:

$$K_d = A \cdot e^{-\frac{E_{des}}{K_b T}} \quad 3.4.4.3$$

where A is the inverse of a time and it is the pre-exponential factor. By replacing this expression of the Arrhenius equation (equation 3.4.4.3) in the

adsorption rate equation (equation 3.4.4.2), we obtain the following equation which describes the activation desorption energy  $E_{des}$ :

$$r_{des} = - \frac{d\theta}{dT} = A \cdot \theta^m \cdot e^{-\frac{E_{des}}{K_b T}} \quad 3.4.4.4$$

Usually, TPDs are run with a linear heating ramp,  $h_r$ :

$$T(t) = T_0 + h_r \cdot t \quad 3.4.4.5$$

therefore, deriving respect to time:

$$\frac{dT}{dt} = h_r \quad 3.4.4.6$$

So, we can obtain the Polanyi - Wigner equation (3.4.4.1) by writing the equation as follows:

$$r_{des} = - \frac{d\theta}{dT} = \frac{A}{h_r} \cdot \theta^m \cdot e^{-\frac{E_{des}}{K_b T}} \quad 3.4.4.1$$

The shape of the TPD curve changes as a function of the kinetic desorption order  $m$ .

- At the zero-order kinetic,  $m = 0$ , the Polanyi - Wigner equation (3.4.4.1) becomes:

$$r_{des} = \frac{A}{h_r} \cdot e^{-\frac{E_{des}}{K_b T}} \quad 3.4.4.7$$

The zero-order kinetic desorption describes the multilayer desorption. The equation shows that there is no link between the desorption rate and the surface coverage. Figure 24 a) shows that the peak of the curve shifts to higher temperatures as the surface coverage increases. This trend is typical of multilayer desorption. The supply of deposited particles is theoretically unlimited, there is in fact no dependence on surface coverage, and the leading edges are common.

- At the first-order kinetic,  $m = 1$ , the 1.17 equation becomes:

$$r_{des} = \frac{A}{h_r} \cdot \theta \cdot e^{-\frac{E_{des}}{K_b T}} \quad \mathbf{3.4.4.8}$$

The first-order kinetic desorption describes unimolecular desorption, i.e., a molecule adsorbs and then desorbs without dissociating. Figure 24 b) displays that the position of the desorption peak is independent of the surface coverage. The peaks are asymmetrical with an ascending leading edge.

- At the second-order kinetic,  $m = 2$ , the 3.4.4.1 equation becomes:

$$r_{des} = -\frac{d\theta}{dT} = \frac{A}{h_r} \cdot \theta^2 \cdot e^{-\frac{E_{des}}{K_b T}} \quad \mathbf{3.4.4.9}$$

The second-order kinetic desorption describes the recombinative desorption, i.e., the molecule adsorbs, dissociates on the surface, and then desorbs by recombining. The equation shows that the desorption rate follows  $\theta^2$  and Figure 24 c) shows that the peak position shifts to lower temperatures with increasing the surface coverage. From the figure, we can see symmetric peak shape and common trailing edges.<sup>142</sup>

The TPD curves provide information on the desorption rate and desorption energy. If we write the Polanyi-Wigner equation 3.4.4.1 in logarithmic form, we find:

$$\ln(r_{des}) = \ln\left(\frac{A}{h_r} \cdot \theta^m\right) - \frac{E_{des}}{K_b T} \quad \mathbf{3.4.4.10}$$

if we plot  $\ln(r_{des})$  as a function of  $1/T$ , we obtain information on the desorption energy. The slope of the curve is relative to  $E_{des}$  and the intercept is correlated to  $A$ .

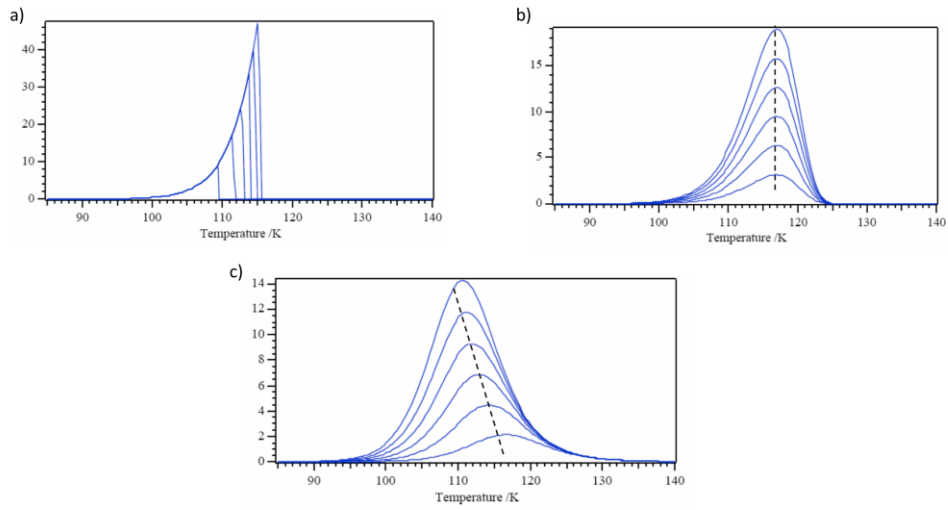


**Figure 24** | The figure shows how the shape of the TPD curves changes as a function of the kinetic order of desorption. The three panels a, b, and c respectively describe the zero, first, and second order of desorption.

---

**REFERENCES**

1. G.A. Blake, E.C. Sutton, C.R. Masson, T.G. Phillips. Molecular abundances in OMC-1 - The chemical composition of interstellar molecular clouds and the influence of massive star formation. *Astrophys J* **1987**, 315, 621.
2. P. Caselli, C. Ceccarelli. Our astrochemical heritage. *The Astronomy and Astrophysics Review* **2012**, 20 (1), 56.
3. A. Bacmann, V. Taquet, A. Faure, C. Kahane, C. Ceccarelli. Detection of complex organic molecules in a prestellar core: a new challenge for astrochemical models. *Astron Astrophys* **2012**, 541, L12.
4. C. Vastel, C. Ceccarelli, B. Lefloch, R. Bachiller. The origin of complex organic molecules in prestellar cores. *Astrophys J* **2014**, 795 (1), L2.
5. S. Cazaux, A.G.G.M. Tielens, C. Ceccarelli, et al. The Hot Core around the Low-Mass Protostar IRAS 16293-2422: Scoundrels Rule! *Astrophys J* **2003**, 593 (1), L51–L55.
6. C. Ceccarelli, P. Caselli, E. Herbst, X. Tielens, E. Caux. Extreme Deuteration and Hot Corinos: The Earliest Chemical Signatures of Low-Mass Star Formation. In *Protostars and Planets V*; University of Arizona Press, Tucson, **2007**; pp 47–62.
7. R. Bachiller, M. Pérez Gutiérrez. Shock Chemistry in the Young Bipolar Outflow L1157. *Astrophys J* **1997**, 487 (1), L93–L96.
8. H.G. Arce, J. Santiago-García, J.K. Jørgensen, M. Tafalla, R. Bachiller. Complex Molecules in the L1157 Molecular Outflow. *Astrophys J* **2008**, 681 (1), L21–L24.
9. C. Codella, B. Lefloch, C. Ceccarelli, et al. The CHESS spectral survey of star forming regions: Peering into the protostellar shock L1157-B1. *Astron Astrophys* **2010**, 518, L112.
10. B. Lefloch, C. Ceccarelli, C. Codella, et al. L1157-B1, a factory of complex organic molecules in a solar-type star-forming region. *Mon Not R Astron Soc Lett* **2017**, 469 (1), L73–L77.
11. L.A. Cieza, S. Casassus, J. Tobin, et al. Imaging the water snow-line during a protostellar outburst. *Nature* **2016**, 535 (7611), 258–261.
12. C. Walsh, R.A. Loomis, K.I. Öberg, et al. First detection of gas-phase methanol in a protoplanetary disk. *Astrophys J* **2016**, 823 (1), L10.

13. L. Podio, F. Bacciotti, D. Fedele, et al. Organic molecules in the protoplanetary disk of DG Tauri revealed by ALMA. *Astron Astrophys* **2019**, 623, L6.
14. K.I. Öberg, V. V. Guzmán, K. Furuya, et al. The comet-like composition of a protoplanetary disk as revealed by complex cyanides. *Nature* **2015**, 520 (7546), 198–201.
15. C. Favre, D. Fedele, D. Semenov, et al. First Detection of the Simplest Organic Acid in a Protoplanetary Disk. *Astrophys J* **2018**, 862 (1), L2.
16. M.L.R. van 't Hoff, J.J. Tobin, L. Trapman, et al. Methanol and its Relation to the Water Snowline in the Disk around the Young Outbursting Star V883 Ori. *Astrophys J* **2018**, 864 (1), L23.
17. J.-E. Lee, S. Lee, G. Baek, et al. The ice composition in the disk around V883 Ori revealed by its stellar outburst. *Nat Astron* **2019**, 3 (4), 314–319.
18. M.A. Cordiner, M.Y. Palmer, C.A. Nixon, et al. Ethyl cyanide on Titan: Spectroscopic detection and mapping using ALMA. *Astrophys J* **2015**, 800 (1), L14.
19. A.E. Thelen, C.A. Nixon, N.J. Chanover, et al. Abundance measurements of Titan's stratospheric HCN, HC<sub>3</sub>N, C<sub>3</sub>H<sub>4</sub>, and CH<sub>3</sub>CN from ALMA observations. *Icarus* **2019**, 319, 417–432.
20. T. Iino, H. Sagawa, T. Tsukagoshi. 14N/15N Isotopic Ratio in CH<sub>3</sub>CN of Titan's Atmosphere Measured with ALMA. *Astrophys J* **2020**, 890 (2), 95.
21. F. Goesmann, H. Rosenbauer, J.H. Bredehöft, et al. Organic compounds on comet 67P/Churyumov-Gerasimenko revealed by COSAC mass spectrometry. *Science (1979)* **2015**, 349 (6247).
22. L.M. Woodney, M.F. A'Hearn, D.G. Schleicher, et al. Morphology of HCN and CN in Comet Hale-Bopp (1995 O1). *Icarus* **2002**, 157 (1), 193–204.
23. E.R. Willis, R.T. Garrod, A. Belloche, et al. Exploring molecular complexity with ALMA (EMoCA): complex isocyanides in Sgr B2(N). *Astron Astrophys* **2020**, 636, A29.
24. K. Taniguchi, A.E. Guzmán, L. Majumdar, M. Saito, K. Tokuda. Chemical Composition in the IRAS 16562–3959 High-mass Star-forming Region. *Astrophys J* **2020**, 898 (1), 54.
25. I. Andron, P. Gratier, L. Majumdar, et al. Methyl cyanide (CH<sub>3</sub>CN) and propyne (CH<sub>3</sub>CCH) in the low-mass protostar IRAS 16293–2422. *Mon Not R Astron Soc* **2018**, 481 (4), 5651–5659.

26. E.G. Bøgelund, B.A. McGuire, M.R. Hogerheijde, E.F. van Dishoeck, N.F.W. Ligterink. Methylamine and other simple N-bearing species in the hot cores NGC 6334I MM1–3. *Astron Astrophys* **2019**, 624, A82.
27. J.B. Bergner, V.G. Guzmán, K.I. Öberg, R.A. Loomis, J. Pegues. A Survey of CH<sub>3</sub>CN and HC<sub>3</sub>N in Protoplanetary Disks. *Astrophys J* **2018**, 857 (1), 69.
28. R. Le Gal, M.T. Brady, K.I. Öberg, E. Roueff, F. Le Petit. The Role of C/O in Nitrile Astrochemistry in PDRs and Planet-forming Disks. *Astrophys J* **2019**, 886 (2), 86.
29. K.I. Öberg, V. V. Guzmán, K. Furuya, et al. The comet-like composition of a protoplanetary disk as revealed by complex cyanides. *Nature* **2015**, 520 (7546), 198–201.
30. R.A. Loomis, L.I. Cleeves, K.I. Öberg, et al. The Distribution and Excitation of CH<sub>3</sub>CN in a Solar Nebula Analog. *Astrophys J* **2018**, 859 (2), 131.
31. E. Bianchi, C. Codella, C. Ceccarelli, et al. The census of interstellar complex organic molecules in the Class I hot corino of SVS13-A. *Mon Not R Astron Soc* **2019**, 483 (2), 1850–1861.
32. A.E. Guzmán, V. V. Guzmán, G. Garay, L. Bronfman, F. Hechenleitner. Chemistry of the High-mass Protostellar Molecular Clump IRAS 16562–3959. *Astrophys J Suppl Ser* **2018**, 236 (2), 45.
33. V. Taquet, A. López-Sepulcre, C. Ceccarelli, et al. Constraining the Abundances of Complex Organics in the Inner Regions of Solar-type Protostars. *Astrophys J* **2015**, 804 (2), 81.
34. C. Codella, C. Ceccarelli, S. Cabrit, et al. Water and acetaldehyde in HH212: The first hot corino in Orion. *Astron Astrophys* **2016**, 586, L3.
35. N. Biver, D. Bockelée-Morvan. Complex Organic Molecules in Comets from Remote-Sensing Observations at Millimeter Wavelengths. *ACS Earth Space Chem* **2019**, 3 (8), 1550–1555.
36. K.-J. Chuang, G. Fedoseev, D. Qasim, et al. Formation of complex molecules in translucent clouds: Acetaldehyde, vinyl alcohol, ketene, and ethanol via nonenergetic processing of C<sub>2</sub>H<sub>2</sub> ice. *Astron Astrophys* **2020**, 635, A199.
37. R.T. Garrod, E. Herbst. Formation of methyl formate and other organic species in the warm-up phase of hot molecular cores. *Astron Astrophys* **2006**, 457 (3), 927–936.
38. K.I. Öberg, R.T. Garrod, E.F. van Dishoeck, H. Linnartz. Formation rates of complex organics in UV irradiated CH<sub>3</sub>OH-rich ices. *Astron Astrophys* **2009**, 504 (3), 891–913.

39. T. Lamberts, M.N. Markmeyer, F.J. Kolb, J. Kästner. Formation of Acetaldehyde on CO-Rich Ices. *ACS Earth Space Chem* **2019**, 3 (6), 958–963.
40. R. Martín-Doménech, K.I. Öberg, M. Rajappan. Formation of NH<sub>2</sub>CHO and CH<sub>3</sub>COH upon UV Photoprocessing of Interstellar Ice Analogs. *Astrophys J* **2020**, 894 (2), 98.
41. J. Enrique-Romero, A. Rimola, C. Ceccarelli, N. Balucani. The (impossible?) formation of acetaldehyde on the grain surfaces: insights from quantum chemical calculations. *Mon Not R Astron Soc Lett* **2016**, 459 (1), L6–L10.
42. J.D.T. Smith, B.T. Draine, D.A. Dale, et al. The Mid-Infrared Spectrum of Star-forming Galaxies: Global Properties of Polycyclic Aromatic Hydrocarbon Emission. *Astrophys J* **2007**, 656 (2), 770–791.
43. B.T. Draine, A. Li. Infrared Emission from Interstellar Dust. IV. The Silicate-Graphite-PAH Model in the Post-Spitzer Era. *Astrophys J* **2007**, 657 (2), 810–837.
44. B.T. Draine, D.A. Dale, G. Bendo, et al. Dust Masses, PAH Abundances, and Starlight Intensities in the SINGS Galaxy Sample. *Astrophys J* **2007**, 663 (2), 866–894.
45. A.G.G.M. Tielens. Interstellar Polycyclic Aromatic Hydrocarbon Molecules. *Annu Rev Astron Astrophys* **2008**, 46 (1), 289–337.
46. T. Onaka, I. Yamamura, T. Tanabé, T.L. Roellig, L. Yuen. Detection of the Mid-Infrared Unidentified Bands in the Diffuse Galactic Emission by IRTS. *Publications of the Astronomical Society of Japan* **1996**, 48 (5), L59–L63.
47. S. Hony, C. Van Kerckhoven, E. Peeters, et al. The CH out-of-plane bending modes of PAH molecules in astrophysical environments. *Astron Astrophys* **2001**, 370 (3), 1030–1043.
48. E. Peeters, S. Hony, C. Van Kerckhoven, et al. The rich 6 to 9  $\mu\text{m}$  spectrum of interstellar PAHs. *Astron Astrophys* **2002**, 390 (3), 1089–1113.
49. I. Sakon, T. Onaka, D. Ishihara, et al. The Unidentified Infrared Bands in the Diffuse Interstellar Medium across the Galaxy Based on the Infrared Telescope in Space Mid-Infrared Spectrometer Observation. *Astrophys J* **2004**, 609 (1), 203–219.
50. B. Acke, M.E. van den Ancker. ISO spectroscopy of disks around Herbig Ae/Be stars. *Astron Astrophys* **2004**, 426 (1), 151–170.
51. M.W. Regan, M.D. Thornley, G.J. Bendo, et al. Spitzer Infrared Nearby Galaxies Survey (SINGS) Imaging of NGC 7331: A Panchromatic View of a Ringed Galaxy. *Astrophys J Suppl Ser* **2004**, 154 (1), 204–210.

- 
52. L. Armus, V. Charmandaris, J. Bernard-Salas, et al. Observations of Ultraluminous Infrared Galaxies with the Infrared Spectrograph on the Spitzer Space Telescope. II. The IRAS Bright Galaxy Sample. *Astrophys J* **2007**, 656 (1), 148–167.
  53. B.R. Brandl, J. Bernard-Salas, H.W.W. Spoon, et al. The Mid-Infrared Properties of Starburst Galaxies from Spitzer-IRS Spectroscopy. *Astrophys J* **2006**, 653 (2), 1129–1144.
  54. A.& P.J.L. Leger. Identification of the “unidentified” IR emission features of interstellar dust? *Astron Astrophys* **1984**, 137, L5–L8.
  55. L.J. Allamandola, A.G.G.M. Tielens, J.R. Barker. Polycyclic aromatic hydrocarbons and the unidentified infrared emission bands - Auto exhaust along the Milky Way. *Astrophys J* **1985**, 290, L25.
  56. D.M. Hudgins, Jr., C.W. Bauschlicher, L.J. Allamandola. Variations in the Peak Position of the 6.2  $\mu\text{m}$  Interstellar Emission Feature: A Tracer of N in the Interstellar Polycyclic Aromatic Hydrocarbon Population. *Astrophys J* **2005**, 632 (1), 316–332.
  57. Jr., C.W. Bauschlicher, A. Ricca. The Far-Infrared Emission from the Mg+-PAH Species. *Astrophys J* **2009**, 698 (1), 275–280.
  58. A. Simon, C. Joblin. The Computed Infrared Spectra of a Variety of [FePAH]+ Complexes: Mid- and Far-Infrared Features. *Astrophys J* **2010**, 712 (1), 69–77.
  59. B. Joalland, A. Simon, C.J. Marsden, C. Joblin. Signature of [SiPAH]<sup>+</sup>  $\pi$ -complexes in the interstellar medium. *Astron Astrophys* **2009**, 494 (3), 969–976.
  60. M. Rapacioli, C. Joblin, P. Boissel. Spectroscopy of polycyclic aromatic hydrocarbons and very small grains in photodissociation regions. *Astron Astrophys* **2005**, 429 (1), 193–204.
  61. A. Simon, C. Joblin. Photodissociation of [Fe<sub>x</sub>(C<sub>24</sub>H<sub>12</sub>)<sub>y</sub>]<sup>+</sup> Complexes in the PIRENEA Setup: Iron-Polycyclic Aromatic Hydrocarbon Clusters as Candidates for Very Small Interstellar Grains. *J Phys Chem A* **2009**, 113 (17), 4878–4888.
  62. Jr., C.W. Bauschlicher, E. Peeters, L.J. Allamandola. The Infrared Spectra of Very Large, Compact, Highly Symmetric, Polycyclic Aromatic Hydrocarbons (PAHs). *Astrophys J* **2008**, 678 (1), 316–327.
  63. C.W. Bauschlicher, E. Peeters, L.J. Allamandola. The Infrared Spectra of Very Large Irregular Polycyclic Aromatic Hydrocarbons (PAHs): Observational Probes of Astronomical PAH Geometry, Size and Charge. *Astrophys J* **2009**, 697 (1), 311–327.

- 
64. J. Cami, J. Bernard-Salas, E. Peeters, S.E. Malek. Fullerenes in Circumstellar and Interstellar Environments. *Proceedings of the International Astronomical Union* **2011**, 7 (S280), 216–227.
  65. G.C. Sloan, M. Jura, W.W. Duley, et al. The Unusual Hydrocarbon Emission from the Early Carbon Star HD 100764: The Connection between Aromatics and Aliphatics. *Astrophys J* **2007**, 664 (2), 1144–1153.
  66. C. Boersma, J. Bouwman, F. Lahuis, et al. The characteristics of the IR emission features in the spectra of Herbig Ae stars: evidence for chemical evolution. *Astron Astrophys* **2008**, 484 (1), 241–249.
  67. L.D. Keller, G.C. Sloan, W.J. Forrest, et al. PAH Emission from Herbig Ae/Be Stars. *Astrophys J* **2008**, 684 (1), 411–429.
  68. T. Pino, E. Dartois, A.-T. Cao, et al. The 6.2 band position in laboratory and astrophysical spectra: a tracer of the aliphatic to aromatic evolution of interstellar carbonaceous dust. *Astron Astrophys* **2008**, 490 (2), 665–672.
  69. B. Acke, J. Bouwman, A. Juhász, et al. Spitzer’s view on aromatic and aliphatic hydrocarbon emission in Herbig Ae stars. *Astrophys J* **2010**, 718 (1), 558–574.
  70. I. Cherchneff, J.R. Barker, A.G.G.M. Tielens. Polycyclic aromatic hydrocarbon formation in carbon-rich stellar envelopes. *Astrophys J* **1992**, 401, 269.
  71. I. Gilmour, C.T. Pillinger. Isotopic compositions of individual polycyclic aromatic hydrocarbons from the Murchison meteorite. *Mon Not R Astron Soc* **1994**, 269 (2), 235–240.
  72. L. Becker, T.E. Bunch. Fullerenes, fulleranes and polycyclic aromatic hydrocarbons in the Allende meteorite. *Meteorit Planet Sci* **1997**, 32 (4), 479–487.
  73. H. Naraoka, A. Shimoyama, K. Harada. Isotopic evidence from an Antarctic carbonaceous chondrite for two reaction pathways of extraterrestrial PAH formation. *Earth Planet Sci Lett* **2000**, 184 (1), 1–7.
  74. M.A. Sephton. Organic compounds in carbonaceous meteorites. *Nat Prod Rep* **2002**, 19 (3), 292–311.
  75. R.G. Smith, K. Sellgren, A.T. Tokunaga. Absorption features in the 3 micron spectra of protostars. *Astrophys J* **1989**, 344, 413.
  76. K. Sellgren, T.Y. Brooke, R.G. Smith, T.R. Geballe. A New 3.25 Micron Absorption Feature toward Monoceros R2/IRS 3. *Astrophys J* **1995**, 449 (1).

- 
77. J. Brooke, D. Bitko, T. F., Rosenbaum, G. Aepli. Quantum Annealing of a Disordered Magnet. *Science (1979)* **1999**, 284 (5415), 779–781.
  78. J.E. Chiar, A.G.G.M. Tielens, D.C.B. Whittet, et al. The Composition and Distribution of Dust along the Line of Sight toward the Galactic Center. *Astrophys J* **2000**, 537 (2), 749–762.
  79. J.D. Bregman, T.L. Hayward, G.C. Sloan. Discovery of the 11.2 Micron Polycyclic Aromatic Hydrocarbon Band in Absorption toward Monoceros R2 IRS 3. *Astrophys J* **2000**, 544 (1), L75–L78.
  80. B.A. McGuire, A.M. Burkhardt, S. Kalenskii, et al. Detection of the aromatic molecule benzonitrile (c-C<sub>6</sub>H<sub>5</sub>CN) in the interstellar medium. *Science (1979)* **2018**, 359 (6372), 202–205.
  81. M.C. McCarthy, B.A. McGuire. Aromatics and Cyclic Molecules in Molecular Clouds: A New Dimension of Interstellar Organic Chemistry. *J Phys Chem A* **2021**, 125 (16), 3231–3243.
  82. B.A. McGuire, R.A. Loomis, A.M. Burkhardt, et al. Detection of two interstellar polycyclic aromatic hydrocarbons via spectral matched filtering. *Science (1979)* **2021**, 371 (6535), 1265–1269.
  83. M.E. and G.S. Palumbo. The 2140 cm<sup>-1</sup> band of frozen CO: laboratory experiments and astrophysical applications. *Astron Astrophys* **1993**, 269, 568–580.
  84. A. Ciaravella, G.M. Caro, A.J. Escobar, et al. Soft X-ray Irradiation of Methanol Ice: Implication for H<sub>2</sub>CO Formation in Interstellar Regions. *Astrophys J* **2010**, 722 (1), L45–L48.
  85. C. Meinert, I. Myrgorodska, P. de Marcellus, et al. Ribose and related sugars from ultraviolet irradiation of interstellar ice analogs. *Science (1979)* **2016**, 352 (6282), 208–212.
  86. V.K. Agarwal, W. Schutte, J.M. Greenberg, et al. Photochemical reactions in interstellar grains photolysis of CO, NH<sub>3</sub>, and H<sub>2</sub>O. *Origins of life and evolution of the biosphere* **1985**, 16 (1), 21–40.
  87. G.M. Muñoz Caro, W.A. Schutte. UV-photoprocessing of interstellar ice analogs: New infrared spectroscopic results. *Astron Astrophys* **2003**, 412 (1), 121–132.
  88. G.M. Muñoz Caro, U. Meierhenrich, W.A. Schutte, W. H.-P. Thiemann, J.M. Greenberg. UV-photoprocessing of interstellar ice analogs: Detection of hexamethylenetetramine-based species. *Astron Astrophys* **2004**, 413 (1), 209–216.

- 
89. A. Kouchi, H. Nakano, Y. Kimura, C. Kaito. Novel Routes for Diamond Formation in Interstellar Ices and Meteoritic Parent Bodies. *Astrophys J* **2005**, 626 (2), L129–L132.
  90. M. Bertin, C. Romanzin, M. Doronin, et al. UV photodesorption of methanol in pure and CO-rich ices: desorption rates of the intact molecule and of the photofragments. *Astrophys J* **2016**, 817 (2), L12.
  91. N. Abou Mrad, F. Duvernay, T. Chiavassa, G. Danger. Methanol ice VUV photoprocessing: GC-MS analysis of volatile organic compounds. *Mon Not R Astron Soc* **2016**, 458 (2), 1234–1241.
  92. Y.& H.E. Aikawa. Molecular evolution in protoplanetary disks. Two-dimensional distributions and column densities of gaseous molecules. *Astron Astrophys* **1999**, 351, 233–246.
  93. E.L. Gibb, D.C.B. Whittet, W.A. Schutte, et al. An Inventory of Interstellar Ices toward the Embedded Protostar W33A. *Astrophys J* **2000**, 536 (1), 347–356.
  94. M. Spaans, M.R. Hogerheijde, L.G. Mundy, E.F. van Dishoeck. Photon Heating of Envelopes around Young Stellar Objects: an Explanation for CO J= 6--5. *Astrophys J* **1995**, 455 (2).
  95. T.A. van Kempen, E.F. van Dishoeck, R. Güsten, et al. APEX-CHAMP+ high-J CO observations of low-mass young stellar objects I. The HH 46 envelope and outflow. *Astron Astrophys* **2009**, 501 (2), 633–646.
  96. A.S. Taha, L. Labadie, E. Pantin, et al. The spatial extent of polycyclic aromatic hydrocarbons emission in the Herbig star HD 179218. *Astron Astrophys* **2018**, 612, A15.
  97. G.H.& G.R.W. Herbig. Near-simultaneous ultraviolet and optical spectrophotometry of T Tauri stars. *Astrophysical Journal* **1986**, 309, 294–305.
  98. M.P. Collings, M.A. Anderson, R. Chen, et al. A laboratory survey of the thermal desorption of astrophysically relevant molecules. *Mon Not R Astron Soc* **2004**, 354 (4), 1133–1140.
  99. T. Hama, N. Watanabe, A. Kouchi, M. Yokoyama. Spin Temperature of Water Molecules Desorbed from the Surfaces of Amorphous Solid Water, Vapor-deposited and Produced from Photolysis of a CH<sub>4</sub>/O<sub>2</sub> Solid Mixture. *Astrophys J* **2011**, 738 (1), L15.
  100. J. Shi, G.A. Grieves, T.M. Orlando. Vacuum Ultraviolet Photon-stimulated Oxidation of Buried Ice: Graphite Grain Interfaces. *Astrophys J* **2015**, 804 (1), 24.

101. H. Chaabouni, S. Diana, T. Nguyen, F. Dulieu. Thermal desorption of formamide and methylamine from graphite and amorphous water ice surfaces. *Astron Astrophys* **2018**, 612, A47.
102. J. Klopogge. Thermal, Mechanical and Chemical Treatments of the Kaolin Minerals; **2019**; pp 161–241.
103. Y. Shinnaka, T. Kasuga, R. Furusho, et al. Inversion Angle of Phase-polarization Curve of Near-Earth Asteroid (3200) Phaethon. *Astrophys J* **2018**, 864 (2), L33.
104. T. Ootsubo, H. Kawakita, Y. Shinnaka, J. Watanabe, M. Honda. Unidentified infrared emission features in mid-infrared spectrum of comet 21P/Giacobini-Zinner. *Icarus* **2020**, 338, 113450.
105. E. Picazzio, I. V. Luk'yanyk, O. V. Ivanova, et al. Comet 29P/Schwassmann-Wachmann 1 dust environment from photometric observation at the SOAR Telescope. *Icarus* **2019**, 319, 58–67.
106. D. Brownlee, P. Tsou, J. Aléon, et al. Comet 81P/Wild 2 Under a Microscope. *Science (1979)* **2006**, 314 (5806), 1711–1716.
107. D. Bockelée-Morvan, N. Biver. The composition of cometary ices. *Philosophical Transactions of the Royal Society A: Mathematical, Physical and Engineering Sciences* **2017**, 375 (2097), 20160252.
108. M. Min, J. Hovenier, A. Dekoter, L. Waters, C. Dominik. The composition and size distribution of the dust in the coma of Comet Hale–Bopp. *Icarus* **2005**, 179 (1), 158–173.
109. F. Przygodda, R. van Boekel, P. Àbrahàm, et al. Evidence for grain growth in T Tauri disks. *Astron Astrophys* **2003**, 412 (2), L43–L46.
110. R. van Boekel, L.B.F.M. Waters, C. Dominik, et al. Spatially and spectrally resolved 10  $\mu\text{m}$  emission in Herbig Ae/Be stars. *Astron Astrophys* **2004**, 418 (1), 177–184.
111. L. Testi, T. Birnstiel, L. Ricci, S. Andrews, J. Blum, J. Carpenter, C. Dominik, A. Isella, A. Natta, J.P. Williams. D.J. Wilner. Dust in Protoplanetary Disks: Properties and Evolution; **2007**; pp 767–781.
112. T. Henning. Cosmic Silicates. *Annu Rev Astron Astrophys* **2010**, 48 (1), 21–46.
113. R. Cesaroni, Á. Sánchez-Monge, M.T. Beltrán, et al. Chasing discs around O-type (proto)stars: Evidence from ALMA observations. *Astron Astrophys* **2017**, 602, A59.

- 
114. C. Jager, F.J. Molster, J. Dorschner, T. Henning, H. Mutschke, L.B.F.M. Waters. Steps toward interstellar silicate mineralogy. IV. The crystalline revolution. *Astron Astrophys* **1998**, 339, 904–916.
  115. S. Weinbruch, H. Palme, B. Spettel. Refractory forsterite in primitive meteorites: Condensates from the solar nebula? *Meteorit Planet Sci* **2000**, 35 (1), 161–171.
  116. S. Messenger, L.P. Keller, D.S. Lauretta. Supernova Olivine from Cometary Dust. *Science (1979)* **2005**, 309 (5735), 737–741.
  117. T. Fujiyoshi, C.M. Wright, T.J.T. Moore. Mid-infrared spectroscopy of SVS13: silicates, quartz and SiC in a protoplanetary disc. *Mon Not R Astron Soc* **2015**, 451 (4), 3371–3384.
  118. M.J. Boruah, A. Gogoi, B.C. Nath, G.A. Ahmed. Light scattering studies of randomly oriented polycrystalline fayalite micro particles as interstellar dust analogues. *J Quant Spectrosc Radiat Transf* **2017**, 196, 213–221.
  119. P.S. Chen, X.H. Wang, J.H. He. Herbig Ae/Be Stars with the IRAS Low-Resolution Spectra. *Astrophys Space Sci* **2000**, 271 (3), 259–276.
  120. M. Honda, H. Kataza, Y.K. Okamoto, et al. Detection of Crystalline Silicates around the T Tauri Star Hen 3-600A. *Astrophys J* **2003**, 585 (1), L59–L63.
  121. C.A. Poteet, S.T. Megeath, D.M. Watson, et al. A Spitzer Infrared Spectrograph Detection of Crystalline Silicates in a Protostellar Envelope. *Astrophys J* **2011**, 733 (2), L32.
  122. P. Abraham, Á. Kóspál, M. Kun, et al. An UXor among FUors: extinction-related brightness variations of the young eruptive star V582 Aur. *Proceedings of the International Astronomical Union* **2018**, 14 (S345), 390–392.
  123. M.A. Corazzi, J.R. Brucato, G. Poggiali, et al. Thermal Desorption of Astrophysically Relevant Ice Mixtures of Acetaldehyde and Acetonitrile from Olivine Dust\*. *Astrophys J* **2021**, 913 (2), 128.
  124. T. Nguyen, I. Fourné, C. Favre, et al. Formation of amines: hydrogenation of nitrile and isonitrile as selective routes in the interstellar medium. *Astron Astrophys* **2019**, 628, A15.
  125. M. Bulak, D.M. Paardekooper, G. Fedoseev, H. Linnartz. Photolysis of acetonitrile in a water-rich ice as a source of complex organic molecules: CH<sub>3</sub>CN and H<sub>2</sub>O:CH<sub>3</sub>CN ices. *Astron Astrophys* **2021**, 647, A82.

- 
126. R. Basalgète, A.J. Ocaña, G. Féraud, et al. Photodesorption of Acetonitrile CH<sub>3</sub>CN in UV-irradiated Regions of the Interstellar Medium: Experimental Evidence. *Astrophys J* **2021**, 922 (2), 213.
  127. L.N.A. Dean J. A. Lange's Handbook of Chemistry; McGraw- Hill, **1999**.
  128. M. de Val-Borro, S.N. Milam, M.A. Cordiner, et al. Measuring molecular abundances in comet C/2014 Q2 (Lovejoy) using the APEX telescope. *Mon Not R Astron Soc* **2018**, 474 (1), 1099–1107.
  129. M.J. Mumma, S.B. Charnley. The Chemical Composition of Comets—Emerging Taxonomies and Natal Heritage. *Annu Rev Astron Astrophys* **2011**, 49 (1), 471–524.
  130. V.M. Rivilla, J. Martín-Pintado, I. Jiménez-Serra, et al. Prebiotic Precursors of the Primordial RNA World in Space: Detection of NH<sub>2</sub>OH. *Astrophys J* **2020**, 899 (2), L28.
  131. N.F.W. Ligterink, H. Calcutt, A. Coutens, et al. The ALMA-PILS survey: Stringent limits on small amines and nitrogen-oxides towards IRAS 16293–2422B. *Astron Astrophys* **2018**, 619, A28.
  132. N.F. Kleimeier, A.K. Eckhardt, R.I. Kaiser. A Mechanistic Study on the Formation of Acetic Acid (CH<sub>3</sub>COOH) in Polar Interstellar Analog Ices Exploiting Photoionization Reflectron Time-of-flight Mass Spectrometry. *Astrophys J* **2020**, 901 (1), 84.
  133. G. Santarossa, M. Iannuzzi, A. Varga A. Baiker. Adsorption of Naphthalene and Quinoline on Pt, Pd and Rh: A DFT Study. *ChemPhysChem* **2008**, 9, 401 – 413.
  134. P.K. Najeeb, U. Kadhane. Relative stability of naphthalene, quinoline and isoquinoline under high energy electron impact. *International Journal of Mass Spectrometry* **2017**, 414, 23–30.
  135. M. Alliat, D. Donaghy, X. Tu, J. W Bradley. Ionic Species in a Naphthalene Plasma: Understanding Fragmentation Patterns and Growth of PAHs. *J. Phys. Chem. A* **2019**, 123, 10, 2107–2113.
  136. C. S. Contreras, F. Salama. Laboratory Investigations of Polycyclic Aromatic Hydrocarbon Formation and Destruction in the Circumstellar Outflows of Carbon Stars. *The Astrophysical Journal Supplement* **2013**, 208 (1) 6-17.
  137. M. P. Bernstein, J. P. Dworkin, S.A. Sandford, L. J. Allamandola Ultraviolet irradiation of naphthalene in H<sub>2</sub>O ice: Implications for meteorites and biogenesis. *Meteoritics & Planetary Science* **2001** 36, 3, 351-358.

138. J. E. Elsila, M. R. Hammond, M. P. Bernstein, S. A. Sandford, R. N. Zare. UV photolysis of quinoline in interstellar ice analogs. *Meteoritics & Planetary Science* **2006**, 41, 5, 785–796.
139. J. B. Bossa, P. Theule, F. Duvernay, and T. Chiavassa. NH<sub>2</sub>CH<sub>2</sub>OH Thermal Formation in Interstellar Ices Contribution to the 5-8 μm Region Toward Embedded Protostars. *The Astrophysical Journal* **2009**, 707:1524–1532.
140. L. Chu, S. Yu, J. Wang. Degradation of pyridine and quinoline in aqueous solution by gamma radiation. *Radiation Physics and Chemistry* **2018**, 144, 322-328.
141. Gary Attard and Colin Barnes. Surfaces; Oxford Chemistry Primers.
142. W. Ranke. Thermal analysis - TDS. Lecture. Fritz-Haber Institute 2005.

# CHAPTER 4

## OXYPAH -POLYMERS AS MEDIATORS FOR PREBIOTIC PROCESSES ON EARLY EARTH: SYNTHESIS AND CHARACTERIZATION

*“The total disorder in the universe, as measured by the quantity that physicists call entropy, increases steadily as we go from past to future. On the other hand, the total order in the universe, as measured by the complexity and permanence of organized structures, also increases steadily as we go from past to future”*

— Freeman Dyson, Page-Barbour lecture, University of Virginia, 2004

### 4.1 Introduction

Polycyclic aromatic hydrocarbons (PAHs), known to be widely diffused in the Universe, represent more than 20% of the carbon in the Universe, being implicated as the key IR emitting components in the interstellar medium.<sup>1</sup> They are considered possible starting materials for the formation of molecules related to life. Besides serving as a possible source of small carbon molecules, PAHs and complex molecular species derived from their polymerization may also provide protective matrices or mineral coating layers that can both promote or catalyze molecular synthesis and preserve biomolecules from damaging radiations. In this context,

growing interest is currently focused on oxyPAHs because of their chemical properties such as higher polarity, ensuring stronger adsorption on minerals, a much higher reactivity and easy polymerization. Even when present as minor components of the organic PAH pool in a given astrophysical system, oxyPAH may play a more impacting role in the carbon conversion processes.

Extensive literature data show the identification of oxygenated derivatives of PAHs, oxyPAHs, as primary photochemical transformation products in water–ice matrices mimicking the interstellar medium.<sup>2</sup> Most of these studies included naphthalene as the probe PAH and indicated extensive oxygenation with the formation of 1-HN as the dominant product, along with dihydroxylated derivatives and naphthoquinones.<sup>3</sup> These oxidated products can undergo oxidative polymerization reactions, which usually involve an interplay of competing free radical and quinone coupling pathways.<sup>4</sup> Another relevant scenario is that oxyPAH formation and photoprocessing are involved as important determinants for the origin of the Insoluble Organic Matter (IOM), the major identified carbonaceous component in meteorites.<sup>5</sup>

An attractive hypothesis in this framework, that guided the design of the present Chapter, is that PAH-based polymers could act as a template, adsorbing selectively molecules, allowing their concentration, and promoting the formation of more complex molecules. Indeed, the polymers, through specific interactions with the molecules, can induce the orientation of reacting groups of neighboring molecules, similarly to the minerals. Moreover, PAH and oxyPAH-polymers could act as both catalytic and photoprotective layers ensuring that prebiotic molecules can be produced, assembled and preserved by extensive photodegradation and may have played a notable role in the self-assembly of the primitive organic molecules, acting as prototypes of enzyme systems. This hypothesis is rooted in the known

photoprotective properties of these types of pigments,<sup>6</sup> strictly associated with their broad band absorption in the whole UV-visible portion of the electromagnetic spectrum.

Chapter 2 stressed the feasibility of the formation of dimeric compounds from 1,8-DHN and 1-HN under conditions of astrochemical relevance, as well as the formation of higher oligomeric species.

Recently the oxidative polymerization of 1-HN, 1,8-DHN, and 1,6-DHN adsorbed on forsterite and anatase was investigated.<sup>7</sup> In accordance with the polymeric material-based Panspermia hypothesis, PAH and oxyPAH-polymers could have had a role in the first stages of life and could have been proposed as primitive panspermia seeds.<sup>8</sup> Based on this background, this Chapter is directed to a detailed investigation of the oxidation reaction of various hydroxylated compounds, such as 1,8-DHN and 1-HN, to assess the structural, physical and chemical properties of the polymeric species and to evaluate their putative role in prebiotic processes.

The Chapter will be structured as follows:

1. isolation and characterization of the polymers isolated from the oxidative polymerization of 1,8-DHN and 1-HN;
2. study of the oxidation pathways and mode of coupling of 1,8-DHN and 1-HN via the isolation and characterization of the main oligomer intermediates.

This work has been carried out in collaboration with Prof. G. Falco of University of Napoli Federico II, Italy, Dr. G. Gentile from Institute for Polymers Composites and Biomaterials-CNR, Pozzuoli, Italy, Prof. M. Bietti of University of Rome “Tor Vergata”, Rome, Italy, Prof. V. Barone from Scuola Normale Superiore, Pisa and Prof. O. Crescenzi from University of Napoli Federico II.

The data reported in this Chapter have been published in the following articles: **P1**, **P2**, **P4**, **P5**, **P6**, **P7** and presented in meeting **PP1** and **PP2**.

## 4.2 Results and discussion

The first part of the work was aimed at the synthesis, structural characterization and properties of the insoluble OxyPAH-polymers starting from 1,8-DHN and 1-HN monomers.

Specific aims are to elucidate the steps leading to the build-up of the oxidative polymer and to characterize their properties for a potential role as a catalytic matrix on which prebiotic molecules could be adsorbed, driving their evolution in prebiotic processes.

The preparation of the OxyPAH-polymers was carried out under physiologically relevant conditions by using the enzymatic system horseradish peroxidase (HRP)/H<sub>2</sub>O<sub>2</sub> in 0.1 M phosphate buffer at pH 7.0. The course of the reaction was monitored by UV-vis spectroscopy and by isolating/characterizing the intermediate oligomeric compounds; finally, the resulting polymers were isolated and characterized.

### 4.2.1 Spectrophotometric analysis

#### 4.2.1.1 1,8-Dihydroxynaphthalene

The oxidative polymerization of 1,8-DHN started rapidly at room temperature and under vigorous stirring as soon as the hydrogen peroxide was added to the solution. The color of the reaction mixture turned from light yellow to bluish-green after 3 minutes and then to dark brown after 30 minutes (Figure 1). The spectrophotometric monitoring of the reaction course revealed marked changes in the absorption profile, with the initial growth of two maxima centred at 583 and 654 nm, accounting for the bluish-green hue of the mixture, followed by evolution toward an absorption profile covering the entire UV-vis spectrum (dark brown colour, Figure 2). Laser flash photolysis experiments and computational calculations demonstrated that the rapidly

developing blue-green stage of the reaction corresponds to the formation of extended quinone forms at the dimer level.<sup>9</sup>

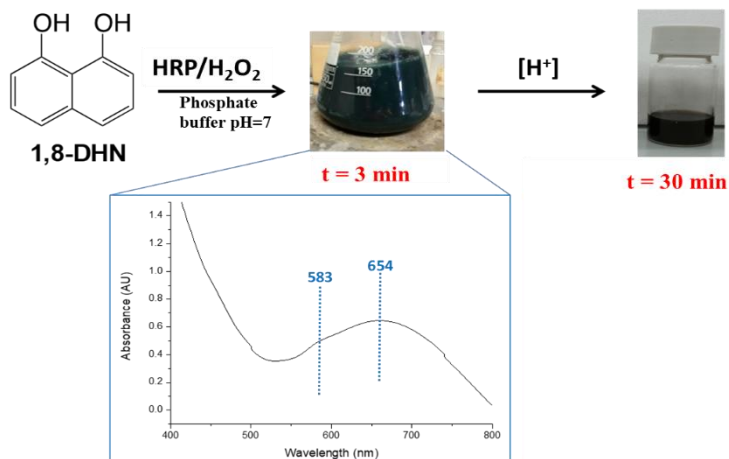


**Figure 1** | Oxidation of 1,8-DHN with the HRP/H<sub>2</sub>O<sub>2</sub> system under physiologically relevant conditions

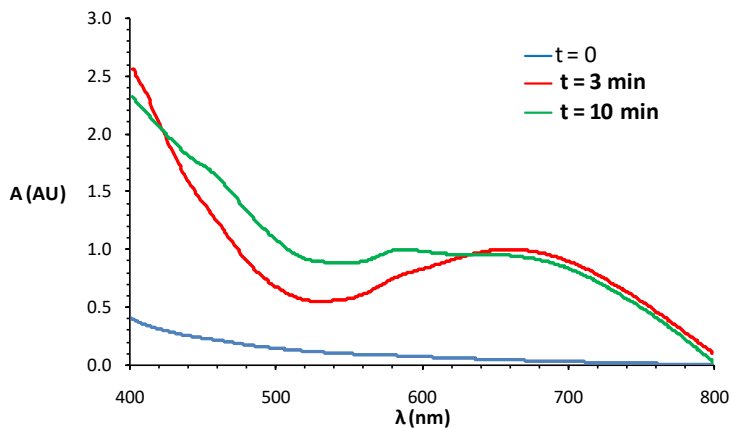


**Figure 2** | Time course of the oxidation reaction of 1,8-DHN by UV-vis spectroscopy. The t<sub>0</sub> spectrum was recorded before the addition of the oxidant.

### 4.2.1.2 1-Naphthol

The oxidative polymerization of 1-HN was carried out under the same conditions adopted for the 1,8-DHN. In this case, the reaction was quite slow, and the mixture turned initially to dark violet after 5 minutes. This colour remained unchanged throughout the reaction time (Figure 3). The spectrophotometric monitoring of the reaction indicated the initial growth of two maxima at 416 and 500 nm and later of a third maximum centred at 650 nm, accounting for the violet colour of the mixture (Figure 4). In this case, the generation of a broadband profile was not observed.

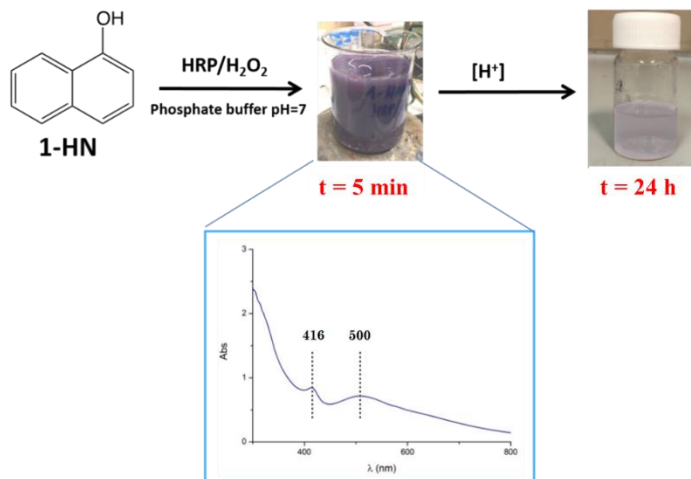


**Figure 3** | Oxidation of 1-HN with the HRP/H<sub>2</sub>O<sub>2</sub> system under physiologically relevant conditions.

### 4.2.2 Laser flash photolysis (LFP) experiments

The characterization of the early transient species produced by the oxidation of 1,8-DHN and 1-HN was performed by LFP.

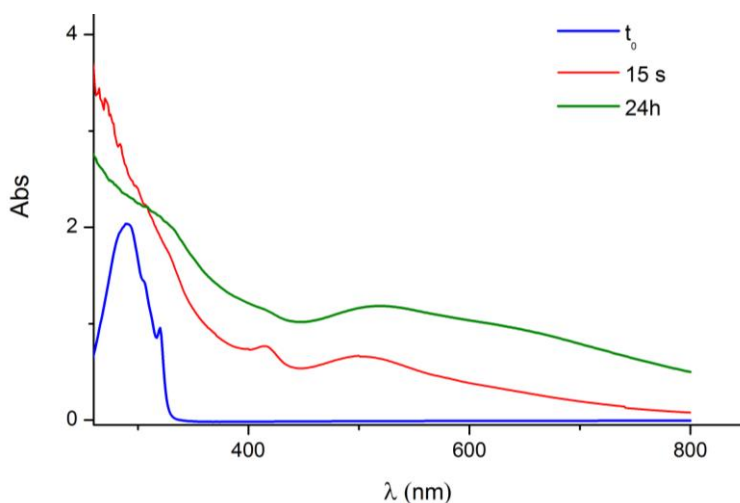
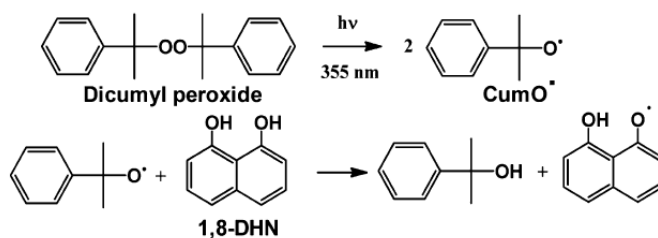


**Figure 4** | Time course of the oxidation reaction of 1-HN by UV-vis spectroscopy. The  $t_0$  spectrum was recorded before the addition of the oxidant.

The absorption properties and kinetics of the species formed from 1,8-DHN under hydrogen atom transfer (HAT) conditions were explored by using, as abstracting species, the cumyloxy radical ( $\text{CumO}\cdot$ ) and two N-oxyl radicals such as phthalimide-N-oxyl (PINO) and benzotriazole-N-oxyl radical (BTNO).  $\text{CumO}\cdot$  was generated by 355 nm LFP of acetonitrile solutions containing dicumyl peroxide as shown in Scheme 1.<sup>10</sup>



**Scheme 1** | Generation of the cumyloxy radical by LFP and its action on 1,8-DHN.<sup>11</sup>

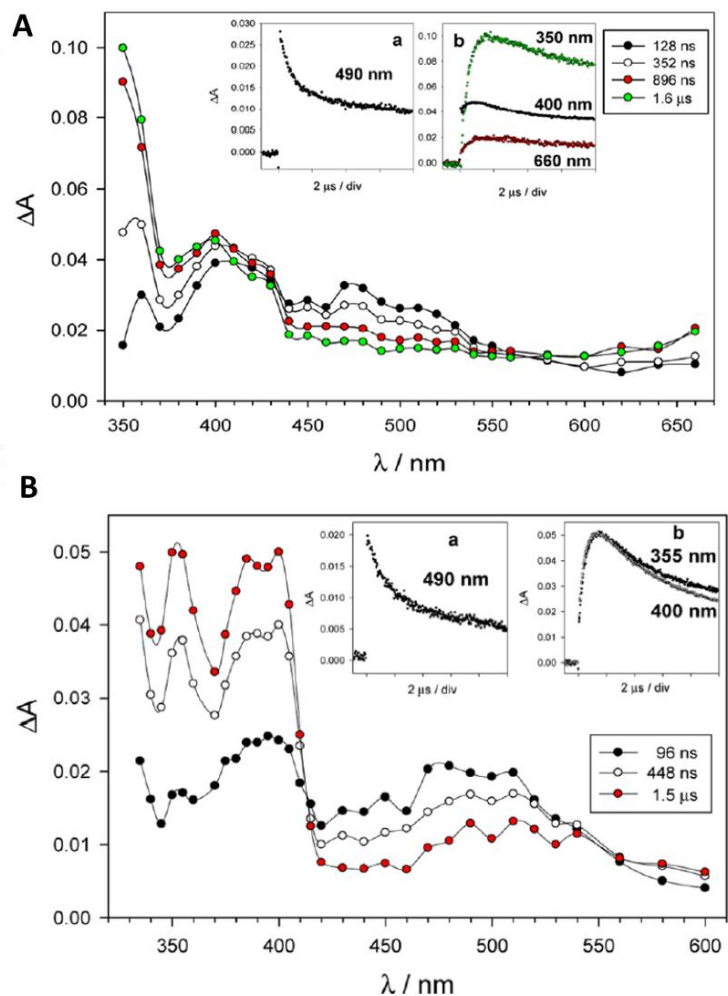


**Figure 5** | Time-resolved absorption spectra observed after 355 nm LFP of an argon-saturated MeCN solution ( $T = 25\text{ }^{\circ}\text{C}$ ) containing dicumyl peroxide (1.0 M) and 1,8-DHN (3.0 mM) (A) or 1-naphthol (7.7 mM) (B) recorded at various time after the 8 ns, 10 mJ laser pulse. Insets: (a) Decay of the cumyloxyl radical monitored at 490 nm and (b) buildup and subsequent decay of absorption monitored at various wavelengths.

Figure 5 showed the spectral changes of an acetonitrile solution containing dicumyl peroxide and 1,8-DHN (A) or 1-naphthol (B) observed after 355 nm LFP. In the case of 1,8-DHN, the accumulation of a transient species characterized by three absorption bands centered at 350, 400, and >660 nm, which can be attributed to the 8-hydroxy-1-naphthoxyl radical generated by HAT, occurred concurrently with the decay of CumO• seen at 490 nm.

Comparative analysis of the traces obtained from 1-HN collected under the same conditions revealed a significantly different profile.<sup>12</sup> This finding suggested that the contribution of the second OH group on the adjacent ring was more significant in defining the free-radical absorption capabilities than intramolecular H-bonding.

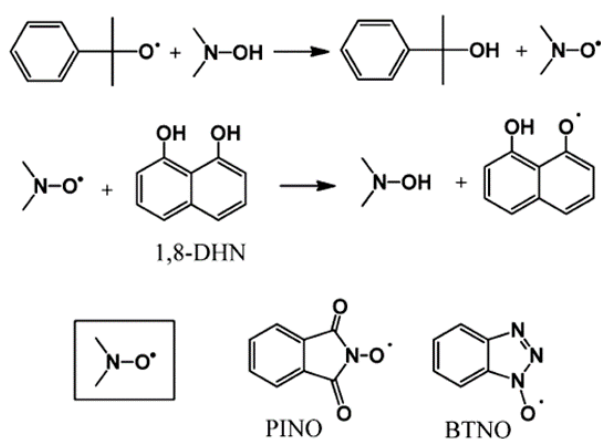
The slope of the observed rate constant ( $k_{\text{obs}}$ ) versus [substrate] plots, whose  $k_{\text{obs}}$  values were measured after the development of the naphthoxyl radical absorption band at the various substrate concentrations, was used to determine the second-order rate constants ( $k_{\text{H}}$ ) for the reaction of CumO• with these substrates. The  $k_{\text{H}}$  values so obtained confirm the previously reported stabilizing role of H-bonding exerted by the peri OH group, showing an approximately threefold increase in moving from mono to dihydroxynaphthalenes (Table 1).

**Table 1** | Second-order rate constants ( $k_{\text{H}}/\text{M}^{-1} \text{s}^{-1}$ ) for the reaction of the cumyloxyl radical with hydroxynaphthalenes, measured in MeCN at  $T = 25 \text{ }^{\circ}\text{C}$ .

Substrate	$\lambda_{\text{monit}}$ (nm)	$k_{\text{H}}^{\text{a}}$
1-HN	400	$1.43 \pm 0.02 * 10^8$
1,8-DHN	360	$3.90 \pm 0.02 * 10^8$

<sup>a</sup>Measured following the buildup of the naphthoxyl radical absorption bands between 360 and 420 nm. Average of two independent kinetic experiments.

HAT from 1,8-DHN was also evaluated on the longer millisecond scale using two aminoxyl radicals, PINO and BTNO, which are substantially less reactive than CumO• as hydrogen atom abstractors. In the LFP experiments, PINO and BTNO were produced by HAT from N-hydroxyphthalimide and 1-hydroxybenzotriazole (HBT) to CumO• (Scheme 2), respectively, which in turn was generated as previously mentioned.<sup>13–17</sup>



**Scheme 2** | Generation of PINO and BTNO by LFP and their action on 1,8-DHN.

Figure 6 showed the time-resolved absorption spectra observed after 355 nm LFP of an argon-saturated MeCN solution with dicumyl peroxide (1.0 M), HBT (9.2 mM), and 1,8-DHN (0.57 mM).

The production of a species with an absorption maximum at around 370 nm occurred concurrently with the millisecond timescale decay of the BTNO radical at the maximum absorption wavelength (480 nm).<sup>18</sup> The species absorbing at 370 nm was probably attributed to a coupling product produced from the dimerization of the 1,8-DHN phenoxyl radical since the lifetime of the naphthoxyl radical formed after HAT from 1,8-DHN was too short to allow its detection on this timescale (Figure 5(A), inset b).

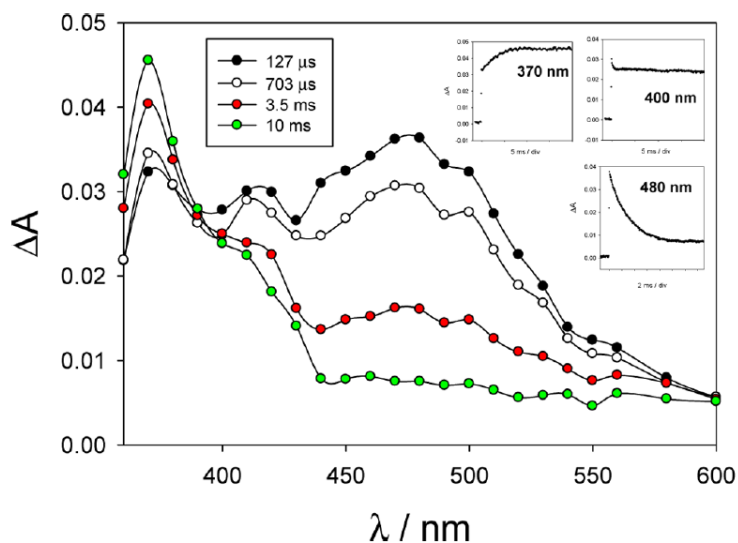


**Figure 6** | Time-resolved absorption spectra observed after 355 nm LFP of an argon-saturated MeCN solution ( $T = 25\text{ }^{\circ}\text{C}$ ) containing dicumyl peroxide (1.0 M), HBT (9.2 mM), and 1,8-DHN (0.57 mM) recorded at 127  $\mu\text{s}$  (black circles), 703  $\mu\text{s}$  (white circles), 3.5 ms (red circles), and 10 ms (green circles) after the 8 ns, 10 mJ laser pulse. Insets: Buildup of absorption monitored at 370 nm; buildup and subsequent decay of absorption monitored at 400 nm; and decay of absorption monitored at 480 nm.

Support to this hypothesis was given by the observation of a similar spectrum, characterized by an absorption band centered at 370 nm, when the reaction of  $\text{CumO}\cdot$  with 1,8-DHN was analyzed 1 ms after the laser pulse, that is, at a significantly longer time delay as compared to those of the spectra showed in Figure 4 (Figure 7).

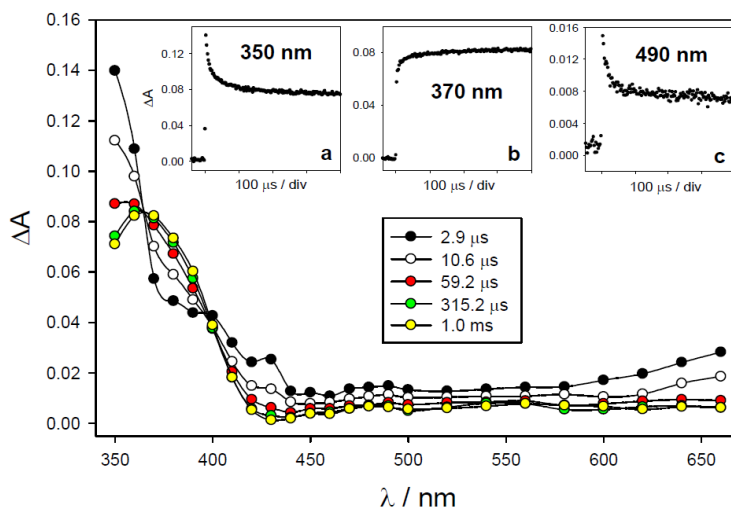


**Figure 7** | Time-resolved absorption spectra observed after 355 nm LFP of an argon saturated MeCN solution ( $T = 25\text{ }^{\circ}\text{C}$ ) containing dicumyl peroxide (1.0 M) and 1,8-DHN (3.0 mM) recorded at various times after the 8 ns, 10 mJ laser pulse. Insets: (a) decay of absorption monitored at 350 nm; (b) buildup of absorption monitored at 370; (c) decay of absorption monitored at 490 nm.

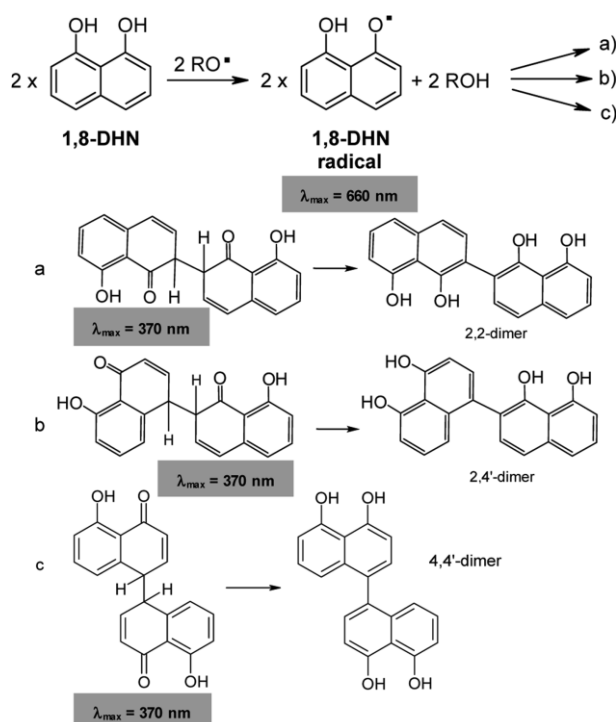
The observed rate constants ( $k_{\text{obs}}$ ) were determined during the decay of PINO or BTNO at their maximum absorption wavelengths (380 and 480 nm, respectively) using an excess of the substrate under pseudo-first-order conditions.<sup>18,19</sup> The slope of the  $k_{\text{obs}}$  versus [substrate] plots was used to calculate the  $k_{\text{H}}$  values for the HAT from 1-HN and 1,8-DHN to PINO and BTNO. The resulting rate constants are reported in Table 2.

As seen for HAT promoted by  $\text{CumO}\cdot$ , the measured  $k_{\text{H}}$  values increased from mono to dihydroxynaphthalenes. However, compared to  $\text{CumO}\cdot$ , the N-oxyl radicals showed noticeably bigger differences [ $k_{\text{H}}(1,8\text{-DHN})/k_{\text{H}}(1\text{-naphthol}) = 21.8, 14.6,$  and  $2.7$  for PINO, BTNO, and  $\text{CumO}\cdot$ , respectively]; this behavior is reasonable considering the lower intrinsic reactivity of the former radicals with respect to the

latter one. In Scheme 3, some of the possible species that may account for the dynamic absorption data in Figures 5 and 6 with significant absorption maxima are shown.

**Table 2** | Second-order rate constants ( $k_H/M^{-1} s^{-1}$ ) for the reaction of the PINO and BTNO radicals with hydroxynaphthalenes, measured in MeCN at  $T = 25\text{ }^\circ\text{C}$ .

Substrate	$k_H$ (PINO)	$k_H$ (BTNO)
1-HN	$5.5 \pm 0.3 \times 10^4$	$3.5 \pm 0.5 \times 10^4$
1,8-DHN	$1.2 \pm 0.1 \times 10^6$	$5.1 \pm 0.1 \times 10^5$

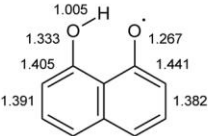
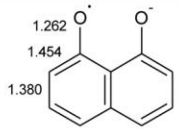
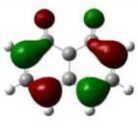
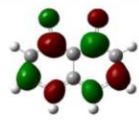


**Scheme 3** | Mechanism Accounting for the Formation of 1,8-DHN Dimers.

Furthermore, a detailed computational investigation of the structural and spectroscopic properties of the principal oxidation products of 1,8-DHN was performed at the DFT level of theory.

To address the regiochemistry of the initial coupling step, the investigation of the properties of the first-formed radical was carried out. A representation of the most stable form of the 1,8-DHN free radical [(8-hydroxynaphthalen-1-yl)oxidanyl] and its anion, such as structural parameters, spin density, singly occupied molecular orbital (SOMO), and main electronic transitions with relevant oscillator strengths<sup>20–24</sup> was shown in Table 3. The simulated absorption spectrum was provided in Figure 8.

**Table 3** | Computed (PBE0/6-31+G(d,p)/PCM) Properties of the 1,8-DHN Radical and Its Anion.

Bond distances / Å	PG	SOMO	LUMO	Spin density	$\lambda$ / nm ( $f$ ) <sup>a</sup>
	$C_s$				675.5 (0.06); 345.0 (0.05); 309.5 (0.12); 304.3 (0.07)
	$C_2$				977.8 (0.06); 326.3 (0.16); 311.6 (0.09)

<sup>a</sup>Selected ( $\lambda > 300$  nm,  $f > 0.05$ ) electronic transitions (TD-PBE0/6-311++G(2d,2p)/PCM).

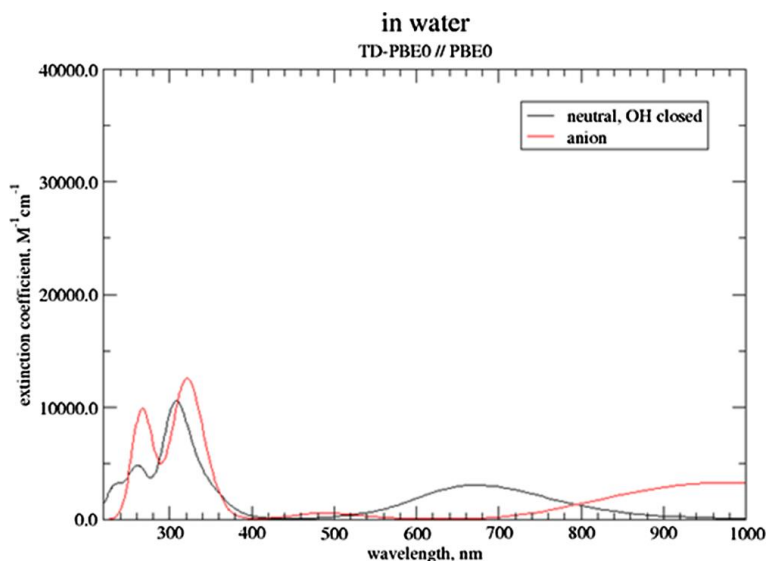


**Figure 8** | Simulated(TD-PBE0/6-311++G(2d,2p)/PCM//PBE0/6-31+G(d,p)/PCM) absorption spectrum of the 1,8-DHN radical and its anion.

Examining the simulated radical spectra revealed distinct maxima expected at around 320 and 670 nm. These spectra closely matched the trace of the evolving species in the LFP experiment, which was ascribed to the first generated free radical. The relative stability of the early coupling products before aromatization was then compared to look into the regioselectivity issue caused by the radical coupling phase. The underlying premise was that the free-radical dimerization step obeys the Bell-Evans-Polanyi principle and is under kinetic control, whereby the distribution of the dimer product is determined by the energies of the transition states, which reflect the relative stability of the isomeric 2,2'-, 2,4'-, and 4,4'-coupling products (Scheme 3). The energies calculated for the most stable conformers of the isomeric coupling products are listed in Table 4. The 2,2'-dimer seems to be a little bit more stable than the 2,4'- and 4,4'-dimers in that order.

**Table 4** | Relative Stabilities of Isomeric 1,8-DHN Coupling Products (Neutral Forms in Water, PBE0/6-31+G(d,p)/ PCM)<sup>a</sup>.

isomer	most stable conformer	PG	G <sub>SMD,RRHO</sub> /H <sub>a</sub> <sup>b</sup>
<b>2,2', DL</b>	T, OH closed	C2	-1070.096322 (0.4)
<b>2,2', meso</b>	G-, OH closed	C1	-1070.096901 (0.0)
<b>2,4', RR</b>	T, OH closed	C1	-1070.095650 (0.8)
<b>2,4', RS</b>	G-, OH closed	C1	-1070.095064 (1.2)
<b>4,4', DL</b>	T, OH closed	C2	-1070.093814 (1.9)
<b>4,4', meso</b>	G-, OH closed	C1	-1070.092763 (2.6)

<sup>a</sup>In parentheses relative energies (kcal mol<sup>-1</sup>) referred to the most stable form (in bold). <sup>b</sup>Free energy computed at the rigid rotor/ harmonic oscillator level, including SMD nonelectrostatic contributions.

Figure 9 reported the simulated absorption spectra of the coupling products. For all species, a similar absorption at about 360 nm could be expected. This maximum is close to the absorption maximum discovered in the LFP studies using the BTNO radical, thus supporting the identification of the transient species produced in the LFP experiment as dimers of 1,8- DHN.

### 4.2.3 Isolation and characterization of oligomer intermediates in the oxidation of 1,8-DHN and 1-HN

To gain further insight into the mode of polymerization of 1,8-DHN and 1-HN, the oligomer intermediates formed during the course of the oxidation reaction, were isolated and characterized.

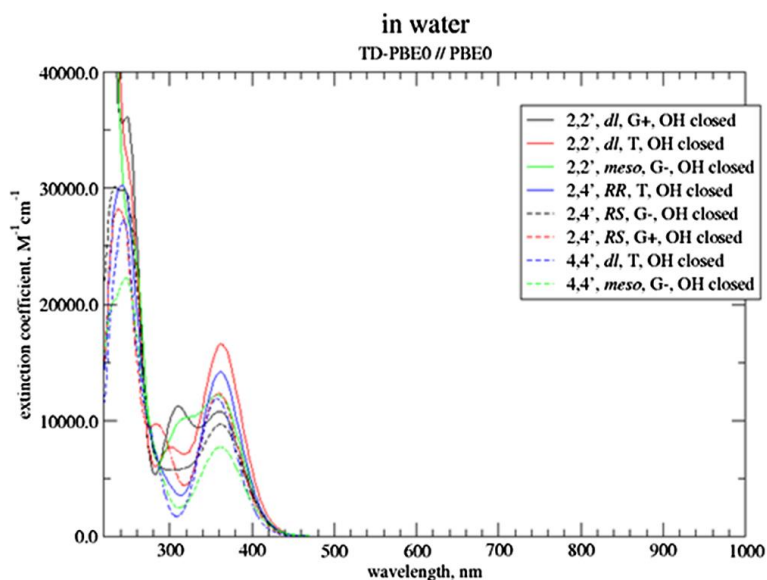


**Figure 9** | Simulated(TD-PBE0/6-311++G(2d,2p)/PCM//PBE0/6-31+G(d,p)/PCM) absorption spectra of the most stable 1,8-DHN coupling products.

The oxidation reactions were run under the same conditions reported in the previous section but, in this case, the reaction was stopped with the reducing agent sodium dithionite. Each mixture was extracted with ethyl acetate and the organic layers were subjected to acetylation by treatment with acetic anhydride and pyridine, to prevent further oxidation processes. The acetylated mixture was subjected to liquid chromatography on silica gel and the resulting products were all analysed by mono- and bi-dimensional NMR spectroscopy and mass spectrometry (Figure 10).

#### 4.2.3.1 1,8-Dihydroxynaphthalene

The oxidative polymerization of 1,8-DHN was carried out according to the scheme in Figure 10. After 5 seconds the reaction mixture was reduced, worked up and subjected to acetylation. LC-ESI(+)-MS analysis of the acetylated reaction mixture revealed the presence of a main band eluted at 30-31 minutes that was identified as

a mixture of three acetylated dimers (Figure 11). These latter were isolated in pure form by repeated chromatographic steps and subjected to 1D and 2D NMR analysis.

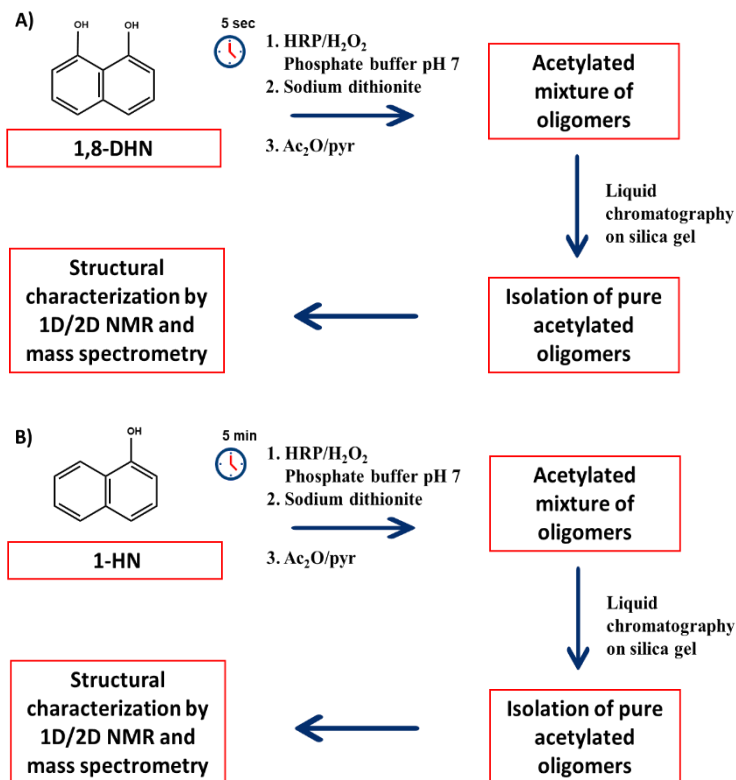


**Figure 10** | General procedure for the isolation of oligomeric intermediates from 1,8-DHN (A) and 1-HN (B).

Inspection of the <sup>1</sup>H NMR spectra in comparison with that of acetylated 1,8-DHN allowed us to deduce that two of the three dimers were characterized by a symmetric structure (Figure 12).

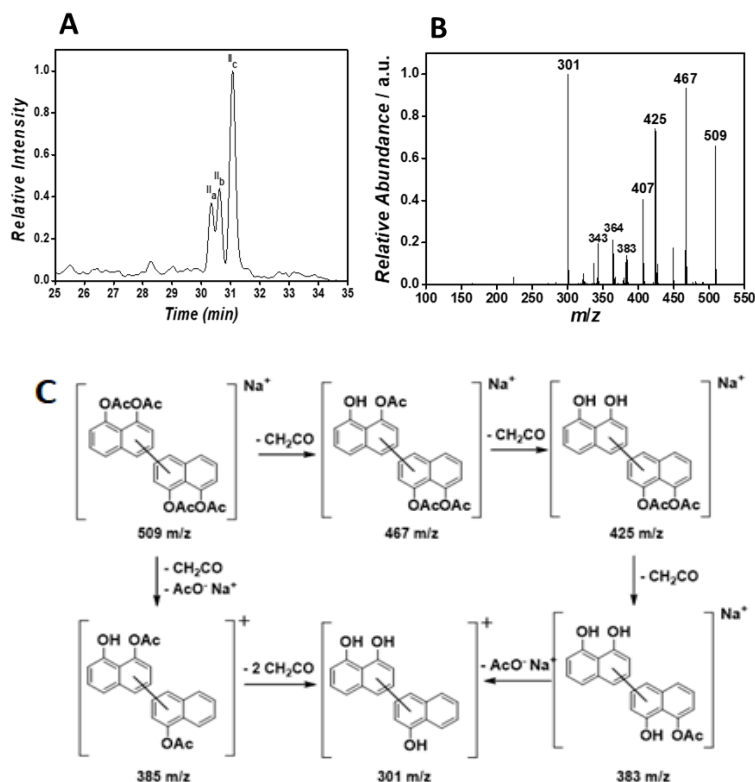


**Figure 11** | LC-ESI(+)-MS chromatogram of the acetylated mixture of 1,8-DHN. (A), corresponding ESI MS/MS spectrum in positive ion mode (B) and proposed fragmentation pattern of the pseudomolecular ion peak at  $m/z$  509 (C).

By inspection of the  $^1\text{H}$ ,  $^1\text{H}$  COSY,  $^1\text{H}$ ,  $^{13}\text{C}$  HSQC and  $^1\text{H}$ ,  $^{13}\text{C}$  HMBC spectra it was possible to assign to the three compounds the structures of the 2,2'-dimer **1**, 2,4'-dimer **2** and 4,4'-dimer **3**. Figure 13 reported the two-dimensional NMR spectra of dimer **1**, as an example. Figure 14 showed the  $^1\text{H}$  and  $^{13}\text{C}$  NMR assignments for 1,8-DHN dimers.

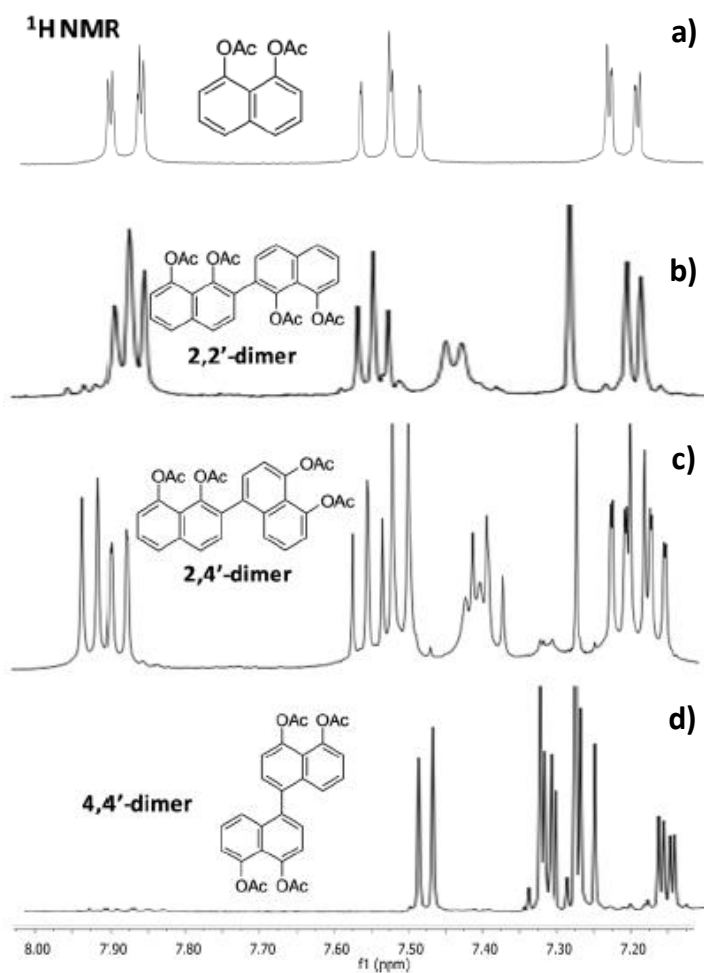


**Figure 12** |  $^1\text{H}$  NMR (aromatic protons region) spectra of: acetylated 1,8-DHN (a), acetylated 2,2'-dimer (b), acetylated 2,4'-dimer (c), acetylated 4,4'-dimer (d).

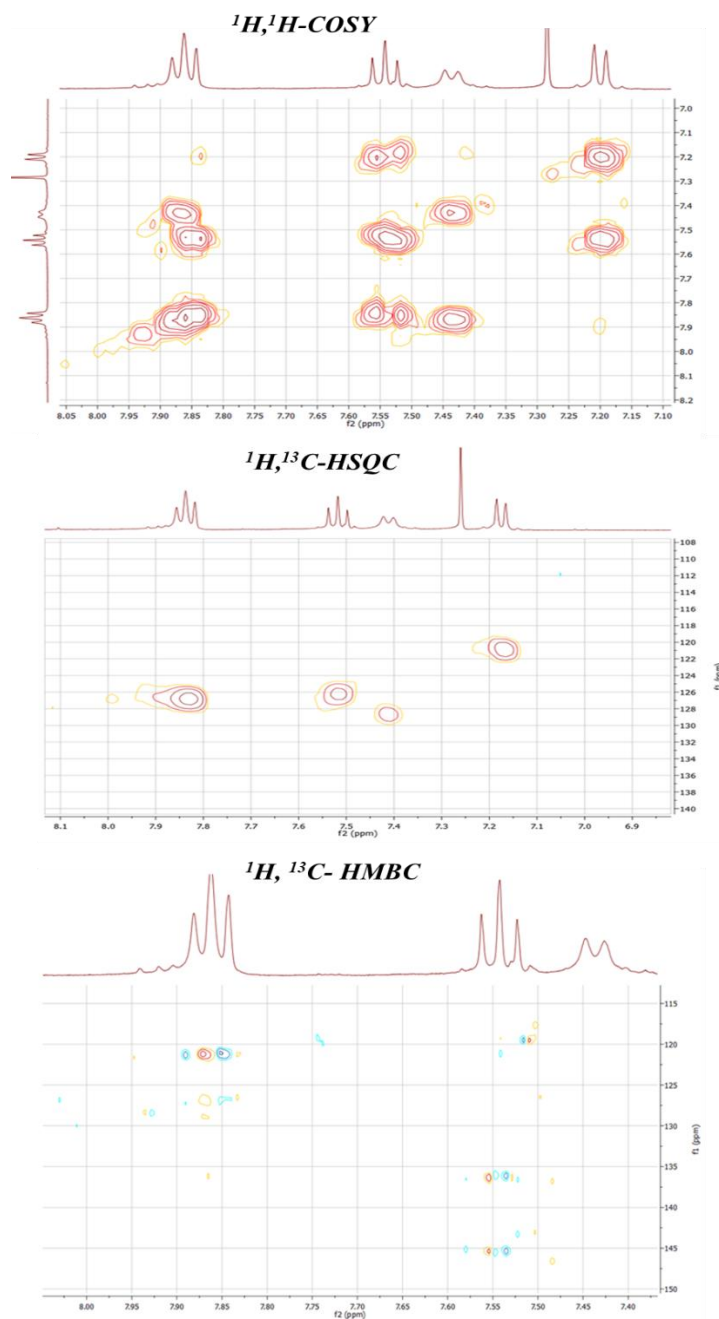


**Figure 13** | <sup>1</sup>H, <sup>1</sup>H-COSY, <sup>1</sup>H, <sup>13</sup>C-HSQC, <sup>1</sup>H, <sup>13</sup>C-HMBC spectra (CDCl<sub>3</sub>) of **1** (selected region).



Finally, the structural characterization by 1D and 2D NMR spectroscopy of the isolated 1,8-DHN dimers as acetyl derivated indicated that the connectivities between the aromatic rings are of C-C type and are regiochemically determined by the substitution pattern of the starting monomer.

The coupling between the naphthalene units occurred preferentially at the C-2 and C-4 positions.

Further studies have indicated, through a combined experimental and theoretical investigation, that the first stages of oxidative polymerization were triggered by the initial H-atom abstraction from 1,8-DHN (Figure 15), leading to the formation of a naphthoxyl radical. This latter radical is highly stabilized via intramolecular H bonding deriving from the peculiar peri asset of the hydroxyl groups on the naphthalene ring. Evidence for this came from the analogies found between the simulated UV-vis absorption spectrum of the naphthoxyl radical and the time-resolved absorption spectra registered in the early phase of the oxidative polymerization process. Moreover, as mentioned before, DFT calculations predicted that 2,2'-dimer is slightly more stable than the 2,4'- and the 4,4'- dimers in that order. Thus, after the formation of the naphthoxyl radical the formation the 2,2'-dimerization is the most likely event, followed by a further oxidation step affording the corresponding extended quinones (Figure 15).<sup>9</sup>

#### 4.2.3.2 1-Naphthol

Because of the slower oxidation kinetic, the oxidation of 1-HN was stopped after 5 minutes and the oligomer intermediates could be isolated without the acetylation step. The reaction mixture was subjected to liquid chromatography on silica gel affording a single main product.

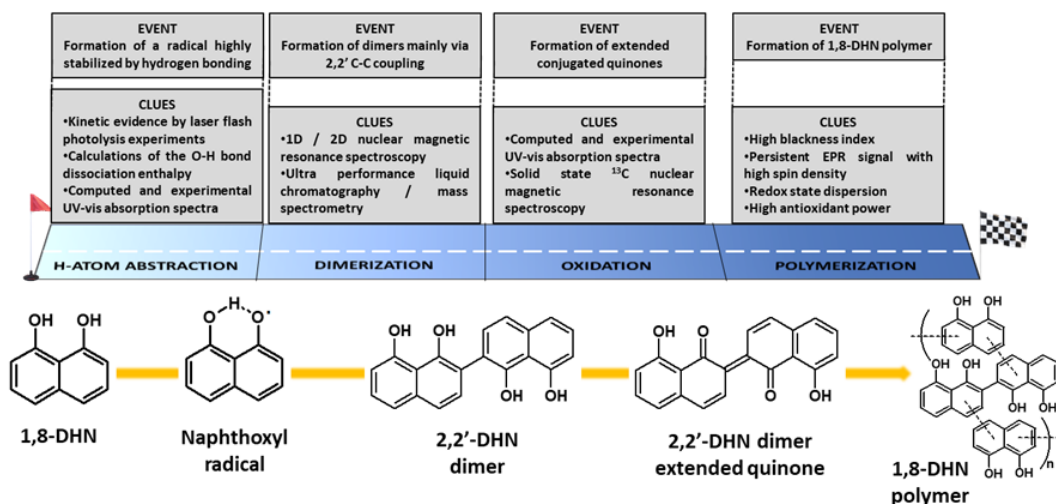


**Figure 15** | Key steps in the formation of 1,8-DHN polymers. The image adapted from Ref.<sup>25</sup>

The <sup>1</sup>H NMR spectrum (Figure 16) showed a number of signals accounting for a symmetric dimer of 1-HN. In detail, two double doublets at 7.89 and 8.36 ppm were clearly evident and easily ascribable to the H-5 and H-8 protons of the unsubstituted ring unit, and a doublet at 7.43 ppm relative to one of the two protons on the substituted ring unit. In the 7.55-7.65 region a multiplet was present accounting for the other protons of the 1-HN ring. The <sup>13</sup>C NMR spectrum (Figure 17) revealed the presence of ten signals supporting the symmetric nature of the compound. By inspection of the <sup>1</sup>H, <sup>1</sup>H COSY, <sup>1</sup>H, <sup>13</sup>C HSQC and <sup>1</sup>H, <sup>13</sup>C HMBC spectra (Figure 18) it was possible to assign to the product the structure of the 2,2'-dimer **4** (Figure 19).

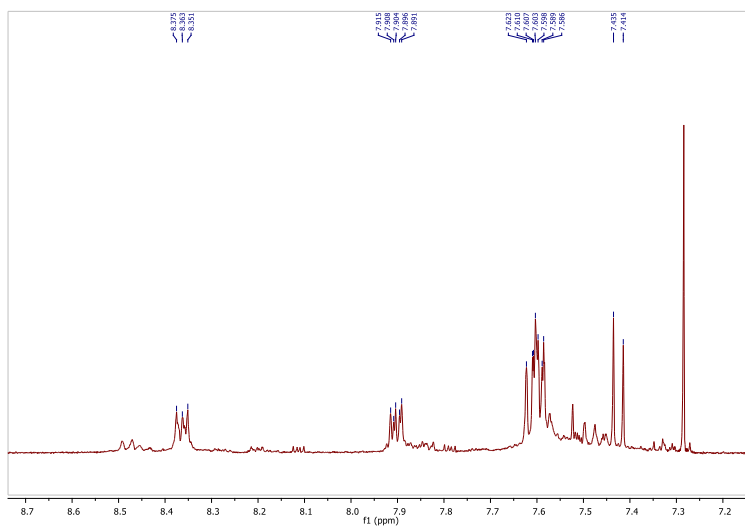


**Figure 16** |  $^1\text{H-NMR}$  spectrum ( $\text{CDCl}_3$ ) of **4** (selected region).

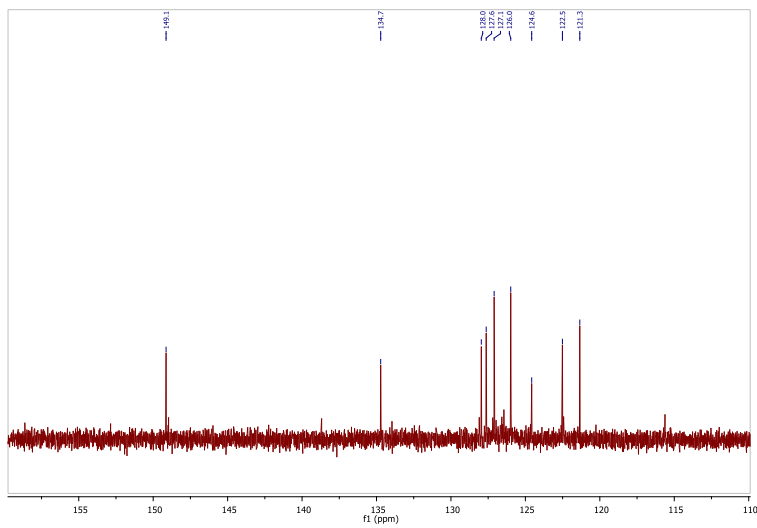


**Figure 17** |  $^{13}\text{C-NMR}$  spectrum ( $\text{CDCl}_3$ ) of **4** (selected region).

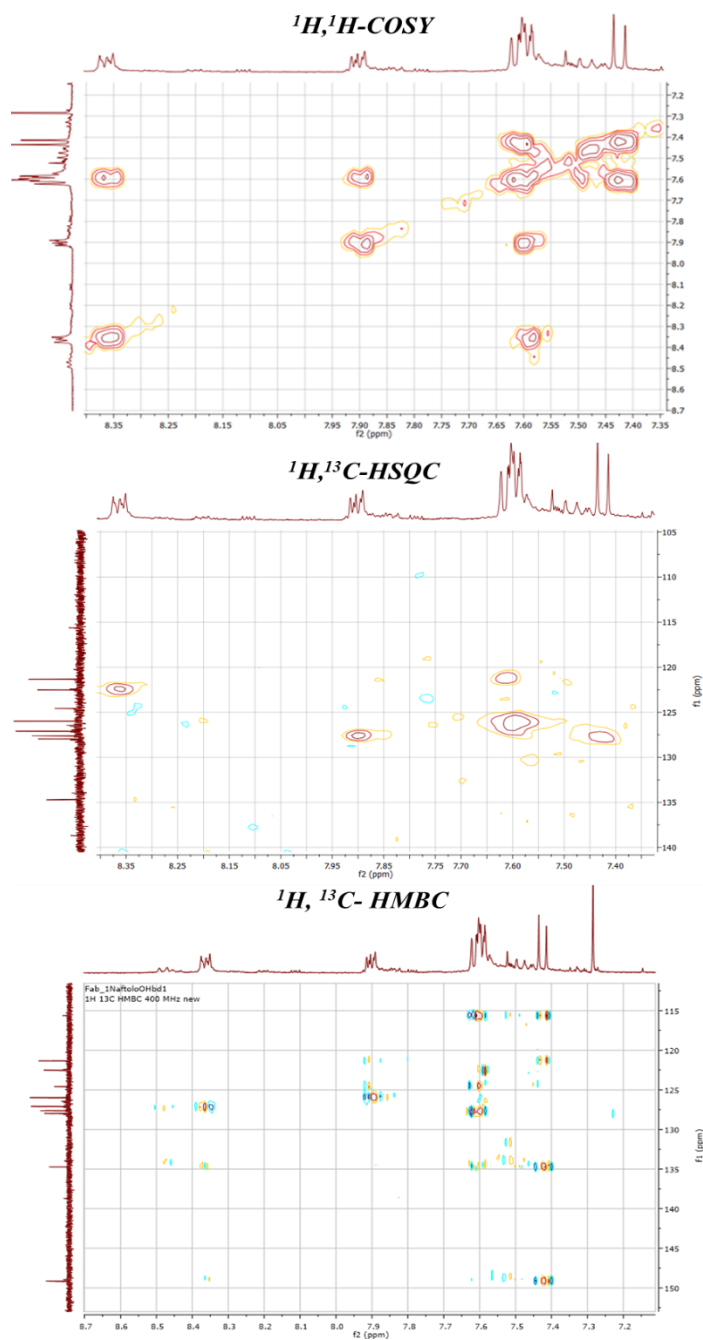


**Figure 18** |  $^1\text{H}, ^1\text{H}$ -COSY,  $^1\text{H}, ^{13}\text{C}$ -HSQC,  $^1\text{H}, ^{13}\text{C}$ -HMBC spectra ( $\text{CDCl}_3$ ) of **4** (selected region).

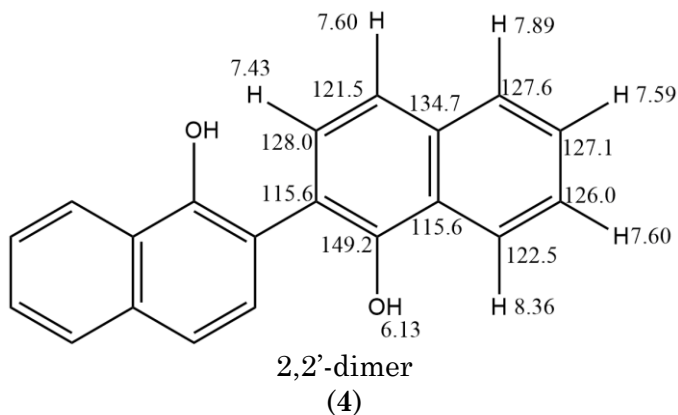


**Figure 19** |  $^1\text{H}$  and  $^{13}\text{C}$  NMR assignments for **4**.

#### 4.2.4 Isolation and characterization of polymers from 1,8-DHN and 1-HN

To isolate and characterize the insoluble precipitate formed by the oxidation of the 1-HN and 1,8-DHN, the reactions were carried out, under the same conditions described in the previous sections, for 24 hours. Then, the reaction mixtures were treated with HCl to pH = 2 to favor the precipitation of the solids that were collected by centrifugation and dried under reduced pressure

##### 4.2.4.1 1,8-Dihydroxynaphthalene

Oxidation of 1,8-DHN led to a dark brown precipitate (p-1,8-DHN) (Figure 20). Once isolated the dark precipitate was subjected to characterization by means of MALDI-MS, solid-state  $^{13}\text{C}$  NMR, UV-visible, ATR and electron paramagnetic resonance (EPR) analysis. The morphologic characterization of the polymer has been carried out through transmission electron microscopy (TEM) and scanning electron microscope (SEM) analysis.



**Figure 20** | Solid p-1,8-DHN.

The MALDI-MS spectrum of the freshly synthesized p-1,8-DHN is shown in Figure 21. The spectrum confirmed the polymeric nature of p-1,8-DHN, highlighting the presence of a regular pattern of oligomers up to  $m/z$  2400. The peaks were separated by 158 Da, corresponding to the “in-chain” 1,8-DHN unit and a matching series of  $([M+Na]^+)$  and  $([M+K]^+)$  species were detected. The dominant peaks were assigned to singly-charged distributions, up to 15 repeating units. The spectrum denoted the relative structural integrity of this polymer.

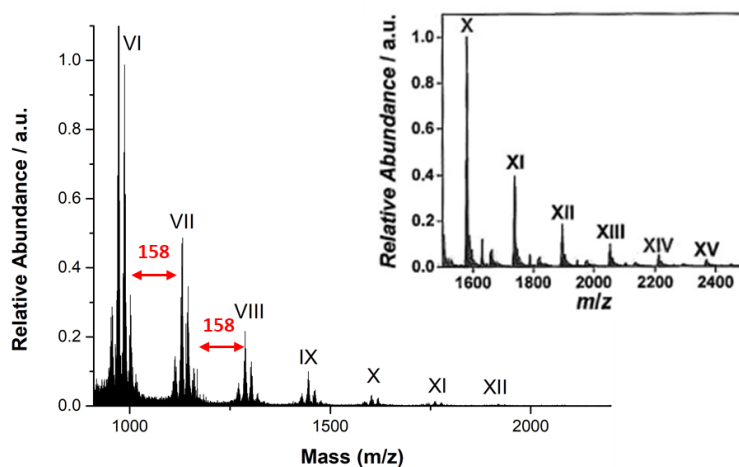


**Figure 21** | MALDI mass spectra of p-1,8-DHN.

Closer inspection of the clusters in the MALDI mass spectra provided important information on their redox state and behavior (Figure 21). In particular, each cluster was made of pseudomolecular ion peaks ( $[M+Na]^+$ ), for the fully reduced oligomeric structures, accompanied by peaks at lower  $m/z$  values, compatible with oxidized species (quinone-type or phenoxyl radical). These features of the peak clusters were consistent with the availability of each oligomer level of various oxidation states corresponding to sequential losses of H atoms.

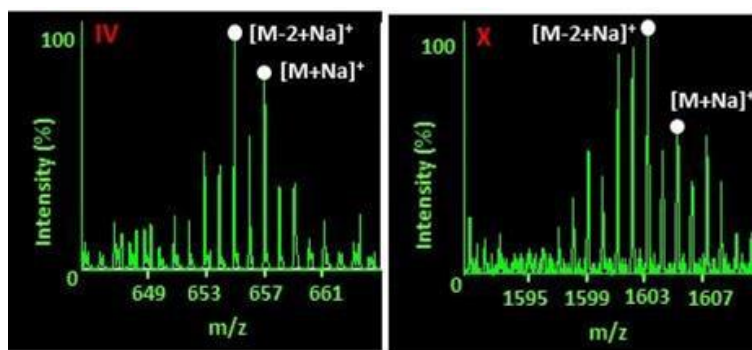


**Figure 22** | Comparison of the clusters of the  $[M+Na]^+$  pseudomolecular ion peaks for the 4-mer (IV) and 10-mer (X) oligomeric species of synthetic p-1,8-DHN.

A second relevant observation was that cluster complexity increased with increasing oligomer molecular weight, as shown in Figure 22 when comparing the clusters of the polymer at the early stage (4-mer stage) with those of the grown polymer (10-mer stage). Finally, the relative height of the pseudomolecular ion peaks for the fully reduced species usually decreased with increasing molecular mass, in accord with a shift of the dominant member of the cluster toward higher oxidation levels (lower  $m/z$  values). Overall these data indicated that higher oxidation levels with higher degrees of electronic/redox disorder become prevailing at higher levels of polymerization.

$^{13}\text{C}$  cross-polarization/magic-angle-spinning (CP/MAS) NMR analysis (Figure 23) revealed the presence of a wide overlap of bands in the range of  $\delta$  100-150, attributable to the aromatic carbons, with a small peak around 160 ppm, attributed to OH-bearing carbons, and a broader band at 190 ppm consistent with carbonyl-type carbons. These resonances overall were compatible with extended quinone-methide moieties framed within more or less large oligomeric scaffolds. No detectable aliphatic resonances, denoting oxidative breakdown of quinonoid moieties.

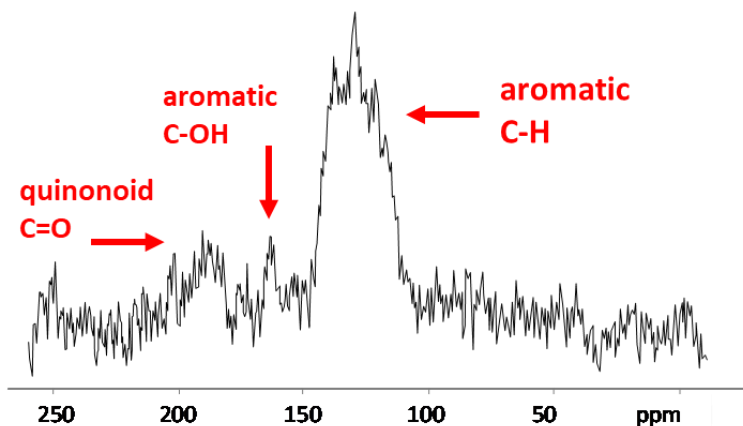


**Figure 23** | Solid-state  $^{13}\text{C}$  NMR spectrum of p-1,8-DHN.

The UV-visible spectrum of the DMF suspension of p-1,8-DHN showed a broadband absorption throughout the whole spectrum with minor shoulders at 390, 460 and 580 nm suggesting the presence of quinonoid moieties (Figure 24).

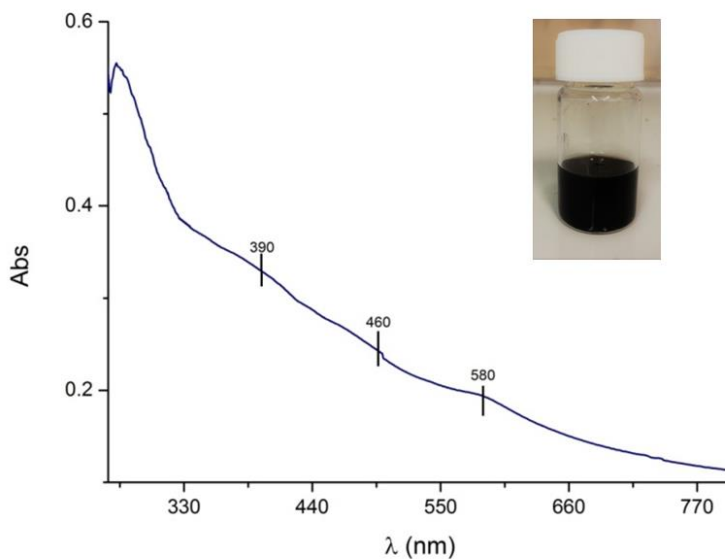


**Figure 24** | UV-Vis absorption spectrum of p-1,8-DHN in DMF.

ATR-FTIR analysis revealed the presence of a typical polymeric spectrum with main bands at  $1243$ ,  $1428$  and  $1621\text{cm}^{-1}$ , the latter due to the C=O stretching and C=C stretching of the aromatic rings, and a broadband around  $3400\text{ cm}^{-1}$  due to stretching vibrations of strongly hydrogen-bonded OH groups (Figure 25).

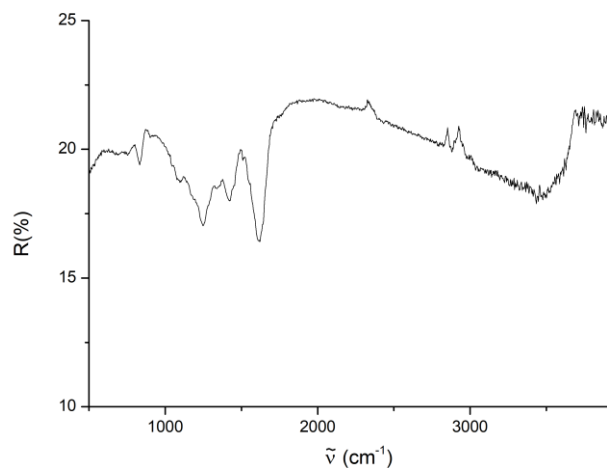


**Figure 25** | ATR spectrum of p-1,8-DHN.

Electron paramagnetic resonance (EPR) spectra (Figure 26) recorded on solid p-1,8-DHN revealed an unusually intense signal with spin density values close to  $10^{18}$  spin/g (Table 5).<sup>26,27</sup>

**Table 5** | EPR spectral parameters ( $W$  = line width in Gauss) recorded for p-1,8-DHN.

Sample	$W$ (G)	$g$ -factor	Spin/g
p-1,8-DHN	4.8	2.0030	$8.1 \times 10^{18}$

The  $g$ -factor value determined for p-1,8-DHN ( $g = 2.0030$ ) suggested a pronounced C-centered character, likely due to the lack of o-semiquinone moieties in the polymers.

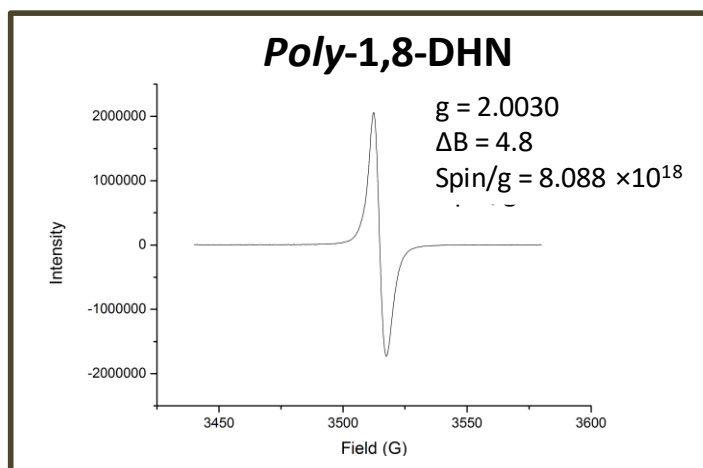


**Figure 26** | EPR spectrum of p-1,8-DHN in the solid state.

This observation would be compatible with extended quinone-methide moieties ensuring larger delocalization across planar segments of polymeric carbon platforms. A recent study, in which a comparative analysis of the properties of synthetic polymers obtained starting from different isomeric DHN was carried out, demonstrated a correlation between the optical properties, electron spin density and the redox state of DHN polymers. Thus, the blackness, defined as the property of polymer to absorb in the visible part of the spectrum, was proposed as a primary index of redox inhomogeneity and electron complexity reflecting the shift of oligomer populations toward the highest oxidation states.<sup>28</sup>

Zeta potential measurements performed on the 1,8-DHN polymer aqueous dispersions demonstrated that it is highly stable under a wide range of pH values, as shown in Figure 27. These data are in good agreement with those reported in McCallum et al.<sup>29</sup>

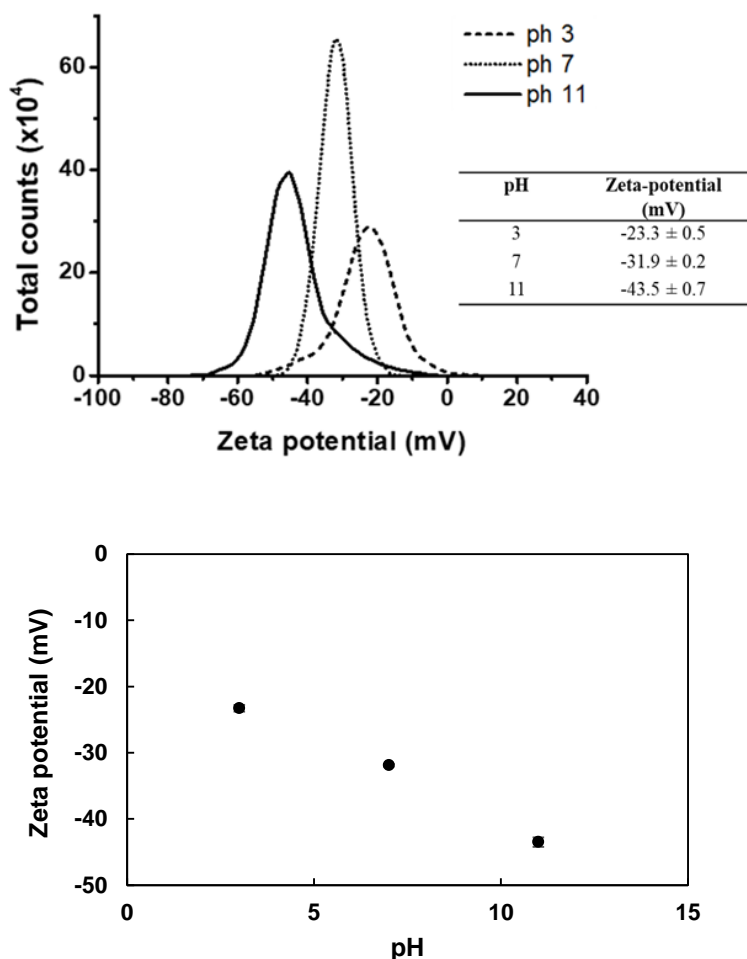


**Figure 27** | Zeta potential measurements carried out on 1,8-DHN polymers. The reported results represent the mean  $\pm$  SD of three separate experiments.

Overall, these results indicate that 1,8-DHN polymer exhibit high structural integrity.

To evaluate the microporous and adsorbing properties of p-1,8-DHN, the morphologic analysis of p-1,8-DHN by TEM and SEM analyses and gas adsorption experiments were performed (Figure 28).

TEM analysis (Figure 28 a,b,c) showed that this polymer is constituted by quasi-spherical primary particles, with an average diameter in the range between 20-40 nm, connected in loose aggregates. SEM analysis (Figure 28, d) revealed the aggregate structure of p-1,8-DHN, with the nanoparticle aggregates constituted by isodimensional primary particles.

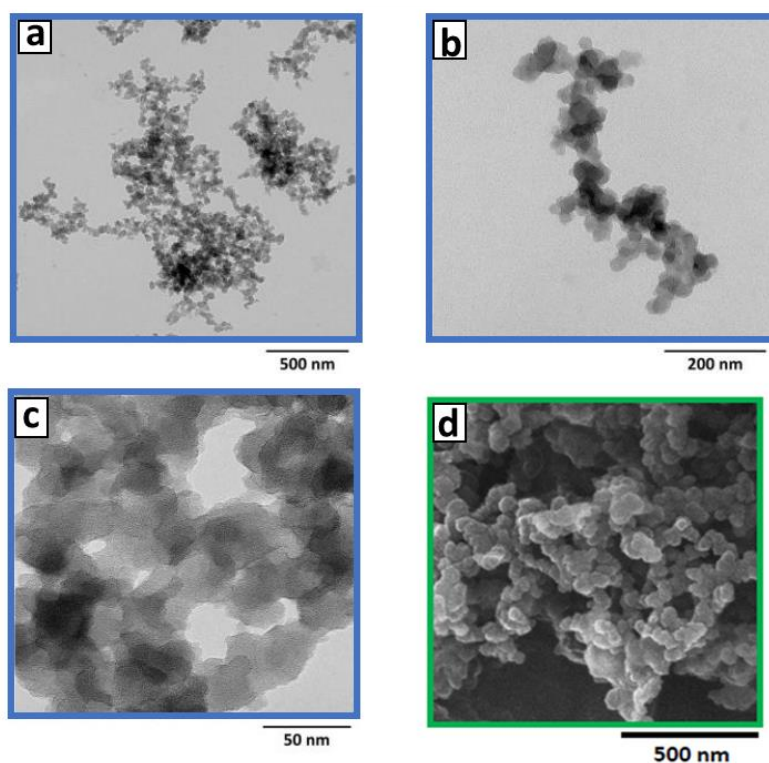


**Figure 28** | TEM (a, b, c) and SEM (d) images of p-1,8-DHN.

For gas adsorption experiments, nitrogen and carbon dioxide adsorption analyses were carried out. The p-1,8-DHN showed a type I nitrogen adsorption/desorption isotherm at  $-196\text{ }^{\circ}\text{C}$ , which is typical of microporous materials, with a sharp saturation at high relative pressure, ascribable to nitrogen condensation in the nanoparticles interstitial voids (Figure 29a). The p-1,8-DHN were characterized by

a Langmuir specific surface area (SSA) of 560 m<sup>2</sup>/g and a total pore volume of 0.32 cm<sup>3</sup>/g, 65 % of which is in the micropores range. Indeed, the nonlocal density functional theory (NLDFT) evidenced a prevalently microporous distribution, with a major peak centered at about 1.2 nm (Figure 29b). Moreover, the p-1,8-DHN showed carbon dioxide uptake capacity of 1.74 mmol/g and 2.24 mmol/g at 1 bar and 0 °C and 25 °C, respectively, (Figure 29c) and heat of adsorption that varies from 35 to 20 kJ/mol in the 0.1 – 1.7 mmol/g range (Figure 29d). These results indicate that the gas adsorption properties of p-1,8-DHN are comparable to those of carbon-based microporous organic polymers (MOPs) of many high surface area.<sup>29</sup>

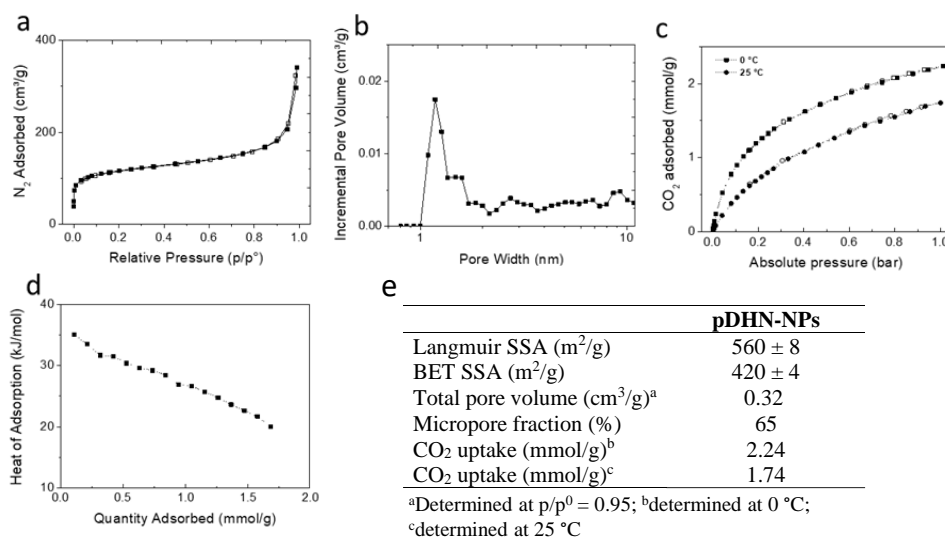


**Figure 29** | (a) p-1,8-DHN nitrogen adsorption-desorption isotherm at -196 °C (adsorption in full points, desorption in hollow points); (b) NLDFT pore size distribution; (c) carbon dioxide adsorption-desorption isotherms at 0 °C and 25 °C (adsorption in full points, desorption in hollow points); (d) carbon dioxide heat of adsorption; (e) adsorption measurement data.

The adsorbing properties of p-1,8-DHN were also assessed toward a water solution of methylene blue (MB). The ability of p-1,8-DHN to adsorb MB was preliminarily tested by incubating the 1,8-DHN polymer nanoparticles (1 mg/mL) into a 20 mg/L water solution of the dye. As shown in Figure 30a, the typical blue colouration of the dye completely disappeared in the water solution after 30 minutes of incubation time, suggesting that the adsorption of MB by p-1,8-DHN had occurred. This evidence was also supported by the investigation of the UV-visible spectrophotometric course of the water treatment. The spectra reported in Figure 30b showed that the absorption maxima of the dye at 613 and 663 nm rapidly slowed down after the addition of p-1,8-DHN, with 80% of MB removal registered after 5 minutes, indicative of a very fast process (Figure 30c). To check if the disappearance of the blue colour was due to the dye adsorption by p-1,8-DHN rather than to the reduction of the dye promoted by the p-1,8-DHN, the water incubation mixture was filtered to remove the nanoparticles and the supernatant was subjected to  $^1\text{H}$  NMR spectroscopy. This revealed the complete absence of signals ascribable to protons of the reduced form of MB, so indicating that the dye was completely adsorbed by p-1,8-DHN.

The adsorption was also supported by TEM images of p-1,8-DHN collected after the incubation with the water solution of MB (Figure 30d), showing a reduced contrast of the nanoparticles due to the surface adsorption of the organic dye, in comparison to TEM images of pristine p-1,8-DHN nanoparticles (Figure 28).

Equilibrium adsorption tests performed at different dye concentrations (in the range 5-500 mg/L) revealed that the MB uptake at equilibrium ( $Q_e$ ) increased from 5.0 to 221.3 mg/g as the initial MB concentration increased from 5 to 500 mg/L, suggesting a significant dependency of the dye adsorption with its initial concentration (Table 6).

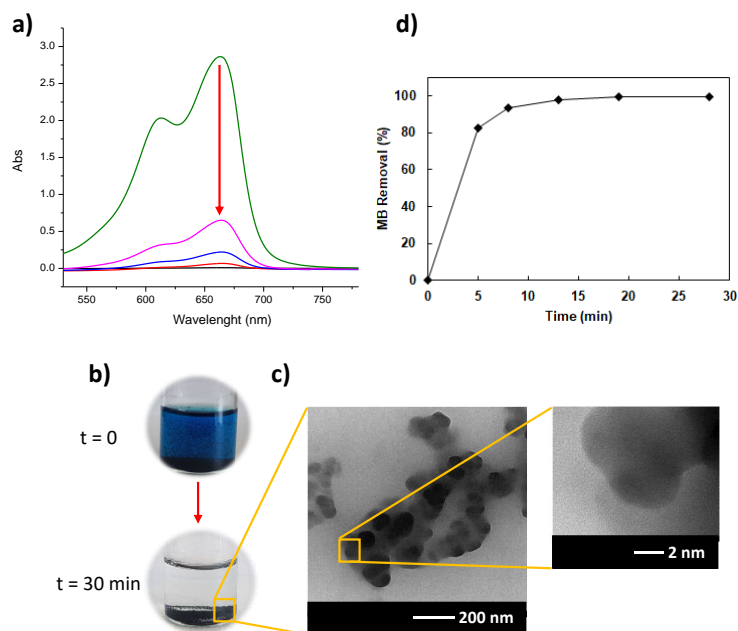


**Figure 30** | MB removal by p-1,8-DHN. Incubation mixture: 20 mg/mL water solution of MB, 1 mg/mL p-1,8-DHN. (a) Spectrophotometric course of the incubation ( $t_0$  = green trace; 5 min = magenta trace; 10 min = blue trace; 15 min = red trace; 30 min = black trace); (b) pictures of the MB water solutions before (top) and after (down) the incubation with p-1,8-DHN; (c) TEM images of p-1,8-DHN after MB absorption; (d) Time course of the MB removal by p-1,8-DHN.

Accordingly, the MB removal proved to be quite high ( $> 99\%$ ) for MB concentrations in the range 5-100 mg/L, whereas a marked reduction was observed for higher concentrations (500 mg/L). This effect can be considered as a consequence of the steric hindrance occurring on the surface of the p-1,8-DHN with the saturation of the adsorption sites.

**Table 6** | Effect of the initial concentration of the dye on the MB equilibrium adsorption capacity per gram of p-1,8-DHN ( $Q_e$ ) and MB removal.

	Initial MB concentration (mg/L)								
	5	10	20	30	50	100	250	400	500
$Q_e$ (mg/g)	4.97	9.95	19.95	29.92	49.88	99.78	188.67	212.59	221.29
MB removal (%)	99.5	99.5	99.7	99.7	99.8	99.8	64.0	64.0	20.0

The high MB removal efficiency was not affected by the pH of the water solution in the 3-11 range, with over 99% of MB being adsorbed independently from the initial concentration of the dye (Figure 31a). These data suggest that the interaction between MB and p-1,8-DHN is mainly driven by hydrogen bonding,  $\pi$ - $\pi$  and n- $\pi$  interactions, and micropore filling (Figure 31b).<sup>30</sup> The electrostatic interactions proved not to be so efficient considering that the MB removal was as high as 99 % even below pH 6, when the phenolic groups on p-1,8-DHN are not dissociated.

To further delineate the interaction mechanism between MB and p-1,8-DHN, the experimental data of the adsorption process were fitted with the isotherm models of Langmuir, Freundlich and Temkin. The Langmuir model describes the monolayer adsorption process on a surface with homogeneous sites, whereas the Freundlich model implies a multilayer adsorption process on a heterogenous surface; the Temkin model contains a factor that explicitly takes into account the heat of adsorption.

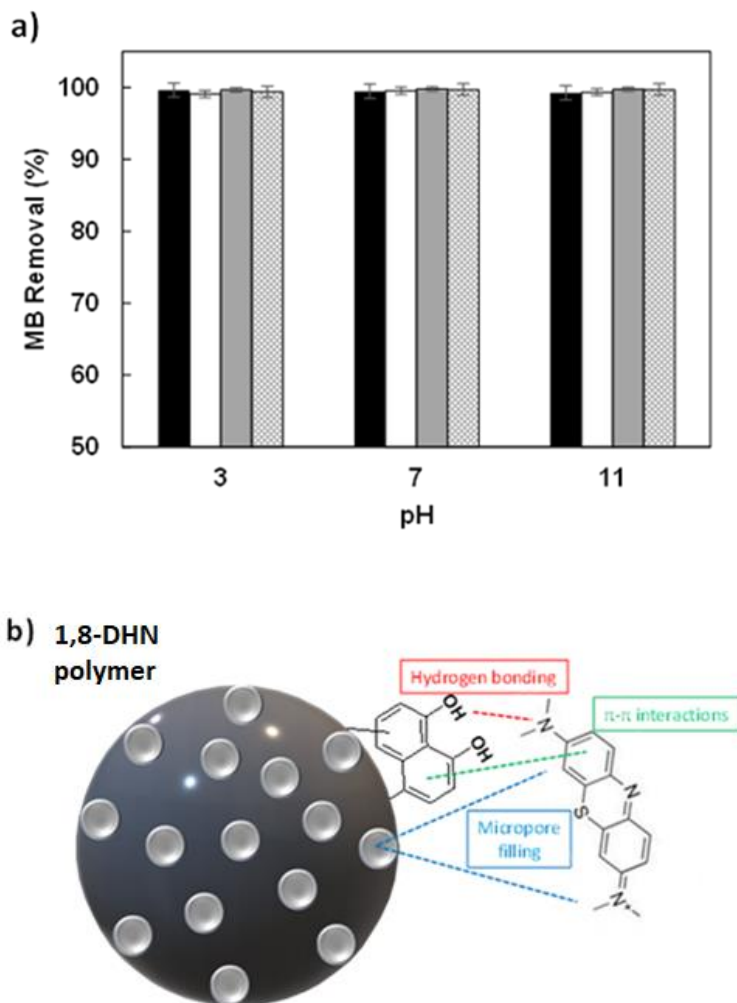


**Figure 31** | (a) MB removal by p-1,8-DHN at different pH values. MB concentration: 5 mg/L (black bars), 10 mg/L (white bars), 20 mg/L (grey bars) and 30 mg/L (dotted bars). The results represent the mean  $\pm$  SD of three separate experiments. (b) Proposed mechanism of adsorption of MB on p-1,8-DHN nanoparticles.

The Langmuir, Freundlich and Temkin isotherm models are described by the following equations 1-3:

$$C_e/Q_e = 1/Q_{max}K_L + C_e/Q_{max} \quad (1)$$

$$\ln Q_e = \ln K_F + 1/n \ln C_e \quad (2)$$

$$Q_e = B_T \ln A_T + B_T \ln C_e \quad (3)$$

where  $C_e$  is the equilibrium concentration (mg/L),  $Q_e$  is the amount of adsorbed dye at equilibrium (mg/g),  $Q_{max}$  (mg/g) is the theoretical maximum adsorption capacity,  $K_L$  (L/mg) is the Langmuir constant,  $K_F$  (mg/g) is the Freundlich constant, both related to the adsorption capacity,  $n$  is a constant related to the adsorption intensity. Values of  $n$  within the range 1 - 10 are indicative of an efficient adsorption process.  $A_T$  is the Temkin binding energy constant at equilibrium (L/g),  $B_T = RT/b$  is an indicator of the adsorption heat (J/mol), with  $T$  = absolute temperature (K),  $R$  = universal gas constant,  $b$  = Temkin isotherm constant.

The Langmuir, Freundlich and Temkin isotherm plots and the isotherm parameters are reported in Figure 32. The results highlighted the best fit of the Langmuir isotherm model with the experimental data, with a correlation coefficient  $r^2 = 0.998$ , indicating that monolayer adsorption occurred on the homogeneous surface of p-1,8-DHN. The good correlation coefficient observed also for the fitting with the Temkin isotherm model ( $r^2 = 0.963$ ) suggests that the MB adsorption process is exothermic and driven by physisorption, as denoted by the  $B_T$  value.

To further evaluate the feasibility of the MB adsorption process, the separation factor  $R_L$  related to the Langmuir isotherm model was calculated as follows:

$$R_L = 1/1 + K_L C_0 \quad (4)$$

The  $R_L$  value is indicative of irreversible ( $R_L = 0$ ), favourable ( $0 < R_L < 1$ ), linear ( $R_L = 1$ ) and unfavourable ( $R_L > 1$ ) adsorption processes. The  $R_L$  values calculated for the MB adsorption onto p-1,8-DHN were in the range 0.07 – 0.3, suggesting a favourable process. According to the Langmuir model the maximum adsorption

capacity of MB onto p-1,8-DHN is 220 mg/g. This represents a quite high value for a biosorbent if we consider that no treatment has been carried out to improve its adsorbing properties, comparable to those obtained from inorganic porous materials (Table 7).<sup>31</sup>

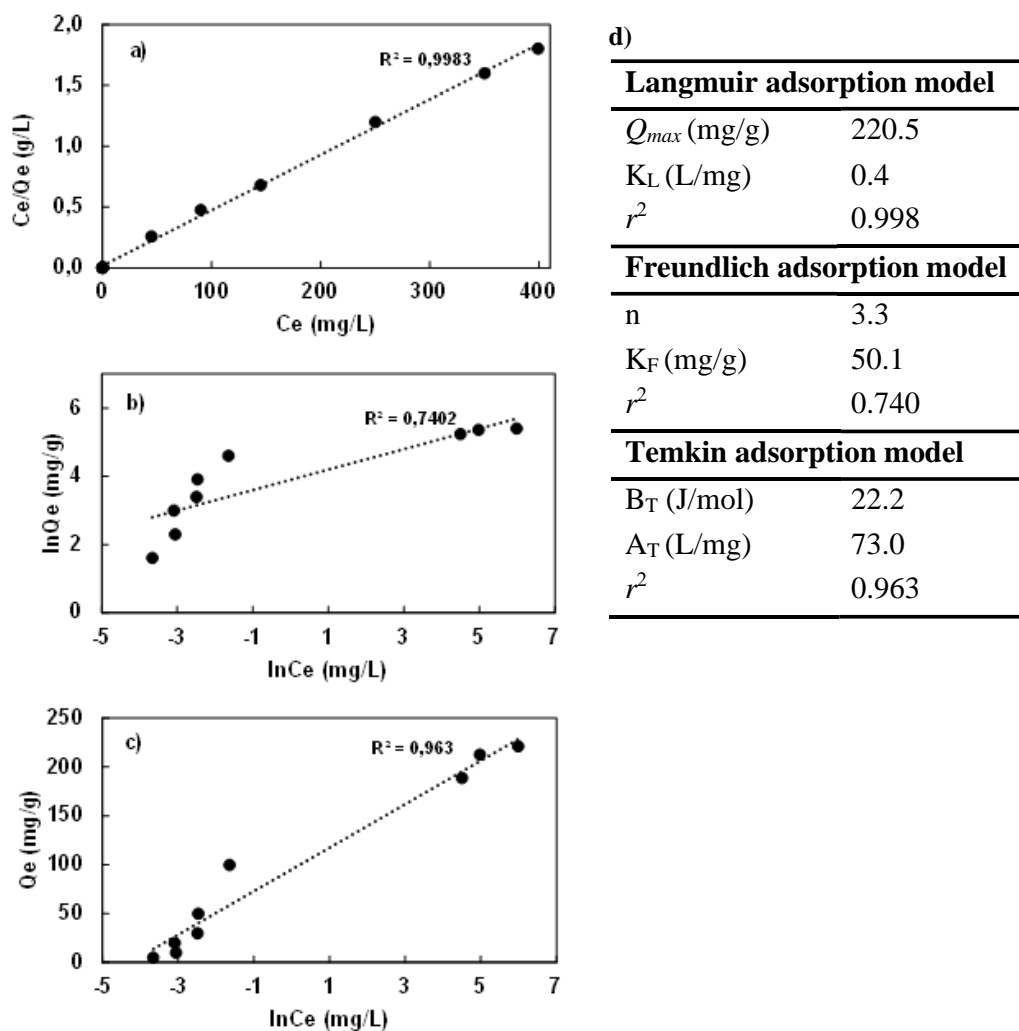


**Figure 32** | Langmuir (a), Freundlich (b) and Temkin (c) isotherm plots and relative parameters (d).

**Table 7** | MB adsorption capacities measured for different adsorbents.

Adsorbent	Adsorption capacity (mg/g)	Reference
Organosolvent extracted lignin	40.0	(Zhang et al., 2016)
Alkali extracted lignin	121.2	(Feng et al., 2014)
Native <i>Casuarina lanatus</i> rinds	44.5	(Lakshmipathy and Sarada, 2015)
Activated carbon from <i>Casuarina lanatus</i> rinds	231.5	(Üner et al., 2016)
Coconut fiber	50.0	(Wong et al., 2013)
Activated carbon coconut shells	156.3	(Yagmur and Kaya, 2021)
Biochar Pine cone	106.4	(Dawood et al., 2017)
Titania nanotubes	290.0	(Hsieh et al., 2008)
Mixed oxide of Ti and Si	163.0	(Pal et al., 2016)
<b>p-1,8-DHN</b>	<b>220.5</b>	<b>This work</b>

Finally, the nature of the adsorption process of MB on p-1,8-DHN has been investigated from thermodynamic point of view. To this aim, the Gibbs free energy change ( $\Delta G^\circ$ ), the enthalpy change ( $\Delta H^\circ$ ) and the entropy change ( $\Delta S^\circ$ ) were calculated according to the following equations 5 and 6:

$$K = Q_e/C_e \quad (5)$$

$$\ln K = \Delta S^\circ/R - \Delta H^\circ/RT \quad (6)$$

where  $K$  is the equilibrium constant of the adsorption process,  $R$  is the universal gas constant (8.314 J/mol $\times$ K) and  $T$  is the system temperature (K).

By plotting  $\ln K$  as a function of  $1/T$ , the  $\Delta S^\circ$  and  $\Delta H^\circ$  values were calculated as the intercept and slope of the linear regression (Figure 33), whereas the  $\Delta G^\circ$  value was calculated by applying the following equation 7:

$$\Delta G^0 = \Delta H^0 - T\Delta S^0 = -RT\ln K \quad (7)$$

The negative  $\Delta G^0$  values clearly indicate that the adsorption process is spontaneous and favourable; moreover, the negative  $\Delta H^0$  value proved that the MB adsorption is an exothermic process, in good agreement with data obtained from equilibrium isotherms (Table 8).

**Table 8** | Thermodynamic parameters calculated for the adsorption of MB onto p-1,8-DHN determined at 20mg/L MB concentration and at pH 6.5.

$T$ (K)	$\Delta G$ (kJ·mol <sup>-1</sup> )	$\Delta H$ (kJ·mol <sup>-1</sup> )	$\Delta S$ (kJ·mol <sup>-1</sup> ·K <sup>-1</sup> )
303	-19.49		
313	-18.39		
323	-17.30	-52.72	-0.11
333	-16.20		

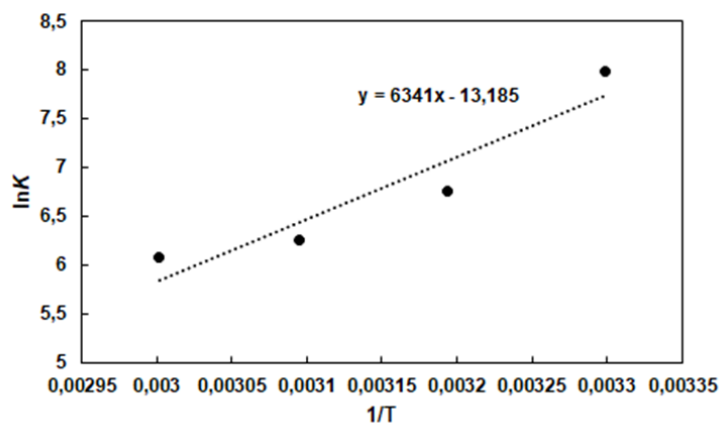


**Figure 33** | Plot of  $\ln K$  as a function of  $1/T$  for p-1,8-DHN.

In the final experiments, to assess the feasibility of p-1,8-DHN as mediators for prebiotic processes on early Earth, biocompatibility experiments were performed on the HEK-293 cell line.

To this aim, thin films of synthetic polymers from 1,8-DHN were deposited on quartz substrates or on the Petri dishes, as shown in Figure 34, following the AISSP (ammonia-induced solid state polymerization) protocol.<sup>32</sup>

The AISSP technique is based on the following two steps: a) deposition of the monomer thin film by spin coating a methanol solution onto a proper substrate (e.g. quartz); b) exposure of the monomer thin film to ammonia vapours in air-equilibrated atmosphere. As clearly visible in Figure 35, after the *step b* the colourless thin film of DHN immediately turned into dark brown suggesting that polymerization has occurred. This hypothesis was supported by UV-vis, FT-IR and mass analysis.

UV-visible analysis of the film before and after AISSP (Figure 35B) confirmed the polymeric nature of the material, as apparent from the intense broadband absorption in both the UV and visible region of the spectrum and from the brown color of the substrate.



**Figure 34** | 1,8-DHN polymer thin films obtained by spin coating on Petri dishes before (on the left) and after AISSP (100 mM and 200 mM, respectively).

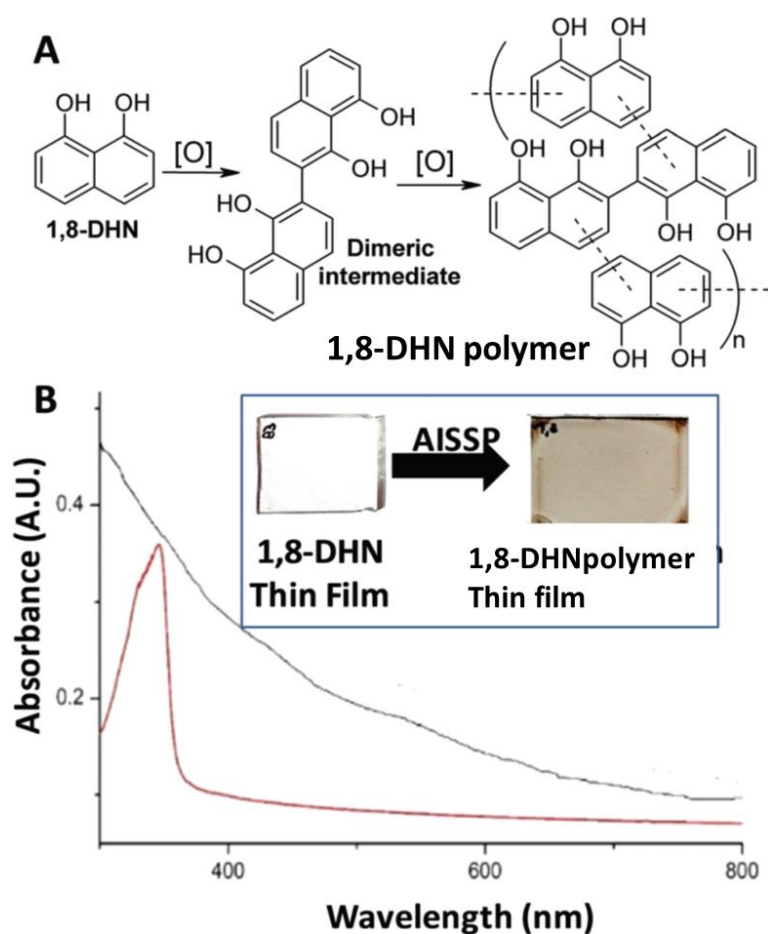


**Figure 35** | (A) The proposed mechanism for the oxidative polymerization of 1,8-DHN. (B) UV-vis spectra of 1,8-DHN thin films on quartz substrates before (red trace) and after (black trace) AISSP; the insets show the quartz substrates before and after exposure to ammonia vapours.

The mass spectrum of the film recorded in the MALDI mode confirmed the polymeric nature of the film revealing the presence of regular patterns of peaks separated by 158 Da, corresponding to the “in-chain” dihydroxynaphthalene unit (Figure 36). The dominant peaks were assigned to singly-charged distributions up to 20 units, confirming the lack of any detectable ammonia incorporated into the

chemical structure of the polymer. Compared to the MALDI-MS data previously reported for polymers produced by aqueous polymerization, the spectra obtained from the film denoted a minor degree of distribution for each of the clusters, suggesting a more regular structure of the polymer.

The micro ATR spectrum registered on the film showed the presence, among others, of bands at 1700–1550  $\text{cm}^{-1}$ , attributable to C=O and C=C stretching of the conjugated quinonoid structures, and bands between 1400–1200  $\text{cm}^{-1}$  suggesting the presence of C–O residues, in agreement with the spectrum obtained by the oxidation in the solution of 1,8-DHN (Figure 37).

Then, to perform the biocompatibility experiments, The HEK-293 cells were plated on 100 and 200 nm p-1,8-DHN-coated dishes, or on standard tissue culture plates. As shown in Figure 38, the HEK-293 cells adhered to both p-1,8-DHN-treated dishes with a similar morphology with respect to the control plates. The p-1,8-DHN coatings also proved to be able to support the efficient growth of HEK-293 cells, with a proliferation rate at 72 h comparable to standard growth conditions.

Further experiments were carried out to investigate whether p-1,8-DHN thin films from 1,8-DHN could also promote clonogenic cell growth in an embryonic stem cell (ESC) colony assay. ESCs are of particular interest for their sensitivity to small changes under culture conditions which can affect the morphology and behavior of the ESC colony. ESCs were cultured for 3 days in a regular medium on cell culture plates coated with either 100 and 200 nm 1,8-DHN polymer films, or gelatin as the control.

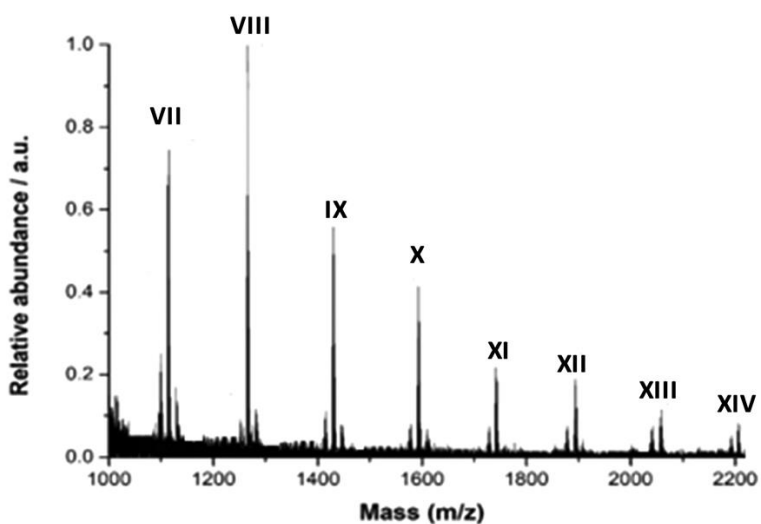


**Figure 36** | MALDI-mass spectrum of the p-1,8-DHN thin film from 1,8-DHN.

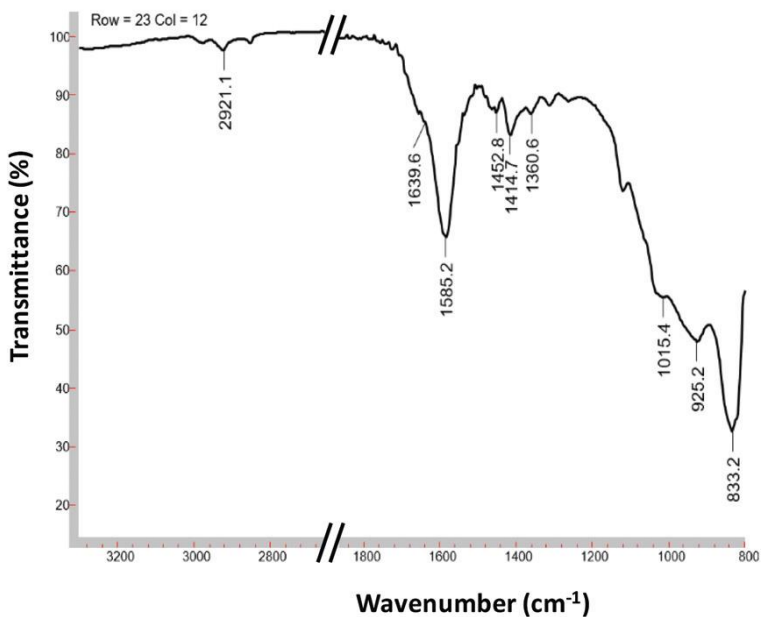


**Figure 37** | Micro ATR spectrum of the p-1,8-DHN thin film from 1,8-DHN.

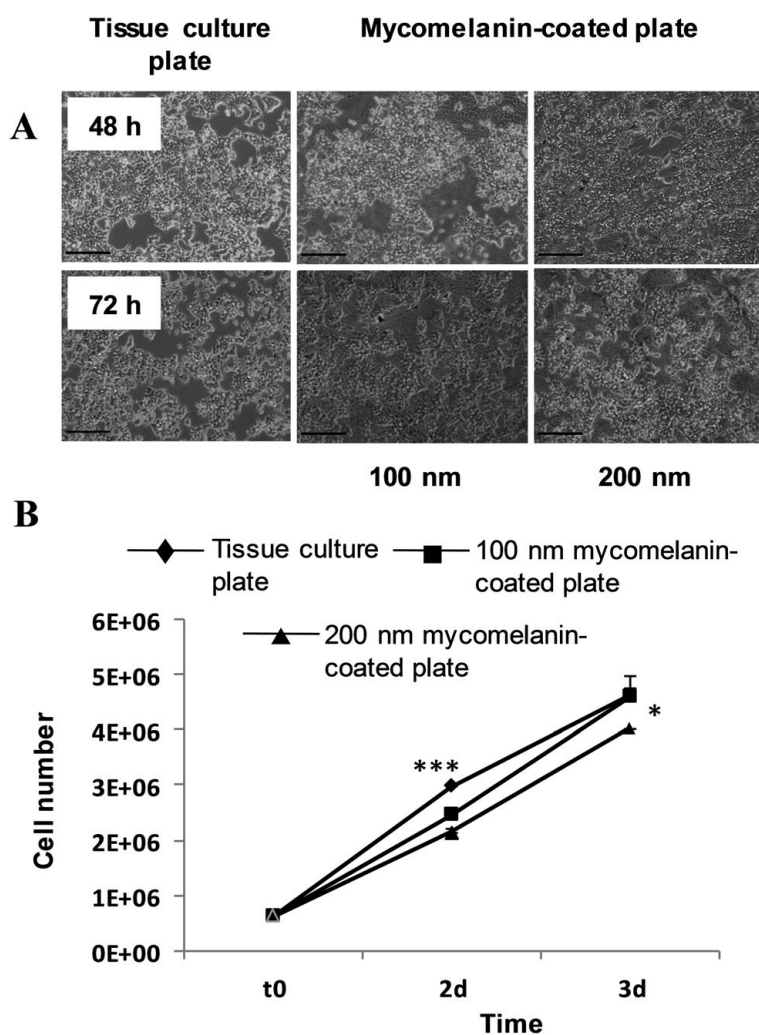


**Figure 38** | (A) Phase contrast images of the HEK-293 cells 48 and 72 h after seeding on dishes coated with 100 nm and 200 nm 1,8-DHN polymer thin films or tissue culture plates, as the control. Images were taken using a Leica DMI8 at 10x magnification. Scale bars: 250  $\mu$ m. (B) Growth curves of HEK-293 cells during 72 h are shown. Cells ( $6 \times 10^4$ ) were seeded on a tissue culture plate (◆), 100 nm 1,8-DHN polymer (■) and 200 nm 1,8-DHN polymer (▲) coated plates and triplicate cultures were counted at daily intervals. Data are expressed as mean  $\pm$ SD (\* $p < 0.05$  and \*\*\* $p < 0.001$ ).

At 24 h, ESCs adhered to the plates under all conditions with different degrees of cell attachment. After 48 h, the cells proliferated forming regular dome-shaped colonies, although ESCs cultured on 1,8-DHN polymer-coated plates were smaller compared to the control plates. Finally, at 72 h, cells on 100 nm 1,8-DHN polymer coatings retained the morphology and attachment to the plate in a similar way to the control, while the cells on 200 nm 1,8-DHN polymer coatings seemed to lose adhesion, floating in the medium.

Moreover, p-1,8-DHN showed unprecedented effects in inducing the spontaneous differentiation of embryonic stem cells prevalently towards the endodermal lineages. Therefore, these results showed good biocompatibility exhibited by the 1,8-DHN polymer confirming its suitability as a mediator for prebiotic processes on early Earth.

#### 4.2.4.2 1-Naphthol

The oxidation of 1-HN led to the formation of a violet precipitate (p-1-HN, Figure 39).

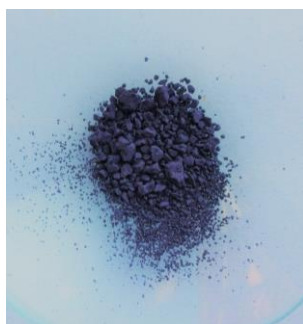


**Figure 39** | Solid p-1-HN.

This was first subjected to MALDI-MS analysis (Figure 40). The spectrum was characterized by a repetitive pattern of peaks (up to 15 repeating units) separated by 142 Da, corresponding to the “in-chain” HN-unit, relative to  $[M+H]^+$  species.

Each pseudomolecular ion peak was associated with a fragmentation peak due to loss of water ( $[M-H_2O+H]^+$ ).

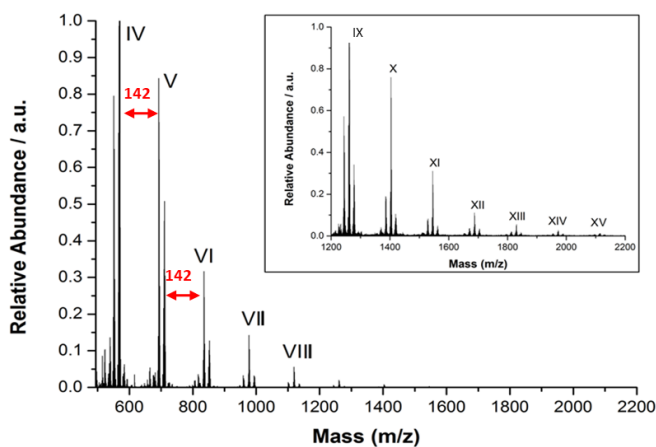


**Figure 40** MALDI mass spectra of p-1-HN.

Unlike the MALDI spectrum of p-1,8-DHN, the inspection of the clusters of p-1-HN showed a lesser degree of electronic/redox disorder, since ion peaks for the fully reduced state prevailed at each oligomeric stage (Figure 41).

The UV-visible spectrum (Figure 42) of the DMF solution of p-1-HN was characterized by a broad maximum at 520 nm and a shoulder at 326 nm. In this case, there is no broadband absorption profile, observed above for p-1,8-DHN.

The ATR-FTIR spectrum of p-1-HN (Figure 43) revealed a main band at 1226, a group of two bands at 1347 and 1370  $\text{cm}^{-1}$ , two bands at 1505 and 1610  $\text{cm}^{-1}$ , two bands at 1585 and 1653  $\text{cm}^{-1}$ , the latter due to C-O, C=C and C=O stretching of aromatic rings, and a band at 3050  $\text{cm}^{-1}$  attributable to C-H stretching which may partially overlap with the broadband at 3300  $\text{cm}^{-1}$  attributable to hydrogen-bonded OH stretching vibrations.

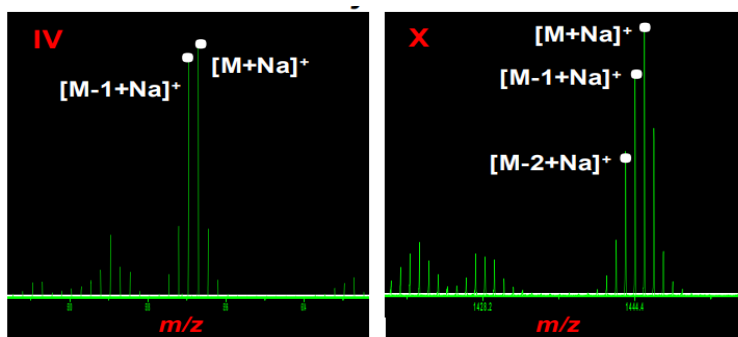


**Figure 41** | Comparison of the clusters of the  $[M+Na]^+$  pseudomolecular ion peaks for the 4-mer (IV) and 10-mer (X) oligomeric species of synthetic polymer from 1-HN.

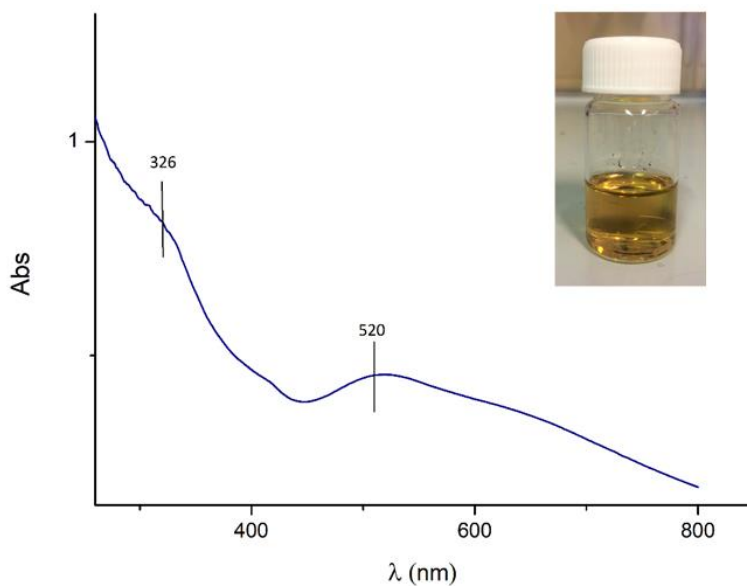


**Figure 42** | UV-Vis absorption spectrum of p-1-HN in DMF.

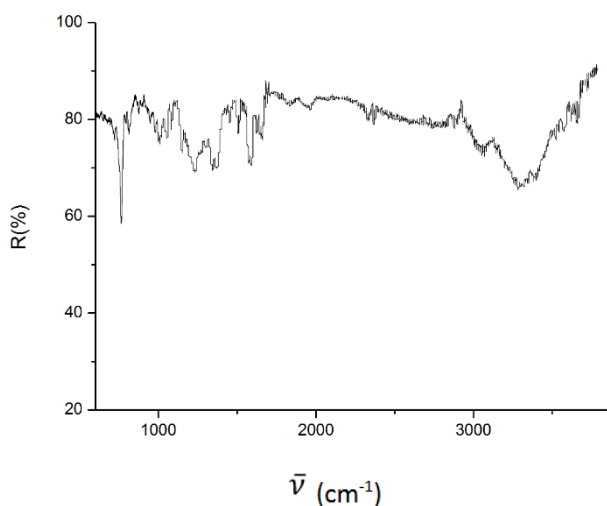


**Figure 43** | ATR spectrum of p-1-HN

The EPR spectrum recorded on solid p-1-HN (Figure 44) revealed an intense signal centered at a  $g$ -value of 2.0030, typical of C-centered free radical species, and a spin density less intense than for p-1,8-DHN.

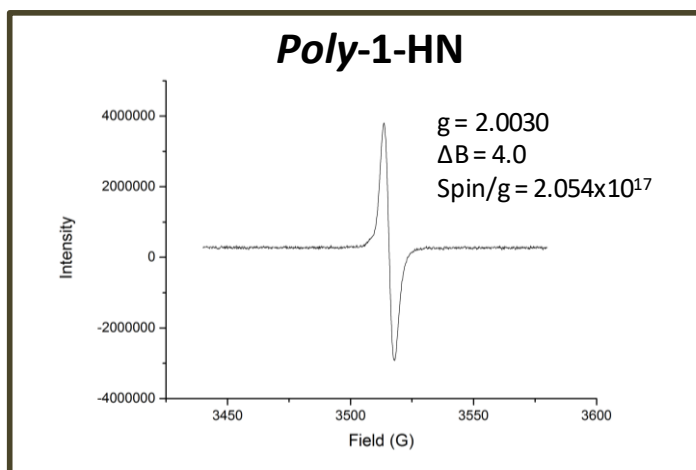


**Figure 44** | EPR spectrum of p-1-HN in the solid state.

### 4.3 Conclusions

PAHs, known to be widely diffused in the Universe, and their oxygenated derivatives, OxyPAHs, primary photochemical transformation products in water–ice matrices mimicking the interstellar medium,<sup>2</sup> recently captured the interest of the scientific community for their potential properties as prebiotic molecules.

Polymerization of PAHs and OxyPAHs may generate organic surfaces on which adsorbed prebiotic molecules can concentrate and benefit from catalytic effect and protection from hydrolysis and UV radiation. In particular the structure and the physicochemical properties of OxyPAHs polymers and their potential application as mediators for prebiotic processes on early Earth are little understood.

In this Chapter, for the first time, novel insights into the oxidative polymerization of 1,8-DHN and 1-HN were provided. The oxidative reactivity of 1,8-DHN and 1-HN has been examined under physiological relevant conditions by the isolation and characterization of oligomeric intermediates. Moreover, a preliminary screening of the adsorbing properties of the p-1,8-DHN as well as the biocompatibility tests have been presented.

The main outcomes of the study described in this Chapter can be summarized as follows:

1. structural data for a variety of dimers indicate that in both polymers the connectivities between the aromatic rings are of C-C type;
2. polymer obtained by the oxidation of 1,8-DHN show a strong broadband absorption throughout the whole visible spectrum and a strong EPR signal denoting a marked paramagnetic character;
3. nanoparticles of 1,8-DHN polymer proved to be an efficient microporous adsorbent with high affinity for cationic dyes such as MB;

4. tests performed on the polymer thin film from 1,8-DHN showed good biocompatibility and unprecedented effects in inducing the spontaneous differentiation of embryonic stem cells prevalently towards the endodermal lineages.

Overall, these results provide a new background to inquire into the origin and properties of organic polymers from PAHs under conditions of astrochemical relevance.

## 4.4 Experimental section

### 4.4.1 Materials and Methods

1,8-Dihydroxynaphthalene, 1-hydroxynaphthalene, horseradish peroxidase (HRP) and hydrogen peroxide were purchased from Sigma and used without further purification.

Analytical and preparative TLC analyses were performed on F<sub>254</sub> silica gel plates (0.25 and 0.5 mm, respectively). TLC plates were visualized using a UV lamp ( $\lambda = 254$  nm) and a fluorescence lamp ( $\lambda = 366$  nm). Liquid chromatography was performed on silica gel (60-230 mesh).

<sup>1</sup>H and <sup>13</sup>C-NMR spectra were recorded with a Bruker DRX-400 MHz instrument, using deuterated chloroform (CDCl<sub>3</sub>) as solvent. *J* values are given in Hz. <sup>1</sup>H, <sup>1</sup>H COSY, <sup>1</sup>H, <sup>13</sup>C HSQC and <sup>1</sup>H, <sup>13</sup>C HMBC experiments were run at 400.1 MHz using standard pulse programs. In the assignment of peaks, the following abbreviations were used: s = singlet, d = doublet, dd = double doublet, t = triplet, m = multiplet.

UV-Vis spectra were recorded with a Jasco V-560 instrument.

EPR measurements were performed using an X-band (9 GHz) BrukerElexys E-500 spectrometer (Bruker, Rheinstetten, Germany), equipped with a super-high sensitivity probe head. Samples were transferred to flame-sealed glass capillaries which, in turn, were coaxially inserted in a standard 4 mm quartz sample tube. Measurements were performed at room temperature. The instrumental settings were as follows: sweep width, 100 G; resolution, 1024 points; modulation frequency, 100.00 kHz; modulation amplitude, 2.0 G. Several scans, typically 16, were accumulated to improve the signal-to-noise ratio. Subsequently, to run the power saturation experiments, the microwave power was gradually incremented from 0.02 to 160 mW. The *g* value and the

spin density were evaluated by means of an internal standard, Mn<sup>2+</sup> -doped MgO, prepared by a synthetic protocol previously reported.<sup>49</sup>

MALDI mass spectra were recorded on a Sciex 4800 MALDI ToF/ToF instrument using 2,5-dihydroxybenzoic acid as the matrix. The laser was operated at 3700 Hz in the positive reflectron mode. The mass spectrometer parameters were set as recommended by the manufacturer and adjusted for optimal acquisition performance. The laser spot size was set at medium focus (B50 mm laser spot diameter). The mass spectra data were acquired over a mass range of  $m/z$  100– 4000 Da, and each mass spectrum was collected from the accumulation of 1000 laser shots. Raw data were analyzed using the computer software provided by the manufacturers and reported as monoisotopic masses.

ATR spectra of the powders in transmission mode have been recorded with a Nicolet 5700 spectrometer. The spectra have been scanned on the wave number range of 400-4000 cm<sup>-1</sup> with a resolution fixed to 4 cm<sup>-1</sup>.

Micro ATR spectra of the powders in transmission mode have been recorded with a Cary 660 FTIR Spectrometer with a Germanium crystal and a liquid nitrogen cooled Mercurium Cadmium Telluride (MCT) detector in the range from 4000 to 900 cm<sup>-1</sup>, with 32 scans both for background and samples, with a resolution of 4 cm<sup>-1</sup>.

Spin-coating experiments were conducted with a spin-coater Laurell WS-650MZ-23NPP/LITE.

TEM analysis was performed in bright field mode using a FEI-Tecnai G12 Spirit Twin (LaB6 source) operating at 120 kV. TEM images were collected on a FEI Eagle 4 k CCD camera. Before the analysis, p-1,8-DHN

was suspended in ethyl alcohol and collected by dipping a carbon coated copper grid in the suspension. TEM micrographs were analysed by means of the software ImageJ (release 1.43u) and the size of primary p-1,8-DHN particles was measured. The size distribution of the particles was statistically analysed using the software Origin Pro (release 8.5).

SEM analysis was performed on p-1,8-DHN with a FEI Quanta 200 FEG SEM using a secondary electron detector and an acceleration voltage of 10–30 kV. Before analysis, small amounts of p-1,8-DHN were deposited on aluminum stubs covered by carbon adhesive disks and the sample was sputter coated with gold/palladium.

Zeta-potential measurements were performed on p-1-8-DHN at different pH values by laser Doppler micro-electrophoresis, using a Zetasizer Nano ZS (Malvern Instruments). p-1-8-DHN were dispersed at the concentration of 1 mg/mL in distilled water (pH 7), in a HCl solution at pH 3 and in a NaOH 120 solution at pH 11 by sonication in a Transsonic Digital ultrasonic bath for 5 min. Measurements were performed in triplicate at 25 °C.

#### **4.4.2 Synthesis and characterization of oxyPAH-polymers**

##### **4.4.2.1 UV-vis monitoring of the HRP/H<sub>2</sub>O<sub>2</sub>-mediated oxidation of 1-HN and 1,8-DHN: general procedure**

A 0.2 mM solution of the proper 1-HN and 1,8-DHN in aqueous phosphate buffer (0.1 M, pH = 7) was treated under vigorous stirring with HRP (15 U/mL) and H<sub>2</sub>O<sub>2</sub> (1.2 eqs). At regular interval time, aliquots of the reaction mixture were withdrawn and analyzed by UV-vis spectroscopy.

#### 4.4.2.2 Ammonia-induced solid-state polymerization (AISSP): a general procedure

Suitable amounts of 1,8-DHN were dissolved in methanol and the solutions were filtered with 0.45 mm syringe filters before use. For each deposition, 100 mL of the methanol solution of 1,8-DHN was pipetted onto the upper side of the substrate just before spinning. The spin coating parameters were as follows  $\alpha = 500 \text{ rpm s}^{-1}$ ,  $\omega = 2000 \text{ rpm}$ , and  $t = 30 \text{ s}$ . The 1,8-DHN-coated substrate was placed in a glass chamber under an ammonia atmosphere equilibrated with air. After 24 h, the polymerization was complete, and the substrate was removed from the chamber. 1,8-DHN polymer thin films of different thickness (100 and 200 nm) were prepared by spin coating 1,8-DHN methanolic solutions at appropriate concentrations (100 and 200 mM)

#### 4.4.2.3 LFP Experiments

LFP experiments were carried out with an Applied Photophysics LK-60 laser kinetic spectrometer providing 8 ns pulses, using the third harmonic (355 nm) of a Quantel Brilliant-B Q-switched Nd:YAG laser. The laser energy was adjusted to  $\leq 10 \text{ mJ/pulse}$  by the use of an appropriate filter. A 3.5 mL Suprasil quartz cell (10 mm  $\times$  10 mm) was used for all experiments.  $\text{N}_2$ -saturated  $\text{CH}_3\text{CN}$  solutions of hydroxynaphthalenes (1,8-DHN and 1-HN 1.5–14 mM) and dicumyl peroxide (1 M), N-hydroxyphthalimide (5.0 mM) or 1-hydroxybenzotriazole (9.2 mM), and naphthols (0.1–2.0 mM) were used. All experiments were carried out at  $T = 25 + 0.5 \text{ }^\circ\text{C}$  under magnetic stirring. Data were collected at individual wavelengths with an Agilent Infinium oscilloscope and analyzed with the kinetic package implemented in the instrument. Rate constants were obtained by monitoring the change of absorbance at the

maximum absorption wavelengths of the cumyloxyl or N-oxyl radicals or of the product naphthoxyl radicals by averaging 3–5 values. Each kinetic trace obeyed a first-order kinetic, and second-order rate constants were obtained from the slopes of the plots of the observed rate constants  $k_{\text{obs}}$  versus substrate concentration.

#### 4.4.2.3.1 Computational investigation of structural and spectroscopic properties of 1,8- dihydroxynaphthalene oxidation products

All calculations were performed with the Gaussian package of programs. All structures were geometry optimized at the DFT level, with a hybrid functional (PBE0)<sup>23</sup> and a reasonably large basis set [6-31+G(d,p)]. For each species, different tautomers / conformers, as well as different protonation states were explored. In those cases where conformational enantiomers exist, a single enantiomeric series has been explored. Computations were performed either in vacuo, or by adoption of a polarizable continuum medium (PCM)<sup>33–36</sup> to account for the influence of the solution environment. In view of the faster convergence, a scaled van der Waals cavity based on universal force field (UFF) radii<sup>37</sup> was used, and polarization charges were modeled by spherical Gaussian functions;<sup>38,39</sup> non-electrostatic contributions to the solvation free energy were disregarded at this stage: these terms were accounted for in single-point PCM calculations (at the PCM geometries) employing radii and non-electrostatic terms of the SMD solvation model. Vibrational-rotational contributions to the free energy were also computed. UV-Vis spectra of the main species were computed in vacuo or in solution using the time dependent density functional theory (TD-DFT) approach,<sup>20–24</sup> with the PBE0 functional and the 6- 311++G(2d,2p) basis set. To produce graphs, transitions below 5.6

eV were selected, and an arbitrary Gaussian line width of 0.25 eV was imposed; the spectra were finally converted to a wavelength scale.

#### **4.4.2.4 HRP/H<sub>2</sub>O<sub>2</sub>-mediated oxidation of 1-HN and 1,8-DHN: a general procedure for the isolation of the oligomeric intermediates**

A 20 mM solution of the proper HN/DHN in aqueous phosphate buffer (0.1 M, pH = 7) was treated under vigorous stirring with HRP (15 U/mL) and H<sub>2</sub>O<sub>2</sub> (1.2 eqs). After the proper reaction time, the mixture was treated with sodium dithionite and extracted with water/ethyl acetate. The organic fractions were dried on anhydrous sodium sulphate and evaporated under reduced pressure. The residue was treated with acetic anhydride and pyridine overnight. The acetylated mixture was subjected to liquid chromatography on silica gel to afford the oligomeric intermediates.

#### **1,8-Dihydroxynaphthalene**

The reaction was quenched with sodium dithionite after 5 seconds from the addition of H<sub>2</sub>O<sub>2</sub>. The acetylated mixture was purified by liquid chromatography on silica gel (gradient from pure petroleum ether to petroleum ether/ethyl acetate 8:2). Three bands were isolated: **1** (13 mg, 2.6%, R<sub>f</sub> = 0.81), **2** (19 mg, 3.8%, R<sub>f</sub> = 0.76), **3** (45 mg, 9%, R<sub>f</sub> = 0.73), eluent chloroform/ethyl acetate 1:1 (v/v).

#### ***Acetylated 2,2'-dimer (1)***

<sup>1</sup>H-NMR (400 MHz, CDCl<sub>3</sub>) δ ppm: 7.85 (d, J = 7.6 Hz, H-4 + H-4'), 7.82 (d, J = 8.4 Hz, H-5 + H-5'), 7.51 (t, J = 7.6 Hz, H-6 + H-6'), 7.41 (d, J = 7.6 Hz, H-3 + H-3'), 7.17 (d, J = 8.4 Hz, H-7 + H-7'), 2.39 (s, CH<sub>3</sub>), 2.01 (s, CH<sub>3</sub>).

$^{13}\text{C}$ -NMR (100 MHz,  $\text{CDCl}_3$ )  $\delta$  ppm: 170.1(C=O), 170.0 (C=O), 145.7 (C-1 + C-1'), 145.5 (C-8 + C-8'), 136.7 (C-2 + C-2'), 136.2 (C-4a + C4a'), 128.7 (C-3 + C-3'), 126.7 (C-5 + C-5'), 126.6 (C-4 + C-4'), 126.2 (C-6 + C-6'), 121.1 (C-7 + C-7'), 120.5 (C-8a + C-8a'), 21.1 ( $\text{CH}_3$ ), 20.3 ( $\text{CH}_3$ );

ESI(+)-MS ( $m/z$ ): 509 ( $[\text{M} + \text{Na}]^+$ ).

#### *Acetylated 2,4'-dimer (2)*

$^1\text{H}$ -NMR (400 MHz,  $\text{CDCl}_3$ )  $\delta$  ppm: 7.93 (d,  $J = 8.0$  Hz, H-4), 7.89 (dd,  $J = 8.0, 0.7$  Hz, H-5), 7.56 (t,  $J = 8.0$  Hz, H-6), 7.52 (d,  $J = 8.0$  Hz, H-3, H-5'), 7.42 (d,  $J = 8.0$  Hz, H-3'), 7.40 (t,  $J = 8.0$  Hz, H-6'), 7.23 (dd,  $J = 8.0, 0.7$  Hz, H-7), 7.20 (d,  $J = 8.0$  Hz, H-2'), 7.18 (dd,  $J = 8.0, 0.7$  Hz, H-7'), 2.46 (s,  $2 \times \text{CH}_3$ ), 2.33 (s,  $\text{CH}_3$ ), 1.76 (s,  $\text{CH}_3$ ).

$^{13}\text{C}$ -NMR (100 MHz,  $\text{CDCl}_3$ )  $\delta$  ppm: 170.0 (C=O), 169.9 (C=O), 169.5 (C=O), 169.3 (C=O), 145.9 (C-1), 145.8 (C-8), 145.3 (C-8'), 145.1 (C-1'), 136.7 (C-4'), 136.4 (C-2), 136.0 (C-4a), 135.5 (C4a'), 128.5 (C-3 + C-3'), 126.8 (C-5), 126.4 (C-4), 126.2 (C-5'), 126.1 (C-6), 125.9 (C-6'), 121.0 (C-7 + C-8a'), 120.2 (C-8a + C-7'), 120.1 (C-2'), 21.6 ( $\text{CH}_3$ ), 21.5 ( $\text{CH}_3$ ), 21.0 ( $\text{CH}_3$ ), 20.5 ( $\text{CH}_3$ ).

ESI(+)-MS ( $m/z$ ): 509( $[\text{M} + \text{Na}]^+$ ).

#### *Acetylated 4,4'-dimer (3)*

$^1\text{H}$ -NMR (400 MHz,  $\text{CDCl}_3$ )  $\delta$  ppm: 7.49 (d,  $J = 8.0$  Hz, H-3 + H-3'), 7.3 (m, H-5 + H-5' + H-6 + H-6'), 7.25 (d,  $J = 8.0$  Hz, H-2 + H-2'), 7.16 (dd,  $J = 6.0, 2.8$  Hz, H-7 + H-7'), 2.49 (s,  $\text{CH}_3$ ), 2.48 (s,  $\text{CH}_3$ ).

$^{13}\text{C}$ -NMR (100 MHz,  $\text{CDCl}_3$ )  $\delta$  ppm: 169.7 (C=O), 169.6 (C=O), 145.3 (C-8 + C-8'), 145.1 (C-1 + C-1'), 136.5 (C-4 + C-4'), 135.9 (C-4a + C4a'), 128.3 (C-3

+ C-3'), 126.3 (C-5 + C-5'), 125.7 (C-6 + C-6'), 121.1 (C-8a + C-8a'), 120.8 (C-7 + C-7'), 120.1 (C-2 + C-2'), 21.4 (CH<sub>3</sub>), 21.3 (CH<sub>3</sub>).

ESI(+)-MS (*m/z*): 509 ([M + Na]<sup>+</sup>).

## 1-Naphthol

The reaction was quenched with sodium dithionite after 5 minutes from the addition of H<sub>2</sub>O<sub>2</sub> and was not submitted to the acetylation step. The oxidation mixture was purified by liquid chromatography on silica gel plates (diethyl ether/hexane 1:1 (v/v)). A main band was isolated: **4** (16 mg, 6.4%, R<sub>f</sub> = 0.58), eluent diethyl ether/hexane 1:1 (v/v).

### 4,4'-dimer (**4**)

<sup>1</sup>H-NMR (400 MHz, CDCl<sub>3</sub>) δ ppm: 8.36 (m, H-8), 7.89 (m, H-5), 7.60 (m, H-4, H-7), 7.59 (m, H-6), 7.43 (d, J = 8.8, Hz, H-3), 6.13 (s, OH).

<sup>13</sup>C-NMR (100 MHz, CDCl<sub>3</sub>) δ ppm: 149.16 (C-1), 134.7 (C-4a), 128.0 (C-3), 127.1 (C-6), 127.6 (C-5), 126.0 (C-7), 122.5 (C-8), 121.5 (C-4), 115.6 (C-8a).

### 4.4.2.5 HRP/H<sub>2</sub>O<sub>2</sub>-mediated oxidation of 1-HNs and 1,8-DHN: a general procedure for the isolation of the polymers

A 20 mM solution of the proper 1-HN and 1,8-DHN (250 mg) in aqueous phosphate buffer (0.1 M, pH = 7) was treated under vigorous stirring with HRP (15 U/mL) and H<sub>2</sub>O<sub>2</sub> (1.2 eqs). After 24 h, the mixture was treated with HCl 2 M until pH was 2. The resulting precipitate was collected by centrifugation (7000 rpm for 15 minutes at 4°C), washed three times with water and essiccated under reduced pressure. The weights of the isolated polymers are reported in the following table.

**Table 9** | Amount of polymers obtained after the oxidative polymerization reaction

Starting Compound	Polymer (mg)	Starting Compound	Polymer (mg)
1,8-DHN	215	1-HN	196

#### 4.4.2.6 Study of adsorbing properties of p-1,8-DHN

##### 4.4.2.6.1 MB adsorption tests

MB solutions at a concentration of 5, 10, 20, 30, 50, 100, 250, 400 and 500 mg/L were prepared in deionized water. For the adsorption tests, in each experiment 10 mg of p-1,8-DHN were suspended in 10 mL of the dye solution and stirred at a rate of 250 rpm at ambient conditions (pH 6.5, 25 °C) until the equilibrium was reached (30 minutes). The MB concentration in the solution was measured at different interval times by using a Jasco V-560 UV-vis spectrophotometer (MB absorption maximum at  $\lambda_{\max} = 663$  nm). Additional tests were carried out by changing the pH of the incubation mixtures. To this aim the initial pH of the solution was adjusted by adding dropwise 0.1 M NaOH or 0.1 M HCl solutions.

The adsorption capacity at equilibrium ( $Q_e$ ) and the MB removal percentage ( $R$ ) were calculated as follows:

$$Q_e = [(C_0 - C_e)/W] \times V \quad (8)$$

$$R = [(C_0 - C_e)/C_0] \times 100 \quad (9)$$

where  $C_0$  and  $C_e$  are the initial and equilibrium dye concentration (mg/L), respectively;  $W$  (g) is the amount of used adsorbent;  $V$  (L) is the employed dye solution volume.

In all experiments the ratio between the volume of the dye solution and the adsorbent mass was kept equal to one.

#### 4.4.2.6.2 Adsorption isotherm

The adsorption isotherms experiments were carried out by incubating 1 mg/mL of p-1,8-DHN into MB water solutions (pH 6.5, 25 °C) at different concentrations of the dye (in the range 5-500 mg/L) and under stirring (rate = 250 rpm). The data were adjusted to the following Langmuir (Equation 10), Freundlich (Equation 11) and Temkin (Equation 12) isotherm models to investigate the mechanism of MB adsorption by p-1,8-DHN:

$$C_e/Q_e = 1/Q_{max}K_L + C_e/Q_{max} \quad (10)$$

$$\ln Q_e = \ln K_F + 1/n \ln C_e \quad (11)$$

$$Q_e = B_T \ln A_T + B_T \ln C_e \quad (12)$$

where  $C_e$  is the equilibrium concentration (mg/L),  $Q_e$  is the amount of adsorbed dye at equilibrium (mg/g),  $Q_{max}$  (mg/g) is the theoretical maximum adsorption capacity;  $K_L$  (L/mg) is the Langmuir constant and  $K_F$  (mg/g) is the Freundlich constant, both related to the adsorption capacity,  $n$  is a constant related to the adsorption intensity.  $A_T$  is the Temkin binding energy constant at equilibrium (L/g),  $B_T = RT/b$  is an indicator of the adsorption heat (J/mol), with  $T$  = absolute temperature (K),  $R$  = universal gas constant,  $b$  = Temkin isotherm constant.

#### 4.4.2.6.3 Thermodynamic analysis

Thermodynamic analysis was performed by incubating 1 mg/mL of p-1,8-DHN into a 20 mg/L MB water solution (pH 6.5) at different temperatures (in

the range 30-60 °C) and under stirring (rate = 250 rpm). After 30 minutes of incubation time, aliquots of the mixture were taken, and subjected to UV-vis spectroscopic analysis for the determination of  $Q_e$  and the thermodynamic parameters calculated according to the following equations **13-15**:

$$K = Q_e/C_e \quad (13)$$

$$\ln K = \Delta S^0/R - \Delta H^0/RT \quad (14)$$

$$\Delta G^0 = \Delta H^0 - T\Delta S^0 = -RT \ln K \quad (15)$$

#### 4.4.2.7 Cell culture

E14Tg2a.4 ES cells, derived from strain 129P2/OlaHsd were purchased from ATCC company and were cultured for two passages on gelatin-coated feeder-free plates and subsequently maintained in gelatin-coated plates in Glasgow Minimum Essential Medium (Gibco) supplemented with 15% FBS (EuroClone), 1,000 units/mL ESGRO leukaemia inhibitory factor (LIF) (Merck Millipore), 1.0 mM sodium pyruvate (Invitrogen), 0.1 mM non-essential amino acids (Invitrogen), 2.0 mM L-glutamine (Invitrogen), 0.1 mM  $\beta$ -mercaptoethanol (Sigma Aldrich) and 500 U/mL penicillin/streptomycin (Invitrogen). ESCs were incubated at 37°C in 5% CO<sub>2</sub>; medium was changed daily and cells were split every 2 to 3 days routinely. The human embryonic kidney (HEK-293) cell line were obtained from the CEINGE Cell Culture Facility (Naples, Italy) and were grown in DMEM medium containing 15% fetal bovine serum (Euroclone). For the growth curve,  $6 \times 10^5$  cells were seeded in triplicate on 60-mm dishes coated or not with melanin and cell count was performed after 48 h and 72 h from plating.

## References

1. E.R. Micelotta, A.P. Jones, A.G.G.M. Tielens. Polycyclic aromatic hydrocarbon processing by cosmic rays. *Astron Astrophys* **2011**, 526, A52.
2. M.P. Bernstein, J.P. Dworkin, S.A. Sandford, L.J. Allamandola. Ultraviolet irradiation of the polycyclic aromatic hydrocarbon (PAH) naphthalene in H<sub>2</sub>O. Implications for meteorites and biogenesis. *Advances in Space Research* **2002**, 30 (6), 1501–1508.
3. M.P. Bernstein, S.A. Sandford, L.J. Allamandola, et al. UV Irradiation of Polycyclic Aromatic Hydrocarbons in Ices: Production of Alcohols, Quinones, and Ethers. *Science (1979)* **1999**, 283 (5405), 1135–1138.
4. S. Kobayashi, H. Higashimura. Oxidative polymerization of phenols revisited. *Prog Polym Sci* **2003**, 28 (6), 1015–1048.
5. C.M.O. Alexander, G.D. Cody, B.T. De Gregorio, L.R. Nittler, R.M. Stroud. The nature, origin and modification of insoluble organic matter in chondrites, the major source of Earth's C and N. *Geochemistry* **2017**, 77 (2), 227–256.
6. E. Dadachova, A. Casadevall. Ionizing radiation: how fungi cope, adapt, and exploit with the help of melanin. *Curr Opin Microbiol* **2008**, 11 (6), 525–531.
7. S. Potenti, P. Manini, T. Fornaro, et al. Solid State Photochemistry of Hydroxylated Naphthalenes on Minerals: Probing Polycyclic Aromatic Hydrocarbon Transformation Pathways under Astrochemically-Relevant Conditions. *ACS Earth Space Chem* **2018**, 2 (10), 977–1000.
8. M. Sithamparam, N. Sathiyasilan, C. Chen, T.Z. Jia, K. Chandru. A material-based panspermia hypothesis: The potential of polymer gels and membraneless droplets. *Biopolymers* **2022**, 113 (5).
9. P. Manini, M. Bietti, M. Galeotti, et al. Characterization and Fate of Hydrogen-Bonded Free-Radical Intermediates and Their Coupling Products from the Hydrogen Atom Transfer Agent 1,8-Naphthalenediol. *ACS Omega* **2018**, 3 (4), 3918–3927.

10. M. Salamone, M. Bietti. Reaction Pathways of Alkoxy Radicals. The Role of Solvent Effects on C–C Bond Fragmentation and Hydrogen Atom Transfer Reactions. *Synlett* **2014**, 25 (13), 1803–1816.
11. N. Walalawela, A. Greer. Heterogeneous photocatalytic deperoxidation with UV and visible light. *J Phys Org Chem* **2018**, 31 (6), e3807.
12. P.K. Das, M. V. Encinas, S. Steenken, J.C. Scaiano. Reaction of tert-butoxy radicals with phenols. Comparison with the reactions of carbonyl triplets. *J Am Chem Soc* **1981**, 103 (14), 4162–4166.
13. E. Baciocchi, M. Bietti, M.F. Gerini, O. Lanzalunga. Electron-Transfer Mechanism in the *N*-Demethylation of *N,N*-Dimethylanilines by the Phthalimide-*N*-oxyl Radical. *J Org Chem* **2005**, 70 (13), 5144–5149.
14. E. Baciocchi, M. Bietti, M. Di Fusco, O. Lanzalunga. A Kinetic Study of the Electron-Transfer Reaction of the Phthalimide-*N*-oxyl Radical (PINO) with Ferrocenes. *J Org Chem* **2007**, 72 (23), 8748–8754.
15. E. Baciocchi, M. Bietti, O. Lanzalunga, A. Lapi, D. Raponi. *N*-Demethylation of *N,N*-Dimethylanilines by the Benzotriazole *N*-Oxyl Radical: Evidence for a Two-Step Electron Transfer–Proton Transfer Mechanism. *J Org Chem* **2010**, 75 (5), 1378–1385.
16. E. Baciocchi, M. Bietti, M. Di Fusco, O. Lanzalunga, D. Raponi. Electron-Transfer Properties of Short-Lived *N*-Oxyl Radicals. Kinetic Study of the Reactions of Benzotriazole-*N*-oxyl Radicals with Ferrocenes. Comparison with the Phthalimide-*N*-oxyl Radical. *J Org Chem* **2009**, 74 (15), 5576–5583.
17. E. Baciocchi, M. Bietti, C. D'Alfonso, et al. One-electron oxidation of ferrocenes by short-lived *N*-oxyl radicals. The role of structural effects on the intrinsic electron transfer reactivities. *Org Biomol Chem* **2011**, 9 (11), 4085.
18. C. Galli, P. Gentili, O. Lanzalunga, M. Lucarini, G.F. Pedulli. Spectrophotometric, EPR and kinetic characterisation of the  $>N-O\cdot$  radical from 1-hydroxybenzotriazole, a key reactive species in mediated enzymatic oxidations. *Chem. Commun.* **2004**, No. 20, 2356–2357.
19. F. Recupero, C. Punta. Free Radical Functionalization of Organic Compounds Catalyzed by *N*-Hydroxyphthalimide. *Chem Rev* **2007**, 107 (9), 3800–3842.

- 
20. R.E. Stratmann, G.E. Scuseria, M.J. Frisch. An efficient implementation of time-dependent density-functional theory for the calculation of excitation energies of large molecules. *J Chem Phys* **1998**, 109 (19), 8218–8224.
21. R. Bauernschmitt, R. Ahlrichs. Treatment of electronic excitations within the adiabatic approximation of time dependent density functional theory. *Chem Phys Lett* **1996**, 256 (4–5), 454–464.
22. M.E. Casida, C. Jamorski, K.C. Casida, D.R. Salahub. Molecular excitation energies to high-lying bound states from time-dependent density-functional response theory: Characterization and correction of the time-dependent local density approximation ionization threshold. *J Chem Phys* **1998**, 108 (11), 4439–4449.
23. C. Adamo, G.E. Scuseria, V. Barone. Accurate excitation energies from time-dependent density functional theory: Assessing the PBE0 model. *J Chem Phys* **1999**, 111 (7), 2889–2899.
24. G. Scalmani, M.J. Frisch, B. Mennucci, et al. Geometries and properties of excited states in the gas phase and in solution: Theory and application of a time-dependent density functional theory polarizable continuum model. *J Chem Phys* **2006**, 124 (9), 094107.
25. V. Lino, P. Manini. Dihydroxynaphthalene-Based Allomelanins: A Source of Inspiration for Innovative Technological Materials. *ACS Omega* **2022**, 7 (18), 15308–15314.
26. P. Manini, P. Margari, C. Pomelli, et al. Nanoscale Disassembly and Free Radical Reorganization of Polydopamine in Ionic Liquids. *J Phys Chem B* **2016**, 120 (46), 11942–11950.
27. L. Panzella, G. Gentile, G. D’Errico, et al. Atypical Structural and  $\pi$ -Electron Features of a Melanin Polymer That Lead to Superior Free-Radical-Scavenging Properties. *Angewandte Chemie International Edition* **2013**, 52 (48), 12684–12687.
28. P. Manini, V. Lino, G. D’Errico, et al. “Blackness” is an index of redox complexity in melanin polymers. *Polym Chem* **2020**, 11 (31), 5005–5010.

- 
29. N.C. McCallum, F.A. Son, T.D. Clemons, et al. Allomelanin: A Biopolymer of Intrinsic Microporosity. *J Am Chem Soc* **2021**, 143 (10), 4005–4016.
30. E. P. Serjeant, Boyd Dempsey. Ionisation constants of organic acids in aqueous solution. In *International Union of Pure and Applied Chemistry*; Oxford, Pergamon Press, **1979**.
31. M.A. Mohammed, A. Shitu, A. IbrahiM. Removal of Methylene Blue Using Low Cost Adsorbent: A Review. *Research Journal of Chemical Sciences* **2014**, 4 (1), 91–102.
32. A. Pezzella, M. Barra, A. Musto, et al. Stem cell-compatible eumelanin biointerface fabricated by chemically controlled solid state polymerization. *Mater Horiz* **2015**, 2 (2), 212–220.
33. J. Tomasi, B. Mennucci, R. Cammi. Quantum Mechanical Continuum Solvation Models. *Chem Rev* **2005**, 105 (8), 2999–3094.
34. S. Miertuš, E. Scrocco, J. Tomasi. Electrostatic interaction of a solute with a continuum. A direct utilization of AB initio molecular potentials for the prevision of solvent effects. *Chem Phys* **1981**, 55 (1), 117–129.
35. M. Cossi, G. Scalmani, N. Rega, V. Barone. New developments in the polarizable continuum model for quantum mechanical and classical calculations on molecules in solution. *J Chem Phys* **2002**, 117 (1), 43–54.
36. G. Scalmani, V. Barone, K.N. Kudin, et al. Achieving linear-scaling computational cost for the polarizable continuum model of solvation. *Theor Chem Acc* **2004**, 111 (2–6), 90–100.
37. A.K. Rappe, C.J. Casewit, K.S. Colwell, W.A. Goddard, W.M. Skiff. UFF, a full periodic table force field for molecular mechanics and molecular dynamics simulations. *J Am Chem Soc* **1992**, 114 (25), 10024–10035.
38. D.M. York, M. Karplus. A Smooth Solvation Potential Based on the Conductor-Like Screening Model. *J Phys Chem A* **1999**, 103 (50), 11060–11079.
39. G. Scalmani, M.J. Frisch. Continuous surface charge polarizable continuum models of solvation. I. General formalism. *J Chem Phys* **2010**, 132 (11), 11411

# CHAPTER 5

## CATALYTIC EFFECT OF OXYPAH-POLYMERS IN THE CHEMICAL PROCESSES LEADING TO THE FORMATION OF THE PEPTIDE BOND

*“All of us who study the origin of life find that the more we look into it, the more we feel it is too complex to have evolved anywhere. We all believe as an article of faith that life evolved from dead matter on this planet. It is just that life's complexity is so great, it is hard for us to imagine that it did.”*

— Harold C. Urey, Christian Science Monitor, 1962

### 5.1 Introduction

Among the different research lines developed with the aim of shedding light on the complex sequence of events that have led to the emergence and evolution of life on the early Earth, the most intriguing and inspiring ones deal with the formation of the molecules of life, i.e. amino acids and proteins, nucleobases and nucleic acids.

One of the earliest attempts to elucidate plausible mechanisms proceeding in prebiotic environments for the synthesis of amino acids was the Urey-Miller experiment, in 1953.<sup>1</sup>

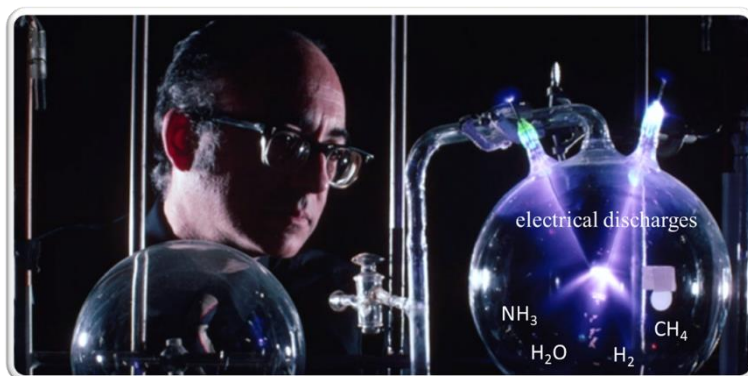


**Figure 1** | Miller-Urey experiment showing the formation of amino acids in an environment of water, methane, ammonia, and hydrogen following electrical discharges.

In this landmark experiment by sparking a reducing atmosphere (Figure 1) they detected the amino acids in the reaction products demonstrating that basic molecules of life could be synthesized, through natural processes, from simple molecules, which were supposed to be present in the primitive atmosphere of Earth.

The abiotic synthesis of amino acids has been demonstrated in a lot of experiments,<sup>2-4</sup> including those under hydrothermal conditions. Amino acids have been found in meteorites<sup>5</sup> and their presence on the Hadean Earth is considered very likely. However, once the amino acids have formed, how can they combine to form more complex biomolecules?

In view of the chemical evolution of life on Earth, the polymerization of amino acids is an essential process leading to the formation of proteins. The most reasonable pathway for the formation of oligopeptide would surely be the condensation between two amino acids, followed by the release of a water molecule and the formation of an amide bond. However, the condensation

process is very challenging, because even if the reaction is mostly favoured under high temperatures for its endothermic nature, the presence of water makes the reverse hydrolytic process thermodynamically favoured (Figure 2).

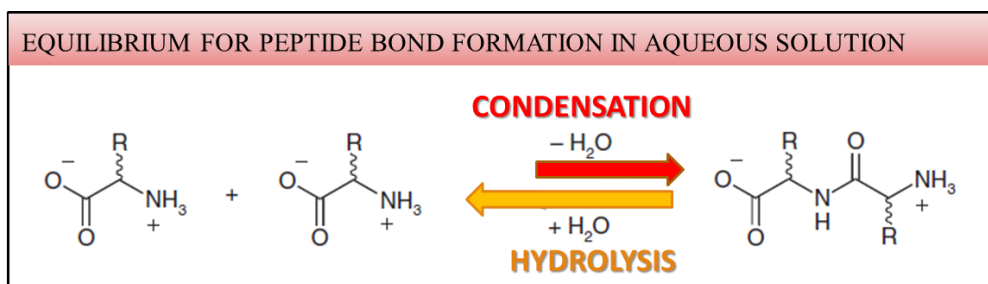


**Figure 2** | Scheme showing equilibrium for peptide bond formation in aqueous solution.

Unquestionably, water is a mandatory prerequisite for life and ubiquitous on Earth. It is assumed that water has been readily available on primitive Earth since also its ubiquity in the universe. Thus, life requires water but, at the same time, it is inherently toxic to polymers (e.g. nucleotides or proteins) necessary for life, leading to the “water paradox”.<sup>6</sup>

To overcome this difficulty, researchers have tested different methods including the use of condensing agents, high temperatures, and water-free solvents. Besides some of these being successful, not all of these routes would have been plausible on early Earth.

Currently, condensation reactions are catalysed by enzymes and energetically driven by pyrophosphate hydrolysis, but there is no reason to believe that other types of catalysts couldn't have existed on primitive Earth.

Recently, the formation of peptide bonds under prebiotic conditions has become more feasible if driven by a wet-dry cycling process. In these

conditions, the polymerization does not require activated monomers or condensing agents.

In the wet-dry process, each cycle involves two phases: 1) a hot and dry phase in which the bond formation is favourable, but diffusion is not allowed or much slower than in solution, so only monomers that are very close can polymerize; 2) a wet phase in which diffusion is allowed so that molecules are brought closer each other, ready to polymerize in the next dry phase. The net effect of iterative cycles leads to an increase in polymerization.<sup>7</sup>

Wet-dry cycles are regarded as characteristic of extreme natural fluctuating environments like hydrothermal pools and primordial rock pools at volcanic sites. These are areas of elevated temperatures where hot spring water raised to the surface and where rainstorms and flooding occurred (Figure 3). So dynamic cycling between the anhydrous surface phase and the hydrated bulk phase is established.



**Figure 3** | wet and dry cycles at hydrothermal pools where the elevated temperatures allow the evaporation of water and the rainfalls fill them again.

Geothermal fields and geothermal water catalysis have gained increasing interest within the astrobiology community since they are considered ideal environments to allow life to emerge, providing the proper supply of thermal

energy and catalysts.<sup>8</sup> In this regard, considerable interest is being focused on the well-characterized geothermal system of the caldera of the Phlegrean Fields. This site, situated to the west of Naples, is a large volcanic area of about 12 km in diameter that comprises 24 craters and volcanic features, including the Solfatara volcano with large and spectacular fumarole vents. The area exhibits a continuous rising of hydrothermal fluids generating diffuse bubbling, with impressive degassing manifestations and intense fumarolic activity in the Pisciarelli area located a few hundred meters east of the Solfatara crater. Fumaroles eject mainly H<sub>2</sub>O and to a lesser extent CO<sub>2</sub> and H<sub>2</sub>S and have a surface temperature of up to 165 °C (up to ~115 °C for Pisciarelli).<sup>9</sup> Such conditions may resemble the environment of the early Earth so the Solfatara and Pisciarelli areas have been considered as a natural prebiotic laboratory offering a broad range of opportunities for rich and diversity-oriented chemistry.

Clays, minerals and silicates located at hydrosphere–lithosphere interface may have played a vital role in this context because they might have adsorbed key monomers on their surface. In this way, minerals can concentrate monomers from dilute solutions and provide a matrix for polymerization. Extensive literature data have demonstrated that minerals are efficient catalysts for peptide formation reactions in wet–dry cycle experiments.<sup>10–12</sup> Studies carried out on montmorillonite suggested that this catalytic effect is due to the formation of hydrogen bonds between the amino acids and mineral surface causing the breaking of the stronger intermolecular hydrogen bonds among the amino acids.<sup>13,14</sup> However, other experimental evidence suggested that the minerals couldn't exhibit their catalytic properties in the formation of peptides from amino acids but only in the chain elongation of dipeptides.

Wetting and drying cycles have also been used in the so-called “salt-induced peptide formation” (SIPF), by exploiting the dehydrating ability of concentrated NaCl solutions.<sup>15</sup> A key role in this reaction is played by  $\text{Cu}^{2+}$ , which coordinates two amino acid ligands to form a copper complex intermediate. In this way, the reaction proceeds intramolecularly and with much more efficiency. If the reaction takes place in combination with a clay catalyst, longer peptides are obtained.<sup>16</sup>

Starting from this solid background, the scientific activity described in this chapter has been mainly focused on the mechanisms of formation of the peptide bond between amino acids in conditions of astrochemical relevance. In particular, we focused on the study of the peptide bond formation process starting from the amino acid glycine under wet-dry conditions.

By performing a combined approach based on ion-pairing high-performance liquid chromatography (IP-HPLC-UV), attenuated total reflection (ATR-FTIR) and mass spectrometry (MALDI-MS) analyses, the effect of two novel potential catalytic systems on the wet-dry oligomerization process of glycine has been investigated:

- 1) the thermal water of the natural geothermal environment of Pisciarelli spring inside Phlegrean Fields;
- 2) the polymers obtained from the oxidation of two representative oxy-PAHs, namely 1,8-DHN and 1-HN (for polymer synthesis and characterization see Chapter 4).

This work has been presented at XVII Congresso Nazionale di Scienze Planetarie **OP2**.

## 5.2 Results and discussion

Starting from the background disclosed in the Introduction section, here the results obtained exploring the possible implication of insoluble oxyPAH-polymers and thermal water of Solfatara as an alternative to inorganic rocks in the wet-dry oligomerization process of glycine will be reported.

In Chapter 4, the synthesis and structural characterization of insoluble OxyPAH-polymers starting from 1,8-DHN and 1-HN monomers were reported. Instead, the thermal water of Solfatara was collected in situ directly from pools of Pisciarelli spring, as shown in Figure 4.



**Figure 4** | Collection of water samples from the mud pool of Pisciarelli fumarolic field.

In an effort to provide more insight into their potentialities as catalysts to facilitate the oligomerization of glycine, wet-dry experiments were carried out using OxyPAH-polymers or thermal water in comparison with blank experiments carried out without any catalyst. In addition, the influence of a silicate mineral, montmorillonite, on the peptide bond formation was studied.

To this aim, a mixture of 0.1 M water solution of glycine (10 mL) and oxyPAH-polymers/thermal water has been prepared and treated at high temperatures to induce water removal. Subsequently, the same amount of water was used to rinse the residue and then another heating cycle was started (Figure 5).

After the final cycle, the residue was allowed to cool down to room temperature and treated with  $\text{CaCl}_2$  to allow the release of all formed oligopeptides.<sup>17</sup>

After the  $\text{CaCl}_2$  treatment some insoluble precipitate was also observed. So, the mixture was subjected to a centrifugation step to afford a liquid phase that was analysed by ion-pairing high-performance liquid chromatography (IP-HPLC), and a solid residue that was analysed by attenuated total reflection (ATR) spectroscopy and matrix assisted laser desorption ionization mass spectrometry (MALDI-MS).

Control experiments, in which wet-dry cycles were performed only in the presence of catalysts, were revealed that the oxyPAH-polymers did not release any product.

To better understand the trend in product formation, the oligomerization reaction was investigated under different conditions, that is by varying the temperatures (90 °C and 150 °C) and the number of cycles (2, 7 and 14).

The next paragraphs will illustrate the main outcomes obtained by testing the potential role of OxyPAH-polymers and thermal water of Solfatara as catalysts on the oligomerization reaction of glycine.

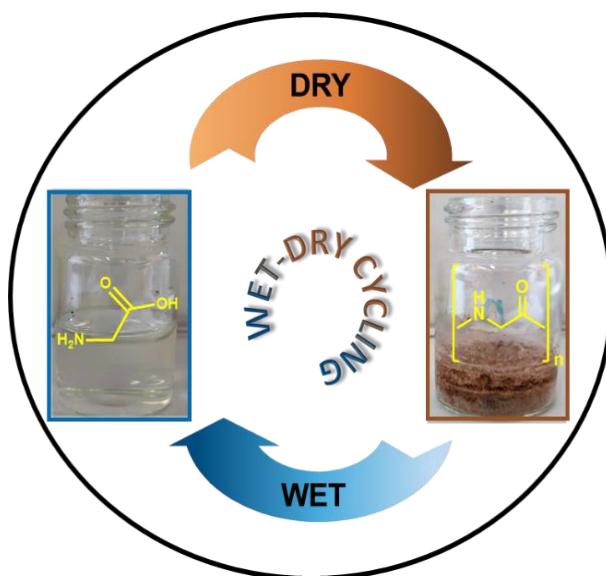


**Figure 5** | An illustration of the wet-dry cycling process

## **5.2.1 Study of catalytic effect of oxyPAH-polymers on oligomerization of glycine**

### **5.2.1.1 IP-HPLC analysis of supernatant solutions**

Glycine is the simplest amino acid, the most prevalent in the earliest proteins and the most abundantly produced in prebiotic experiments. Generally, the reaction pathways for the oligomerization of glycine lead to the formation of the dipeptide (gly-gly) that is often in equilibrium with the diketopiperazine (DKP) form obtained via its intramolecular cyclization. Both gly-gly and DKP may evolve leading to the formation of the tripeptide and superior oligomers (Figure 6).

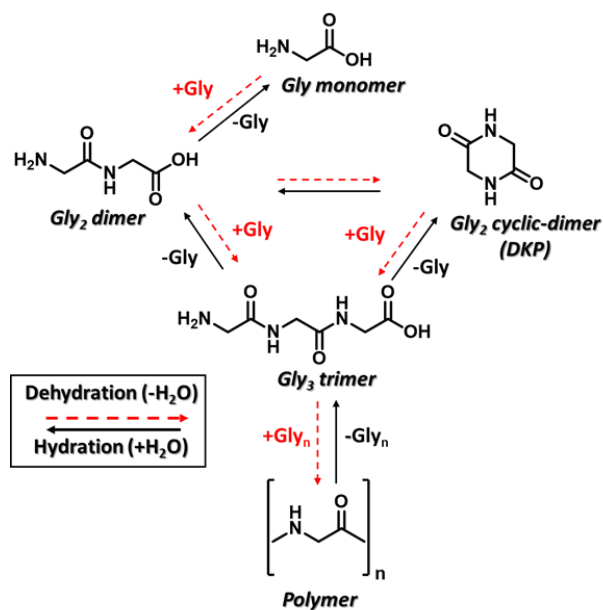


**Figure 6** | Reaction pathway of oligomerization of Glycine.

In table 1, the reaction yields of the products formed by heating glycine are shown. Each experiment was run in triplicate and the data reported are the average results  $\pm$  SD. As shown, two main products were detected in the liquid phase: gly<sub>2</sub> and DKP. The HPLC analysis showed the progressive consuming of the starting glycine and the simultaneous formation of both DKP and gly<sub>2</sub>. For each reaction, the DKP yield was mostly higher than that of gly<sub>2</sub>. The easier formation of DKP can be explained considering the higher stability of the cyclic form. Moreover, the intramolecular reaction is much easier, from a kinetic point of view, than the intermolecular condensation between the dipeptide and other amino acids, because the distance between the amino group and the carboxyl group in the dipeptides is short.

**Table 1** | Yields of the products formed by heating glycine.

Experiment	150 °C 14 cycles			90 °C 14 cycles		
	%mol/mol (DKP)	%mol/mol (GLY)	%mol/mol (GLY- GLY)	%mol/mol (DKP)	%mol/mol (GLY)	%mol/mol (GLY- GLY)
<b>p-1,8-DHN</b>	2.9± 0.4	-	0.21± 0.05	0.57±0.09	50±4	0.20±0.05
<b>p-1-HN</b>	2.9± 0.3	-	0.28± 0.04	0.27±0.02	57±5	0.17±0.09
<b>Blank</b>	0.56± 0.08	69±8	0.05± 0.01	-	90±4	0.03±0.06
<b>Blank+mineral</b>	3.22± 0.01	-	0.17± 0.02	0.18±0.01	81±2	0.07±0.02
	150 °C 7 cycles			90 °C 7 cycles		
<b>p-1,8-DHN</b>	3.4± 0.3	-	0.21±0.09	0.51±0.05	72±3	0.083±0.003
<b>p-1-HN</b>	1.12±0.10	59.0±0.9	0.20±0.02	0.18±0.09	82±6	0.08±0.02
<b>Blank</b>	0.24± 0.03	81.5±1.3	0.03±0.01	-	94±2	-
<b>Blank+mineral</b>	2.70±0.02	52±5	0.34±0.03	0.040±0.003	88.28±0.05	0.04±0.01
	150 °C 2 cycles					
<b>p-1,8-DHN</b>	2.05±0.05	52±8	0.21±0.02			
<b>p-1-HN</b>	0.10±0.01	94±1	0.030±0.004			
<b>Blank</b>	-	99.78±0.27	-			
<b>Blank+mineral</b>	1.14 ± 0.16	92±9	0.21±0.04			

Even if some studies have often concluded that the DKP formation is a dead-end for peptide elongation under continuous dry conditions,<sup>18,19</sup> it is suggested that the cis-form of peptide bonds in DKP would have higher energy than the trans-form in linear dipeptides, thus, the ring-opening of DKP could supply the free energy necessary to form a new peptide bond. If sufficient water exists, peptides could be elongated to more than trimer via hydrolysis of DKP (i.e.,  $\text{DKP} + \text{H}_2\text{O} \rightarrow \text{Gly}_2$ ).

Figures 7-9 show the most representative chromatograms. Figure 10 displayed the comparison between supernatants obtained conducting the reaction at 90°C with 7 wet and dry cycles and at 150°C with 14 cycles.

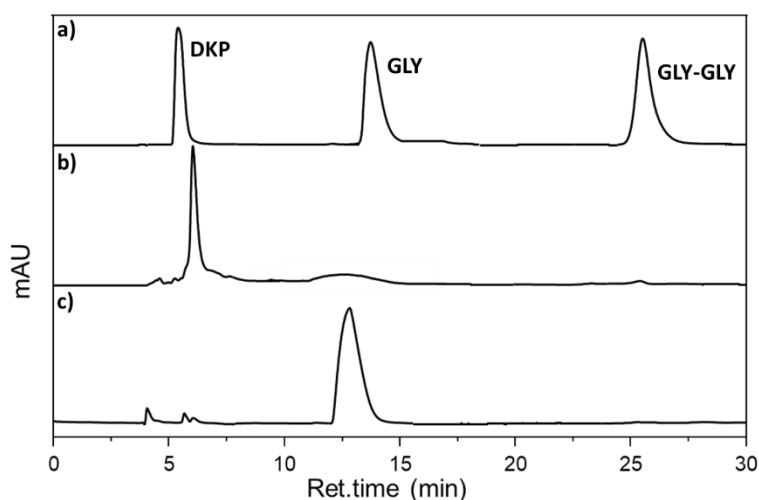


**Figure 7** | Chromatograms of (a) DKP, GLY and GLY-GLY standards, (b) the supernatant of the reaction with p-1,8-DHN after heating at 150 °C with 2 wet-dry cycles, and (c) blank experiment after heating at 150 °C with 2 wet-dry cycles.

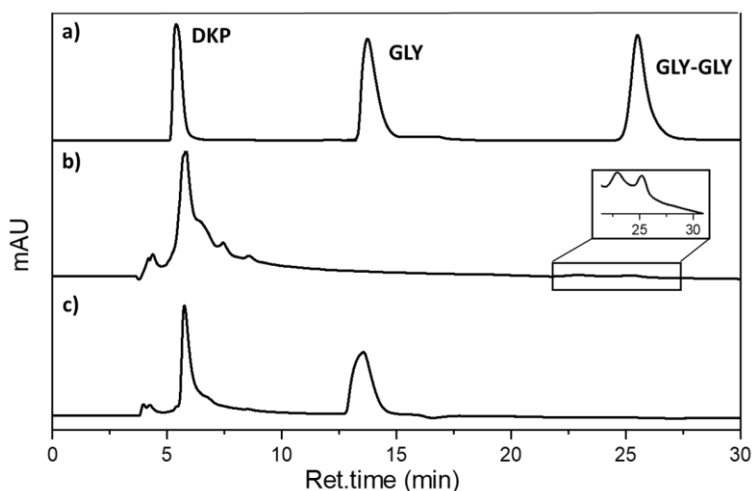


**Figure 8** | Chromatograms of (a) DKP, GLY and GLY-GLY standards, (b) the supernatant of the reaction with p-1,8-DHN after heating at 150 °C with 14 wet-dry cycles, and (c) blank experiment after heating at 150 °C with 14 wet-dry cycles.

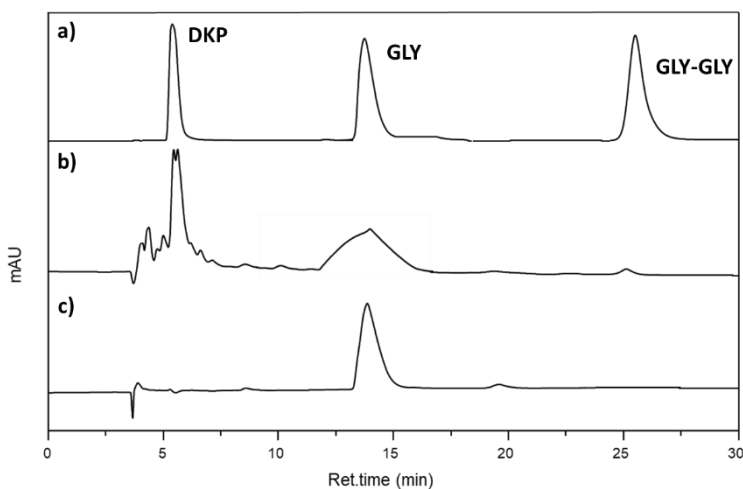


**Figure 9** | Chromatograms of (a) DKP, GLY and GLY-GLY standards, (b) the supernatant of the reaction with p-1,8-DHN after heating at 90 °C with 7 wet-dry cycles, and (c) blank experiment after heating at 90 °C with 7 wet-dry cycles.

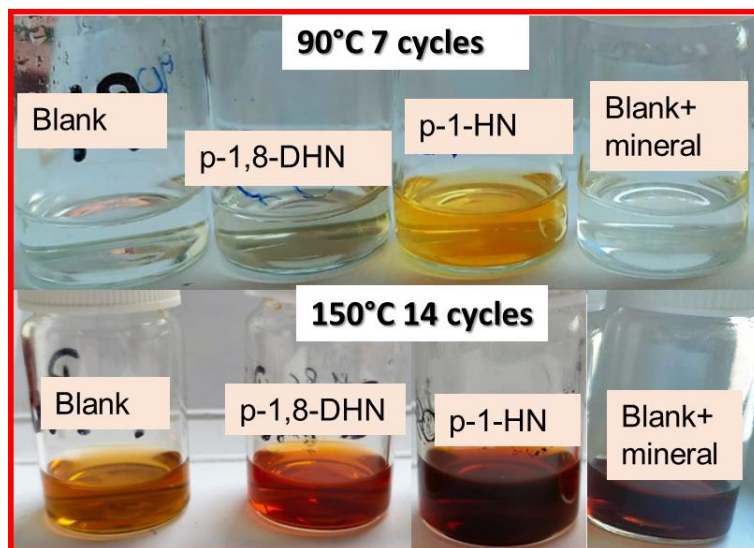


**Figure 10** | Picture of supernatants obtained conducting the reaction at 90°C with 7 wet and dry cycles and at 150°C with 14 cycles.

The reaction yields of DKP and gly<sub>2</sub> formed in the presence of a catalysts, both montmorillonite and oxyPAH-polymers, proved to be higher than those of blank experiments.

HPLC data obtained performing the reaction at 150 °C showed that: 1) with two wet-dry cycles, the catalytic effect of polymers or of inorganic mineral in comparison with blank was clearly evident (Figure 7, Table 1). In this latter case, the chromatogram showed the presence of almost 100% residual glycine (Figure 7). Among the catalysts tested, the effect of p-1,8-DHN was truly remarkable since about half of the initial glycine seems to have reacted and the DKP yield is twice compared with that obtained in presence of mineral; 2) by increasing the number of cycles to 7, the dimerization products were formed in the blank experiment. The activity of p-1,8-DHN and mineral seems quite

comparable although in the case of the mineral the yield of gly<sub>2</sub> is higher than that of DKP. However, considering that the reaction in the presence of the mineral led to a higher concentration of residual glycine and that the intramolecular cyclization of DKP followed the formation of gly<sub>2</sub>, it can be deduced that, also in this case, p-1,8-DHN had a greater catalytic effect than the mineral;

3) the effect of catalysts on the oligomerization reaction of glycine became comparable only by carrying out the reaction with 14 cycles.

By performing the reaction at 90 °C, the higher catalytic effect of p-1,8-DHN in comparison with p-1-HN and mineral is much clearer. This is especially evident when comparing with the blank experiment (residual glycine in blank experiment: 90%, residual glycine in experiments carried out with p-1,8-DHN: 50%).

To evaluate how factors such as the temperature and the number of cycles may affect the product formation, we should compare the yields of dimeric product and residual glycine obtained both at the same temperature varying the number of cycles and at the same number of cycles varying the temperature. Comparing the reaction performed with 14 wet and dry cycles at 90 °C and 150°C, we noticed that at 90°C the yields of dimeric products were lower and the amount of residual glycine was higher than 150°C.

The same trend was observed by analyzing the reaction performed with 7 wet-dry cycles. Noteworthy is the effect of p-1,8-DHN when the temperature in the dry phase was risen up to 150°C. A significant increase in dimeric products has been observed and the residual glycine, which was 70% at 90°C, is completely absent at 150°C.

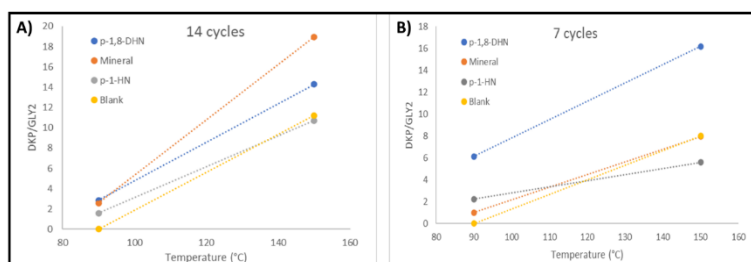


**Figure 11** | Ratio of products (DKP/gly<sub>2</sub>) with increasing the temperature for 14 (A) and 7 (B) wet and dry cycles.

Figure 11 shows the ratio of products (DKP/gly<sub>2</sub>) as the temperature increases. The ratio gradually increased with increasing the temperature, indicating that DKP formation from Gly<sub>2</sub> was promoted with increasing the temperature. This trend indicates that the cyclization of Gly<sub>2</sub> (i.e. DKP formation) followed the formation of linear peptides. Overall, these results showed that the formation of gly<sub>2</sub> and DKP increased with temperature in accordance with the endothermic nature of the reaction. Moreover, at 150 °C the wet phase is shorter than at 90 °C because the evaporation is faster thus reducing the possibility of hydrolysis.

Increasing the number of cycles from 7 to 14, and leaving the temperature unchanged, it can be noticed that: 1) at 150°C the decrease in glycine is more evident than the increase in dimeric products suggesting the formation of higher oligomers 2) performing the reaction in presence of the catalysts at 90 °C, there was a general increase in the yields of dimeric products and a corresponding decrease of residual glycine. Nevertheless, this effect is less significant with respect to that obtained by increasing the temperature. On the other hand, in blank experiments the yields were unaffected. These data showed that the oligomerization reaction of glycine was promoted by increasing the number of wet-dry cycles.

### 5.2.1.2 Analysis of residue

During the wet-dry experiments carried out on glycine, the formation of brown residues has been observed. This may be due to the precipitation of longer oligomeric products or to secondary decomposition processes. To shed more light on this issue, the residue has been analyzed by mass spectrometry (MALDI) and attenuated total reflection (ATR) spectroscopy. For all residues, mass spectrometry revealed the presence of a regular pattern of peaks separated by 57 Da, corresponding to the mass of a glycine unit, suggesting the presence of higher oligomeric products. This was also confirmed by ATR spectra (Figures 12, 13) showing the presence of bands related to the stretching of C=O and N-H bonds that were also visible in the spectrum of gly<sub>2</sub> standard and not detectable in the spectrum of the monomer glycine.

In Table 2, the amounts and the length of the glycine oligomers detected in the solid residues formed in all the reaction conditions investigated have been reported.

As can be seen, on raising the reaction temperature from 90 °C to 150 °C, a general increase in the amounts and in the length of the glycine oligomers was observed. Moreover, these analyses revealed that this effect was more pronounced by increasing the temperature than the number of cycles. As a matter of fact, performing the reaction at 90 °C, the formation of glycine oligomers was shown only in the presence of oxyPAH-polymers.

In Figure 14, MALDI spectra of the residues obtained at 150°C after 14 wet-dry cycles in presence of the catalysts are shown.

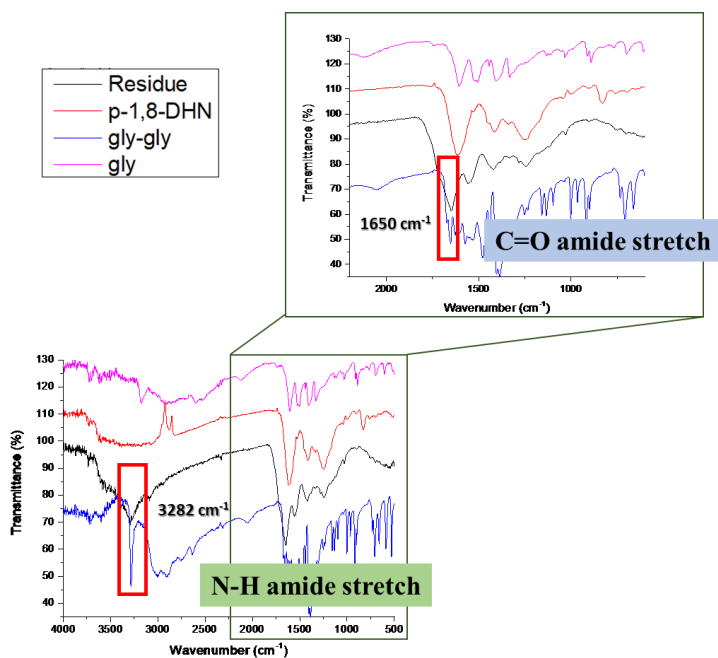


**Figure 12** | ATR spectra in the region 4000–500 cm<sup>-1</sup> showing the N–H amide stretching of residue formed after 14 wet-dry cycles at 150°C in presence of p-1,8-DHN. b) Zoom-in of the 2500–500 cm<sup>-1</sup> spectral region of showing the C=O amide stretching.

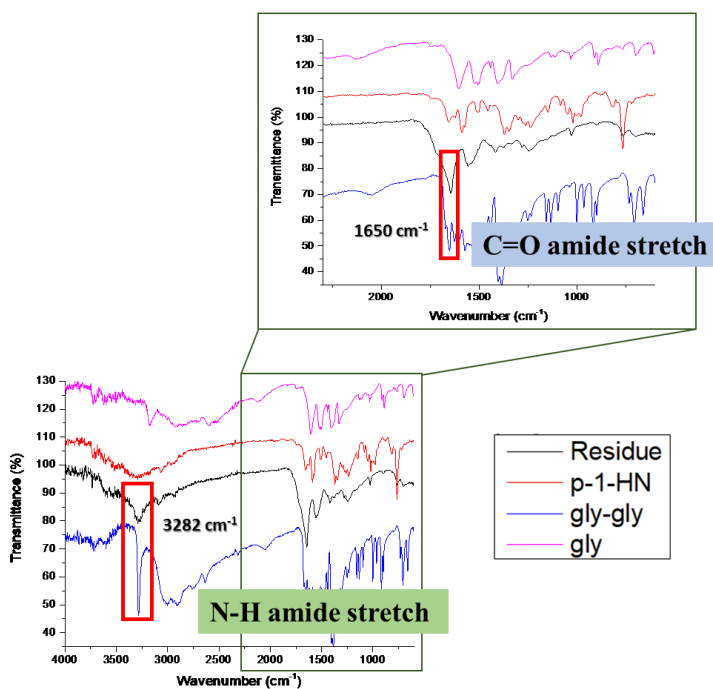


**Figure 13** | ATR spectra in the region 4000–500 cm<sup>-1</sup> showing the N–H amide stretching of residue formed after 14 wet-dry cycles at 150°C in presence of p-1-HN. b) Zoom-in of the 2500–500 cm<sup>-1</sup> spectral region of showing the C=O amide stretching.

**Table 2** | Quantity and length of glycine oligomer of residue formed in all the reaction conditions investigated.

Residue	quantity	Length glycine polymer	quantity	Length glycine polymer
<b>150 °C 2 cycles</b>				
<b>p-1,8-DHN</b>	6 mg	Gly <sub>5</sub>		
<b>p-1-HN</b>	1mg	Gly <sub>5</sub>		
<b>Blank</b>	-	-		
<b>Mineral</b>	1 mg	Gly <sub>5</sub>		
<b>150 °C 7 cycles</b>			<b>90 °C 7 cycles</b>	
<b>p-1,8-DHN</b>	8 mg	Gly <sub>6</sub>	1mg	Gly <sub>5</sub>
<b>p-1-HN</b>	2 mg	Gly <sub>5</sub>	1 mg	Gly <sub>5</sub>
<b>Blank</b>	2 mg	Gly <sub>6</sub>	-	-
<b>Blank+Mineral</b>	10	Gly <sub>5</sub>	-	-
<b>150 °C 14 cycles</b>			<b>90 °C 14 cycles</b>	
<b>p-1,8-DHN</b>	7 mg	Gly <sub>11</sub>	1mg	Gly <sub>6</sub>
<b>p-1-HN</b>	7 mg	Gly <sub>12</sub>	1 mg	Gly <sub>6</sub>
<b>Blank</b>	2 mg	Gly <sub>7</sub>	-	-
<b>Blank+Mineral</b>	13 mg	Gly <sub>8</sub>	-	-

The MALDI spectra of the blank experiments have been reported as reference (Figure 14d). It can be observed the presence of oligomers up to 11 glycine units when p-1,8-DHN was used as catalyst (Figure 14a) and up to 12 glycine units when the catalyst was p-1-HN (Figure 14b). The catalytic effect was evident when comparing these data with those from the MALDI spectra of the solid residues recovered in blank experiments and in experiments carried out in presence of montmorillonite, in which the length of the oligomers was up to 8 units of glycine (Figure 14c,d). In Figure 15, the comparison between MALDI spectra of the residues formed in presence of oxy-PAH polymers and montmorillonite at 150°C after 2 wet-dry cycles, is shown.

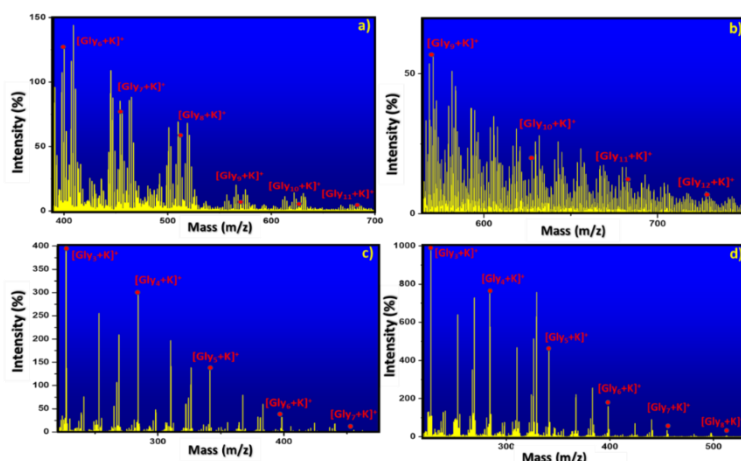


**Figure 14** | MALDI-MS spectra of glycine oligomers formed after 14 wet-dry cycles at 150°C in the presence of a) p-1,8-DHN, b) p-1-HN, c) mineral and d) blank.

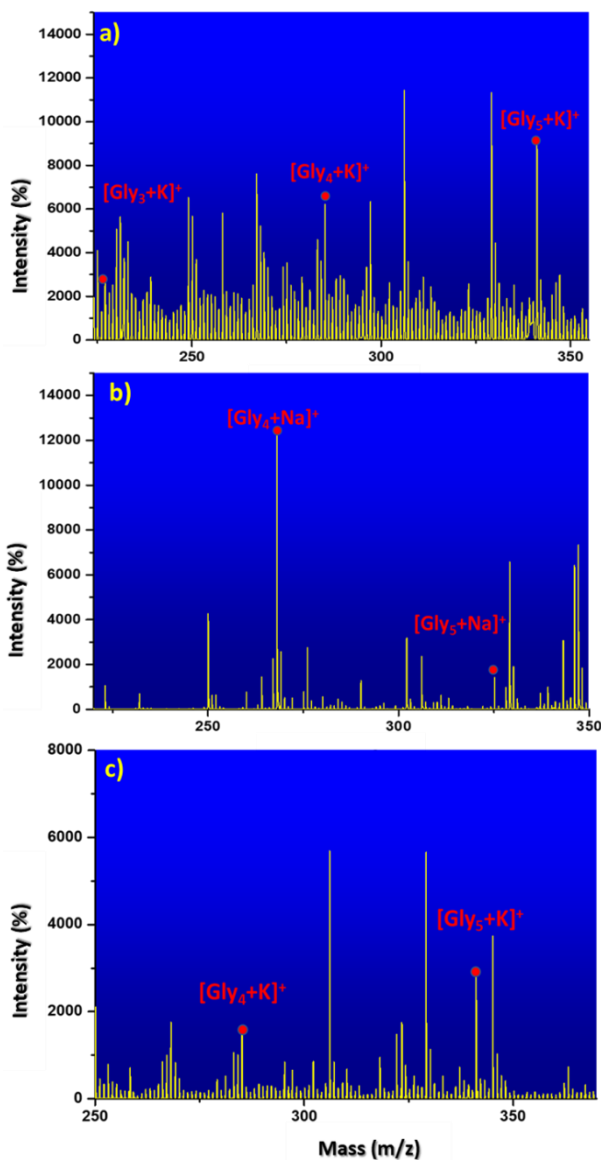


**Figure 15** | MALDI-MS spectra of glycine oligomers formed after 2 wet-dry cycles at 150°C in the presence of a) p-1,8-DHN, b) p-1-HN and c) mineral.

The more efficient catalytic effect of p-1,8-DHN and p-1-HN with respect to inorganic matrices may be due to the chemical properties and to the morphology of these polymers. As reported in the literature,<sup>20</sup> p-1,8-DHN

exhibits several aromatic rings that allow for numerous interactions that go beyond the classic hydrogen bonds, such as lone pair- $\pi$  interactions (Figure 16). Since the pH of the glycine solution used for experiments is 6.4, most of the glycine existed as zwitterions, so also cation- $\pi$  interactions are likely to occur.

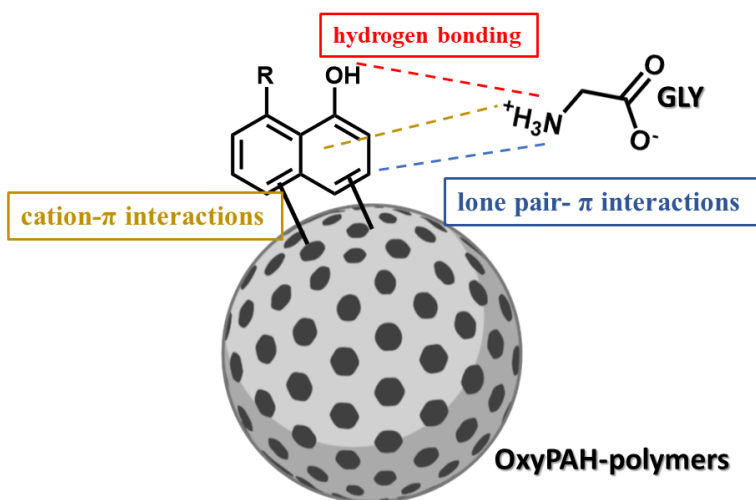


**Figure 16** | Proposed interactions between oxyPAH-polymers and glycine that explain the catalytic role of these polymers.

All these interactions allow for the redistribution of the charges, thus activating the carboxylic groups toward the peptide bond formation.

The formation of hydrogen bonds between the amino acids and the hydroxyl groups on the polymer surface could cause the breaking of the stronger intermolecular hydrogen bonds among the amino acids, as it happens with the mineral. The higher catalytic effect of p-1,8-DHN in comparison with p-1-HN could be justified by the greater presence of hydroxylic groups in p-1,8-DHN that could give rise to more hydrogen bond interactions.

However, theoretical investigations will be carried out to better clarify the modalities of glycine adsorption on organic polymers.

In addition to the chemical interactions, also the microporosity of the material could have played a key role in facilitating the adsorption of glycine. As reported in literature,<sup>20</sup> oxyPAH-polymers such as p-1,8-DHN exhibits greater microporosity (up to 860 m<sup>2</sup>/g) than montmorillonite (up to 61 m<sup>2</sup>/g). This data can justify a better adsorption of the glycine onto the surface of the polymer, so forcing the amino acids to stay close to each other and react more easily.

## **5.2.2 Study of catalytic effect of Solfatara thermal water on oligomerization of glycine**

### **5.2.2.1 Analysis of thermal water**

Thermal waters from Phlegrean Fields are generally characterized by high temperatures, are rich in Cl<sup>-</sup> and SO<sub>4</sub><sup>2-</sup>, suggesting the interaction with higher enthalpy fluids, and show high concentrations of elements such as Al, Fe, Mn and B.<sup>21</sup> As observed also in other geothermal areas where sediments and fine-grained mud are often highly enriched in mercury,<sup>22,23</sup> the trace element analysis showed also the presence of high concentrations of Hg.

For these peculiarities, the geothermal samples taken from two different pools at Pisciarelli springs (Figure 17) were subjected to a chemical-physical analysis for the determination of parameters such as the pH, the electrical conductivity and hardness, and the identification of metals, metalloids and main anions.



**Figure 17** | Hydrothermal manifestations at the Solfatara volcano: (A) Pool 1 and (B) Pool 2.

Data obtained from the two thermal water samples, namely Pool 1 and Pool 2, obtained from the geothermal samples after the separation of the mud, are reported in Tables 3 and 4.

The data obtained from the two pools denoted a variable distribution of the chemical components, responsible for appreciable differences in terms of temperature, pH, hardness and electrical conductivity. Worthy of note is the slightly acidic pH between 4.4 and 5.4 ascribable to the high levels of sulfate ions detected in both Pool 1 and Pool 2. The Pisciarelli springs, as well as the Solfatara, are rich in  $H_2S$  that can suffer oxidation to sulfuric acid when the hot fluids rising from depth interact with shallow meteoric water. In this support are also the many sulfate minerals and native sulfur samples located all around the hot water pools at Pisciarelli.<sup>24</sup> The relatively high iron ion and boron content are also relevant features to orient chemical and mechanistic discussions for the purpose of this investigation.

**Table 3** | Metals and metalloids concentration in the thermal water expressed in  $\mu\text{g L}^{-1}$ .

	Al	Sb	As	Ba	B <sup>a</sup>	Cd	Cr	Co	Fe
<b>Pool 1</b>	3513	1.5	3.0	69.7	1.1	0.5	< 0.1	5.97	1584
<b>Pool 2</b>	6582	< 0.2	8.2	22.3	0.44	0.5	< 0.1	13.6	89540
	Mn	Hg	Ni	Pb	Cu	Se	Sr	V	Zn
<b>Pool 1</b>	475	214	45.3	3.62	74.8	< 1	64.8	14.9	49.7
<b>Pool 2</b>	2084	7.96	861	3.89	61.9	< 1	101	8.55	40.7

<sup>a</sup> Data reported in  $\text{g L}^{-1}$ .

**Table 4** | Chemical-physical analysis of the Pisciarelli thermal water. The concentration of elements was reported in  $\text{mg L}^{-1}$ .

	pH	E.C. ( $\mu\text{S cm}^{-1}$ )	Hardness ( $^{\circ}\text{f}$ )	Na <sup>+</sup>	K <sup>+</sup>	Ca <sup>2+</sup>
<b>Pool 1</b>	5.4	8630	15.8	1790	6.2	53.2
<b>Pool 2</b>	4.4	10380	45.4	2126	19.7	149
	Mg <sup>2+</sup>	F <sup>-</sup>	Cl <sup>-</sup>	NO <sub>3</sub> <sup>-</sup>	SO <sub>4</sub> <sup>2-</sup>	Br <sup>-</sup>
<b>Pool 1</b>	6.20	0.68	4.96	6.6	3994	1.1
<b>Pool 2</b>	19.7	0.60	8.10	6.3	5374	< 0.5

### 5.2.2.2 IP-HPLC analysis of supernatant solutions

Table 5 shows the reaction yields of the products formed by heating glycine. Also, in this case, two major products are observed: gly<sub>2</sub> and DKP.

HPLC data showed the progressive consuming of the starting glycine and the simultaneous formation of both DKP and gly<sub>2</sub>, increasing the temperature and

number of wet-dry cycles. For each reaction, the DKP yield was mostly higher than that of gly<sub>2</sub>, for the same reasons previously explained for oxyPAH-polymers. Each experiment was run in triplicate and the data reported are the average results  $\pm$  SD. Figures 18 and 19 show the most representative chromatograms.

**Table 5** | Yields of the products formed by heating glycine.

Experiment	150 °C 14 cycles			90 °C 14 cycles		
	%mol/mol (DKP)	%mol/mol (GLY)	%mol/mol (GLY-GLY)	%mol/mol (DKP)	%mol/mol (GLY)	%mol/mol (GLY-GLY)
<b>Solfatara</b>	2.31 $\pm$ 0.19	-	0.12 $\pm$ 0.04	1.06 $\pm$ 0.12	76 $\pm$ 3	0.05 $\pm$ 0.01
<b>Blank</b>	0.71 $\pm$ 0.07	62.26 $\pm$ 0.30	0.07 $\pm$ 0.03	-	90 $\pm$ 4	-
<b>Solfatara+ mineral</b>	2.40 $\pm$ 0.29	-	0.11 $\pm$ 0.03	0.83 $\pm$ 0.09	87 $\pm$ 2	0.06 $\pm$ 0.01
<b>Blank +mineral</b>	3.33 $\pm$ 0.17	-	0.20 $\pm$ 0.08	-	81 $\pm$ 2	-
	150 °C 7 cycles			90 °C 7 cycles		
<b>Solfatara</b>	3.76 $\pm$ 0.09	4.35 $\pm$ 3.61	0.08 $\pm$ 0.02	0.58 $\pm$ 0.04	86.86 $\pm$ 1.15	0.11 $\pm$ 0.02
<b>Blank</b>	0.24 $\pm$ 0.03	81.47 $\pm$ 1.25	0.03 $\pm$ 0.01	-	93.6 $\pm$ 2.02	-
<b>Solfatara+ mineral</b>	3.84 $\pm$ 0.07	3.70 $\pm$ 2.25	0.18 $\pm$ 0.06	0.45 $\pm$ 0.07	88.44 $\pm$ 0.98	0.19 $\pm$ 0.04
<b>Blank +mineral</b>	2.70 $\pm$ 0.02	51.71 $\pm$ 4.85	0.34 $\pm$ 0.03	0.040 $\pm$ 0.00 3	88.28 $\pm$ 0.05	0.04 $\pm$ 0.01

The reaction yields of these products formed, both in presence of thermal water of Solfatara and of mineral, were higher than those of blank experiments.

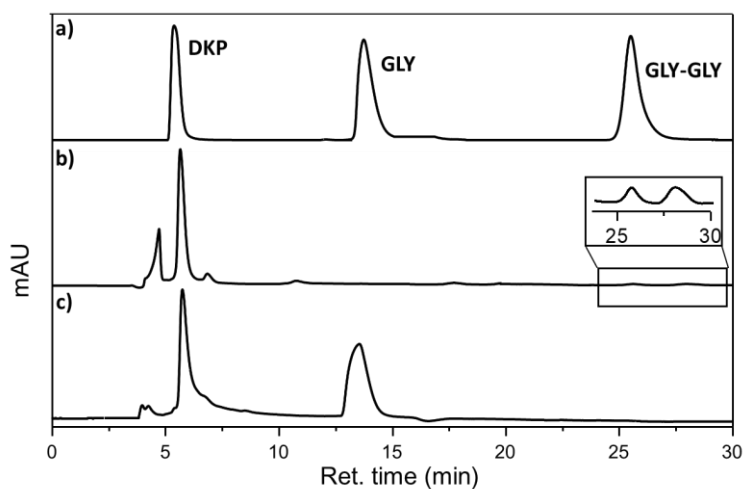
Moreover, the thermal water of Solfatara showed an improved catalytic effect than blank experiments in presence of montmorillonite, except in the case of the reaction carried out at 150°C with 14 cycles, in which DKP and gly<sub>2</sub> yields are slightly higher in presence of mineral.

HPLC data obtained performing the reaction at 150 °C showed that with 7 wet-dry cycles in the blank reaction, a small amount of dimeric products was formed with still 81% of residual glycine, while in the presence of Solfatara thermal water the residual glycine was only 4% and the formation of DKP was higher. Increasing the number of cycles up to 14, the yields of dimeric products generally increased but performing the reaction only with distilled water there was still the presence of 62% residual glycine.

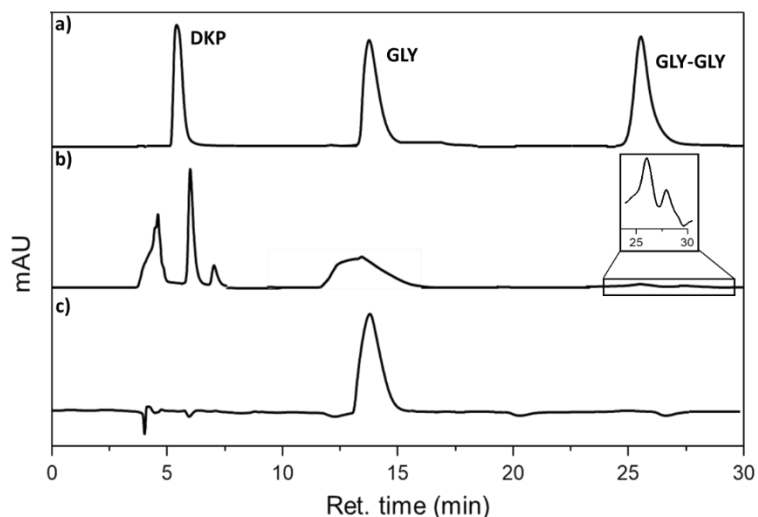
At 90°C, after 7 wet-dry cycles, the HPLC chromatogram of the supernatant of the experiment performed using thermal water of Solfatara, showed that these conditions have already been enough for the formation of both dimer glycine, DKP and gly-gly (Figure 19b). Instead, in the same conditions, the HPLC chromatogram of the blank experiment showed the presence of only glycine (Figure 19c).

Figure 21 displayed the comparison between supernatants obtained conducting the reaction at 90°C with 7 wet and dry cycles and at 150°C with 14 cycles.

Overall, these results showed that the formation of gly<sub>2</sub> and DKP increased with temperature, in accordance with the endothermic nature of the reaction, and as increasing the number of cycles. By adding the mineral to the thermal water of Solfatara didn't strongly affect the yields of dimeric products.



**Figure 18** | Chromatograms of (a) DKP, GLY and GLY-GLY standards, (b) the supernatant of the reaction with Solfatara thermal water after heating at 150 °C with 14 wet-dry cycles, and (c) blank experiment after heating at 150 °C with 14 wet-dry cycles.



**Figure 19** | Chromatograms of (a) DKP, GLY and GLY-GLY standards, (b) the supernatant of the reaction with Solfatara thermal water after heating at 90 °C with 14 wet-dry cycles, and (c) blank experiment after heating at 90 °C with 14 wet-dry cycles.

°C with 7 wet-dry cycles, and (c) blank experiment after heating at 90 °C with 7 wet-dry cycles.

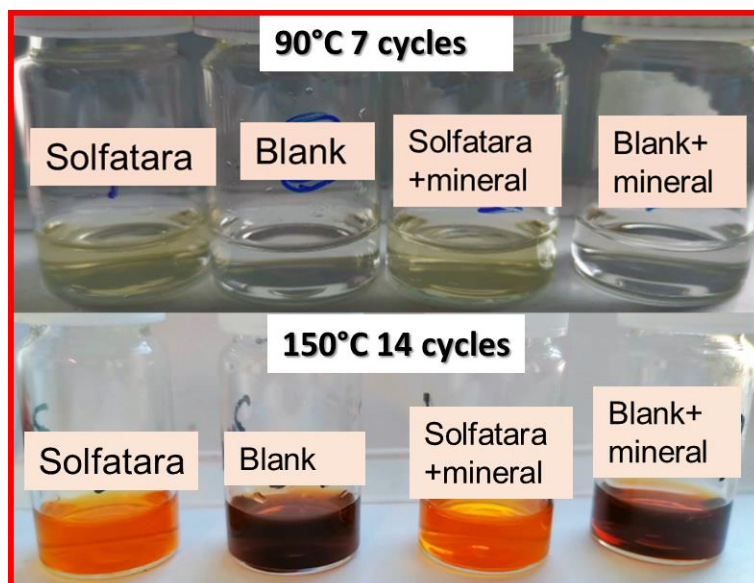


**Figure 20** | Picture of supernatants obtained conducting the reaction at 90°C with 7 wet and dry cycles and at 150°C with 14 cycles.

### 5.2.2.3 Analysis of residue

Performing the wet-dry experiments on glycine using the thermal water of Solfatara as the solvent, the formation of grey residues has been observed. To evaluate the nature of the residue, mass spectrometry (MALDI) and attenuated total reflection (ATR) spectroscopy were performed. For all residues, mass spectrometry (Figures 21-23) revealed the presence of a regular pattern of peaks separated by 57 Da, corresponding to the mass of a glycine unit, suggesting the presence of higher oligomeric products. This is also confirmed by ATR spectra of residues that showed the presence of bands related to the

stretching of C=O and N-H bonds, absent in the glycine monomer spectrum, while visible in the spectrum of gly<sub>2</sub> standard (Figures 24 and 25).

In Table 7, the length of glycine oligomer of residue formed in all the reaction conditions investigated has been reported.

**Table 6** | Length of glycine oligomer of residue formed in all the reaction conditions.

<b>Residue</b>	<b>Length glycine polymer</b>	<b>Residue</b>	<b>Length glycine polymer</b>
<b>150 °C 14 cycles</b>		<b>90 °C 14 cycles</b>	
<b>Solfatara</b>	Gly <sub>22</sub>	<b>Solfatara</b>	Gly <sub>11</sub>
<b>Blank</b>	Gly <sub>7</sub>	<b>Blank</b>	Gly <sub>7</sub>
<b>Solfatara+ mineral</b>	Gly <sub>15</sub>	<b>Solfatara+mineral</b>	Gly <sub>8</sub>
<b>Mineral</b>	Gly <sub>8</sub>	<b>Mineral</b>	Gly <sub>9</sub>
<b>150 °C 7 cycles</b>		<b>90 °C 7 cycles</b>	
<b>Solfatara</b>	Gly <sub>13</sub>	<b>Solfatara</b>	Gly <sub>9</sub>
<b>Blank</b>	Gly <sub>6</sub>	<b>Blank</b>	-
<b>Solfatara+ mineral</b>	Gly <sub>13</sub>	<b>Solfatara+ mineral</b>	Gly <sub>9</sub>
<b>Mineral</b>	Gly <sub>5</sub>	<b>Mineral</b>	-

On raising the reaction temperature from 90 °C to 150 °C, a general increase in the length of glycine oligomers has been observed. Also from these analyses emerged that this effect was more consistent with increasing the temperature than the number of cycles, beyond the reaction conducted in the presence of thermal water of Solfatara, in which a remarkable increase in the length of glycine oligomers was shown at 150 °C from 7 cycles to 14 cycles.

Performing the reaction at 90 °C, the formation of glycine oligomers was shown only in the presence of Solfatara thermal water.

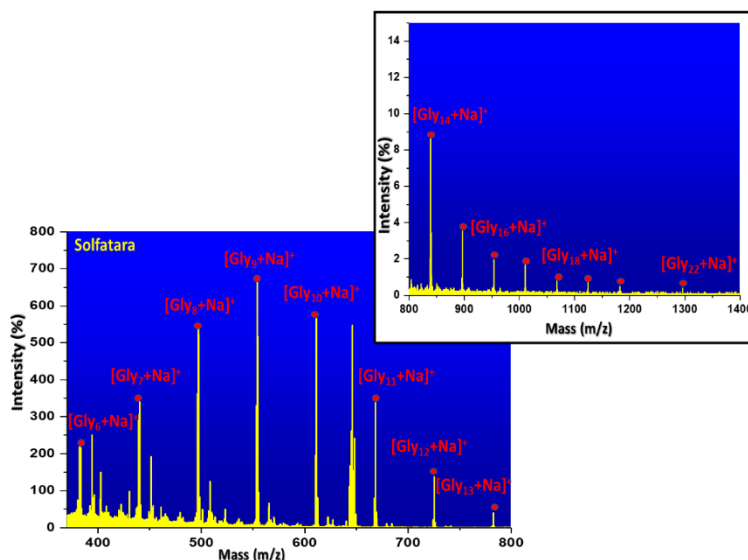


**Figure 21** | MALDI spectrum of the residue obtained after 14 wet-dry cycles at 150°C using thermal water of Solfatara.

In all the conditions investigated (Table 6), the thermal water of Solfatara showed an improved catalytic effect with respect to distilled water, selected as a medium for reference experiments, and to montmorillonite.

The best catalytic effect was obtained from experiments carried out at 150 °C and after 14 cycles, with the formation of oligomers up to the XXIImer (GLY<sub>22</sub>) clearly visible in the MALDI spectrum shown in Figure 20. This result is worth noting if compared with the MALDI spectra registered in the case of the residues obtained from blank experiments and in presence of minerals (Figure 22a, b), showing only low-weight oligomers up to the VIIImer (GLY<sub>8</sub>) and VIImer (GLY<sub>7</sub>), respectively. In this way, it is possible to justify the lower formation yields of DKP and gly<sub>2</sub> when using thermal water compared with that obtained in presence of the mineral (Table 5). Indeed, at 150°C and with 14 wet-dry cycles, the dimeric products are already consumed to form the higher oligomeric product of glycine, when thermal water was used. Thus, in all conditions analysed, by using the thermal water of Solfatara as the solvent of reaction, the formation of oligomers of glycine was always enhanced.

A possible explanation for the catalytic effect of the thermal water of Solfatara relies in the rich pool of metals, metalloids and redox ions that can promote the formation of the peptidic bond through the activation of the carboxyl moiety of glycine.<sup>25</sup>

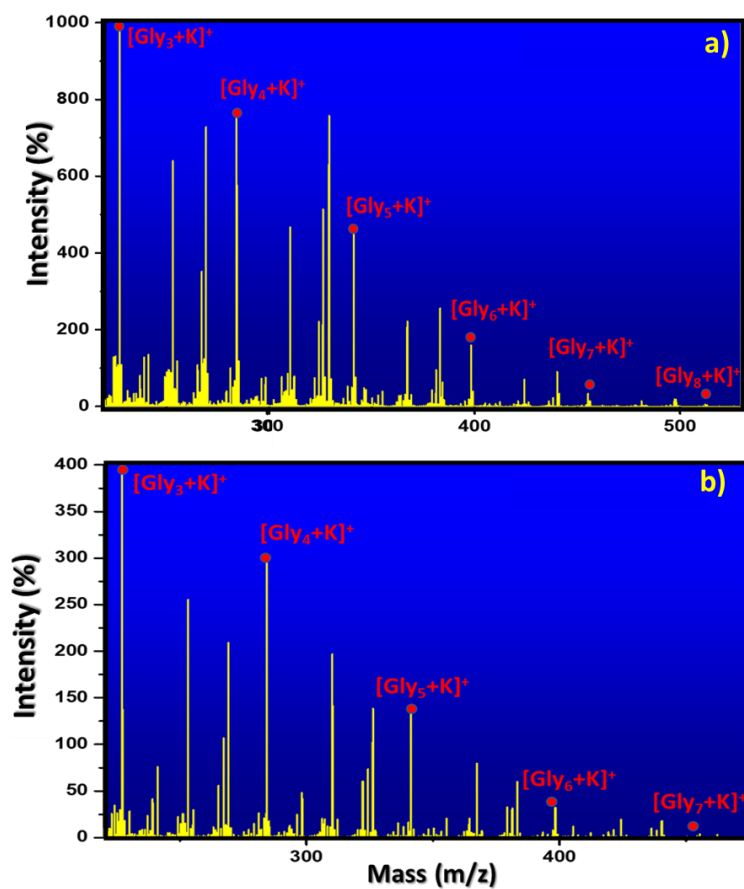


**Figure 22** | MALDI spectrum of the residue obtained after 14 wet-dry cycles at 150°C using distilled water (a) and distilled water in presence of mineral (b).

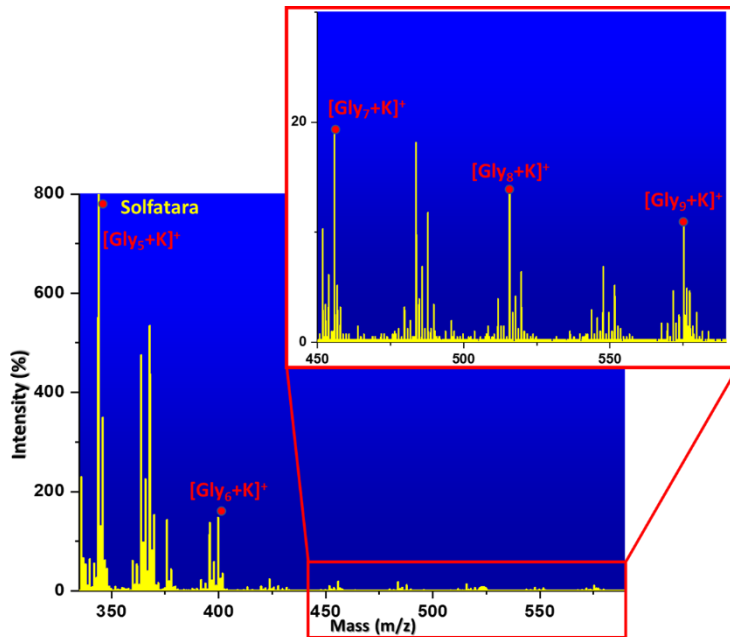


**Figure 23** | MALDI spectrum of the residue obtained after 7 wet-dry cycles at 90°C using thermal water of Solfatara.

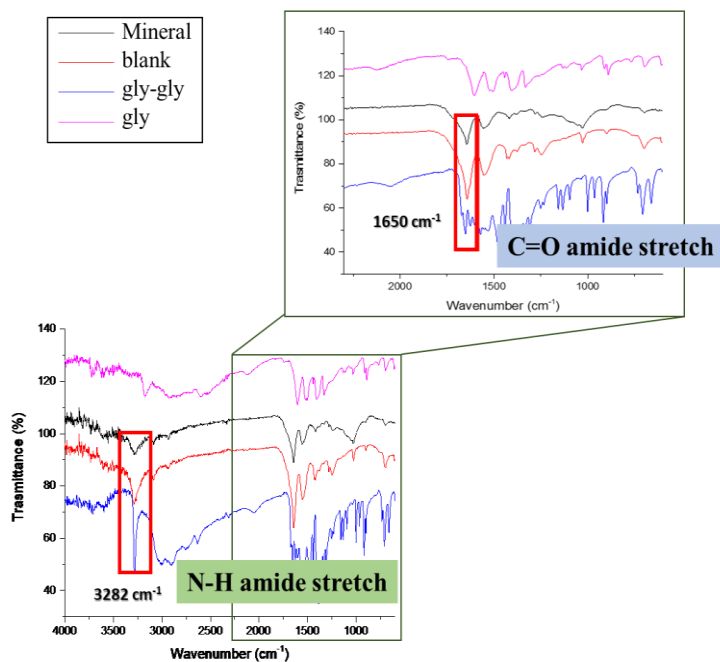


**Figure 24** | ATR spectra in the region 4000–500 cm<sup>-1</sup> showing the N–H amide stretching of residue formed after 14 wet-dry cycles at 150°C for blank reactions and in presence of the mineral. b) Zoom-in of the 2500–500 cm<sup>-1</sup> spectral region of showing the C=O amide stretching.

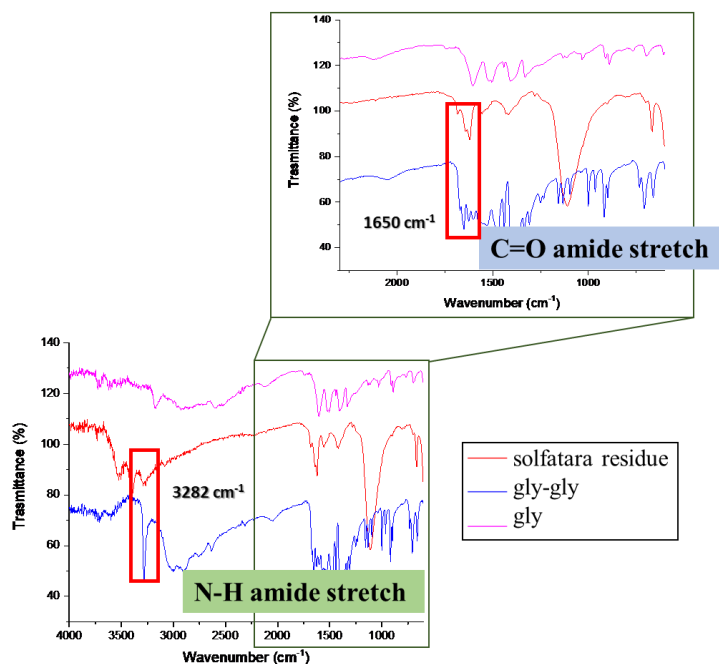


**Figure 25** | a) ATR spectra in the region 4000–500 cm<sup>-1</sup> showing the N–H amide stretching of residue formed after 14 wet-dry cycles at 150°C in presence of thermal water of Solfatara b) Zoom-in of the 2500–500 cm<sup>-1</sup> spectral region of showing the C=O amide stretching.

### 5.3 Conclusions

In this Chapter, the results of the study of the peptide bond formation process starting from the amino acid glycine under wet-dry conditions have been reported. By performing a combined approach based on IP-HPLC-UV, ATR-FTIR and MALDI-MS analyses, the effect of two novel potential catalytic systems on the wet-dry oligomerization process of glycine has been investigated: 1) the polymers obtained from the oxidation of two representative oxy-PAHs, namely 1,8-DHN and 1-HN; 2) the thermal water of the natural geothermal environment of Pisciarelli spring inside Phlegrean Fields.

In an effort to provide more insight into their potentialities as catalysts to facilitate the oligomerization of glycine, wet-dry experiments were carried out using thermal water of Solfatara in comparison with blank experiments conducted using distilled water. In addition, the influence of montmorillonite on peptide formation has been studied.

Combining HPLC and MALDI data with the quantity of residues obtained from each experiment conducted in presence of oxyPAH-polymers, it has emerged that:

- ❖ experiments performed with p-1-HN, p-1,8-DHN and the mineral showed a better catalytic effect in comparison with blank ones. It increases with temperature and cyclic numbers;
- ❖ at 90°C, both with 14 and 7 cycles, p-1,8-DHN appeared better able to promote oligomerization of glycine, compared with p-1-HN and mineral;
- ❖ at 150°C and 14 cycles, catalytic activity of p-1,8-DHN and p-1-HN became comparable. Indeed, MALDI spectra of both showed glycine oligomers up to gly<sub>12</sub>;

- ❖ at 150°C, after only 2 cycles, p-1,8-DHN was already able to enhance the formation of DKP and gly-gly, products that are completely absent in the blank experiment.

The main relevant outcomes obtained by conducting the oligomerization reaction of glycine in the presence of the second catalytic medium, namely the thermal water of Solfatara, are the following:

- the thermal water of Solfatara showed a better catalytic effect than blank experiments (conducted using distilled water) and blank experiments in presence of montmorillonite;
- the best catalytic effect of the thermal water of Solfatara is obtained from experiments conducted at 150°C and after 14 cycles with the formation of higher oligomers up to (gly)<sub>22</sub>. This result is worth nothing if compared with the MALDI spectrum of the residue of the blank experiment, performed in the same conditions, that showed oligomers of glycine up to gly<sub>6</sub>;
- at 90°C, after 7 wet-dry cycles, the HPLC chromatogram of supernatant of the experiment performed using thermal water of Solfatara, showed the presence of DKP, glycine and gly-gly. Glycine oligomers up to gly<sub>9</sub> are revealed by the MALDI spectrum of the residue. Instead, in the same conditions, the HPLC chromatogram of the blank experiment showed the presence of only glycine, and no residue is formed.

Overall, these results highlight the feasibility of the Solfatara environment and the oxyPAH-polymers to catalyze prebiotic peptide formation and their relevance to drive the chemical evolution of life, supporting the hypothesis that life on Earth may have developed in Solfatara-like environments and opening up new avenues towards the exploration of these catalytic media for prebiotic processes.

## 5.4 Experimental section

### 5.4.1 Materials and Methods

Glycine (pure grade: 99.0 %), glycylglycine (Gly<sub>2</sub>, pure grade: 98 %), 2,5-piperazine dione (DKP, pure grade: 99 %) and montmorillonite K-10 were purchased from Sigma and used without further purification.

IP-HPLC analysis was performed with an instrument equipped with a UV-Vis detector (Agilent, G1314A).

UV-Vis spectra were recorded with a Jasco V-560 instrument.

MALDI mass spectra were recorded on a Sciex 4800 MALDI ToF/ToF instrument using 2,5-dihydroxybenzoic acid as the matrix. The laser was operated at 3700 Hz in the positive reflectron mode. The mass spectrometer parameters were set as recommended by the manufacturer and adjusted for optimal acquisition performance. The laser spot size was set at medium focus (B50 mm laser spot diameter). The mass spectra data were acquired over a mass range of  $m/z$  100–4000 Da, and each mass spectrum was collected from the accumulation of 1000 laser shots. Raw data were analyzed using the computer software provided by the manufacturers and reported as monoisotopic masses.

ATR spectra of the powders in transmission mode have been recorded with a Nicolet 5700 spectrometer. The spectra have been scanned on the wave number range of 400-4000  $\text{cm}^{-1}$  with a resolution fixed to 4  $\text{cm}^{-1}$ .

### 5.4.2 wet-dry reaction procedure for oligomerization of glycine

10 mL of 0.1M glycine monomer were mixed with 10 mg oxyPAH-polymers or in an alternative with 10 mL of thermal water of Solfatara in a vial. It was

heated to induce the evaporation of water. Then it was stored at room temperature for 10 minutes. Subsequently, 10 ml of water was used to rinse the residue and the vial was placed again in the oven for another heating cycle. Performing the reaction at 150°C, the heating times per cycle were 8h and 16h, alternatively, at 90 °C the heating time was 24h.

Reactions carried out in absence of the catalysts or in presence of the same amount of montmorillonite instead of the catalysts were performed as references. After the last cycle, 4 ml of CaCl<sub>2</sub> solution 0.1 M was added to the residue to release all formed oligopeptides. The mixture was sonicated and kept under stirring for 4 h. Then, it was subjected to a centrifugation step to afford a supernatant solution, analysed by ion-pairing high-performance liquid chromatography (IP-HPLC), and a solid, analysed by attenuated total reflection (ATR) spectroscopy and mass spectrometry (MALDI).

#### **5.4.4. IP-HPLC analysis of supernatant solutions**

To prepare a solution for analysis, the CaCl<sub>2</sub> solution was filtered with 0.45 µm syringe filters and analysed by ion-pairing high-performance liquid chromatography (IP-HPLC). Residual glycine, DKP and gly<sub>2</sub> were identified by co-injection with standards. The reaction yields were determined as the percentage of the reactant converted into the reaction product. Additionally, the concentrations of glycine, DKP, diglycine were determined by using the calibration curves. For calibration, a series of standard solutions with known concentrations were prepared. IP-HPLC analysis was performed with an instrument equipped with a UV-Vis detector (Agilent, G1314A). A Phenomenex Spherclone ODS column (250 × 4.60 mm, 5 µm) was used, at a flow rate of 0.5 mL/min. The eluent was a 90% solution of sodium

octanesulfonate (10mM) adjusted to pH 2.5 by H<sub>3</sub>PO<sub>4</sub> and 10% methanol. The detection wavelength was 210 nm.

#### 5.4.5 Analysis of thermal water

Parameters such as pH, and electrical conductivity (E.C.,  $\mu\text{S cm}^{-1}$ ) were determined by a multiparametric probe (multimeter 3420, TetraCon 325, SenTix pH electrodes, WTW).

Major ions such as NO<sub>3</sub><sup>-</sup>, SO<sub>4</sub><sup>2-</sup>, Cl<sup>-</sup>, F<sup>-</sup>, Ca<sup>2+</sup>, Mg<sup>2+</sup>, Na<sup>+</sup>, and K<sup>+</sup> were determined by ion chromatography, IC Metrohm 850 Professional. Cations were separated by a Metrosep C4 250/4.0 column using 3.0 mM HNO<sub>3</sub> as eluent and a flow rate of 0.9 mL/min, whereas anions by a Metrosep A supp7 250/40 column using 3.6 mM Na<sub>2</sub>CO<sub>3</sub> as eluent at a flow rate of 0.7 mL/min, and was used as a conductivity detector for qualitative and quantitative analysis.<sup>26</sup>

Determination of metals and metalloids as Al, Sb, As, Ba, Be, B, Cd, Co, Cr, Fe, Mn, Hg, Mo, Ni, Pb, Cu, Se, V, and Zn, the sample was filtered using 0.45  $\mu\text{m}$  regenerated cellulose membrane filter and acidified with a 3% v/v HNO<sub>3</sub> solution. The samples were analyzed with inductively coupled plasma with mass spectrometry (ICP-MS, Aurora M90, Bruker, USA)

## References

1. S.L. Miller, H.C. Urey. Organic Compound Synthesis on the Primitive Earth. *Science (1979)* **1959**, 130 (3370), 245–251.
2. W.L. Marshall. Hydrothermal synthesis of amino acids. *Geochim Cosmochim Acta* **1994**, 58 (9), 2099–2106.
3. K.H. Lemke, R.J. Rosenbauer, D.K. Bird. Peptide Synthesis in Early Earth Hydrothermal Systems. *Astrobiology* **2009**, 9 (2), 141–146.
4. L. Jiang, P. Dziejczak, Z. Spacil, et al. Abiotic synthesis of amino acids and self-crystallization under prebiotic conditions. *Sci Rep* **2014**, 4 (1), 6769.
5. M.H. Engel, S.A. Macko. Isotopic evidence for extraterrestrial non-racemic amino acids in the Murchison meteorite. *Nature* **1997**, 389 (6648), 265–268.
6. S.A. Benner, H.-J. Kim, M.A. Carrigan. Asphalt, Water, and the Prebiotic Synthesis of Ribose, Ribonucleosides, and RNA. *Acc Chem Res* **2012**, 45 (12), 2025–2034.
7. D. Deamer. *First Life: Discovering the Connections between Stars, Cells, and How Life Began*; **2011**.
8. B. Damer, D. Deamer. The Hot Spring Hypothesis for an Origin of Life. *Astrobiology* **2020**, 20 (4), 429–452.
9. A. Fedele, M. Pedone, R. Moretti, et al. Real-time quadrupole mass spectrometry of hydrothermal gases from the unstable Pisciarelli fumaroles (Campi Flegrei): Trends, challenges and processes. *Int J Mass Spectrom* **2017**, 415, 44–54.
10. H. Le Son, Y. Suwannachot, J. Bujdak, B.M. Rode. Salt-induced peptide formation from amino acids in the presence of clays and related catalysts. *Inorganica Chim Acta* **1998**, 272 (1–2), 89–94.
11. T.D. Campbell, R. Febrian, J.T. McCarthy, et al. Prebiotic condensation through wet–dry cycling regulated by deliquescence. *Nat Commun* **2019**, 10 (1), 4508.

12. V. Erastova, M.T. Degiacomi, D. G. Fraser, H.C. Greenwell. Mineral surface chemistry control for origin of prebiotic peptides. *Nat Commun* **2017**, 8 (1), 2033.
13. M. Sato. Preparation of Kaolinite-Amino Acid Intercalates Derived from Hydrated Kaolinite. *Clays Clay Miner* **1999**, 47 (6), 793–802.
14. S. Fuchida, H. Masuda, K. Shinoda. Peptide Formation Mechanism on Montmorillonite Under Thermal Conditions. *Origins of Life and Evolution of Biospheres* **2014**, 44 (1), 13–28.
15. B.M. Rode. Peptides and the origin of life1. *Peptides (N.Y.)* **1999**, 20 (6), 773–786.
16. B.M. Rode, H.L. Son, Y. Suwannachot, J. Bujdak. The Combination of Salt Induced Peptide Formation Reaction and Clay Catalysis: A Way to Higher Peptides under Primitive Earth Conditions. *Origins of Life and Evolution of the Biosphere* **1999**, 29 (3), 273–286.
17. J. Bujdák, B.M. Rode. Silica, alumina and clay catalyzed peptide bond formation: enhanced efficiency of alumina catalyst. *Origins of Life and Evolution of the Biosphere* **1999**, 29 (5), 451–461.
18. S. Steinberg, J.L. Bada. Diketopiperazine Formation During Investigations of Amino Acid Racemization in Dipeptides. *Science (1979)* **1981**, 213 (4507), 544–545.
19. V.A. Basiuk, T.Yu. Gromovoy, V.G. Golovaty, A.M. Glukhoy. Mechanisms of amino acid polycondensation on silica and alumina surfaces. *Origins of Life and Evolution of the Biosphere* **1990**, 20 (6), 483–498.
20. V. Lino, R. Castaldo, G. Gentile, P. Manini. Reusable melanin-based biosorbents for efficient methylene blue removal: the new frontier of fungi-inspired allomelanin coatings for sustainable water remediation processes. *Materials Today Sustainability* **2023**, 21, 100283.
21. A. Aiuppa, W. D’Alessandro, C. Federico, B. Palumbo, M. Valenza. The aquatic geochemistry of arsenic in volcanic groundwaters from southern Italy. *Applied Geochemistry* **2003**, 18 (9), 1283–1296.
22. J.A. Coderre, S. Steinthórsson. Natural concentrations of mercury in Iceland. *Geochim Cosmochim Acta* **1977**, 41 (3), 419–424.

23. P.C. Legittimo, G. Piccardi, M. Martini. Mercury Pollution in the Surface Environment of a Volcanic Area. *Chemistry and Ecology* **1986**, 2 (3), 219–231.
24. G.M. Valentino, G. Cortecchi, E. Franco, D. Stanzione. Chemical and isotopic compositions of minerals and waters from the Campi Flegrei volcanic system, Naples, Italy. *Journal of Volcanology and Geothermal Research* **1999**, 91 (2–4), 329–344.
25. J.P. Collman, Eiichi. Kimura. Formation of peptide bonds in the coordination sphere of cobalt(III). *J Am Chem Soc* **1967**, 89 (24), 6096–6103.
26. V. Allocca, S. Coda, P. De Vita, et al. Hydrogeological and hydrogeochemical study of a volcanic-sedimentary coastal aquifer in the archaeological site of Cumae (Phlegraean Fields, southern Italy). *J Geochem Explor* **2018**, 185, 105–115.

# CHAPTER 6

## CHEMICAL TRANSFORMATIONS OF PAHs AND OXYPAHs IN THE THERMAL WATER OF SOLFATARA

*“There is grandeur in this view of life, with its several powers, having been originally breathed into a few forms or into one; and that, whilst this planet has gone cycling on according to the fixed law of gravity, from so simple a beginning endless forms most beautiful and wonderful have been, and are being, evolved.”*

— Charles Darwin, *On the Origin of Species*, 1859

### 6.1 Introduction

Geothermal fields and geothermal water catalysis have gained increasing relevance in current theories (like the hot spring hypothesis) on the origin of life in the early Earth and are commonly invoked as the most suitable candidate environments to provide the proper supply of thermal energy, catalysts and reaction media for a broad diversity of abiogenic processes.<sup>1,2</sup> Following the delivery of a substantial mass of organic compounds via meteoritic infall some

4 billion years ago,<sup>3</sup> conditions were created for a rich prebiotic chemistry driven by the lack of oxygen through more persisting channels and promoted at volcanic land masses exposed to the atmosphere. At these sites a marked increase in concentration on mineral surfaces would be accompanied by flushing into pools connected to hydrothermal systems, enabling participation in a complex interplay of prebiotic transformations.

The growth of extremophilic microorganisms<sup>4</sup> in sulfurous cauldrons near hydrothermal vents is evidence of the operation of ideal conditions to allow for the emergence of life on early Earth. A rich literature documents the benefits of this environment for the formation of a range of biomolecules as the key requisite for the development of primitive forms of life. Noticeable examples include the advantageous synthesis of amino acids and carbohydrates, by means of Strecker-type and formose reactions, under hydrothermal conditions.<sup>5-7</sup>

A viable approach to overcome the limitations inherent to the laboratory reconstructions of prebiotic scenarios would involve on one side the use of natural environmental models that comply with most of the requisites imposed by abiogenic processes and, on the other side, the selection of suitable sets of molecules with solid record of astrochemical detections and reasonable entry routes to prebiotic scenarios.

Of considerable interest in this regard is the well-characterized geothermal system of the caldera of the Phlegrean Fields (Figure 1). This site, situated to the west of Naples, (Figure 1) is a large volcanic area of about 12 km in diameter that comprises 24 craters and volcanic features, including the Solfatara volcano with large and spectacular fumarole vents. The area exhibits a continuous rising of hydrothermal fluids generated by diffuse bubbling, with

impressive degassing manifestations and intense fumarolic activity<sup>8</sup> in the Pisciarelli area located a few hundred meters east of the Solfatara crater. Fumaroles eject mainly H<sub>2</sub>O and to a lesser extent CO<sub>2</sub> and H<sub>2</sub>S and have surface temperatures up to 165 °C (up to ~ 115 °C for Pisciarelli).<sup>9</sup> The soil of solfataric fields is characterized by an upper oxidized zone often rich in ferric iron and an underlying layer as a black-colored zone rich in ferrous sulfide. Elemental sulfur is produced by chemical oxidation of the H<sub>2</sub>S coming from below by molecular oxygen penetrating from the surface into the soil.<sup>10</sup>



**Figure 1** | Localization map of Phlegrean fields area. Zoom on the map of Solfatara crater and Pisciarelli springs.

In view of these and other characteristics that make this caldera a suitable environment for extremophilic microorganisms, the Solfatara and Pisciarelli area could provide an ideal setting for the emergence of life on Earth. It may provide a natural prebiotic laboratory offering a broad range of opportunities for rich and diversity-oriented chemistry. In support of this view, a recent paper demonstrated the generation of numerous organic biological compounds including carboxylic acids, nucleobases, amino acids, and sugars by exposure of the prebiotic building block formamide (NH<sub>2</sub>CHO) to thermal water (358

K) in the presence of meteorites in the hydrothermal physical-chemical environment of the Phlegrean Fields.<sup>11</sup>

A most relevant class of compounds that has been implicated in different astrochemical contexts but that has never been given due consideration in prebiotic scenarios includes PAHs.

In this Chapter, taking the natural geothermal environment of Solfatara as a realistic model for the hydrothermal fields on the early Earth, we report the chemical transformations suffered by NAPH, 1-HN and 1,8-DHN (Figure 2) when immersed in thermal water and mud samples from Pisciarelli spring. The aim of the study was to assess whether, under high-temperature conditions mimicking plausible prebiotic environments, simple PAH derivatives that could have been delivered to the early Earth from meteorites or that could have been generated via mineral-catalyzed polymerization of small hydrocarbons, display a reactivity compatible with the generation of life molecule precursors and building blocks.

This work has been performed in collaboration with Prof. Marco Trifuoggi and Prof. Marco Moracci from the University of Naples Federico II, Naples (Italy).

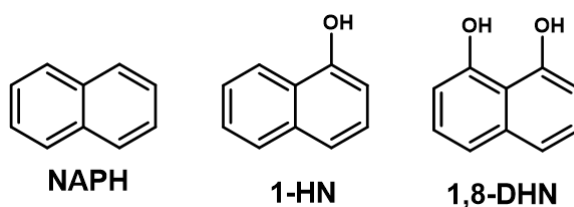


**Figure 2** | Structures of investigated substrates.

## 6.2 Results and discussion

This section will be reported the results deriving from the exposure of naphthalene (NAPH), the smallest member of PAHs, as well as 1-HN and 1,8-DHN to thermal water collected at the Pisciarelli spring inside Phlegrean Fields. The chemical and physical characteristics of the thermal water of the two pools located in Pisciarelli spring are already reported in Chapter 5.

### 6.2.1 Incubation of PAHs in thermal water samples

Proper amounts of the probe molecules, NAPH, 1-HN and 1,8-DHN, were suspended in thermal water samples freshly collected from Pisciarelli spring and the mixture was kept under stirring in a sealed vial at 95 °C for 48h.

To assess the role of oxygen in the formation of the reaction products, PAHs were heated in thermal water under an argon atmosphere, whereas incubation reactions carried out by using distilled water as the medium were taken as reference. Blank reactions carried out by heating thermal water samples without adding PAHs revealed the formation of no relevant product.

After 48 h, each incubation mixture was subjected to centrifugation: this step allowed the separation of a solid fraction from a supernatant fraction. The first one was subjected to structural characterization by UV-vis, ATR and by MALDI mass spectrometry, whereas the supernatant fraction was subjected to gas chromatography coupled with mass spectrometry (GC-MS) analysis.

#### 6.2.1.1 Analysis of the solid component

The formation of a solid precipitate was observed only in the incubation mixtures of 1-HN and 1,8-DHN, whereas the incubation mixture from NAPH remained clear throughout the reaction time (Figure 3). About half of the solid

was isolated from 1-HN and 1,8-DHN when incubating in distilled water, suggesting a catalytic effect of thermal water (Table 1). It can be noted that in the case of 1,8-DHN much more precipitated than the 1-HN was formed since the formation of the naphthoxyl radical is strongly favoured by the peculiar peri asset of the hydroxyl groups on the naphthalene ring stabilizing the radical via intramolecular H bonding.

Noteworthy is the occurrence of the solid precipitate from the reactions of 1-HN and 1,8-DHN in thermal water under an oxygen-purged atmosphere, as it is believed to be the atmosphere of early Earth. Probably oxidant agents available in the thermal water of Pisciarelli spring, such as nitrate, chloride and iron ions, were able to catalyze the oxidative polymerization of the oxy-PAH.

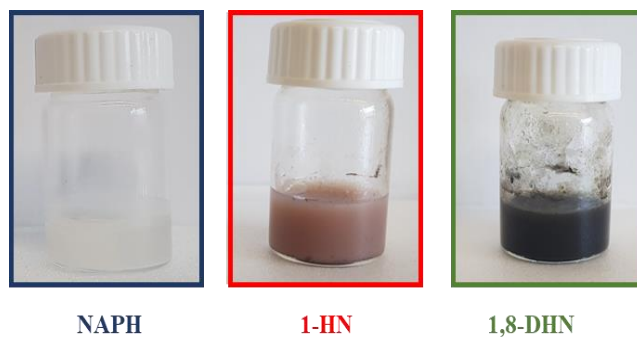


**Figure 3** | Reaction mixtures of NAPH, 1-HN and 1,8-DHN in thermal water after the heating at 95 °C for 48h.

**Table 1** | Weights of precipitates obtained in the reaction conditions investigated.

Reaction mixtures	Weight (mg)
1,8-DHN in thermal water	18
1,8-DHN in distilled water	9
1-HN in thermal water	1
1-HN in distilled water	0.5

The structural characterization of the solids revealed many similarities with the polymers obtained by the enzyme-mediated oxidation of 1-HN and 1,8-DHN in the aqueous phosphate buffer at pH 7, shown in Chapter 4. In particular, the MALDI mass spectra supported the polymeric nature of the solids (Figure 4 showed the MALDI spectrum of 1-HN precipitate). Regular clusters of peaks separated by 158 Da, in the case of 1,8-DHN, and 142 Da, in the case of 1-HN, were clearly visible and ascribable to the  $[M+Na]^+$  pseudomolecular ion peaks of oligomeric species.

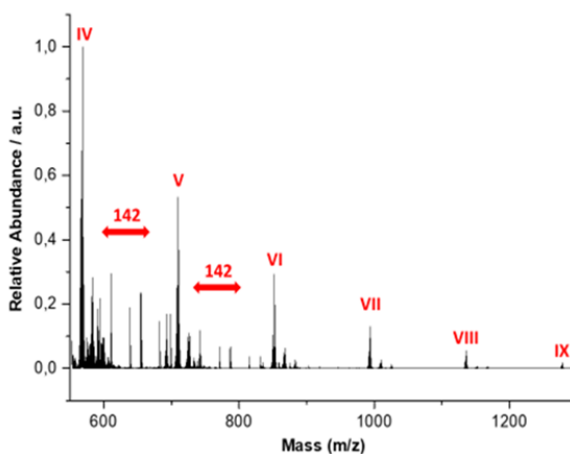


**Figure 4** | MALDI mass spectrum of 1-HN precipitate obtained in the thermal water of Solfatara.

The UV-visible spectrum of the DMSO suspension of 1,8-DHN dark precipitate showed broadband absorption covering the entire spectrum, with more intense absorption around 400 nm and a shoulder at 600 nm (Figure 5), whereas in the case of the MeOH solution of soluble 1-HN precipitate a very labile absorption maximum was visible at around 500 nm, with the most relevant absorption set in the UV region of the spectrum (Figure 6).

Similar features are also identified in the UV-vis spectra of 1-HN and 1,8-DHN precipitates formed by blank reactions (Figure 7).

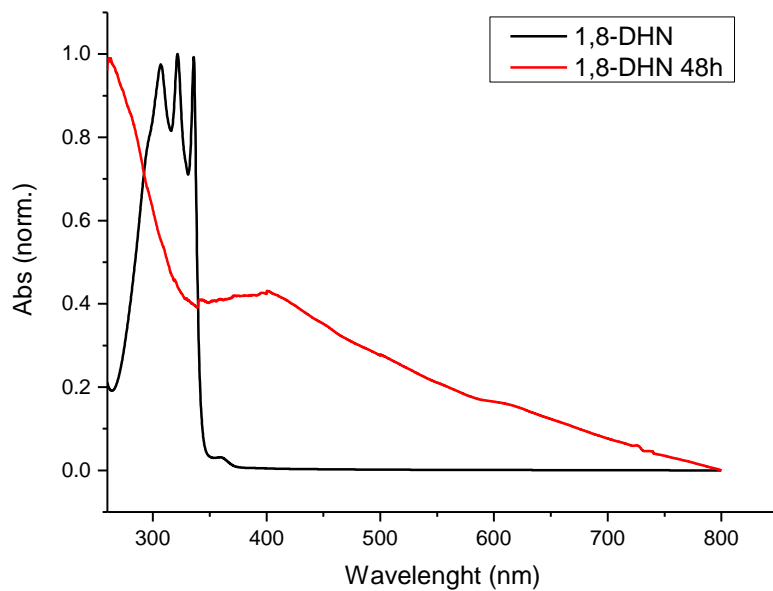


**Figure 5** | UV-Vis absorption spectra of 1,8-DHN and 1,8-DHN precipitate, as suspension in DMSO.

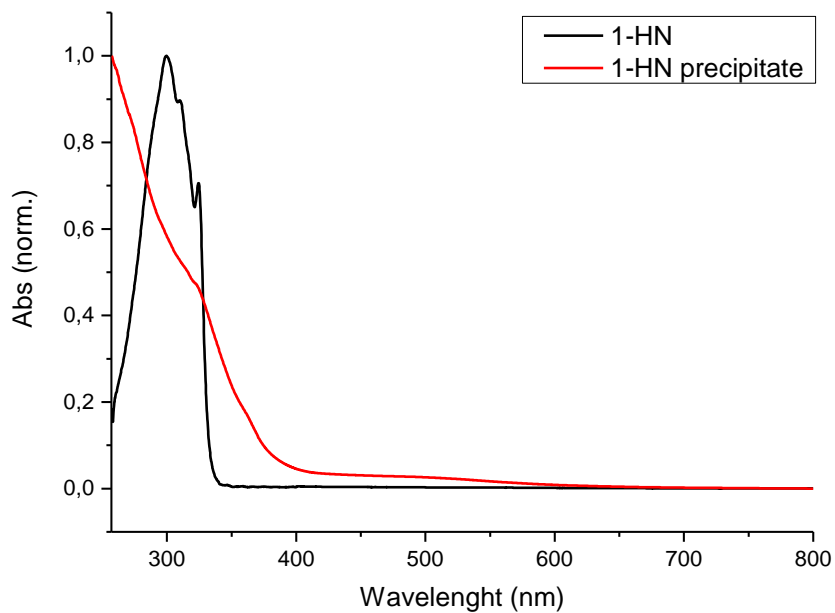


**Figure 6** | UV-Vis absorption spectra of 1-HN and 1-HN precipitate in MeOH.

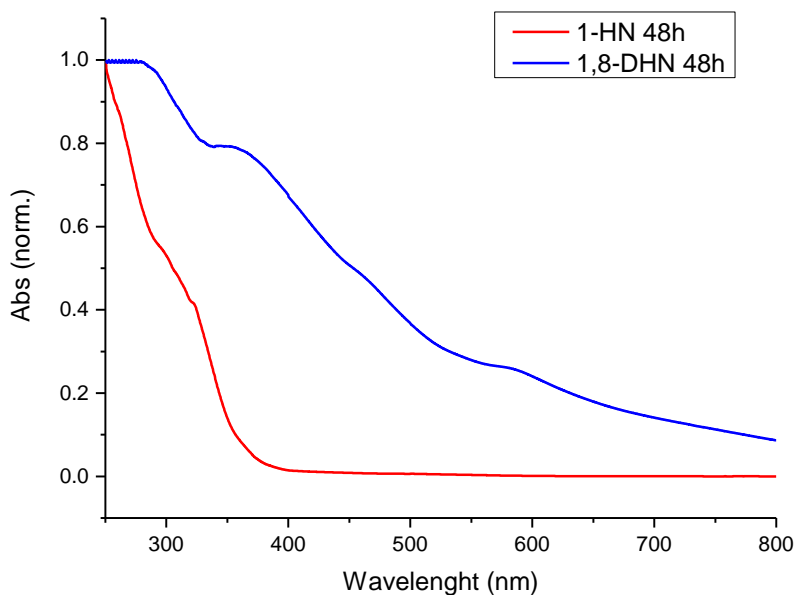


**Figure 7** | UV-Vis absorption spectra of 1,8-DHN and 1-HN precipitates formed by blank reactions in DMSO and MeOH, respectively.

Noteworthy is the formation of a precipitate (1-2 mg) from 1,8-DHN and 1-HN under an atmosphere with less or no oxygen (Figure 8 and 9). As displayed in the UV-vis spectra (Figure 8 and 9), under the argon atmosphere the polymerization reaction is slower than in presence of oxygen since the typical featureless profile covering the entire UV-vis spectrum is absent.

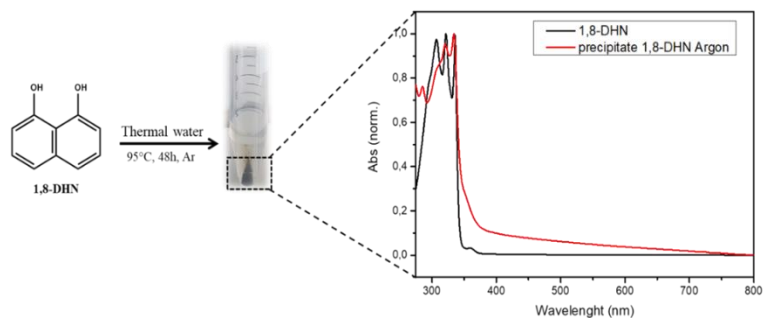


**Figure 8** | Reaction conditions of 1,8-DHN in thermal water taken at Pisciarelli spring, under an argon atmosphere and UV-vis spectra of 1,8-DHN and 1,8-DHN precipitate.

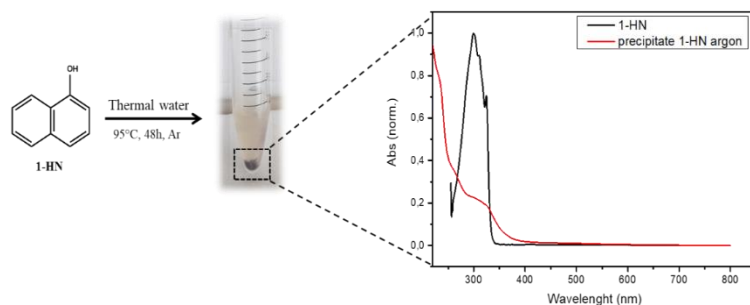


**Figure 9** | Reaction conditions of 1-HN in thermal water taken at Pisciarelli spring, under an argon atmosphere and UV-vis spectra of 1-HN and 1-HN precipitate.

The polymerization was further confirmed by ATR-FTIR spectroscopy revealing for the solids from 1-HN and 1,8-DHN similar resonances detected for the corresponding monomer, with broader features, in accordance with what was previously reported in Chapter 4 for oxidative polymers from 1,8-DHN and 1-HN (Figure 10). Moreover, in Figures 11 and 12 the ATR spectra

of precipitates formed from blank reactions and under the argon atmosphere are also shown.

Spectra of 1-HN and 1,8-DHN precipitates formed from blank reactions are slightly different as compared to precipitates formed in thermal water, suggesting an involvement of this environment in the reaction products.

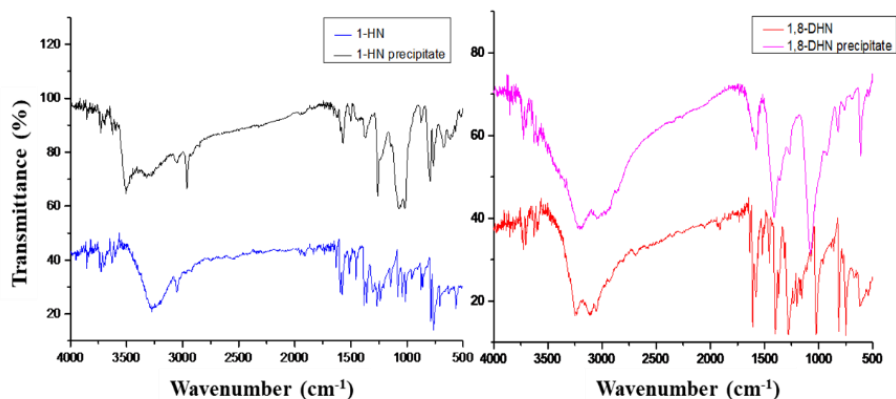


**Figure 10** | ATR spectra of 1-HN and 1-HN precipitate on the right and of 1,8-DHN and 1,8-DHN precipitate.

These results unambiguously show that under the chemical-physical conditions of Pisciarelli fumaroles hydroxylated naphthalenes can undergo polymerization.

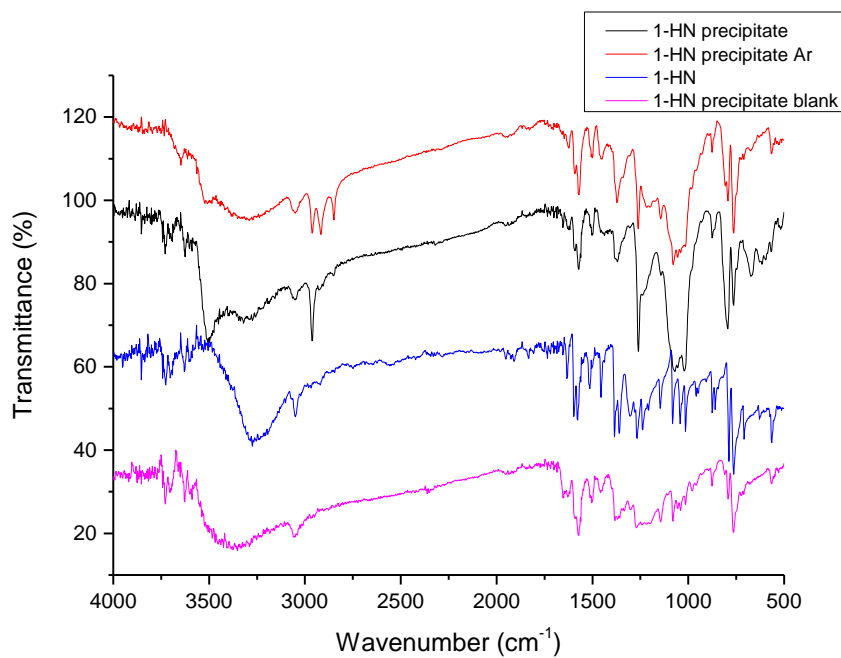


**Figure 11** | ATR spectra of 1-HN, 1-HN precipitate, 1-HN precipitate produced from reactions occurring under an argon atmosphere and 1-HN precipitate formed from blank reactions.

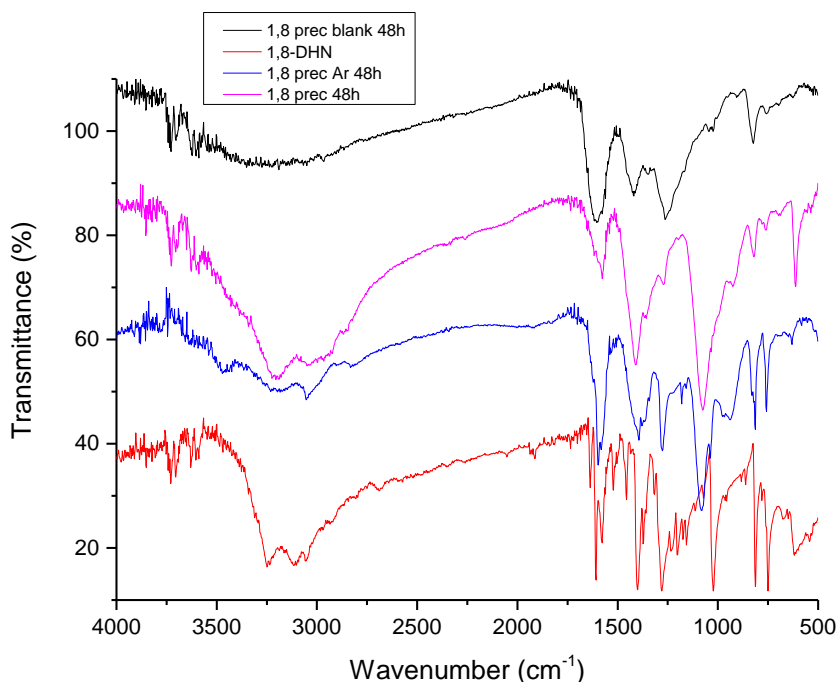


**Figure 12** | ATR spectra of 1,8-DHN, 1,8-DHN precipitate, 1,8-DHN precipitate produced from reactions occurring under an argon atmosphere and 1,8-DHN precipitate formed from blank reactions.

### 6.2.1.2 Analysis of the supernatant fraction

The supernatant fractions collected from each of the incubation mixtures were subjected to GC-MS analysis. Two different protocols were used for the detection of semivolatile and volatile organic compounds. For the analysis of the semivolatile organic compounds (SVOCs), the mixtures were subjected to a derivatization step with 2,2,2-trifluoro-*N*-methyl-*N*-(trimethylsilyl)acetamide (MSTFA) before injection into the gas chromatograph; for the

determination of the volatile organic compounds (VOCs), a purge and trap extraction was performed before the GC-MS analysis. The same analyses were performed also on thermal water without the PAHs molecules before and after the heating at 95°C, to ensure that the products detected by the GC-MS analysis are not derived from pre-existing molecules in the thermal water.

In Table 2 and in Figure 13, the main products identified in the incubation mixtures of NAPH, 1-HN and 1,8-DHN are reported. The identification was derived by the comparison with NIST mass spectral library. Salient data can be summarized as follows:

1. Virtually all compounds suffered extensive degradation of the naphthalene ring leading to the formation of small fragments featuring the isopropyl moiety. Evidence of oxidative breakdown came also from the identification of partially branched phenolic/benzenic derivatives.
2. 1-HN led to the formation of 1,4-naphthoquinone via an oxidation/hydroxylation pathway, whereas 1,8-DHN led to the formation of 1-HN via a reductive step.
3. Both the oxy-PAHs led to the formation of a set of regioisomeric diisopropyl naphthalenes, denoting also in this case that a reductive loss of the phenolic -OH groups has occurred.
4. Figures 14-16 show the representative chromatograms obtained from analyzing the supernatant solutions of NAPH, 1,8-DHN and 1-HN heated in thermal water, in distilled water and under an argon atmosphere. In Table 3, the retention times for each compound are listed.

**Table 2** | Reaction products obtained by heating NAPH, 1,8-DHN and 1-HN in thermal water taken at Pisciarelli spring.

Molecules	Reaction conditions		
	Geothermal water/O <sub>2</sub>	Geothermal water/Ar	Water/O <sub>2</sub>
Naphthalene (NAPH)	1,2-Benzenedicarboxylic acid, bis(2-methylpropyl) ester (1) Methacrylic acid (2)	-	Naphthalene (10)
1-Naphthol (1-HN)	1,4-Naphthalenedione (3) Di-iso-propylnaphthalenes (4) p-Trimethylsilyloxyphenyl-bis(trimethylsilyloxy)ethane (5)* 3-Penten-2-one, 4-methyl (6)* 2-Pentanone, 4-hydroxy-4-methyl (7)*	1-Naphthol (8)	1-Naphthol (8)  Silane, trimethyl(1-naphthyloxy)-(12)

1,8-Dihydroxynaphthalene (1,8-DHN)	Di-iso-propylnaphthalene (4) 1-Naphthol (8) 3-Hydroxymandelic acid, ethyl ester (9)* 3-Penten-2-one, 4-methyl (6) 2-Pentanone,4-hydroxy-4-methyl (7)	1,4-Naphthalenedione, 5-hydroxy (14) 1,8-dihydroxynaphthalene (11) Di-iso-propylnaphthalene (4)	Dimethyl-1,8-naphthalenedioxysilane (13) 1,8-dihydroxynaphthalene (11)
---------------------------------------	---	---	---

\*Products deriving from Purge and Trap technique

**Table 3** | List of main products 1-14 formed by heating NAPH, 1,8-DHN and 1-HN and their retention times.

Molecules	Retention Time (min)	Molecules	Retention Time (min)
(1)	11.16	(8)	8.8
(2)	8.7	(9)	6.4
(3)	7.9	(10)	6.43
(4)	9.26-9.62	(11)	10.19
(5)	6.9	(12)	8.5
(6)	7.6	(13)	9.6
(7)	16.1	(14)	8.7

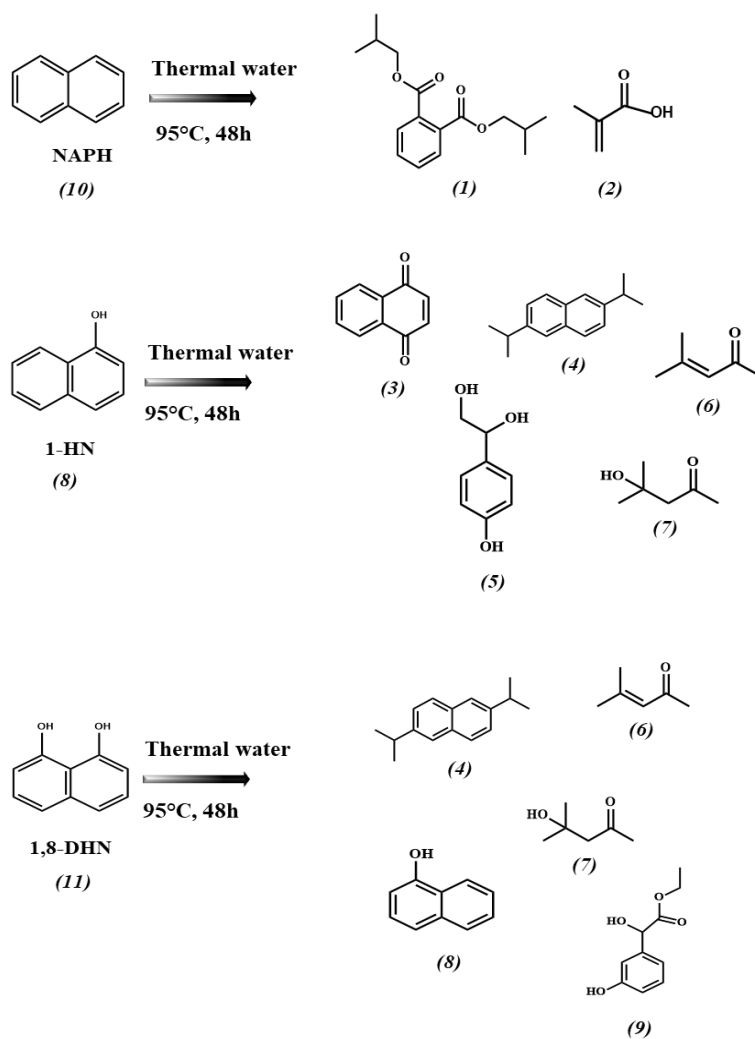


**Figure 13** | Chemical structures of the products 1-9 obtained by heating NAPH, 1,8-DHN and 1-HN in thermal water taken at Pisciarelli spring.

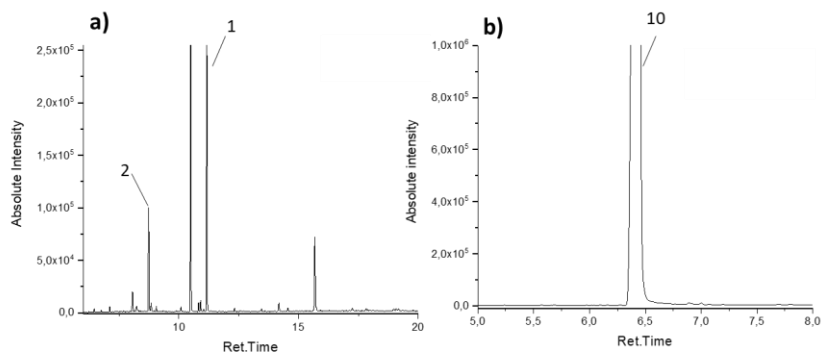


**Figure 14** | Chromatograms obtained by heating NAPH in (a) thermal water and (b) in distilled water.

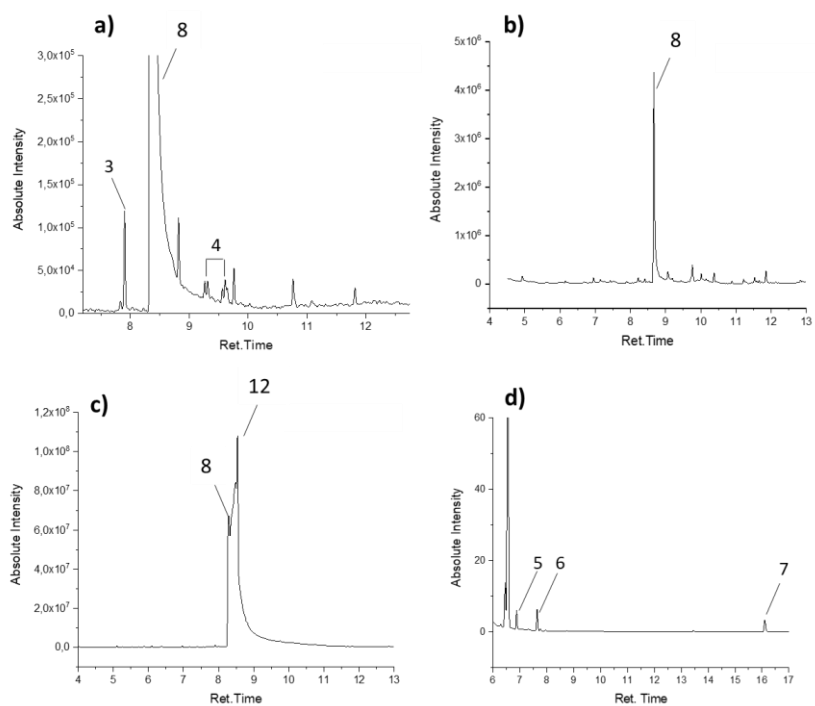


**Figure 15** | Chromatograms obtained by heating 1-HN (a) in thermal water (SVOCs), (b) under an argon atmosphere, (c) in distilled water and (d) in thermal water (VOCs).

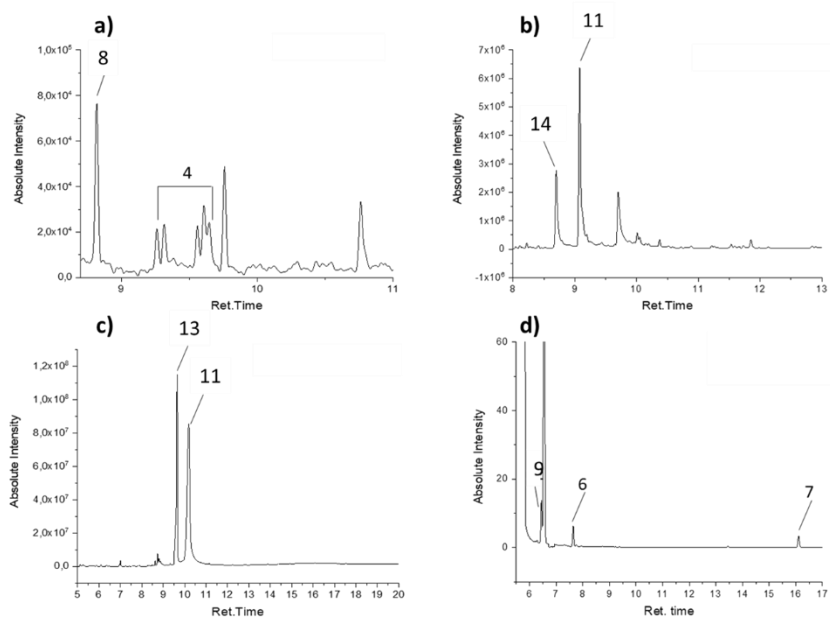


**Figure 16** | Chromatograms obtained by heating 1,8-DHN (a) in thermal water (SVOCs), (b) under an argon atmosphere, (c) in distilled water and (d) in thermal water (VOCs).

Worthy of note is the formation of 1,4-Naphthalenedione, 5-hydroxy (**14**), a precursor of oligomeric or polymeric structures, from the reaction mixture of 1,8-DHN and thermal water conducted under an argon atmosphere (Figures 16b and 17). The presence of an oxidation product in absence of oxygen suggests the possible availability of oxidant agents in the thermal water of Pisciarelli spring, such as nitrate, chloride and iron ions, able to catalyze oxidative polymerization. Quinones are of particular interest from the prebiotic chemistry perspective because closely related compounds are widely used in current living systems for electron transport across cell membranes. Moreover,

1,4-naphthoquinone derivatives have been detected also in meteorites,<sup>21,22</sup> including ALH 85013 and Murchison meteorites.

It is possible that the easy formation of 1,4-Naphthalenedione, 5-hydroxy in prebiotic geothermal environments like Solfatara, even in absence of oxygen, is somewhat related to the selection of this class of coenzymes during the origin of life and/or its early evolution.

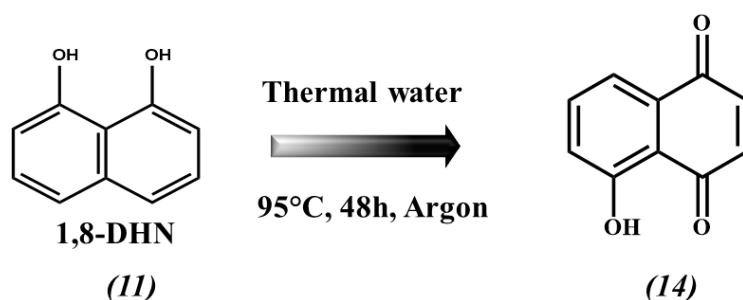


**Figure 17** | Reaction scheme for the formation of 1,4-Naphthalenedione, 5-hydroxy (14).

### 6.2.1.3 Main outcomes

Exploiting the opportunity offered by the geothermal waters collected from the Pisciarelli spings as a unique chemical-physical environment mimicking the prebiotic scenario, it has been possible to delineate three possible chemical pathways accounting for the overall transformation of PAHs: 1) a polymerization route, 2) a functionalization route and 3) an erosion route (Figure 18). All these processes account for the formation of a plethora of compounds related to PAHs exhibiting different characteristics and properties such as molecular mass, volatility and solubility.

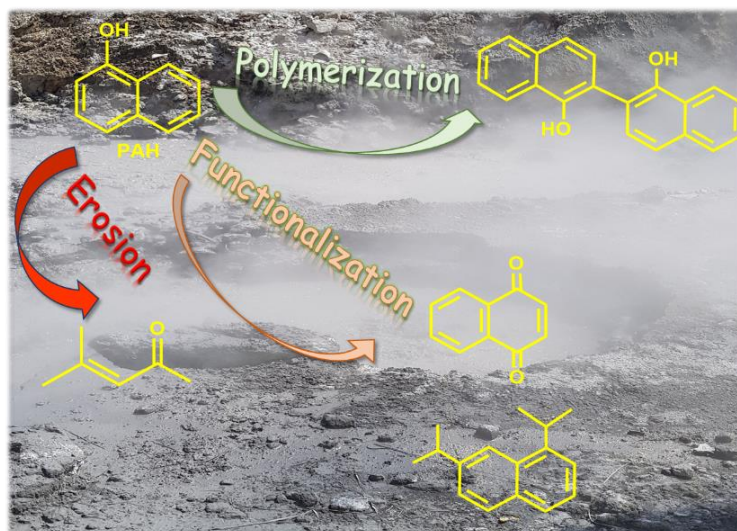


**Figure 18** | Chemical mechanisms of PAH transformation into water samples of Pisciarelli spring.

Functionalization of the PAH scaffold via addition, removal or modification of functional groups, may generate a range of catalytic and templating sites that can direct self-assembly and synthetic processes. Degradation pathways leading to the erosion of the polycyclic scaffold can afford small aliphatic or chain-branched precursors/building blocks with reactive groups like acids or ketones for the construction of diverse scaffolds of higher structural complexity. Polymerization, on the other hand, may generate organic surfaces, coatings, particles and layers on which adsorbed organic molecules can benefit from catalytic and protective effects under UV irradiation conditions.

The actual significance and possible prebiotic implications of these results can be appreciated if it is considered that most of the structural scaffolds and functionalities produced from PAHs in the thermal waters, and chiefly

carboxylic acids, aliphatic carbonyl derivatives and alkylated PAHS, have been detected among the organic components of meteorites, especially carbonaceous chondrites. Thus, for example, 1,2-benzenedicarboxylic acid, bis(2-methylpropyl) ester, was detected also in the soluble compounds of Tagish Lake carbonaceous chondrite.<sup>23,24</sup>

Of particular prebiotic relevance is the generation of 1,4-naphthoquinone from 1-HN. First identified from 1-HN by UV irradiation in water ices,<sup>17</sup> 1,4-naphthoquinones have been implicated as mediators of electron transfer processes in primitive prebiotic systems. The propension of PAHs, mainly oxyPAHs, to undergo oxidative polymerization is well established and supported by many reports in the literature analysing the process in the very early stages<sup>25</sup> and revealing how the structure of the PAH may deeply influence the physical-chemical properties of the resulting polymer.<sup>26</sup> However viable routes for the provision of this quinone in terrestrial prebiotic environments are still missing and not yet well recognized.

Besides the polymerization route, hypothetically involved in the formation of the IOM (has been accounting for the formation of melanin-like precipitate), and the oxidation/hydroxylation route, previously reported by Allamandola, a functionalization route and an erosion route have to be evoked to justify the formation of alkylated naphthalenes and products deriving from the more or less pronounced fission of the naphthalene backbone.

Alkylation products of naphthalene have been also detected in carbonaceous chondrites.<sup>23,24,27</sup>

The detailed mechanisms underlying the above transformation pathways cannot be assessed on the basis of present data and are the focus of ongoing studies. It appears however that specific ingredients in the Pesciarelli spring

waters and the mildly acidic pH conditions are critical, since simple heating in water is not sufficient to bring about the complex sequence of reactions. Ferric/ferrous ions are likely candidates to mediate most of the processes though it seems likely that the entire pool of salts can act in concert.

Overall these results suggest that similar collections of species have been supplied to prebiotic factories of life molecules or their precursors via completely different processes and events like meteorite infall and hydrothermal processing.

### 6.3 Conclusions

In the last decades many efforts have been made to delineate the physical-chemical processes relevant for the emergence of life on the early Earth. A consistent body of experiments has been focused on the analysis of the soluble organic fraction extracted from different kind of meteoritic sample, mainly chondrites, with the aim of tracing a chemical picture of the prebiotic reactions occurring in the early solar system and involved in the origin of life on Earth.

In this context, the present study offers a different approach based on the investigation of the chemical reactivity of three main representative PAHs, NAPH, 1-HN and 1,8-DHN, under chemical conditions of prebiotic relevance. Their exposure to thermal water collected at the Pisciarelli spring inside Phlegrean Fields generates an unexpectedly broad range of structurally diverse products via oxidation, polymerization and aromatic-to-aliphatic fragmentation pathways of possible relevance to prebiotic processes. Of special relevance is the formation of polymers from the two oxyPAHs and the identification by GC-MS analysis of diisopropyl naphthalenes, a new pathway of alkylation of naphthalene rings, methacrylic acid and the ethyl ester of 3-hydroxymandelic acid, deriving from the naphthalene ring fission, bis(2-methylpropyl) ester of 1,2-benzenedicarboxylic acid, detected also in the Tagish Lake carbonaceous chondrite and 1,4-naphthoquinone, a key redox shuttling system which may play a role in the electron transducing mechanisms sustaining primitive life. The formation of naphthoquinones in prebiotic Solfatara-like environments even in absence of oxygen may have been a possible route for the provision of quinones for the first functional living systems.

Moreover, both the oxy-PAHs led to the formation of a set of regioisomeric diisopropylnaphthalenes, denoting that a reductive loss of the phenolic -OH groups and a reaction with isopropyl moiety, deriving from the degradation pathways of the naphthalene ring, have occurred.

Summarizing, PAH processing in hydrothermal systems is proposed as a hitherto overlooked prebiotic scenario underlying the formation and accumulation of structurally and chemically diverse molecules that may be relevant to the emergence of life on early Earth. The results disclosed in this Chapter may provide an important contribution toward filling this gap and adding another small piece to the huge puzzle of prebiotic players at the origin of life.

## 6.4 Experimental section

### 6.4.1 Materials and methods

Naphthalene (NAPH), 1,8-Dihydroxynaphtalene (1,8-DHN), 1-hydroxynaphtalene (1-HN) were purchased from Sigma and used without further purification.

UV-Vis spectra were recorded with a Jasco V-560 instrument.

MALDI mass spectra were recorded on a AB Sciex TOF/TOF 5800 instrument using 2,5-dihydroxybenzoic acid as the matrix. Spectra represent the sum of 15000 laser pulses from randomly chosen spots per sample position. The laser was operated at 3700 Hz in the positive reflectron mode. The mass spectra data were acquired over a mass range of  $m/z$  100– 4000 Da.

ATR spectra of the powders in transmission mode have been recorded with a Nicolet 5700 spectrometer. The spectra have been scanned on the wave number range of 400-4000  $\text{cm}^{-1}$  with a resolution fixed to 4  $\text{cm}^{-1}$ .

Gas-chromatography analyses for determination of the semivolatile organic compounds were performed with a gas chromatograph (Shimadzu 2010 Plus, Japan) coupled with a mass spectrometer (MS-TQ8030- Shimadzu, Japan) and a fused silica HP5-MS capillary column (30 m~ 0.25 mm i.d.) with film thickness of 0.25  $\mu\text{m}$  (Agilent Technologies, US). High purity helium (99.9%) was used as carrier gas at a flow rate of 1.0  $\text{mL min}^{-1}$ . The gas chromatograph was operated in splitless mode and separation was conducted with oven temperature programmed as follows: initial setting at 80  $^{\circ}\text{C}$  (2 min hold) ramped to 180  $^{\circ}\text{C}$  at 20  $^{\circ}\text{C min}^{-1}$  and finally to 300  $^{\circ}\text{C}$  at 5  $^{\circ}\text{C min}$  (9 min hold). The injector was held at 280  $^{\circ}\text{C}$ . The mass spectrometer was operated in scan mode and tuned with perfluorotributylamine (PFTBA)

according to the manufacture criteria. Samples were analyzed after treatment with MSTFA (2,2,2-Trifluoro-N-methyl-N-(trimethylsilyl) acetamide) and mixture of deuterated PAHs as internal standard for quantitative analyses.

For determination of the volatile organic compounds (VOCs) were performed with purge and trap extraction (Atomx, Teledyne Tekmar, USA) followed by a gas chromatographic analysis (Agilent 7820A, USA) coupled with a mass spectrometer (MS-5977B- Agilent, USA). The gas chromatographic separation was conducted with fused silica DB 624-MS capillary column (30 m ~ 0.25 mm i.d. and f.t. of 0.25  $\mu\text{m}$ ) and oven temperature programmed as follows: initial setting at 35 °C (3 min hold) ramped to 100 °C at 6 °C  $\text{min}^{-1}$  and finally to 200 °C at 20 °C  $\text{min}$  (5 min hold). The injector was held at 250 °C. The mass spectrometer was operated in scan mode.

### **6.4.2 Reaction procedure**

The reactions were carried out immersing naphthalene, 1,8-dihydroxynaphthalene and 1-hydroxynaphthalene in the water and mud samples taken at the Pisciarelli spring up to final concentration of 3mg/ml. Only in the case of naphthalene, in order to allow a better dissolving of the compound in water samples, a minimum amount of acetone was added. Reaction mixtures were maintained at 95°C, under stirring, for 48 h. Due to higher reactivity of 1,8-DHN, the latter was further investigated after 20 minutes from the beginning of the reaction. Water samples were used under the same conditions for blank reactions. To avoid any possible microbial contamination, the thermal water taken at the Pisciarelli spring was micro-filtered using 0.20  $\mu\text{m}$  syringe filter.

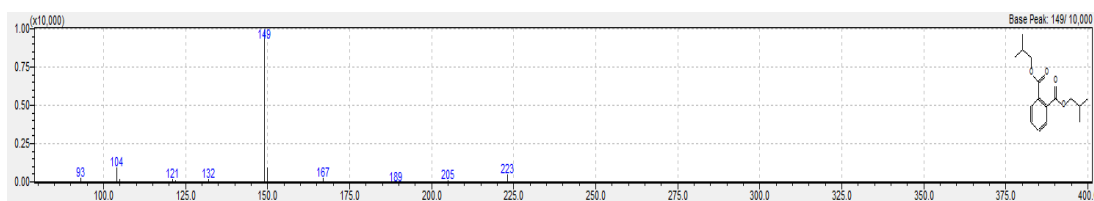
Products formed by heating at 95°C of water samples (10 mL) without selected molecules were performed as references. PAHs molecules were heated at 95°C in thermal water under an argon atmosphere. At the end of the reaction solid precipitate was recovered by centrifugation (7000 rpm for 15 minutes at 4°C) and lyophilization and was characterized by UV-vis, ATR spectroscopies and mass spectrometry (MALDI-MS). The supernatants were extracted by a solid-phase extraction (SPE), 10 ml of sample was filtered and was preconcentrated on a C18 disk (ENVI, -18 DSK SPE Disk, diam. 47 mm). Before starting the extraction process, samples were spiked with 25 µl of decachlorobiphenyl as surrogate standard starting from a solution of 100 µg l<sup>-1</sup>. The disks were pre-condition with methanol and then distilled water. The filter was eluted with a solution of 1:1 dichloromethane and n- hexane. The extract was then concentrated to 200 µl in multivap under nitrogen flow. To the extract was added the 25 µl of MSTFA (2,2,2-Trifluoro-N-methyl-N-(trimethylsilyl) acetamide) and mixed gently. Allow the mixture to react at room temperature for at least 1 min. Successively, was added to the extract the internal standard (mixture of deuterated PAHs) and was injected to a GC-MS (MS-TQ8030-Shimadzu, Japan). Mass range investigated was between m/z 50 and 300. For the qualitative analyses, the spectra were compared with mass spectrum libraries such as NIST.

Another portion of supernatant (5 ml) were extracted with purge and trap system, the samples were heated at 40°C for 10 min followed by purge with helium at flow rate of 40 ml min<sup>-1</sup> for 10 min. The purged analytes are allowed to flow out of the vial through a glass-lined transfer line to a trap packed with suitable sorbent materials. After the purge, place the purge-and-trap system in the desorb mode and preheat the trap to 245°C without a flow of desorption

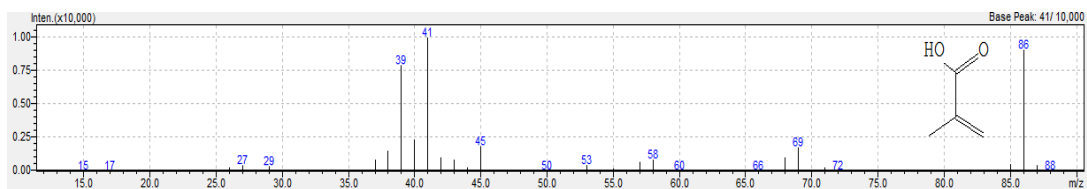
gas. Start the flow of desorption gas at 10 mL/minute for 5 min. and the analytes were injected to a GC-MS.

### 6.4.3 Mass spectra

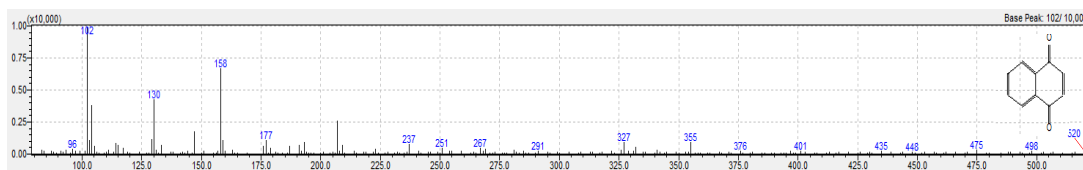
Mass-fragmentation spectrum **1**: 1,2-Benzenedicarboxylic acid, bis(2-methylpropyl) ester



Mass-fragmentation spectrum **2**: Methacrylic acid



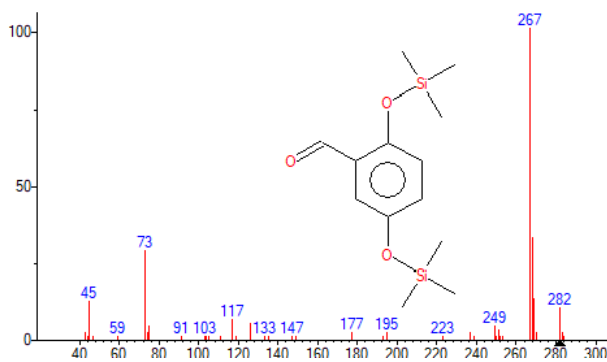
Mass-fragmentation spectrum **3**: 1,4-Naphthalenedione



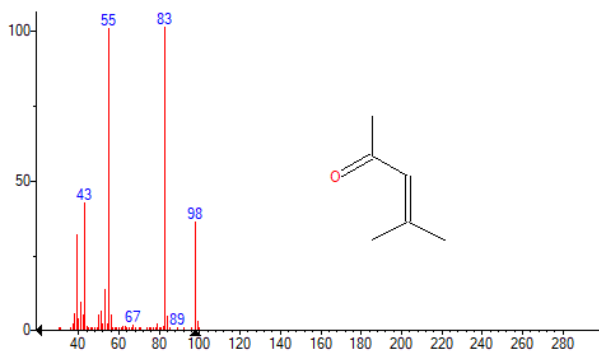
Mass-fragmentation spectrum **4**: di-iso-propylnaphthalene



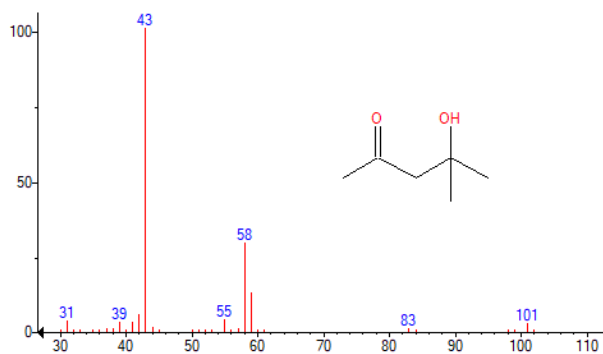
Mass-fragmentation spectrum **5**: p-Trimethylsilyloxyphenyl-bis(trimethylsilyloxy)ethane



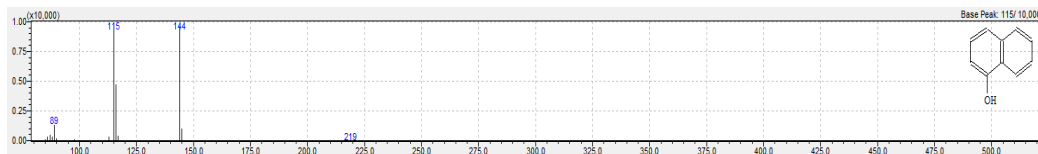
Mass-fragmentation spectrum **6**: 3-Penten-2-one, 4-methyl



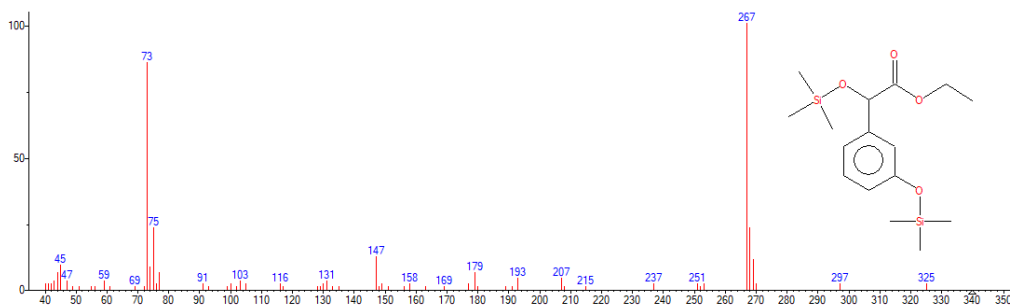
Mass-fragmentation spectrum **7**: 2-Pentanone,4-hydroxy-4-methyl



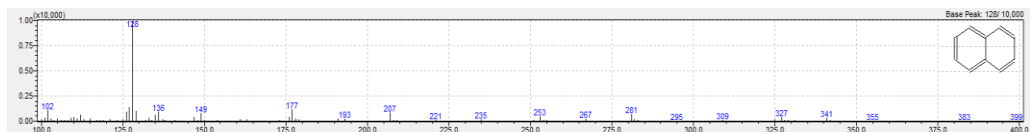
Mass-fragmentation spectrum **8**: 1-Naphthol



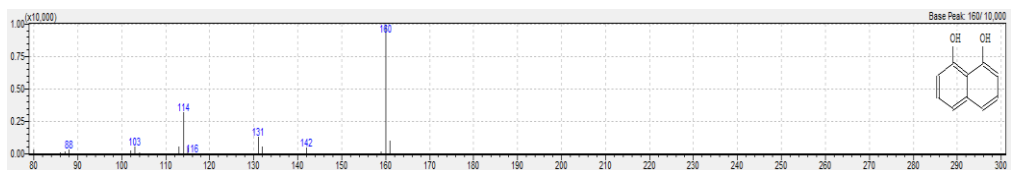
Mass-fragmentation spectrum **9**: 3-Hydroxymandelic acid, ethyl ester



Mass-fragmentation spectrum **10**: Naphthalene



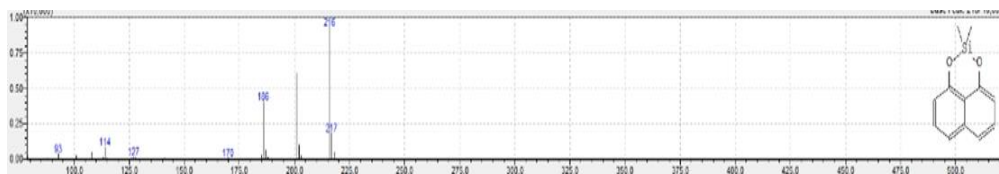
Mass-fragmentation spectrum **11**: 1,8-dihydroxynaphthalene



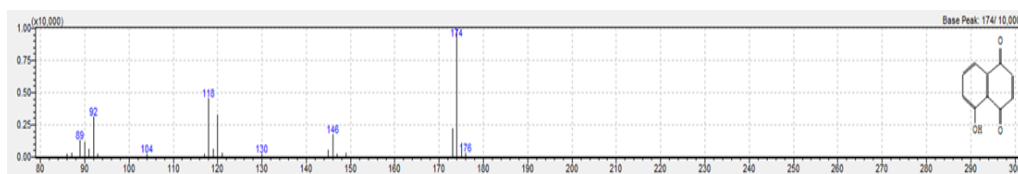
Mass-fragmentation spectrum **12**: Silane, trimethyl(1-naphthyloxy)



Mass-fragmentation spectrum **13**: Dimethyl-1,8-naphthalenedioxysilane



Mass-fragmentation spectrum **14**: 1,4-Naphthalenedione, 5-hydroxy



## References

1. A.Y. Mulkidjanian, A.Yu. Bychkov, D. V. Dibrova, M.Y. Galperin, E. V. Koonin. Open Questions on the Origin of Life at Anoxic Geothermal Fields. *Origins of Life and Evolution of Biospheres* **2012**, 42 (5), 507–516.
2. B. Damer, D. Deamer. The Hot Spring Hypothesis for an Origin of Life. *Astrobiology* **2020**, 20 (4), 429–452.
3. B.K.D. Pearce, R.E. Pudritz, D.A. Semenov, T.K. Henning. Origin of the RNA world: The fate of nucleobases in warm little ponds. *Proceedings of the National Academy of Sciences* **2017**, 114 (43), 11327–11332.
4. N. Merino, H.S. Aronson, D.P. Bojanova, et al. Living at the Extremes: Extremophiles and the Limits of Life in a Planetary Context. *Front Microbiol* **2019**, 10.
5. W.L. Marshall. Hydrothermal synthesis of amino acids. *Geochim Cosmochim Acta* **1994**, 58 (9), 2099–2106.
6. R.J.-C. Hennet, N.G. Holm, M.H. Engel. Abiotic synthesis of amino acids under hydrothermal conditions and the origin of life: A perpetual phenomenon? *Naturwissenschaften* **1992**, 79 (8), 361–365.
7. D. Kopetzki, M. Antonietti. Hydrothermal formose reaction. *New Journal of Chemistry* **2011**, 35 (9), 1787.
8. A. Strazzulli, R. Iacono, R. Giglio, M. Moracci, B. Cobucci-Ponzano. Metagenomics of Hyperthermophilic Environments: Biodiversity and Biotechnology. In *Microbial Ecology of Extreme Environments*; Springer International Publishing, Cham, **2017**; pp 103–135.
9. A. Fedele, M. Pedone, R. Moretti, et al. Real-time quadrupole mass spectrometry of hydrothermal gases from the unstable Pisciarelli fumaroles (Campi Flegrei): Trends, challenges and processes. *Int J Mass Spectrom* **2017**, 415, 44–54.
10. R. Huber, H. Huber, K.O. Stetter. Towards the ecology of hyperthermophiles: biotopes, new isolation strategies and novel metabolic properties. *FEMS Microbiol Rev* **2000**, 24 (5), 615–623.

11. L. Botta, R. Saladino, B.M. Bizzarri, et al. Formamide-based prebiotic chemistry in the Phlegrean Fields. *Advances in Space Research* **2018**, 62 (8), 2372–2379.
12. A. Leger, J.L. Puget. Identification of the ‘unidentified’ IR emission features of interstellar dust? *Astron. Astrophys.* **1984**, 137, L5–L8.
13. L.J. Allamandola, A.G.G.M. Tielens, J.R. Barker. Polycyclic aromatic hydrocarbons and the unidentified infrared emission bands - Auto exhaust along the Milky Way. *Astrophys J* **1985**, 290, L25.
14. A. Blasberger, E. Behar, H.B. Perets, N. Brosch, A.G.G.M. Tielens. Observational Evidence Linking Interstellar UV Absorption to PAH Molecules. *Astrophys J* **2017**, 836 (2), 173.
15. M. López-Puertas, B.M. Dinelli, A. Adriani, et al. Large Abundances Of Polycyclic Aromatic Hydrocarbons In Titan’s Upper Atmosphere. *Astrophys J* **2013**, 770 (2), 132.
16. M. d’Ischia, P. Manini, M. Moracci, et al. Astrochemistry and Astrobiology: Materials Science in Wonderland? *Int J Mol Sci* **2019**, 20 (17), 4079.
17. M.P. Bernstein, J.P. Dworkin, S.A. Sandford, L.J. Allamandola. Ultraviolet irradiation of the polycyclic aromatic hydrocarbon (PAH) naphthalene in H<sub>2</sub>O. Implications for meteorites and biogenesis. *Advances in Space Research* **2002**, 30 (6), 1501–1508.
18. A. Ricca, C.W. Bauschlicher Jr. The reactions of polycyclic aromatic hydrocarbons with OH. *Chem Phys Lett* **2000**, 328 (4–6), 396–402.
19. Y.-J. Chen, M. Nuevo, T.-S. Yih, et al. Amino acids produced from the ultraviolet/extreme-ultraviolet irradiation of naphthalene in a H<sub>2</sub>O+NH<sub>3</sub> ice mixture. *Mon Not R Astron Soc* **2008**, 384 (2), 605–610.
20. S. Potenti, P. Manini, T. Fornaro, et al. Solid State Photochemistry of Hydroxylated Naphthalenes on Minerals: Probing Polycyclic Aromatic Hydrocarbon Transformation Pathways under Astrochemically-Relevant Conditions. *ACS Earth Space Chem* **2018**, 2 (10), 977–1000.
21. R.V. Krishnamurthy, S. Epstein, J.R. Cronin, S. Pizzarello, G.U. Yuen. Isotopic and molecular analyses of hydrocarbons and monocarboxylic acids of

the Murchison meteorite. *Geochim Cosmochim Acta* **1992**, 56 (11), 4045–4058.

22. D. Milshteyn, G. Cooper, D. Deamer. Chemiosmotic energy for primitive cellular life: Proton gradients are generated across lipid membranes by redox reactions coupled to meteoritic quinones. *Sci Rep* **2019**, 9 (1), 12447.

23. D.N. Simkus, J.C. Aponte, J.E. Elsila, et al. New insights into the heterogeneity of the Tagish Lake meteorite: Soluble organic compositions of variously altered specimens. *Meteorit Planet Sci* **2019**, 54 (6), 1283–1302.

24. R.W. Hiltz, C.D.K. Herd, D.N. Simkus, G.F. Slater. Soluble organic compounds in the Tagish Lake meteorite. *Meteorit Planet Sci* **2014**, 49 (4), 526–549.

25. P. Manini, M. Bietti, M. Galeotti, et al. Characterization and Fate of Hydrogen-Bonded Free-Radical Intermediates and Their Coupling Products from the Hydrogen Atom Transfer Agent 1,8-Naphthalenediol. *ACS Omega* **2018**, 3 (4), 3918–3927.

26. P. Manini, V. Lino, G. D’Errico, et al. “Blackness” is an index of redox complexity in melanin polymers. *Polym Chem* **2020**, 11 (31), 5005–5010.

27. J.E. Elsila, N.P. de Leon, P.R. Buseck, R.N. Zare. Alkylation of polycyclic aromatic hydrocarbons in carbonaceous chondrites. *Geochim Cosmochim Acta* **2005**, 69 (5), 1349–1357.